

Influence of Water/Hydrocarbons Co-Condensation on Top of the Line Corrosion

A dissertation presented to  
the faculty of  
the Russ College of Engineering and Technology of Ohio University

In partial fulfillment  
of the requirements for the degree  
Doctor of Philosophy

Thunyaluk Pojtanabuntoeng

December 2012

© 2012 Thunyaluk Pojtanabuntoeng. All Rights Reserved.

This dissertation titled  
Influence of Water/Hydrocarbons Co-Condensation on Top of the Line Corrosion

by

THUNYALUK POJTANABUNTOENG

has been approved for  
the Department of Chemical and Biomolecular Engineering  
and the Russ College of Engineering and Technology by

Srdjan Nesic

Professor of Chemical and Biomolecular Engineering

Dennis Irwin

Dean, Russ College of Engineering and Technology

## ABSTRACT

POJTANABUNTOENG, THUNYALUK, Ph.D., December 2012, Chemical Engineering

Influence of Water/Hydrocarbons Co-condensation on Top of the Line Corrosion

(227 pp.)

Director of Dissertation: Srdjan Nestic

Top of the line corrosion (TLC) is a significant concern in wet gas transportation, where temperature gradients between internal pipeline and outside environments lead to the condensation of water vapor and a certain fraction of hydrocarbons. Liquid water from condensation is greatly corrosive as it is saturated with acidic gases; e.g., CO<sub>2</sub>, H<sub>2</sub>S and CH<sub>3</sub>CO<sub>2</sub>H. TLC is specific to a stratified flow regime when the upper portion of the pipe is not in contact with the flowing liquid phase. Therefore, a conventional mitigation technique such as corrosion inhibitor injection is not successful because the delivery of the corrosion inhibitor is governed by the flow regime. Extensive research has been conducted to better understand this phenomenon and develop improved corrosion mitigation techniques.

Up until the commencement of this project, only hydrocarbon-free TLC systems had been studied. In reality, a certain fraction of hydrocarbons will condense along with water and form two immiscible liquids with different wettability and different corrosivity. This study investigates the influences of straight chain hydrocarbon condensation on TLC. The study is divided into three parts: (i) experimental investigation of wettability and co-condensation processes, (ii) experimental study of corrosion in a co-condensation

environment, and (iii) the prediction of water condensation rate in multi-component systems.

The co-condensation process was monitored using various techniques, which were as visual observation and electrochemical method. Results showed that water has the stronger affinity towards the carbon steel surface. Water accumulates on the steel surface and occupies the majority of the surface regardless of test conditions.

During corrosion tests, iron carbonate ( $\text{FeCO}_3$ ) grows on the steel in co-condensation environments but does not do so during water condensation under the same testing conditions. Surface characterization showed that smaller water droplets are found in co-condensation, indicating that the water is segregated. The water chemistry analysis showed that this can lead to a rise in the pH within the aqueous phase, and hence to less corrosion.

Improving the prediction of water condensation rate, which is the primary parameter in determining the severity of TLC, directly helps to assess the TLC severity. Most of the available TLC prediction models assume that the only condensing component is water. In fact, the presence of condensing hydrocarbons affects the heat and mass transfer within the system. A multi-component co-condensation rate prediction model is developed here and validated with experimental data. The results show that the water condensation rate slightly decreases when hydrocarbons are considered. This is because less heat is given away due to condensation of water alone as condensing hydrocarbons contribute a portion of the heat flux. Furthermore, other physical and hydrodynamic properties change in favor of lowering water condensation rate. Yet, the effect is small

because the latent heat of vaporization of water is significantly higher than that of hydrocarbons.

Additionally, a thermodynamic diagram of water and hydrocarbon is created and coupled with the temperature and pressure profile of the pipe to aid in the determination of locations that are liable to suffer from TLC

## ACKNOWLEDGEMENTS

Though only my name is on the front cover of this dissertation, many people are behind one of the biggest accomplishments of my life.

First and foremost, I would like to express my utmost appreciation to my advisor, Prof.Srdjan Nestic, for all his patient guidance, support, and encouragement during my Ph.D. study.

Many thanks to my project leader, Marc Singer, who worked closely with me and guided me every step of the way. I would like to acknowledge Dr. David Young for his help and advice on the chemistry perspective as well as his patient follow up on my academic progress and a very special thanks to the Water Wetting JIP project leader, Dr.Sonja Richter, and the team members. Major parts of this dissertation would not be accomplished without their technology, equipment, and technical support.

I would like to acknowledge the financial support from industrial sponsors; Conoco Phillips, British Petroleum, Occidental Petroleum Corporation, Total, ENI Petroleum, Chevron, Saudi Aramco, and PTT Exploration and Production.

It was also a pleasure to work and spend time with everybody at the Institute for Corrosion and Multiphase Technology. I would like to express my deepest affection for Tanaporn Tanupabrunsun and Ussama Kaewpradap, colleagues/friends who share the same nationality and kept me away from homesickness.

Finally I would like to express my very deepest gratitude to my family for their unconditional love and endless encouragement they have always given me.

## TABLE OF CONTENTS

	PAGE
Abstract.....	3
Acknowledgements.....	6
List of tables.....	10
List of figures.....	11
Chapter 1: Introduction.....	19
Chapter 2: Literature review.....	23
2.1. Introduction.....	23
2.2. Top of the line corrosion (TLC).....	23
2.2.1. The history of TLC.....	23
2.2.2. Mechanism of top of the line corrosion.....	24
2.2.3. Experimental studies.....	27
2.2.4. TLC mitigation techniques.....	30
2.2.5. Prediction of top of the line corrosion.....	32
2.3. Co-condensation of water and hydrocarbons.....	33
2.4. CO <sub>2</sub> corrosion – the role of wettability and hydrocarbons.....	43
2.5. Gaps in the current literature.....	46
2.6. Objectives of this research.....	47
Chapter 3: Wettability and co-condensation process monitoring.....	48
3.1. Introduction.....	48
3.2. Experimental setup and procedure.....	49

3.2.1. Hydrocarbon selection .....	49
3.2.2. Safety concerns and management .....	51
3.2.3. Wettability study: contact angle measurement .....	51
3.2.4. Visual observation of the condensation process .....	55
3.2.5. Electrical-based techniques .....	58
3.3. Results and discussion .....	60
3.3.1. Wettability study .....	60
3.3.2. Visual observation of condensation processes .....	66
3.3.3. Electrical-based techniques for condensation process investigation .....	73
3.3.4. Discussion .....	88
Chapter 4: Study of top of the line corrosion: The co-condensation scenario .....	94
4.1. Introduction .....	94
4.2. Experimental procedure .....	94
4.2.1. Corrosion test in a stagnant condition .....	94
4.2.2. Corrosion tests in a flowing condition .....	96
4.2.3. Sample preparation .....	99
4.2.4. Post processing and analysis .....	101
4.3. Results of corrosion experiments .....	102
4.3.1. Corrosion experiments in a glass cell setup .....	103
4.3.2. Corrosion in flowing conditions .....	142
4.4. Discussion of results from corrosion experiments .....	148
4.4.1. The decrease in $p\text{CO}_2$ .....	148

4.4.2. The decrease in corroded area.....	150
4.4.3. Changes in water chemistry .....	151
Chapter 5: Condensation rate prediction.....	157
5.1. Introduction.....	157
5.2. Thermodynamics calculation .....	159
5.2.1. Phase envelope calculation .....	159
5.2.2. Comparison with literature data and commercial software results.....	171
5.3. Co-condensation rate prediction model .....	175
5.3.1. Calculation method to obtain gaseous hydrocarbons composition at the interface.....	176
5.3.2. The approach for co-condensation rates calculation for water and hydrocarbon mixtures .....	180
5.3.3. Comparison with the experiments .....	187
5.3.4. Parametric study.....	192
5.4. Implementation into TOPCORP .....	197
Chapter 6: Conclusions.....	201
Chapter 7: Proposals for future work.....	202
List of references.....	204
Appendix I: Condensation rate calculation for experimental conditions.....	214
Appendix II: Surface analysis of carbon steel exposed to co-condensation.....	219

## LIST OF TABLES

	PAGE
Table 1: List of previous studies on condensation of immiscible liquids and the derived heat transfer coefficients. ....	35
Table 2: Comparison of flash point, boiling point and molecular weight of water and hydrocarbons commonly present in wet gas production ( $C_1 - C_6$ ) and selected heavier n-alkanes ( $C_7 - C_{10}$ ).....	50
Table 3: Comparison of physical properties of water and alkanes selected for this study	50
Table 4: Liquid solution resistance .....	75
Table 5: Correlations between (solution) resistances and surface area with various salt concentrations. ....	78
Table 6: Test matrix for corrosion test in a glass cell for 3 days .....	95
Table 7: Test matrix for corrosion tests in glass cell for 2 weeks.....	96
Table 8: Test matrix for corrosion in pure water condensation in a flowing condition....	99
Table 9: Test matrix for corrosion in co-condensation in a flowing condition .....	99
Table 10: Compositional analysis of X65 carbon steel (balance is Fe).....	100
Table 11: Binary interaction parameters used in Eq 5-8 and Eq 5-9 .....	166
Table 12: Wet gas compositions (mole %) used for the comparison .....	173
Table 13: Example of gas composition for co-condensation calculation in Figure 103 and Figure 104 ( $T_b = 70^\circ\text{C}$ and Total pressure = 30 bar) .....	194

## LIST OF FIGURES

	PAGE
Figure 1: Schematic diagram of cross sectional wet gas pipeline showing Top of the Line corrosion. ....	25
Figure 2: Illustration of the condensation processes of immiscible liquids.....	38
Figure 3: a) Water-in-Oil and b) Oil-in-Water contact angle measurements of a hydrophilic surface ( $\theta < 90$ ).....	44
Figure 4: Goniometer (Image courtesy of Water Wetting JIP, Ohio University).....	52
Figure 5: Schematic side view of goniometer: a) transparent acrylic lid; b) stainless steel chamber; c) water injection port; d) hydrocarbon injection port; e) steel sample; and f) drainage (Image courtesy of Water Wetting JIP, Ohio University).....	53
Figure 6: 3D image of carbon steel sample polished with 600 SiC paper with the average roughness of $1\mu\text{m}$ .....	54
Figure 7: 3D image of carbon steel sample polished with 32 SiC paper with the average roughness of $4\mu\text{m}$ .....	54
Figure 8: Depth/area distribution of carbon steel sample polished with 600 SiC paper with the average roughness of $1\mu\text{m}$ .....	55
Figure 9: Image of a borescope used to observe the condensation processes. ....	56
Figure 10: Schematic diagram of experimental setup for the condensation processes observation: a) the borescope, b) the $\text{CO}_2$ inlet, c) the heat sink, d) the Peltier cooler, and e) the sample holder embedded with a thermistor. ....	57
Figure 11: Sample assembly for solution resistance measurements using Electrochemical Impedance Spectroscopy (EIS).....	59
Figure 12: Diagram of conductivity probe (courtesy of water wetting JIP). ....	60
Figure 13: Typical images of n-heptane droplet in a water phase. ....	61
Figure 14: Contact angles of n-heptane, n-octane and n-decane droplets in water on X65 carbon steel polished with 32 grit SiC ( $R_a = 4\mu\text{m}$ ). ....	61
Figure 15: Contact angles of n-heptane, n-octane and n-decane droplets in water on X65 carbon steel polished with 600 grit SiC ( $R_a = 1\mu\text{m}$ ). ....	62

Figure 16: The evolution of contact angles of water droplet in n-heptane on a carbon steel with a surface roughness of 4 $\mu\text{m}$ . .....	64
Figure 17: Contact angles of water droplet in hydrocarbons on X65 carbon steel polished with 600 grit SiC.....	65
Figure 18: Contact angles of water droplet in hydrocarbons on X65 carbon steel polished with 32 grit SiC ( $R_a = 4$ ). .....	65
Figure 19: Condensation behavior of only water with time ( $T_v = 40 \pm 1^\circ\text{C}$ , $T_s = 30 \pm 2^\circ\text{C}$ and $\text{WCR} = 0.07 \pm 0.02 \text{ mL/m}^2/\text{s}$ ). .....	69
Figure 20: Condensation process of only n-heptane ( $T_v = 35 \pm 1^\circ\text{C}$ , $T_s = 27 \pm 1^\circ\text{C}$ and $\text{C}_7\text{CR} = 0.3 \pm 0.1 \text{ mL/m}^2/\text{s}$ ).....	70
Figure 21: The observation of co-condensation process with time ( $T_v = 40 \pm 1^\circ\text{C}$ , $T_s = 27 \pm 2^\circ\text{C}$ and $\text{WCR} = 0.08 \pm 0.02 \text{ mL/m}^2/\text{s}$ , $\text{C}_7\text{CR} = 0.5 \pm 0.15 \text{ mL/m}^2/\text{s}$ ). .....	70
Figure 22: The observation of sequential condensation: Water condensed first followed by co-condensation ( $T_v = 40 \pm 1^\circ\text{C}$ , $T_s = 27 \pm 1^\circ\text{C}$ and $\text{WCR} = 0.09 \pm 0.02 \text{ mL/m}^2/\text{s}$ , $\text{C}_7\text{CR} = 0.5 \pm 0.1 \text{ mL/m}^2/\text{s}$ ).....	71
Figure 23: The observation of sequential condensation: n-heptane condensed first followed by co-condensation ( $T_v = 40 \pm 1^\circ\text{C}$ , $T_s = 27 \pm 1^\circ\text{C}$ and $\text{WCR} = 0.09 \pm 0.02 \text{ mL/m}^2/\text{s}$ , $\text{C}_7\text{CR} = 0.5 \pm 0.1 \text{ mL/m}^2/\text{s}$ ). .....	72
Figure 24: Solution resistance of water as a function of salt concentrations.....	74
Figure 25: Experimental setup for the calibration of surface area and solution resistance using Electrochemical Impedance Spectroscopy (EIS). .....	77
Figure 26: Resistances with percentage of area covered with conductive solution; Dots are experimental data, Lines are empirical correlations. ....	78
Figure 27: Percentage area wetted with water with time in water condensation process (From 0 <sup>th</sup> hour to 20 <sup>th</sup> hour) .....	80
Figure 28: Percentage area wetted with water with time in water condensation process (From 0 <sup>th</sup> hour to 4 <sup>th</sup> hour) .....	81
Figure 29: Responses from conductivity pins: Co-condensation of water and hydrocarbons ( $T_v = 40 \pm 2^\circ\text{C}$ , $\Delta T = 3^\circ\text{C}$ ).....	81
Figure 30: Responses from conductivity pins: Co-condensation of water and heptane ( $T_v = 30$ to $50^\circ\text{C}$ $\text{WCR} = 0.019$ to $0.03 \text{ mL/m}^2/\text{s}$ and $\text{C}_7\text{CR} = 0.12$ to $0.19$ ). .....	82

Figure 31: Responses from conductivity pins: Co-condensation of water and octane ( $T_v = 30$ to $50^\circ\text{C}$ $\text{WCR} = 0.02$ to $0.03 \text{ mL/m}^2/\text{s}$ and $\text{C}_8\text{CR} = 0.04$ to $0.7 \text{ mL/m}^2/\text{s}$ ).....	83
Figure 32: Responses from conductivity pins: Co-condensation of water and decane ( $T_v = 30$ to $40^\circ\text{C}$ and $\text{WCR} = 0.017$ to $0.02 \text{ mL/m}^2/\text{s}$ and $\text{C}_{10}\text{CR} = 0.005$ to $0.007 \text{ mL/m}^2/\text{s}$ ). .	84
Figure 33: Responses from conductivity pins: Pre-condensation with water only followed by the co-condensation of water and n-heptane. ( $\text{WCR} = 0.02 \text{ mL/m}^2/\text{s}$ and $\text{C}_7\text{CR} = 0.19 \text{ mL/m}^2/\text{s}$ ). .....	85
Figure 34: Responses from conductivity pins: Pre-condensation with water followed by the co-condensation of water and various hydrocarbons.....	86
Figure 35: Percentage area wetted with water creating the co-condensation scenario of water and n-heptane ( $\text{WCR} = 0.017 \text{ mL/m}^2/\text{s}$ and $\text{C}_7\text{CR} = 0.10 \text{ mL/m}^2/\text{s}$ ). .....	86
Figure 36: Percentage area wetted with water creating the co-condensation scenario of water and various hydrocarbons. ....	87
Figure 37: Illustration of condensation process in the absence and presence of hydrocarbon (blue: water; yellow: hydrocarbon). .....	90
Figure 38: Replacement of pre-condensed n-heptane with water.....	92
Figure 39: Illustration of the replacement of pre-condensed water with hydrocarbon.....	93
Figure 40: Sample assembly for corrosion tests under flow condition: a.) Top view, b.) Side view, and c.) Cross section view.....	98
Figure 41: Schematic diagram of experimental setup for corrosion test in flowing conditions.....	98
Figure 42: Drawings of sample configuration for corrosion tests in a) a stagnant condition and b) a flowing condition. Blue color represented the xylan paint for isolating area exposed to corrosive environment. ....	100
Figure 43: Surface characterization of sample exposed to corrosion in the pure water system ( $\text{WCR} = 0.09 \text{ mL/m}^2/\text{s}$ ).....	104
Figure 44: a) and b) are surface topography of sample exposed to water condensation ( $\text{WCR} = 0.22 \text{ mL/m}^2/\text{s}$ ) after the removal of corrosion product, c) is the depth profile and d) is the depth/area distribution of this sample. ....	105
Figure 45: Visual image of sample exposed to corrosion in the co-condensation of water and n-heptane ( $\text{WCR} = 0.19 \text{ mL/m}^2/\text{s}$ , $\text{C}_7\text{CR} = 1.2 \text{ mL/m}^2/\text{s}$ ).....	106

- Figure 46: SEM Images and EDX analysis of sample exposed to co-condensation of water and n-heptane (WCR and  $C_7CR = 0.19$  and  $1.2 \text{ mL/m}^2/\text{s}$ , respectively). ..... 107
- Figure 47: SEM images of sample exposed to co-condensation of water and n-heptane after cleaning with Clarke solution. .... 108
- Figure 48: a) and b) are surface topography of sample exposed to co-condensation of water and n-heptane (WCR =  $0.19 \text{ mL/m}^2/\text{s}$  and  $C_7CR = 1.2 \text{ mL/m}^2/\text{s}$ ) after the removal of corrosion product, c) is the depth profile and d) is the depth/area distribution of this sample (location 1). ..... 110
- Figure 49: a) and b) are surface topography of sample exposed to co-condensation of water and n-heptane (WCR =  $0.19 \text{ mL/m}^2/\text{s}$  and  $C_7CR = 1.2 \text{ mL/m}^2/\text{s}$ ) after the removal of corrosion product, c) is the depth profile and d) is the depth/area distribution of this sample (location 2). ..... 111
- Figure 50: Schematic diagram of surface topography analysis ..... 112
- Figure 51: Visual image of sample exposed to co-condensation of water and n-octane (WCR =  $0.2 \text{ mL/m}^2/\text{s}$ ,  $C_8CR = 0.5 \text{ mL/m}^2/\text{s}$ ) ..... 113
- Figure 52: SEM and EDX analysis of sample exposed to co-condensation of water and octane (WCR =  $0.2 \text{ mL/m}^2/\text{s}$  and  $C_8CR = 0.5 \text{ mL/m}^2/\text{s}$ ) – Location A ..... 114
- Figure 53: SEM Analysis of sample exposed to co-condensation of water and octane (WCR =  $0.2 \text{ mL/m}^2/\text{s}$  and  $C_8CR = 0.5 \text{ mL/m}^2/\text{s}$ ) – Border of a big droplet (Location B). ..... 115
- Figure 54: SEM Analysis of sample exposed to co-condensation of water and octane (WCR =  $0.2 \text{ mL/m}^2/\text{s}$  and  $C_8CR = 0.5 \text{ mL/m}^2/\text{s}$ ) – On general area (Location C). ..... 116
- Figure 55: presents SEM images of the sample exposed to the co-condensation of water and n-octane (WCR =  $0.2 \text{ mL/m}^2/\text{s}$  and  $C_8CR = 0.5 \text{ mL/m}^2/\text{s}$ ) after the removal of corrosion products. .... 117
- Figure 56: Surface topography of sample exposed to co-condensation of water and octane after the removal of corrosion product- Under a big water droplet (Location A). ..... 118
- Figure 57: Surface topography of sample exposed to co-condensation of water and octane after the removal of corrosion product- At the border of the big droplet (Location B).. 119
- Figure 58: SEM Analysis of sample exposed to co-condensation of water and n-decane (WCR =  $0.22 \text{ mL/m}^2/\text{s}$  and  $C_{10}CR = 0.08 \text{ mL/m}^2/\text{s}$ ). ..... 121

Figure 59: SEM Analysis of sample exposed to co-condensation of water and n-decane after the removal of corrosion product (WCR = 0.22 mL/m <sup>2</sup> /s and C <sub>10</sub> CR = 0.08 mL/m <sup>2</sup> /s) .....	122
Figure 60: Surface topography of sample exposed to co-condensation of water and n-decane after the removal of corrosion product (WCR = 0.22 mL/m <sup>2</sup> /s and C <sub>10</sub> CR = 0.08 mL/m <sup>2</sup> /s) .....	123
Figure 61: Comparison of corrosion rates obtained from weight loss and the maximum penetration rate of sample exposed to water condensation at two different water condensation rates. (T <sub>g</sub> = 35°C and 50°C, T <sub>s</sub> = 25°C and 30°C, Total P = 1 bar). .....	124
Figure 62: Comparison of corrosion rates obtained from weight loss in the various condensation scenarios (T <sub>g</sub> = 35°C and 50°C, T <sub>s</sub> = 25°C and 30°C, Total P = 1 bar).....	125
Figure 63: Comparison of the average penetration rate from various condensation scenarios (T <sub>g</sub> = 35°C and 50°C, T <sub>s</sub> = 25°C and 30°C, Total P = 1 bar).....	127
Figure 64: Comparison of the maximum penetration rate from the various condensation scenarios (T <sub>g</sub> = 35°C and 50°C, T <sub>s</sub> = 25°C and 30°C, Total P = 1 bar). .....	128
Figure 65: Visual image of sample exposed to water condensation of water for 2 weeks. ....	129
Figure 66: SEM and EDX images of sample exposed to the condensation of water for 2 weeks.....	130
Figure 67: SEM image of sample after cleaning which was exposed to the condensation of water only for 2 weeks.....	130
Figure 68: Surface topography of sample after the removal of corrosion product exposed to condensation of water only for 2 weeks (WCR = 0.22 mL/m <sup>2</sup> /s).....	131
Figure 69: Visual image of sample exposed to co-condensation of water and n-heptane for 2 weeks.....	132
Figure 70: SEM images of sample exposed to the co-condensation of water and n-heptane for 2 weeks (WCR = 0.19 mL/m <sup>2</sup> /s, C <sub>7</sub> CR = 1.21 mL/m <sup>2</sup> /s) – Location A (under a water big droplet).....	133
Figure 71: SEM images of sample exposed to the co-condensation of water and n-heptane for 2 weeks (WCR = 0.19 mL/m <sup>2</sup> /s, C <sub>7</sub> CR = 1.21 mL/m <sup>2</sup> /s) – Location B (at the border of a big water droplet). .....	134

Figure 72: SEM images of sample exposed to the co-condensation of water and n-heptane for 2 weeks ( $WCR = 0.19 \text{ mL/m}^2/\text{s}$ , $C_7CR = 1.21 \text{ mL/m}^2/\text{s}$ ) – on a general area (Location C).....	135
Figure 73: SEM images of sample exposed to the co-condensation of water and n-heptane for 2 weeks ( $WCR = 0.19 \text{ mL/m}^2/\text{s}$ , $C_7CR = 1.21 \text{ mL/m}^2/\text{s}$ ) – On the shining area (Location D).....	136
Figure 74: SEM images of sample exposed to the co-condensation of water and n-heptane for two weeks after the removal of corrosion product.....	137
Figure 75: IFM image of sample exposed to the co-condensation of water and n-heptane for 2 weeks - Location A (under big droplet).....	138
Figure 76: IFM image of sample exposed to the co-condensation of water and n-heptane for 2 weeks - Location B (border of big droplet).....	139
Figure 77: Weight loss corrosion rate against test duration.....	140
Figure 78: Maximum penetration depth against test duration.....	141
Figure 79: Maximum penetration rate against test duration.....	141
Figure 80: SEM Images of samples exposed to condensation rate of $0.48 \text{ mL/m}^2/\text{s}$ , $T_g = 65^\circ\text{C}$ , $T_s = 36^\circ\text{C}$ , at a) 1 day and b) 3 days.....	143
Figure 81: SEM Images of samples exposed to condensation rate of $0.6 \text{ mL/m}^2/\text{s}$ , $T_g = 65^\circ\text{C}$ , $T_s = 16^\circ\text{C}$ , at a) 1 day and b) 3 days.....	143
Figure 82: SEM Images of samples exposed to extremely low water condensation rate of $0.004 \text{ mL/m}^2/\text{s}$ , $T_g = 18^\circ\text{C}$ , at a) 1 day and b) 3 days.....	144
Figure 83: Surface morphology of samples exposed to different co-condensation rates (test duration = 1 day).....	145
Figure 84: Surface morphology of samples exposed to different co-condensation rates (test duration = 3 days).....	146
Figure 85: Corrosion rate in co-condensation scenario as a function of water condensation rate.....	147
Figure 86: Corrosion rates in the absence and presence of n-heptane as a function of water condensation rate.....	148

Figure 87: Calculated partial pressure of CO <sub>2</sub> in the presence of water and three hydrocarbons used in this study as a function of temperature. ....	150
Figure 88: Surface to volume ratio as a function of water droplet size. ....	152
Figure 89: Calculated ferrous ion accumulation within water droplet of different diameters (D) against time (Common parameters: T <sub>surface</sub> = 50°C, Total P = 1 bar, Corrosion rate = 0.50 mm/yr). ....	153
Figure 90: The change in pH within water droplet with different diameter (D) against time (Common parameters: T <sub>surface</sub> = 50°C, Total P = 1 bar, Corrosion rate = 0.50 mm/yr) .....	154
Figure 91: Iron carbonate precipitation rate within water droplet with different diameter (D) against time (Common parameters: T <sub>steel</sub> = 50°C, Total P = 1 bar, Corrosion rate = 0.50 mm/yr).....	156
Figure 92: Dew line/Bubble line of a pure water system.....	160
Figure 93: Phase behavior of water and hydrocarbons (Reproduced from Erbar and Maddox [93]) .....	162
Figure 94: Diagram for the hydrocarbons dew line calculation. ....	170
Figure 95: Diagram for the hydrocarbons bubble line calculation. ....	172
Figure 96: Comparison of hydrocarbons phase envelope and water dew line for Gas A to Gas F. ....	174
Figure 97: Diagram illustrating the flash calculation for the determination of vapor and liquid composition. ....	179
Figure 98: Schematic diagram for condensation rate calculation steps.....	186
Figure 99: Vapor temperature profile along the length of condenser and the comparison with the measurement. ....	189
Figure 100: Difference in the calculated and the measured vapor temperature at the outlet of condenser. ....	190
Figure 101: Comparison between the measurement and the predicted value of the integrated water condensation rate in a co-condensaion scenario. ....	191
Figure 102: Comparison between the measurement and the predicted values of the integrated n-heptane condensation rate in a co-condensaion scenario. ....	192

Figure 103: Effect of temperature gradient on condensation rate of water and hydrocarbons of Gas 1 and Gas 2; Total Pressure = 30 bar, Pipe Diameter = 0.2 m, $v_g = 1$ m/s, and $T_b = 70^\circ\text{C}$ .....	195
Figure 104: Effect of temperature gradient on condensation rate of each hydrocarbon of Gas 2; Total Pressure = 30 bar, Pipe Diameter = 0.2 m, $v_g = 1$ m/s, and $T_b = 70^\circ\text{C}$ . .....	196
Figure 105: Effect of temperature gradient on condensation rate of water and hydrocarbons of Gas 1 and Gas 3; Total Pressure = 30 bar, Pipe Diameter = 0.2 m, $v_g = 1$ m/s, and $T_b = 70^\circ\text{C}$ .....	197
Figure 106: Schematic diagram of the implementation of co-condensation into TOPCORP.....	200

## CHAPTER 1: INTRODUCTION

Corrosion is the process of chemical deterioration of materials, usually metals. Corrosion occurs naturally and affects many applications such as transportation infrastructure, manufacturing, petroleum production systems and refineries, etc.

Oil and gas reservoirs are nowadays typically in remote areas both offshore and onshore. Pipeline transportation systems are the most cost effective means for transporting produced oil and gas. It is uneconomic to use stainless steels or corrosion resistant alloys to construct these pipeline networks. The use of carbon steel together with the injection of corrosion inhibitor can be the most economic and effective choice for pipeline internal corrosion management [1]. This is primarily due to carbon steel's low cost, good availability and excellent mechanical strength. However, carbon steel pipe can suffer from corrosion both externally and internally. Corrosion accounts for 70% of pipeline failures with 58% of these occurring internally [2].

Internal corrosion is caused by water and dissolved acid gases produced along with the desired hydrocarbons. The key culprits behind this damage include carbon dioxide ( $\text{CO}_2$ ), hydrogen sulfide ( $\text{H}_2\text{S}$ ) and organic acids ( $\text{HCO}_2\text{H}$ ,  $\text{CH}_3\text{CO}_2\text{H}$ , etc.). Strategies have been developed to mitigate such corrosion. One of the common methods is to inject corrosion inhibitors, which are surface-active chemicals that, when added in small amounts, retard the corrosion processes.

Production of *wet* hydrocarbon gas has been increasing over time. The term *wet gas* refers to the hydrocarbon (and/or water) that can condense at the internal surface because of the change in temperature and pressure in the lines [3]. One specific corrosion

phenomenon related to the wet gas production is known as *Top of the Line Corrosion (TLC)*. TLC received attention from both industry and research laboratories globally as, to date, there is no effective means of combating this type of corrosion. Conventional corrosion inhibitors that are injected into the liquid phase can only stay in the liquid phase, which is dominant at the bottom of the pipe.

TLC is relatively recently recognized as a distinct corrosion phenomenon (in the past decade or two) even if the first TLC failure was reported in the 1960's [4]. Over the past decade, failures related to TLC have been increasingly documented with extensive experimental studies being conducted and published. Various laboratories have been engaged in working closely with industry to investigate the TLC mechanism and develop effective TLC prevention methods. Over the last two decades devoted to investigating the mechanism behind TLC, empirical models were first developed [5] followed by semi-empirical [6] and finally some simplified mechanistic models [7–9].

Though TLC is much better understood now than it was four decades ago, prevention and mitigation of TLC remain ineffective. Moreover, many important phenomena remain poorly understood, necessitating further investigations. For example: exploitable liquid hydrocarbons co-condense with water but their presence has only occasionally been mentioned in the literature and has not been properly accounted for in the analyses and the models. Actually, while it is widely accepted that there is a significant effect of co-condensation on TLC, there is no dedicated research reported which investigates the various aspects of co-condensation of hydrocarbons and water and their effect on TLC.

In wet gas production, only a certain range of hydrocarbons is produced. Commonly, these hydrocarbons range from methane ( $\text{CH}_4$ ) to hexane ( $\text{C}_6\text{H}_{14}$ ). Heavier hydrocarbons may exist in minute amounts and are often referred to as  $\text{C}_{7+}$ . Given appropriate conditions, heavier hydrocarbons may condense during transportation. Since hydrocarbons and water are immiscible, they form two liquid phases when they co-condense.

Study of the co-condensation of immiscible liquids is not new. Researchers have conducted such experiments extensively since the 1940s. Nonetheless, the focus was not on corrosion but rather on heat exchanger design applications. Liquid water and hydrocarbons are immiscible with each other and the two liquids have different wettability and corrosivity. It would be expected that if water is displaced by the presence of hydrocarbons, the TLC would subside. However, it can also be speculated that if water strongly adheres to the steel, TLC would still be a concern.

The main objective of this dissertation is to investigate the influence of hydrocarbon co-condensation on TLC. The present study is divided into three parts; the wettability and co-condensation experimental study, the experimental study of corrosion under co-condensing conditions, and the prediction of water and hydrocarbon condensation rates.

The present study was a part of the long-term Top of the Line Corrosion Joint Industry project (TLC-JIP), conducted at Ohio University. One of the main deliverables of this TLC JIP is TOPCORP (Top of the Line Corrosion Prediction model), which is a fully mechanistic model for the prediction of TLC. One of the identified shortcomings of

TOPCORP is the lack of effect of hydrocarbon condensation and it is hoped that this will be improved based on the results presented below.

## CHAPTER 2: LITERATURE REVIEW

### 2.1. Introduction

Top of the line corrosion (TLC) occurs exclusively in a stratified wet gas transportation line where conventional corrosion mitigation techniques fail. During the transportation of gas, water vapor condenses on the pipeline wall where the temperature is colder than the transported fluid. Acid gases, such as carbon dioxide (CO<sub>2</sub>), hydrogen sulfide (H<sub>2</sub>S) and volatile organic acids (HCO<sub>2</sub>H, CH<sub>3</sub>CO<sub>2</sub>H) dissolve into the condensed water causing severe corrosion.

In this chapter, published experimental data and findings are grouped into three subject areas:

- Top of the line corrosion: history, mechanisms, experimental studies, mitigation techniques and advances in its prediction.
- Condensation processes of water and hydrocarbon.
- CO<sub>2</sub> corrosion – the role of wettability and hydrocarbons

### 2.2. Top of the line corrosion (TLC)

#### 2.2.1. *The history of TLC*

Top of the line corrosion (TLC), as the name suggests, refers to a corrosion attack on the top section of the pipe in (10 – 2 o'clock) position, due to the temperature difference between the inside and outside of the pipe, which results in condensation of water vapor on the upper surface of the pipe. Condensed water is significantly more corrosive than accumulated water at the bottom of the line as it contains no corrosion inhibitor or buffers.

The first TLC failure was published in 1963 [4]. The failure occurred in the gathering system at the LACQ sour gas field, France. The authors observed corrosion occurring where the flow regime was stratified and was caused by the condensation of water located at the top part of the pipe. A light hydrocarbon condensate was present but only in a very minute amount compared to the condensed water. After a gap of 35 years, more field cases related to TLC were published [10–12], returning the focus of the corrosion community to this phenomenon.

Recently, Gunaltun *et al.* reported a special case of TLC termed *cold spot corrosion* [11]. Cathodic protection was employed on that particular pipeline. The insulation was removed in order to apply an anode patch. Inspection under the anode patch revealed severe corrosion of the pipeline due to the significant local water condensation rate at that specific location. Thus, a faster condensation rate of water was again proven to be the primary cause of TLC.

Not only have wet gas transportation systems suffered from TLC, Babakr and Bairamov reported TLC failures in wastewater treatment systems due to multiple pinhole leaks [13].

### 2.2.2. Mechanism of top of the line corrosion

Figure 1 illustrates the cross section of a wet gas transportation pipeline. In some cases, part of the pipe is buried under the soil/seabed which acts as thermal insulation whereas the top section is either not buried or insufficiently insulated. This situation leads to the condensation of water vapor at the top sections of the pipe where the temperature

gradient between the cold environment and warm fluid is the highest. The corrosion at the 10 – 2 o'clock position is usually referred to as the *Top of the Line corrosion (TLC)*.

TLC was often found as localized corrosion or *mesa* attack. Deep pits with flat bottom (*mesa* attack) were reported from both field and laboratory studies [4], [14], [15]. Water condensed on the side of the pipe wall generally runs down due to the gravity which causes less problematic uniform corrosion [10]. Water accumulates at the bottom due to gravity and can cause corrosion, which is usually referred to as *bottom of the line corrosion (BLC)*. Generally, with no inhibitor injection, BLC is more severe than TLC [16]. However, corrosion inhibitors are normally injected and they stay in the accumulated water at the bottom of the line. Hence, BLC is retarded but not TLC.

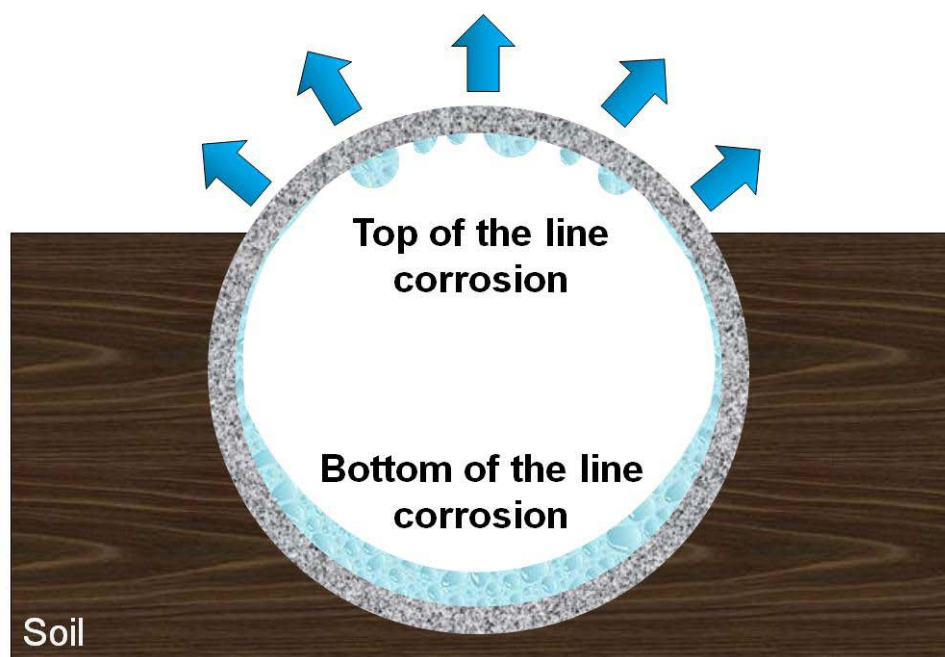


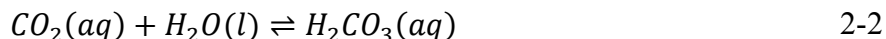
Figure 1: Schematic diagram of cross sectional wet gas pipeline showing Top of the Line corrosion.

The principle corrosion mechanisms are the same for both TLC and BLC. CO<sub>2</sub> dissolves in the aqueous phase (Reaction 2-1) and reacts with water to form a carbonic acid (Reaction 2-2). The carbonic acid then dissociates releasing hydrogen ions and bicarbonate ions (Reaction 2-3), which can further dissociate to release additional hydrogen ions and carbonate ions (Reaction 2-4).

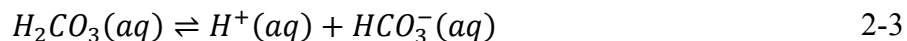
CO<sub>2</sub> dissolution:



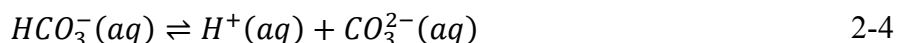
Carbonic acid (H<sub>2</sub>CO<sub>3</sub>) formation:



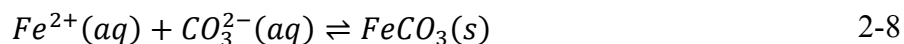
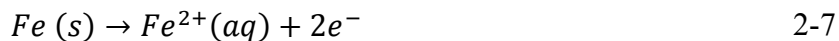
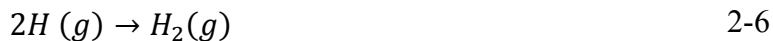
Carbonic acid dissociation:



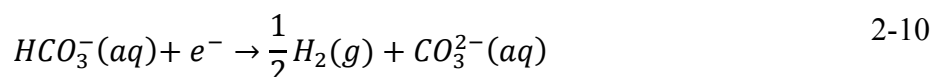
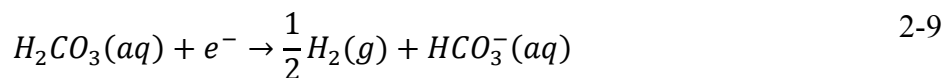
Bicarbonate dissociation:



The primary cathodic reaction is the hydrogen ion reduction, where hydrogen ions receive electrons from iron (Fe) to form hydrogen gas (Reaction 2-5 and Reaction 2-6). The only significant anodic reaction is iron oxidation where Fe, after giving up two electrons to hydrogen ions, becomes a ferrous ion, which then dissolves into the aqueous phase (Reaction 2-7). Under certain conditions, ferrous ions and carbonate ions may nucleate and grow an iron carbonate layer (FeCO<sub>3</sub>) as shown in Reaction 2-8, which can be protective or non-protective depending on various parameters [17–19].



Direct reduction of carbonic acid and bicarbonate ion is also possible.



There is a debate as to whether CO<sub>2</sub> acts only as an indirect reservoir of hydrogen ions (Reaction 2-3 and Reaction 2-4) or if its hydrated derivatives can be directly reduced (Reaction 2-9 and Reaction 2-10). However, resolving this controversy is not within the scope of this dissertation and is the subject of ongoing research within the ICMT.

### 2.2.3. *Experimental studies*

Extensive laboratory research has been conducted and key parameters influencing TLC have been investigated (e.g., temperature, pressure of acid gases, total pressure, acetic acid, etc.) [7], [14–16], [20–29].

The experimental setup design was crucial for conducting representative experiments. Various experimental setups for the investigation of TLC were developed. For example: a 4-inch ID flow loop was used to represent a multiphase wet gas transportation pipeline condition and electrical resistance (ER) probes were utilized to

quantify the corrosion behavior for both TLC and BLC [16]. The authors found that BLC rates were higher than TLC rates under a stratified and wavy stratified flow. When conditions (pressure, gas and liquid velocity) led to annular flow, TLC and BLC rates became similar.

In 2003, Vitse *et al.* conducted TLC studies in a 4-inch high temperature/high pressure stainless steel flow loop [7]. ER probes and weight loss samples were used for the corrosion monitoring. The influences of gas temperature, CO<sub>2</sub> partial pressure, gas velocity, and water condensation rate were investigated. The authors observed that the corrosion rate increased with the gas temperature up to 70°C and decreased when gas temperature was above 80°C. Thicker condensate film, the precipitation of protective iron carbonate, and the higher pH in the condensed water were hypothesized. Increasing pCO<sub>2</sub> caused the corrosion rate to increase, especially when the gas temperature was 70°C and 90°C due to intense condensation. When condensation rate was lower and the gas temperature was 50°C and 90°C, pCO<sub>2</sub> had little influence on corrosion rate due to the precipitation of FeCO<sub>3</sub>. At 90°C, increasing gas velocity promoted higher water condensation rate but the corrosion rate remained constant. On the other hand, at 50°C, both the water condensation rate and the corrosion rate increased with increasing gas velocity. The idea of a critical condensation rate was proposed but exact numbers were not specified. When water condensation rate was lower than the critical threshold, it was likely that the saturation of FeCO<sub>3</sub> was reached. The FeCO<sub>3</sub> layer could be protective because it could act as a diffusion barrier against corrosive species in the bulk. The pH in the condensed water increased as well due to slow replenishing rate of freshly condensed

water. On the other hand, if the water condensation rate was above the critical threshold, this could result in a fast recycling of the condensed water preventing the saturation point from being reached and not allowing  $\text{FeCO}_3$  to form.

In 2004, Singer *et al.* [22] used the same flow loop to investigate the effect of acetic acid on TLC and BLC. Acetic acid is another weak acid present in oil and gas production that can accelerate the corrosion rate in various ways [20], [21], [30], [31]. In this test, the concentration of acetic acid was varied from 0 to 1000 ppm. In stratified flow, the BLC rate was 10 times greater than that obtained in TLC. Dense  $\text{FeCO}_3$  was detected only on TLC samples and corrosion proceeded uniformly whereas localized corrosion was observed at the bottom of the line with no precipitation of  $\text{FeCO}_3$ .

Later, Hinkson *et al.* [25] investigated the composition distribution of acetic acid in the condensed water. It was found that total acetic acid in the condensed water decreased with an increasing water condensation rate. Additionally, the corrosion process produces  $\text{Fe}^{2+}$  which increases condensate pH due to the consumption of hydrogen ions, hence, acetic acid dissociates more, and less of the total acetic acid was measured.

Hydrogen sulfide, another corrosive agent, causes both TLC and BLC pipeline related failures to occur. The so-called “sour” corrosion mechanism is known to be different from that of  $\text{CO}_2$  and remains poorly understood. Many researchers have been studying the effect of this parameter in TLC [23], [24], [26], [27]. Similar to sour BLC, the severity of sour TLC depends mainly on the type and protectiveness of the corrosion product. Pugh proposed that, unlike sweet TLC, temperature was the primary factor whereas the water condensation rate was the secondary one [26].

All in all, extensive research has been conducted to advance the understanding of TLC mechanisms and its influencing parameters. Yet, the presence of hydrocarbons have been mentioned but never been investigated.

#### 2.2.4. *TLC mitigation techniques*

In order to control TLC, two main strategies have been followed:

- Reduction of the condensation rate of water.
- Delivery of a corrosion inhibitor to the top section of the pipe.

Thermal insulation is the most common choice to reduce the water condensation rate. In addition, most pipelines are insulated with layers of coatings. The partial removal of this insulation could result in severe TLC, as was discussed above [11].

Erickson *et al.* [32] simulated the possibility of the transportation of droplets of water containing a corrosion inhibitor from the bottom of the line up to the top, by the flow. The authors suggested that at a high gas flow rate and high liquid holdup up to 70% of the liquid could be entrained as droplets. However, less than 1% of those could reach the top and they could be diluted significantly by the condensation of water.

As conventional inhibitor injection fails to mitigate TLC, many innovative techniques have been developed to deliver a corrosion inhibitor to the top section of the pipe. Gunaltun and Belghazi [21] suggested that a batch treatment could be performed. In this case, the corrosion inhibitor is loaded in between the two plastic spheres called “pigs”, which move with the flow. Laboratory work was conducted to identify the required velocity, frequency, and concentration of the inhibitors. The disadvantages of

this method were pointed out by the authors with the main one being the interruption of production and in some cases it was difficult to meet the required treatment frequency.

Another method is called the “V-jet” pig [33] where a water soluble corrosion inhibitor is added to the bottom of the line fluid, where the V-jet pig sweeps it up and sprays it through a nozzle, which is projected at a 45° angle upward, towards the top of the pipe. Similar restrictions were encountered as the ones described above.

Recently, a new technique involving a foam matrix containing a corrosion inhibitor was introduced [34], [35] as a method to deliver the inhibitor to the top of the line. One of the advantages that the authors claimed for this technique was that there was no need to interrupt the production. Hence, the treatment could be performed as frequently as needed. A foam is injected continuously into the line for a period of time creating a slug containing corrosion inhibitor. The foam expands and coats the pipe with the corrosion inhibitor. The authors expected that the foam matrix would gradually dissipate over a certain length of pipe. There has been no field test reported to confirm whether this novel technique causes any downside such as increased pressure drop.

Vapor phase corrosion inhibitor (*VCI*) is another promising new technique. Volatile compounds having either a neutralizing effect or a film-forming property are injected in the liquid phase. Since they are volatile, an equilibrium is established among liquids at the bottom, vapor phase, and the condensed liquid at the top [36]. However, Schmitt *et al.* suggested that using a volatile compound could lead to an increase safety concerns due to flammability [37].

Glycol is normally injected into the lines to prevent gas hydrate (clathrate) formation. When present in significant quantities (e.g. 50%) it also reduces the partial pressure of the water vapor phase. Hence, there is less water condensation and less TLC is expected. Nyborg *et al.* studied the effect of glycol content in the vapor phase on TLC using a three phase flow loop [38]. The authors found that the glycol content in the vapor phase decreased in the presence of hydrocarbon condensate layer, leading to more TLC.

#### 2.2.5. Prediction of top of the line corrosion

Originally, engineers have relied on simple empirical models based on experimental observations proposed by de Waard *et al.* [5] (Eq 2-11). The authors suggested that the water condensation rate (WCR) rarely exceeded 0.25 mL/m<sup>2</sup>/s, and introduced a corrosion rate reduction factor which has been heavily relied on as there was no better prediction tool available at the time.

$$F_{cond} = 0.4 \times WCR \text{ when } WCR < 0.25 \text{ mL/m}^2/\text{s}$$

$$F_{cond} = 1 \times WCR \text{ when } WCR > 0.25 \text{ mL/m}^2/\text{s}$$

Eq 2-11

Recently, more elaborate calculations have accounted for the effect of water condensation rate and the saturation level of FeCO<sub>3</sub> [39]. After extensive experimentation and advancement in the understanding of the processes that underpin TLC, a semi-empirical model [6] was proposed, which was later upgraded to a mechanistic model [7]. The water condensation was accurately modeled based on the heat and mass transfer relating to the gas phase, pipewall, and a series of coatings/insulation layers and a filmwise condensation of water vapor. For the corrosion process, the model included the influence of a mass transfer of corrosive species through the condensed film to the pipe

wall, the change in water chemistry as corrosion proceeded, and the possibility of the formation of a corrosion product layer.

In 2008, after conducting experiments and verifying that water condensed in a dropwise manner and not filmwise, Zhang *et al.* [9] modified the previous model by improving how the water condensation rate was calculated using the dropwise condensation model. Similar predictive tools were apparently developed elsewhere [40], [41], however, no detail was provided.

Any model can be of little value unless it is validated with field data. Though real pipeline operation can be very complex, a good model that has physical meaning should account for the influence of the key parameters and give meaningful predictions. A comparison of de Waard's empirical factor and a full mechanistic model to the Inline Inspection (ILI) results was presented [7], [42]. The result showed that the de Waard model was too conservative in most cases.

The comparison of recent field inspection results showed that in some cases the most severe TLC attack did not occur at the beginning of the pipeline where the water condensation should be at the highest level [43]. It was suggested that this was due to the presence of hydrocarbon co-condensation that retarded corrosion.

### **2.3. Co-condensation of water and hydrocarbons**

An extensive literature relating to the co-condensation of immiscible liquids in heat exchangers covers the period from 1930-2000. A key focus was on developing a correlation for the heat transfer coefficient when two immiscible liquids condense on a cooled vertical or horizontal surface.

Kirkbride was the first to publish work related to the simultaneous condensation of binary immiscible liquids.[44] The author noted that non-polar organic liquids condensed in a filmwise manner, owing to their lower surface tension, whereas higher surface tension liquids, such as water and aniline, condensed in a dropwise process. By increasing the condensation rate, water and aniline eventually condensed as a continuous film covering the condenser surface. A simple heat transfer coefficient correlation accounting for the effect of co-condensation (shown in Table 1) was proposed and was in good agreement with their experimental data.

Table 1: List of previous studies on condensation of immiscible liquids and the derived heat transfer coefficients.

Ref.	Water with -	Condensing surface		Correlations of condensate heat transfer coefficient
		Type	Orientation	
[44]	Benzene, Naptha	Steel	Horizontal	$h_m = \frac{h_1 Q_1 + h_2 Q_2}{Q_1 + Q_2}$
[45]	Heptane	Wrought iron	Vertical	-
[46]	Benzene, Toluene, Chlorobenzene, Trichloroethylene, Tetrachloroethylene	Copper (oxidized)	Horizontal/ outer	$h = \frac{366 \sqrt[4]{\frac{1}{D} \left(1 - \frac{0.0284}{D}\right)}}{1 - 0.0085 \text{ vol\% } H_2O} + \frac{1.67}{D}$ <p>Where D is O.D. of tube in ft</p>
[47]	Benzene, Toluene, Chlorobenzene	Copper	Vertical	$h_m = 79 \left( \frac{\omega_1 \lambda_1 + \omega_2 \lambda_2}{\omega_1 L} \right)^{0.25}$
[48]	Benzene, Heptane, and Carbon tetrachloride	Brass	Vertical	<p>For Film-Lens pattern;</p> $h_m \left( \frac{\mu^2}{k^3 \rho^2 g} \right)^{1/3} = 1.47 \left( \frac{4\Gamma}{\mu} \right)^{-1/3}$ <p><math>\mu</math> is the viscosity of wall-wetting liquid  <math>\rho</math> is the weight average liquid density  <math>k</math> is the volumetric average of liquid thermal conductivity</p> <p>For Channeling pattern;</p> $h_m = \frac{a\lambda_a h_a + b\lambda_b h_b}{a\lambda_a b\lambda_b}$
[49]	-Toluene, Carbon tetrachloride, Benzene, Chlorobenzene, 1,2-dichloroethane, heptane, and 1,1,2-Trichloroethylene	-	-	$\frac{h_m}{h_1} = \left[ \frac{1}{H_\infty} + \frac{1}{H_{20}(1 + \alpha)e^{B\Delta T_f}} \right]^{-1}$ <p>Where:</p> $H_\infty = 7.6 - 1.8(N_{Pr1} - N_{Pr2})$ $H_{20} = \frac{17.30 \times 10^{-10} N_{Pr1}}{N_{OH1} \left( \frac{\Delta\sigma}{\sigma_1} \right)^{1/2} m \left( \frac{M_2}{M_1} \right)^2}$ $B = 0.035^\circ\text{F}^{-1}$

Table 1 (continue):

Ref.	Water with.	Condensing surface		Correlations of condensate heat transfer coefficient
		Type	Orientation	
[50]	Freon-112, Freon-113, Perchloroethylene, and p-Xylene	Gold plated copper	Vertical	$h_L = v_1 h_1 + v_2 h_2$
[51]	Benzene, Cyclohexane, Carbon tetrachloride, Trichloroethylene	Copper and polytetrafluoroethylene- coated copper	Horizontal	$h_m = \frac{h_{Nu}}{1 - A \left[ \frac{\Delta\sigma^3 \Delta\rho}{\mu^4 g} \right]^B \left[ \frac{\mu\lambda}{k\Delta T_f} \right]^C}$ <p>Where A = <math>1.99 \times 10^4</math>, B = -0.413 and C = -0.286 for copper tube  A = 0.047, B = 0.143 and C = -0.359 for P.T.F.E. coated-copper tube</p>
[52]	Toluene and n- Heptane	-	Vertical	Compared [50] and [48]
[53]	n-Heptane, i-Octane, and n-Octane	Copper	Horizontal, Vertical, and flat surface	$h_m = \frac{\omega_1 \lambda_1 + \omega_2 \lambda_2}{\omega_1 \lambda_1 / h_1 + \omega_2 \lambda_2 / h_2}$

Patterson *et al.* [45] conducted experiments where water and heptane condensed on a vertical tube surface enclosed in a transparent Pyrex glass jacket. Though the authors could observe and monitor the condensation process closely, no detailed description was given. They did not propose a heat transfer co-efficient correlation based on their experimental data.

Baker and Tsao [46] later widened Kirkbride's study. New empirical correlations were proposed based on visual observation of condensation phenomena. When immiscible liquids were condensed, water formed droplets dispersed within the organic film and the surface of the condensate was roughened. The overall heat transfer

coefficient of the condensate was expected to increase because water has a relatively high thermal conductivity and heat capacity. Hence, the more water was present, the higher the heat transfer coefficient. The authors also observed that the variation of the physical properties of all organic liquids over the range of their test conditions was not greater than 10% and the heat transfer coefficient was a strong function of tube diameter and the amount of water condensation.

Possible condensation patterns of binary immiscible liquids were summarized by Hazelton and Baker [47], which served as a basis for illustrations shown in Figure 2. The possible condensation patterns are:

1: Film-Drop (I)

An organic liquid condenses and forms a uniform film covering the surface. Water condenses as droplets on the organic film surface. Water only “floats” and flows along the organic film surface and does not attach to the condensing surface.

2: Film-Drop (II)

Similar to *Film-Drop (I)* except that the water becomes the continuous phase and the organic liquid condenses as droplets at the water surface.

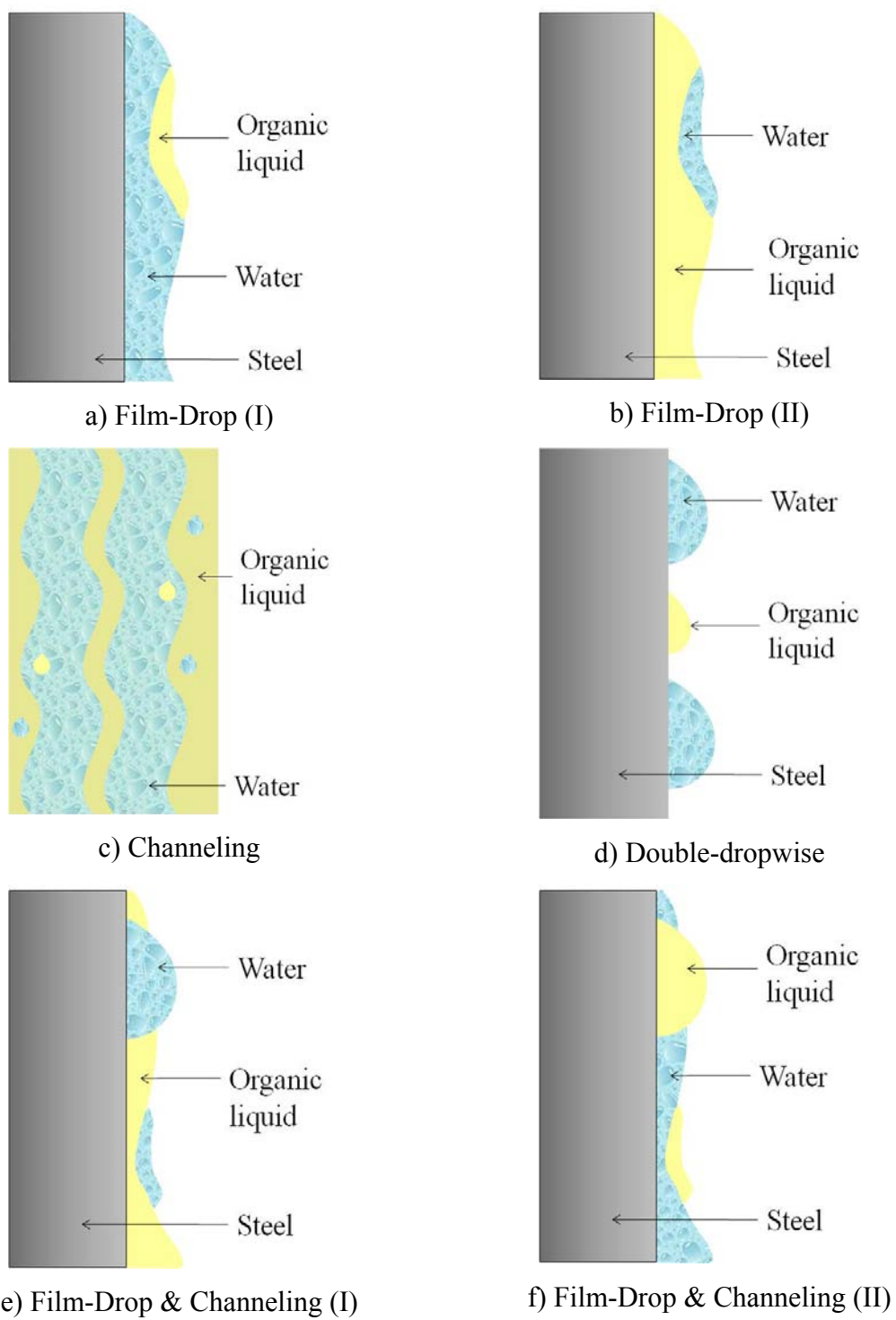


Figure 2: Illustration of the condensation processes of immiscible liquids.

### 3:Channelling

Both liquids condense as films on the condensing surface. Water can condense as droplets on the organic film (similar to in *Film-Drop (I)*), which flow along the vapor/organic liquid interface and join a water rivulets. Similarly, organic liquid can form droplets on the vapor/water interface and join the organic rivulets.

### 4:Double-dropwise

Both liquids wet the condensing surface poorly. Therefore, both liquids are present as isolated droplets on the surface.

### 5:Film-Drop & Channeling (I)

Organic liquid preferentially wets the surface and has droplets of water flowing on it. Additionally, some area is wetted with large droplets of water, which can coalesce and form rivulets.

### 6:Film-Drop & Channeling (II)

Similar to the *Film-Drop & Channeling (I)* except that the water becomes the continuous phase.

It should be pointed out that the condensation patterns described above were primarily observed on either a vertical surface or the outer surface of a horizontal tube. There was no observation made on inner horizontal tube surfaces, which are of interest here. Additionally, for water and most organic liquids, the condensation patterns 1, 3 and 5 are commonly encountered [54]. No literature was found which reported condensation patterns 2, 4 and 6.

In a different study, it was also observed that the presence of organic liquids enhanced the dropwise condensation of water.[55] Again, experiments were conducted in a vertical tube.

Akers and Turner [48] observed the co-condensation process of water/benzene ( $C_6H_6$ ), water/heptane ( $C_7H_{14}$ ) and water/carbon tetrachloride ( $CCl_4$ ) in a stagnant vapor phase. The authors stated that in immiscible liquid co-condensation, the liquid component with the lowest surface tension would wet the condensing surface. The main condensation patterns were types 1, 3 and 5 described above. The authors observed that the condensation pattern followed a *Film-Drop* mechanism at low condensation rates. At higher condensation rates, the condensation process became *Channeling* type. Generally, the *Channeling* type condensation process had higher heat transfer coefficients than the *Film-Drop* type, as water which has higher thermal conductivity, occupied the surface. Two heat transfer coefficient correlations were proposed, one was for the *Film-Drop* type condensation and another for *Channeling* type, as shown in Table 1.

Sykes and Marchello [49] proposed semi-empirical heat transfer coefficients termed the “nucleation model” as shown in Table 1. They showed a comparison with previous experimental data which deviated by 30% for all systems.

Although many researchers claimed that their observations indicated the organic phase preferentially wetting the pipe wall by forming a thin film, whereas water condensed as droplets, direct evidence for this was not reported. The most informative work in this area was that of Bernhardt *et al.* [50] who reported a detailed procedure to confirm the phase wetting scenarios. They combined dyeing and electrical techniques

together with high-speed motion photography to prove that the standing droplets were water droplets whilst the continuous thin film was an organic phase. A water soluble dye (methyl violet) was sprayed into the condenser and the standing drops were colored whereas the liquid film remained colorless, which indicated the *Film-Drop & Channeling* flow-type. On the other hand, based on the difference in electrical conductivity of water and xylenes, they were able to identify which phase wet the pipe wall. Various correlations of heat transfer coefficients of the binary immiscible condensed liquids were compared with laboratory results. Simple correlations for a shared surface model showed good agreement with experimental results. The correlation assumed that both liquids, water and organic, “occupied the area equal to its volume fraction in the mixed condensate” [50].

Ogino *et al.* [53] showed that the heat transfer coefficient of binary immiscible liquids was less than that of pure water but greater than that of a pure organic liquid which agrees with other researchers [56]. Their proposed correlation for the heat transfer coefficient in the *Channeling* flow pattern compared well with the results obtained in their experimental setup. A channeling flow pattern or a parallel flow consisted of two distinct rivulets of individual liquids. They also suggested that their correlation could be applied to the horizontal tube. Additionally, it was mentioned that this type of flow was normally observed at a high condensation rate.

Ponter and Diah [51] introduced the effect of surface force and density difference of both water and organic liquids on the co-condensation process on a vertical surface.

Another empirical correlation was proposed (shown in Table 1) and compared to that of Bernhardt *et al.* [50].

Polley and Calus [57] agreed with previous researchers that the condensation process changed with the condensation rate. Additionally, the authors pointed out that at  $\Delta T < 4$  K, the *Standing drop* dominated and the condensation pattern changed to *Channeling* flow when  $\Delta T > 4$  K. The heat transfer coefficient was higher when the condensation pattern was *Channeling* and was lower when the *Standing drop* was observed. The relationship between temperature difference and heat transfer coefficient seemed to agree with the Nusselt relationship [52].

Most research studies mentioned above focused on the heat transfer coefficient of mixed condensate. Kim and Webb [58] further added the heat transfer and mass transfer calculations for the vapor phase. The authors used the mixed condensate heat transfer coefficient proposed by Bernhardt *et al.* [50]. The Chilton-Colburn analogy was used to calculate the mass transfer coefficient.

In summary, it was found that organic liquids form a thin film which covers the surface due to their low surface tension, while water or higher surface tension liquids condense as droplets. Various empirical and semi-empirical correlations were proposed to calculate the heat transfer coefficient for the mixed condensate scenario. None of the studies attempted to quantify how much of the surface area was occupied with water and how much was covered by hydrocarbon, which is an important factor for corrosion. The observation duration and how the dynamics of systems might change with time were not reported.

#### 2.4. CO<sub>2</sub> corrosion – the role of wettability and hydrocarbons

As mentioned above, the condensation of two immiscible liquids is complicated partly due to the preferential wetting of each liquid on the steel, which is normally referred to as “wettability”. Wettability is defined as “the tendency for one liquid to spread on or adhere to a solid surface in the presence of another immiscible fluid”.[59] During the transportation of petroleum products, there are two distinct liquid phases present; i.e. water and hydrocarbons. Generally, pipeline steel exhibits a hydrophilic property which means that it is preferentially wetted by water. Surface active compounds present in the hydrocarbon phase might change the wettability of the steel to induce hydrophobicity. [60], [61] However, such compounds are not found in TLC.

The contact angle measurement is the simplest, yet most effective, method for evaluating the wettability of any liquid on a solid surface [62–64]. Figure 3 schematically shows the interaction between water-oil-solid surfaces related by the Young-Dupré equation (Eq. 1), which is the force balance of interfacial tensions between oil-solid ( $\gamma_{os}$ ), water-solid ( $\gamma_{ws}$ ), and oil-water ( $\gamma_{ow}$ ). As illustrated in the figure, the surface is hydrophobic if the contact angle ( $\theta$ ) is higher than 90° and *vice versa*.

In terms of the Young-Dupré equation (Eq. 1), when the contact angle is lower than 90°,  $\cos\theta$  is positive and this implies that  $\gamma_{os} > \gamma_{ws}$ . In other words, a higher force is required to spread hydrocarbons on the steel surface, hence water wets.

$$\gamma_{os} - \gamma_{ws} = \gamma_{ow} \cos\theta \quad \text{Eq. 1}$$

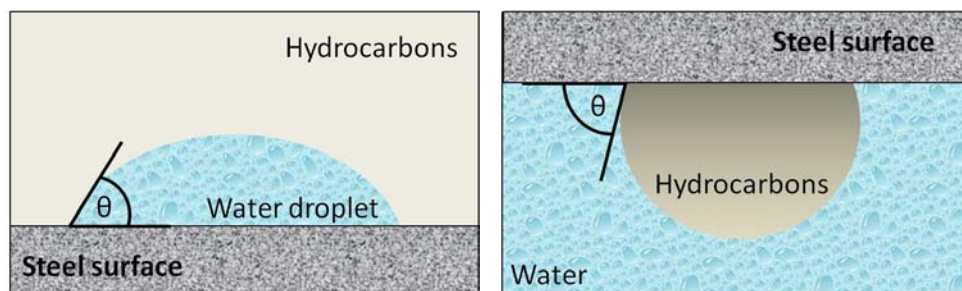


Figure 3: a) Water-in-Oil and b) Oil-in-Water contact angle measurements of a hydrophilic surface ( $\theta < 90$ ).

The influence of surface roughness and the presence of mineral layers on the steel surface was investigated using the contact angle technique [65]. Various hydrocarbons were tested. The results showed that carbon steel remained hydrophilic. Regardless of steel surface characteristics, water still wetted the surface.

Papavinasam *et al.* [64] investigated the internal corrosion of the oil and gas pipelines with various hydrocarbons types. Two techniques were used to determine the wettability of the system. One was the contact angle measurement. Another wettability measurement technique was called the “Spreading Method”, which an electrical conductivity of the liquid was measured across pins and the body of the probe. The authors claimed that if the system was either water-wetted or “mixed-wetted”, corrosion was still likely.

Lotz *et al.* [66] studied the effect of hydrocarbon types on  $\text{CO}_2$  corrosion of carbon steel. Several crudes and artificial gas condensate (36 wt.% of n-C<sub>6</sub>, 32 wt.% of n-C<sub>7</sub> and 32 wt.% of n-C<sub>8</sub>) were used. Corrosion rates were monitored continuously with Electrochemical Impedance Spectroscopy (EIS), which also provided qualitative

information regarding the presence of a corrosion product or hydrocarbon layers that were persistent on the surface. Various hydrocarbons wetted the steel surface differently. The authors noticed that the matured hydrocarbons had a lesser degree of corrosion protection. It was reported in another study that, n-hexane, even at 98%, was unprotective suggesting that it did not preferentially wet the steel surface [67]. The author also proposed that the corrosion rate theoretically depended on the frequency at which the water droplets were impinging on the steel surface, their contact area and their residence time.

Ayello [68] studied the crude oil chemistry effects on CO<sub>2</sub> corrosion. It was not the hydrocarbon type that mattered but rather the presence of oxygen, nitrogen, and sulfur-containing compounds. With different degrees of protection, most of them led to a reduction of the corrosion rate. The author proposed that the main reason for the reduction in the corrosion rate was the change in phase wetting and direct inhibition due the presence of surface active compounds. However, such compounds were not present in the wet gas transportation lines studied here.

Choi [69] focused his research in a stratified flow regime where water and hydrocarbons were concurrently present. He suggested that the most severe corrosion took place at the water/hydrocarbons interface when a distinct phase separation was observed.

In 2000, Groysman and Erdman [70] studied the corrosion of carbon steel in the presence of hydrocarbons and an aqueous phase. Oxygen (O<sub>2</sub>) was the corrosive species in their study. They also observed corrosion at the interface of water and hydrocarbons

due to the higher solubility of  $O_2$  in the hydrocarbons phase. A similar hypothesis was proposed for  $CO_2$  corrosion [71], the solubility of  $CO_2$  is higher in the hydrocarbon phase than in the aqueous phase. For instance, the solubility of  $CO_2$  in n-heptane at  $25^\circ C$  is 0.0139 (mole fraction) [72] whereas that for water is 0.0006 mole fraction at the same temperature [73]. Thus, hydrocarbons can act as a reservoir of  $CO_2$  at the water/hydrocarbon interface.

## **2.5. Gaps in the current literature**

Various types of empirical correlations and mechanistic calculations have been developed to predict TLC and in all cases they appear to be “conservative”. In other words, the models overpredict the corrosion rate which can lead to unnecessarily high capital investment and high operating costs related to the mitigation of the perceived corrosion risk. A large corrosion allowance may be required, which means that a thick pipe is needed. In addition, if the predicted corrosion risk is high, frequent inspections and batch inhibitor treatments are prescribed, which may require interruption in operations [74].

Additionally, the current understanding of TLC suggests that the most severe corrosion should take place where the condensation rate of water is the highest. This location usually corresponds to the entrance of the pipeline where the temperature of the gas is the highest. In that case most of the models predict high TLC levels at the entrance to the wet gas line. However, in some cases, the first few hundred meters of the line show less corrosion than further downstream [43]. This discrepancy can clearly be traced to effects which are not accounted for in the current models, such as co-condensation.

As discussed, the pipelines do not carry only water vapor but a certain range of hydrocarbons that can condense along with water. In BLC, the presence of hydrocarbons may offer some extent of protection due to preferential wetting. It is expected that similar effects could take place for TLC.

## **2.6. Objectives of this research**

As outlined in the previous section, the influence of co-condensation on TLC has not been investigated. The objective of the present work is to investigate how co-condensation of water and hydrocarbons may affect the TLC phenomenon. Based on the literature review, the present study is divided into three parts to answer the following questions:

1.) Wettability and co-condensation process: since the condensate comprises of two immiscible liquids having different degrees of attraction towards the steel surface, the question is: which liquid will wet the surface?

2.) Corrosion behavior: as hydrocarbons are poor electrolytes, how much will the corrosion rate decrease if water is prevented from adhering to the surface?

3.) Heat and mass transfer: The presence of another condensable component affects the heat and mass transfer process. How much will this influence the calculation of water condensation rate?

## CHAPTER 3: WETTABILITY AND CO-CONDENSATION PROCESS

### MONITORING

#### 3.1. Introduction

A primary cause of TLC is the condensation of water vapor. Nonetheless, water is not the only component that condenses but a certain range of hydrocarbons in the wet gas pipelines can also condense. It is anticipated that if hydrocarbons simultaneously condense on the pipeline surface with water, the corrosion will substantially be reduced since hydrocarbons are not corrosive. Therefore, it is important to investigate how water and hydrocarbons co-condense and wet the pipe wall. Understanding this will establish a better insight into the overall TLC process.

In water and oil flow, water may settle down and accumulate at the bottom part of the pipeline due to its higher density and cause corrosion. In some scenarios water can be entrained into the oil phase. Hence, the corrosion rate is reduced. Oil-wetting implies little or no corrosion, water-wetting and intermittent water wetting indicates that the pipeline still suffers from some corrosion. Some recent studies have been investigating the conditions where water would settle and wet the pipe wall. Parameters influencing the water wetting include water cut, chemistry of crude oils, pipeline orientation, liquid and gas flow velocity, temperature, pressure, etc. Additionally, various techniques and equipment were developed to detect the wetting by water and oil.

For TLC, the same question needed to be answered and that is, *which phase, water or hydrocarbons, predominantly occupy the steel surface when both phases simultaneously condense?*

The objectives of the work presented in this chapter are to determine which liquid (water or hydrocarbons) predominantly wets the steel surface during the co-condensation process, as well as to quantify the wetted surface area change with time. The mechanism for the co-condensation process is proposed at the end of this chapter.

### **3.2. Experimental setup and procedure**

Various approaches and techniques were implemented in order to determine both qualitatively and quantitatively the wetting behavior during the different co-condensation scenarios. Part of this chapter has been presented and published [75].

#### *3.2.1. Hydrocarbon selection*

In wet gas pipelines, the hydrocarbons being transported are mostly light straight-chain n-alkanes. Hydrocarbons lighter than n-heptane cause specific safety concerns due to their flammability thus heavier ones were chosen for this study. Table 2 compares flash points and boiling points of water and hydrocarbons commonly present in wet gas production. Table 3 gives the physical properties of water and alkanes used in this study, *i.e.*, n-heptane, n-octane and n-decane. A significant difference in wettability was expected if branched alkanes or aromatics were investigated. Yet, they are not naturally present in real transportation lines.

As the composition of the liquid hydrocarbon mixtures changes with time, it is difficult to simultaneously control their condensation rates. Hence, in all co-condensation experiments described below, only one hydrocarbon was co-condensed with water.

Table 2: Comparison of flash point, boiling point and molecular weight of water and hydrocarbons commonly present in wet gas production ( $C_1 - C_6$ ) and selected heavier n-alkanes ( $C_7 - C_{10}$ ).

<b>Components</b>	<b>Molecular weight (g/mol) [76]</b>	<b>Flash point (<math>^{\circ}</math>C) [77]</b>	<b>Boiling point (<math>^{\circ}</math>C) [76]</b>
Water (w)	18	N/A	100
Methane ( $C_1$ )	16.04	-186.03	-161.4
Ethane ( $C_2$ )	30.07	-134.15	-88.6
Propane ( $C_3$ )	44.09	-102.15	-42.2
i-butane (i- $C_4$ )	58.12	-82.15	-10
n-butane (n- $C_4$ )	58.12	-74	-0.6
i-pentane (i- $C_5$ )	72.15	-55.15	27.9
n-pentane (n- $C_5$ )	72.15	-49	36.3
n-hexane (n- $C_6$ )	86.17	-23	69
n-heptane (n- $C_7$ )	100.2	-4.15	98.4
n-octane (n- $C_8$ )	114.22	14	125.7
n-nonane (n- $C_9$ )	128.25	31.0	150.5
n-decane (n- $C_{10}$ )	142.28	49.7	174.0

Table 3: Comparison of physical properties of water and alkanes selected for this study

<b>Parameters</b>	<b>Water</b>	<b><math>C_7</math></b>	<b><math>C_8</math></b>	<b><math>C_{10}</math></b>
Density @ 25 $^{\circ}$ C (kg/m $^3$ ) [76]	997.18	680.21	697.75	725.13
Viscosity @ 25 $^{\circ}$ C (Pa.S) [77]	0.0009	0.00038	0.00051	0.00085
Surface tension @22 $^{\circ}$ C (mN/m) [78]	70.9	20.5	21.55	23.7
Interfacial tension @22 $^{\circ}$ C (mN/m) [78]	N/A	51.9	52.5	53.2
Latent heat of vaporization @25 $^{\circ}$ C ( $\times 10^{-6}$ kJ/m $^3$ ) [77]	2.43	0.25	0.25	0.26

### 3.2.2. *Safety concerns and management*

The main safety concern was the flammability of light hydrocarbons used in this research. Therefore, experiments were conducted in a ventilation hood or in a well-ventilated area. The amount of flammable liquid was minimized. Hence, tests were conducted on small scale experimental setups only.

After experiments were finished, the remaining hydrocarbons were disposed in a separate container and kept in a flammable liquid storage pending proper disposal.

### 3.2.3. *Wettability study: contact angle measurement*

Static contact angles can be measured by the sessile drop technique in a goniometer. In the present study a goniometer designed and developed by Tang [79] was used. It was made from stainless steel with two transparent windows on both sides (Figure 4). The side view schematic diagram is shown in Figure 5. The system was connected to a digital camera to capture photos and videos of the change in shape of a sessile droplet, which were analyzed with the image analysis software, “Lincoln<sup>TM</sup>”.

Experiments were divided into two parts, *i.e.*, oil-in-water (OIW) and water-in-oil (WIO) contact angles measurements. For the first set of experiments (OIW), the continuous phase was deionized water saturated with CO<sub>2</sub> at ambient temperature and pressure. A droplet of hydrocarbon was also deoxygenated by purging with CO<sub>2</sub> in a separate flask prior to injection. Due to the lower density of the hydrocarbon droplets, they were deposited onto the steel surface as shown schematically in Figure 5. The change in the hydrocarbon droplet’s shape was recorded using the imaging system described above. Three hydrocarbons were tested; *i.e.* n-heptane, n-octane, and n-decane.

Contact angles of hydrocarbon droplets in an aqueous phase usually stabilized after one minute. Three measurements were made and an average value was reported.

A second set of contact angle measurement was to measure WIO. The goniometer chamber was filled with a deoxygenated hydrocarbon. A droplet of deionized water saturated with CO<sub>2</sub> was injected above the sample surface. The water droplet fell and deposited onto the sample surface. The same approach was used to obtain the contact angle of water in hydrocarbon as described above.

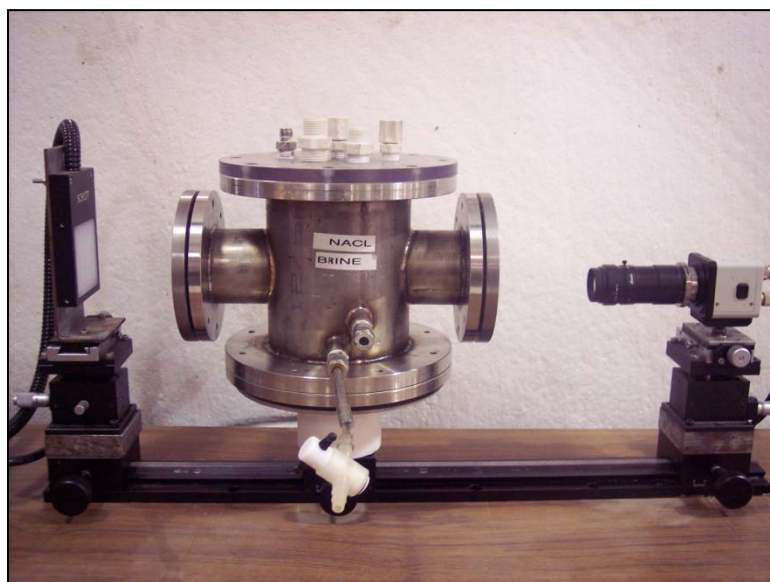


Figure 4: Goniometer (Image courtesy of Water Wetting JIP, Ohio University).

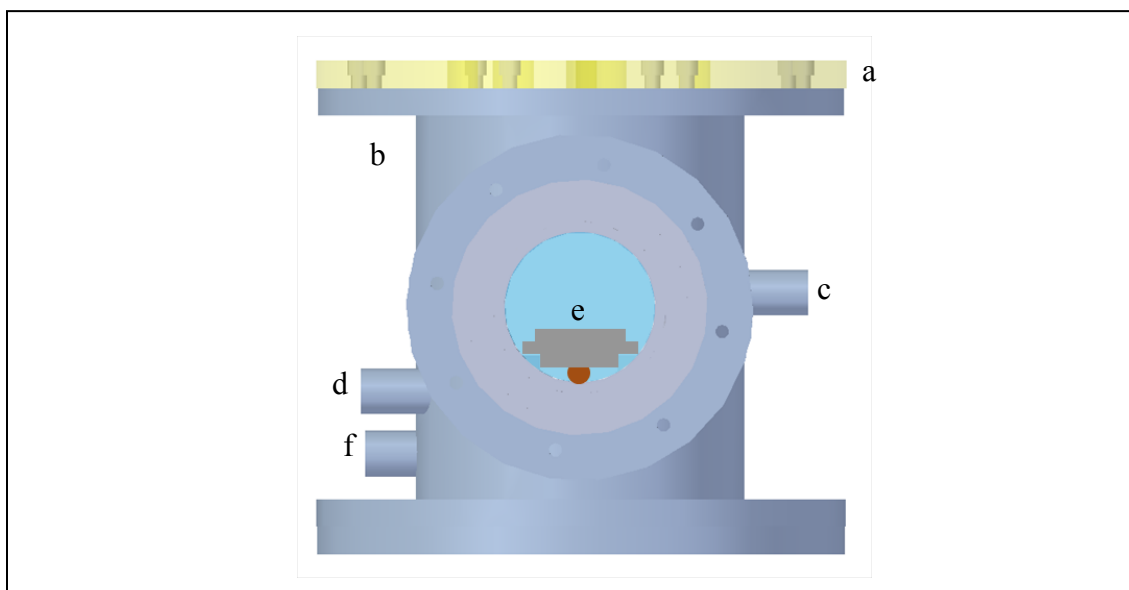


Figure 5: Schematic side view of goniometer: a) transparent acrylic lid; b) stainless steel chamber; c) water injection port; d) hydrocarbon injection port; e) steel sample; and f) drainage (Image courtesy of Water Wetting JIP, Ohio University)

Commercial carbon steel (X65, pipeline grade) was prepared by polishing with 36 and 600 grit sand paper. After that, it was put in an ultrasonic bath filled with isopropanol to be cleaned, and then air-dried. Prior to testing, average roughness,  $R_a$ , was determined using a surface profilometry machine, InfiniteFocus<sup>®</sup> microscopy (IFM), manufactured by ALICONA. The machine uses the focus-variation technique to determine the height distribution of the surface. 3D surface topography was created and the average roughness was determined.

Two samples with different roughnesses were prepared, *i.e.*, 0.5 and 4 microns as shown in Figure 6 and Figure 7, respectively. Figure 8 shows the depth/area analysis of the surface polished with a 600 grit sand paper. Approximately, 80% of the surface was varied from -1 to 1 micron.

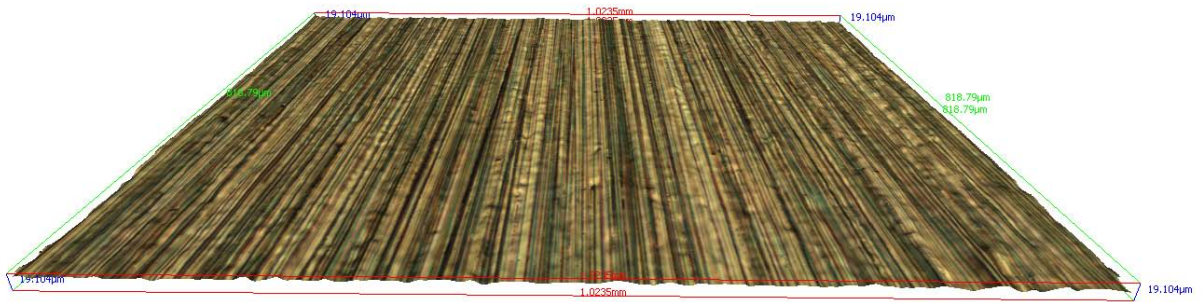


Figure 6: 3D image of carbon steel sample polished with 600 SiC paper with the average roughness of  $1\mu\text{m}$ .



Figure 7: 3D image of carbon steel sample polished with 32 SiC paper with the average roughness of  $4\mu\text{m}$ .

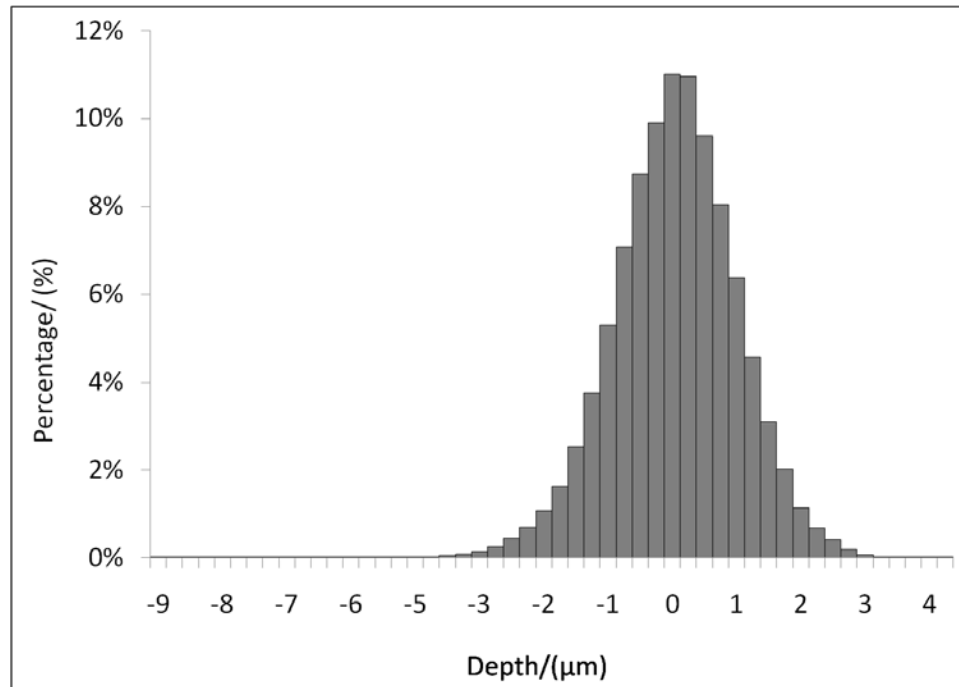


Figure 8: Depth/area distribution of carbon steel sample polished with 600 SiC paper with the average roughness of 1 μm

#### 3.2.4. Visual observation of the condensation process

A borescope was used to observe the condensation process *in situ*. The particular model used in this study was a Hawkeye® Blue Rigid Borescope manufactured by Gradient Lens Corporation as shown in Figure 9. A Luxxor® Portable Video Camera manufactured by Sony was connected to the borescope and recorded the ongoing condensation process.

In order to artificially cool the steel sample, a thermoelectric cooler (Peltier) was used. The Peltier cooler consists of two ceramic plates with semi-conductors in between. When DC current passes through the cooler, one side is cooled and the heat is discarded onto the other side, hence it is hotter at the opposite side. The steel sample was cooled by

attaching the cold side of the Peltier to the back side of the steel sample. A heat sink was attached to the hot side of the Peltier device. The assembly is illustrated in Figure 10.

Experiments were conducted in a 2-L glass cell as shown in Figure 10. The liquid(s) of interest were added and heated to generate a saturated vapor mixed with CO<sub>2</sub>. The CO<sub>2</sub> was purged at a constant rate throughout the test. Once the desired vapor temperature was obtained and was constant, a sample already connected with the Peltier was inserted into the glass cell facing downward.

Once the warm vapor came into contact with the cold surface of the carbon steel sample, condensation took place. A borescope was inserted into the vapor phase and recorded the ongoing condensation process.

All experiments were conducted at atmospheric pressure. Only n-heptane was used in this part of the study.

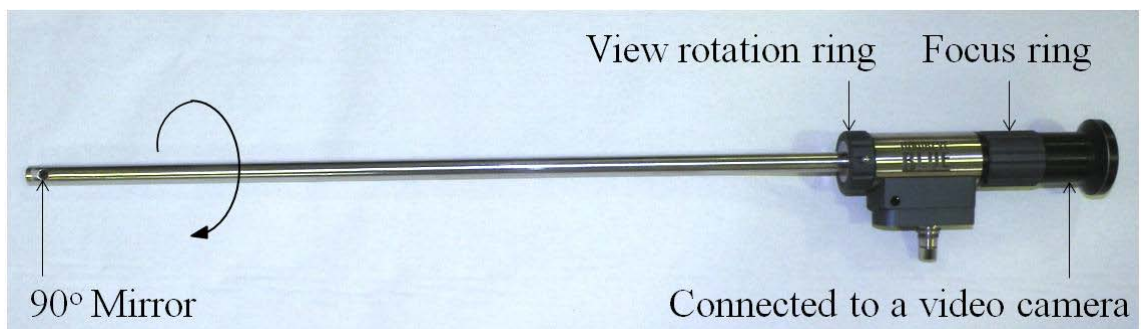


Figure 9: Image of a borescope used to observe the condensation processes.

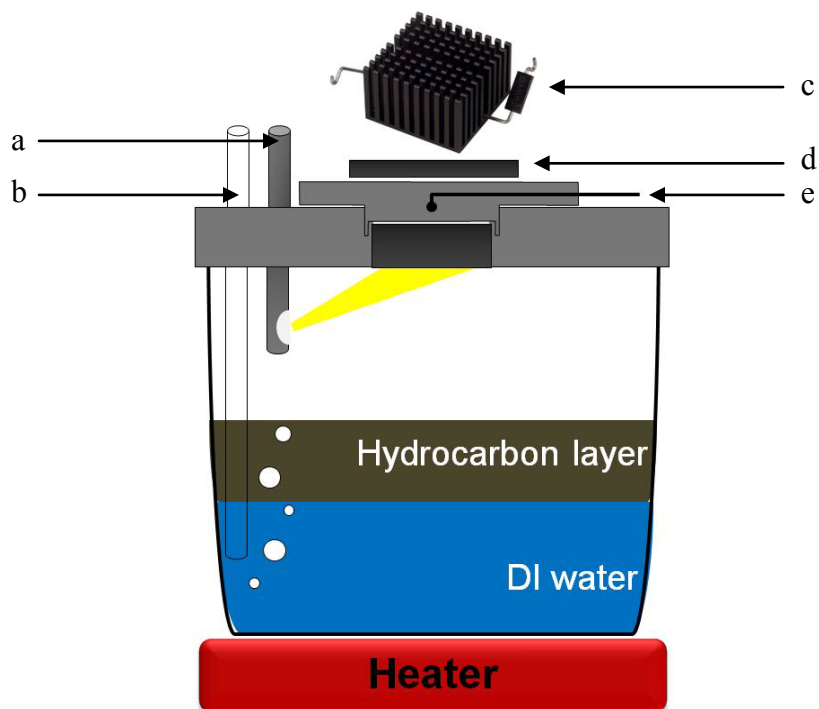


Figure 10: Schematic diagram of experimental setup for the condensation processes observation: a) the borescope, b) the CO<sub>2</sub> inlet, c) the heat sink, d) the Peltier cooler, and e) the sample holder embedded with a thermistor.

Five condensation scenarios were monitored:

1. *Water condensation*: Only water condensed on the steel surface.
2. *n-heptane condensation*: Only n-heptane condensed on the steel surface.
3. *Co-condensation*: water and n-heptane simultaneously condensed on the carbon steel surface.
4. *Sequential condensation (I)* where water condensed first followed by co-condensation.

5. *Sequential condensation (II)* where n-heptane condensed first followed by co-condensation.

### 3.2.5. *Electrical-based techniques*

Water and hydrocarbons have great differences in their electrical properties, which can be utilized to distinguish where water and hydrocarbons are located. Various commercial conductivity probes have been developed for various purposes. However, those conventional conductivity probes typically have conductivity pins which protrude from the sample surface and may induce preferential condensation, which can lead to inaccurate measurements. Therefore two types of conductivity probes were custom designed for the present study and are described below.

- Electrochemical Impedance Spectroscopy Technique

Figure 11 shows the probe designed to measure solution resistance using Electrochemical Impedance Spectroscopy (EIS). Conductivity is the inverse of resistivity and EIS is known to be the technique that can be used to measure the solution resistance. Hence, EIS can be used to identify the type of liquid adhering to the steel surface. In order to electrically insulate the sample, a 1" diameter X65 sample was cut into four pieces (quarters), the sides coated with insulating Teflon<sup>TM</sup> painted and mounted back together using an epoxy. Connection wires led to a Potentiostat (Gamry) which was used to perform the EIS measurements.

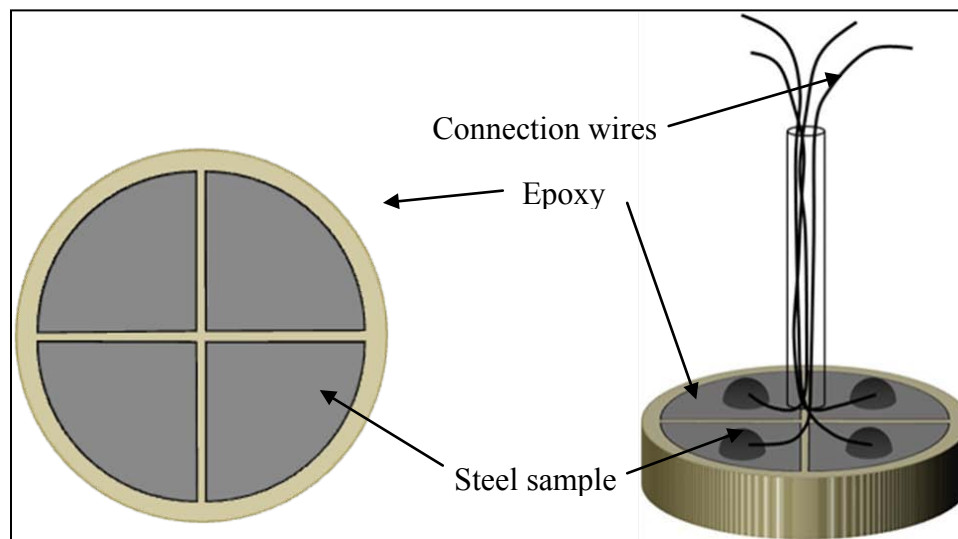


Figure 11: Sample assembly for solution resistance measurements using Electrochemical Impedance Spectroscopy (EIS).

- Electrical conductivity measurement

Another type of conductivity probe contains many flush mounted pins, which allows a more elaborate monitoring of the condensation process. This probe was originally developed within the Water Wetting JIP at Ohio University and was used to locate the presence of water at the bottom of the line in a multiphase oil-water flow. In the present study the same type of probe was used to locate where and when condensed water came into contact with the steel sample. A schematic of the conductivity probe and its photo are shown in Figure 12. The body was made with carbon steel while the pins were stainless steel. The body part was drilled and filled with epoxy-insulated electrical pins. Conductivity of the liquid between each pin and the body of the probe was

measured simultaneously. With a total of 20 pins, the surface area wetted with water and hydrocarbon could be quantified.

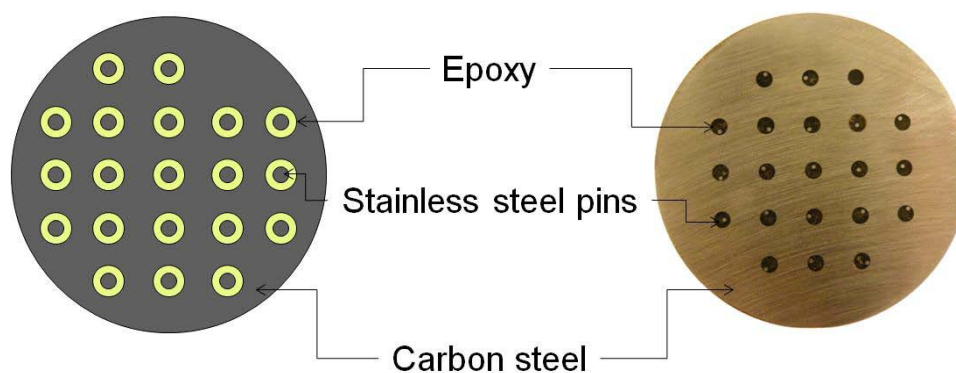


Figure 12: Diagram of conductivity probe (courtesy of water wetting JIP).

The cooling device was not installed on this conductivity probe. Therefore, the condensation was limited to natural convection heat transfer. The temperature difference between the vapor and probe surface was estimated to be 5°C.

### 3.3. Results and discussion

#### 3.3.1. Wettability study

##### Oil-in-water contact angle measurement

Images of an n-heptane drop in a water phase with time are shown in Figure 13. In this case, the steel was immersed and pre-wetted with water. The contact angle was always measured through the water phase. The n-heptane drop deposited on the surface and did not spread out and replace the water. Usually, hydrocarbon drops reached a stable shape in only one minute. All three studied hydrocarbons (heptane, octane and decane)

showed similar behavior, consistent with the carbon steel being hydrophilic. The same results were obtained for both rough and smooth surfaces as shown in Figure 14 and Figure 15, respectively.

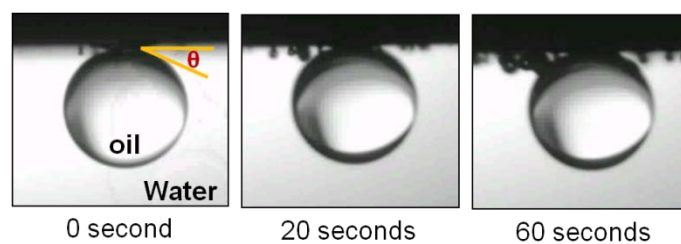


Figure 13: Typical images of n-heptane droplet in a water phase.

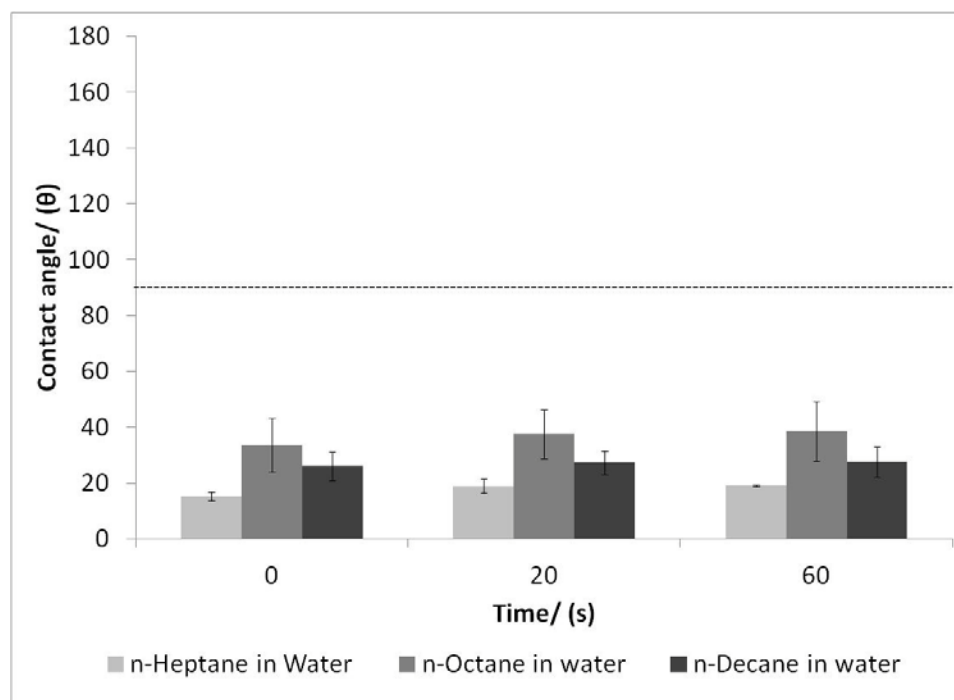


Figure 14: Contact angles of n-heptane, n-octane and n-decane droplets in water on X65 carbon steel polished with 32 grit SiC ( $R_a = 4 \mu\text{m}$ ).

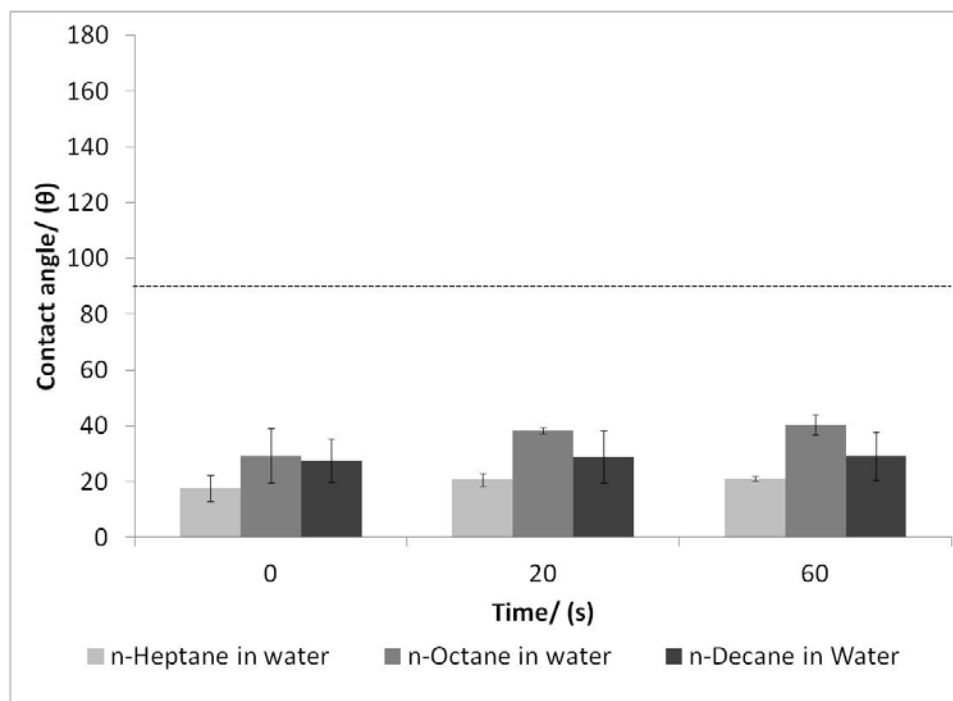


Figure 15: Contact angles of n-heptane, n-octane and n-decane droplets in water on X65 carbon steel polished with 600 grit SiC ( $R_a = 1\mu\text{m}$ ).

#### Water-in-oil contact angle measurement

Figure 16 shows images of the change in the shape of water droplets in a continuous phase of n-heptane with time. This surface was polished with 32 grit SiC paper and had an average roughness of  $4\mu\text{m}$ . The water droplet did not immediately spread out and replace the n-heptane. The contact angle was greater than  $90^\circ$ , which suggested that the carbon steel surface was preferentially wetted with n-heptane at the beginning of the test. The water droplet gradually spread out and replaced the n-heptane. After 50 minutes, the water still continued to spread and the contact angle was lower than  $90^\circ$ , implying that the surface became water-wetted. The shape of the water droplet on a

surface with a roughness of 1  $\mu\text{m}$  changed significantly faster. The contact angle decreased below  $90^\circ$  almost immediately once the water droplet reached the steel surface.

Figure 17 and Figure 18 show the contact angles of water in three hydrocarbons with time on a smooth and a rough surface, respectively. On a smooth surface (Figure 17), the water droplet behaved the same in the three tested hydrocarbons. A spreading occurred and the contact angles dropped below  $90^\circ$  as soon as the water droplet reached the steel surface indicating that the steel was hydrophilic. However, on a rough surface, the contact angle never reached the fully hydrophilic region when the water was in n-octane and n-decane.

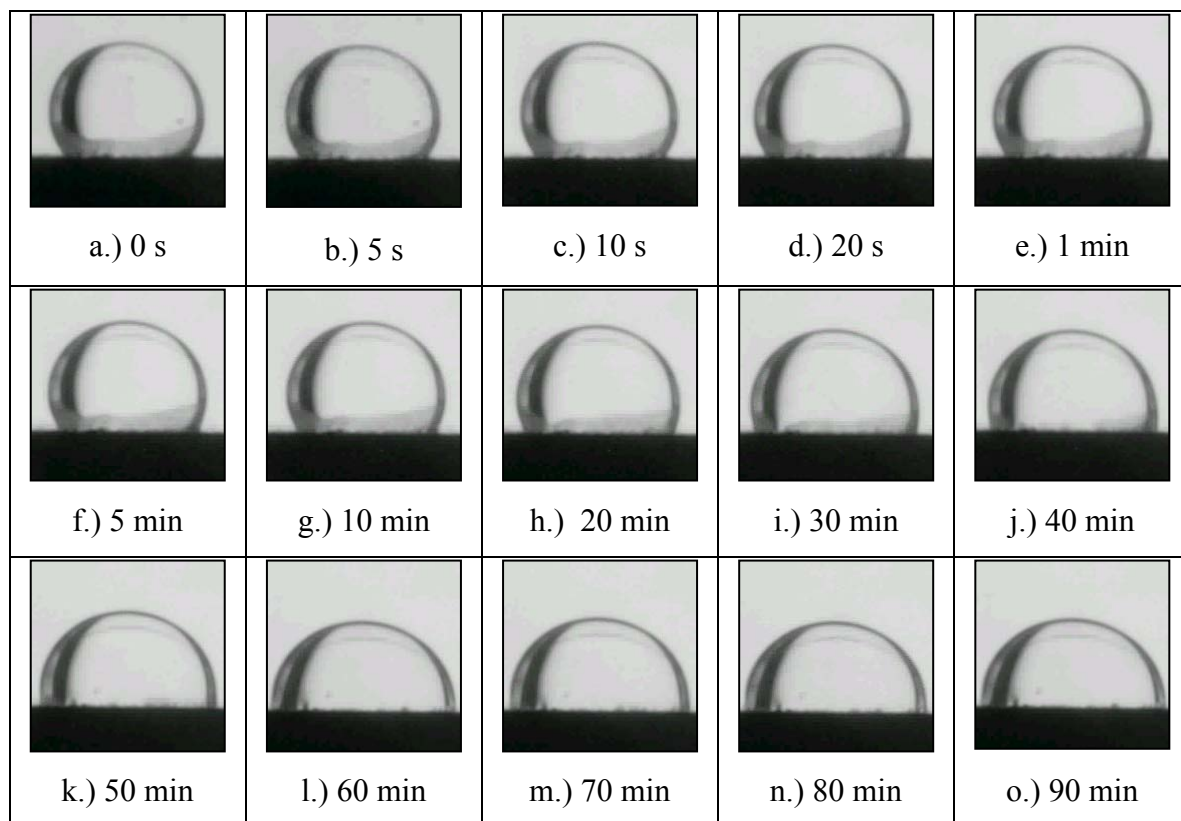


Figure 16: The evolution of contact angles of water droplet in n-heptane on a carbon steel with a surface roughness of 4  $\mu\text{m}$ .

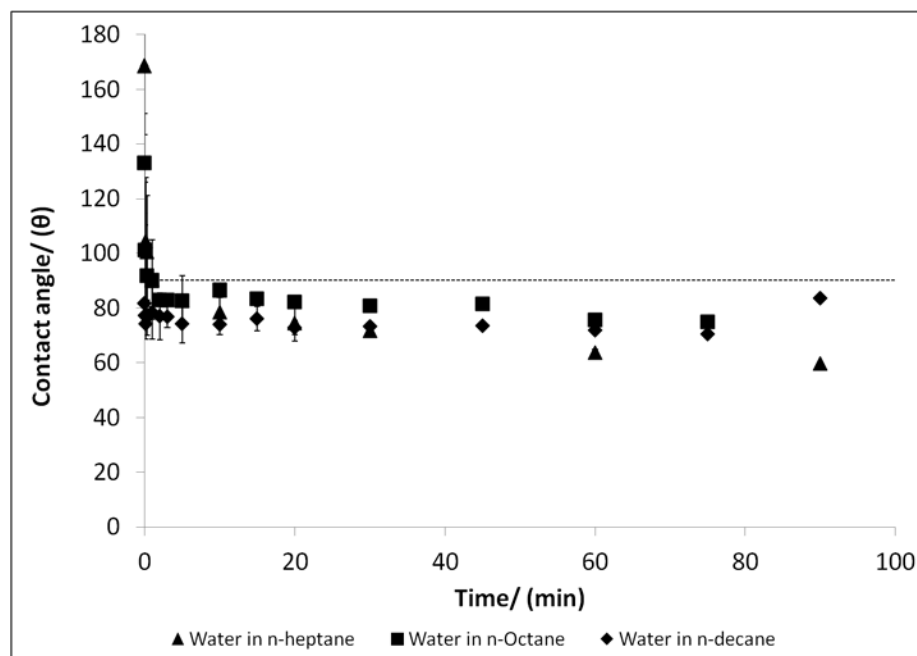


Figure 17: Contact angles of water droplet in hydrocarbons on X65 carbon steel polished with 600 grit SiC.

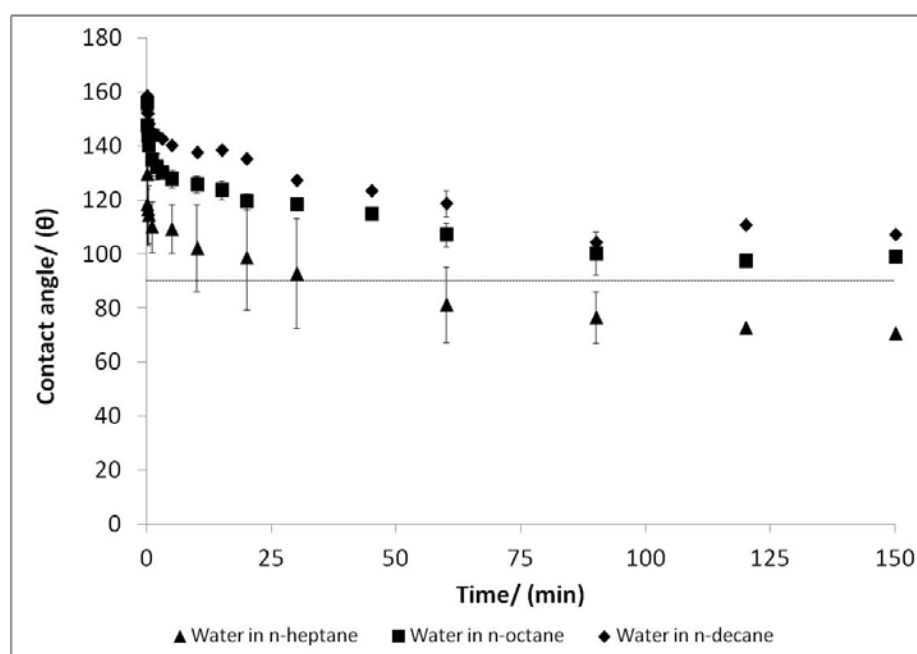


Figure 18: Contact angles of water droplet in hydrocarbons on X65 carbon steel polished with 32 grit SiC ( $R_a = 4$ ).

To summarize, the wettability tests showed that carbon steel naturally preferred water over hydrocarbons. However, the competition of water and hydrocarbons during the co-condensation process could not be represented by the contact angle measurement alone. In static systems, such as the contact angle measurements, only one droplet was allowed to contact the steel in the presence of the other immiscible liquid without being disturbed. However, during the co-condensation process, the system can be much more dynamic. Therefore additional techniques were used to determine the details of the condensation process.

### 3.3.2. *Visual observation of condensation processes*

#### *Water condensation*

Pure water started condensing on the steel surface as isolated droplets (Figure 19a and b). Consequently, adjacent drops coalesced and grew (c). Once a droplet reached its maximum size, the gravitational force exceeded the surface tension and the buoyancy, forcing the drop to fall down (Figure 19d and e). This allowed newly condensed water to start occupying the same area. At higher condensation rates of water, the process was still initiated by forming isolated drops but the coalescence of nearby droplets proceeded more rapidly. This is in agreement with previous research [9].

#### *n-heptane condensation*

The condensation of n-heptane alone, on the other hand, evolved differently as it condensed in a filmwise manner (Figure 20) due to its low surface tension. A uniform thin film of n-heptane grew in the vertical direction. Once the n-heptane layer on a

surface reached the maximum thickness, an n-heptane drop formed and fell down due to gravity (Figure 20b).

#### Co-condensation of water and n-heptane

The co-condensation process is illustrated in Figure 21. After the sample was inserted into the warm vapors of water and heptane, small droplets of water were almost immediately visible (Figure 21a). These droplets coalesced with more difficulty as shown in Figure 21b and Figure 21c. The n-heptane co-condensed in between water droplets and prevented them from easily coalescing. The observation agreed well with what Hazelton [47] and Kern [55] suggested. However, over time, it seemed that only one liquid occupied the steel surface (Figure 21d) – more likely to be water – due to the hydrophilicity of the steel. It has also been suggested that n-heptane may form a very thin film on the surface of water, which may explain why it appears that only one liquid was present on the sample surface [80].

In transportation pipelines, the gas composition fluctuates with time. Components that condense on the specific area may periodically vary and may or may not be replaced by the newly condensed liquid. Thus, the next series of tests were designed to observe if water replaced the pre-condensed layer of heptane and *vice versa*.

Sequential condensation (I) where water condensed first followed by the co-condensation.

Figure 22a shows a steel surface following condensation of water for a long time, and prior to adding n-heptane into the system. Figure 22b and c illustrate that n-heptane started condensing on the steel surface and slightly altered the wetting behavior of water

as the water film was broken up and formed droplets instead. The white spots could be related to the tips of the small droplets of water reflecting the light from the camera. Approximately 20 hours after the sample was exposed to co-condensation, only one liquid was observed by the borescope (Figure 22f) similar to what happened in the simultaneous condensation (Figure 21f).

*Sequential condensation (II)* where n-heptane condensed first followed by co-condensation.

The order of condensation was here reversed. The n-heptane initially condensed on the steel (Figure 23a). Water was introduced after the steady state of n-heptane condensation was reached. Almost immediately, small droplets of water started forming on the surface (Figure 23b and c). As the process continued (Figure 23d and e), more droplets of water were found and the coalescence of water droplets was observed. Over time (>20 hours), water uniformly distributed over the steel surface similar to the previous two scenarios.

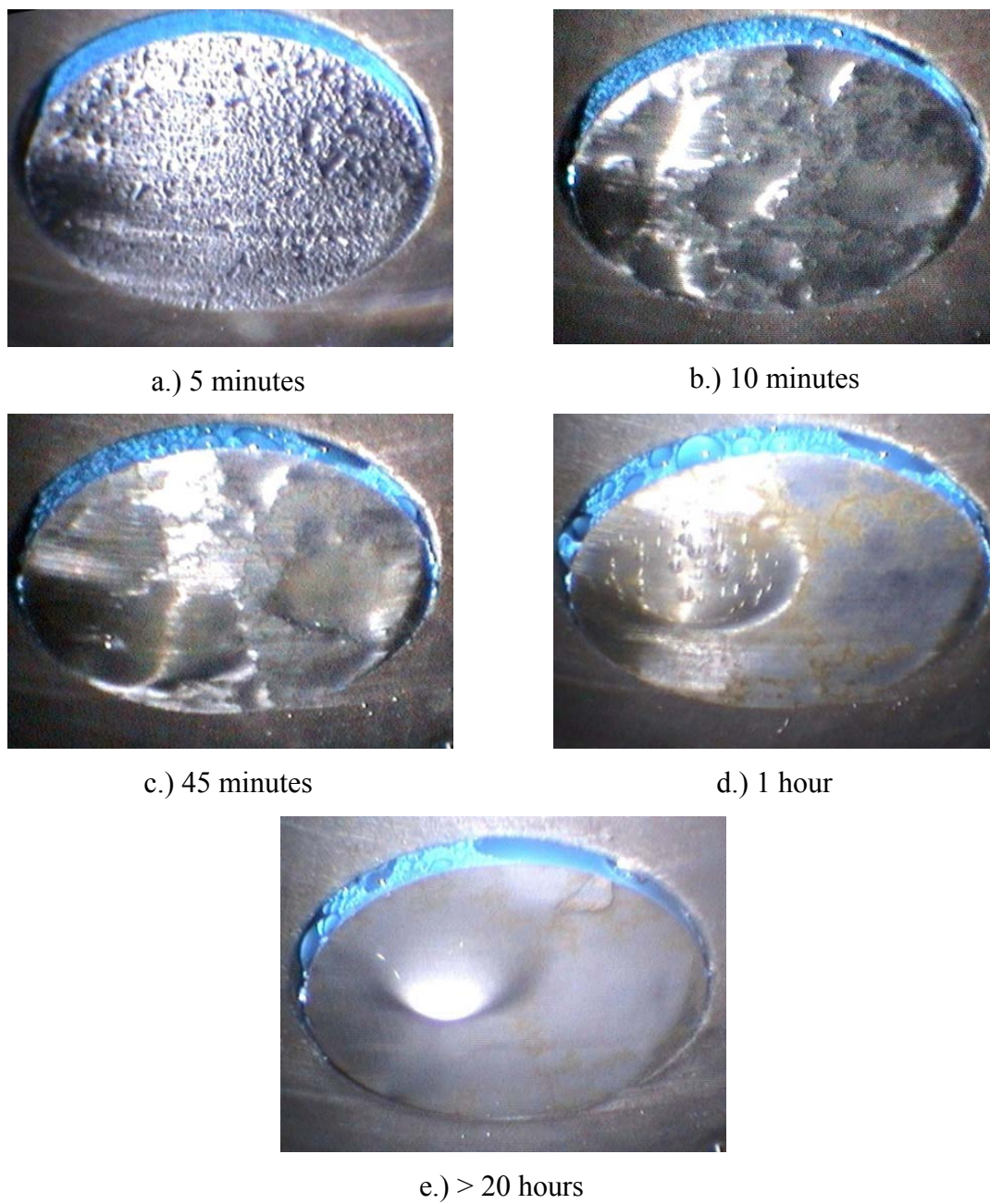


Figure 19: Condensation behavior of only water with time ( $T_v = 40 \pm 1^\circ\text{C}$ ,  $T_s = 30 \pm 2^\circ\text{C}$  and  $\text{WCR} = 0.07 \pm 0.02 \text{ mL/m}^2/\text{s}$ ).

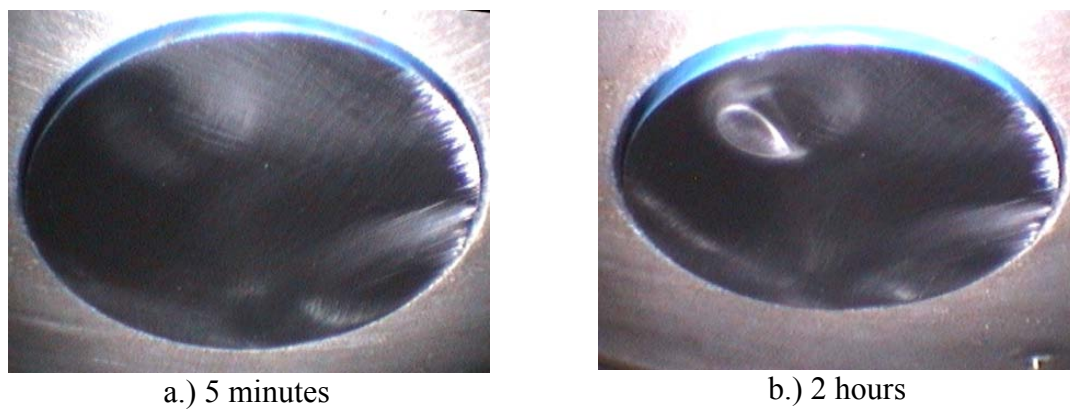


Figure 20: Condensation process of only n-heptane ( $T_v = 35 \pm 1^\circ\text{C}$ ,  $T_s = 27 \pm 1^\circ\text{C}$  and  $C_7\text{CR} = 0.3 \pm 0.1 \text{ mL/m}^2/\text{s}$ ).

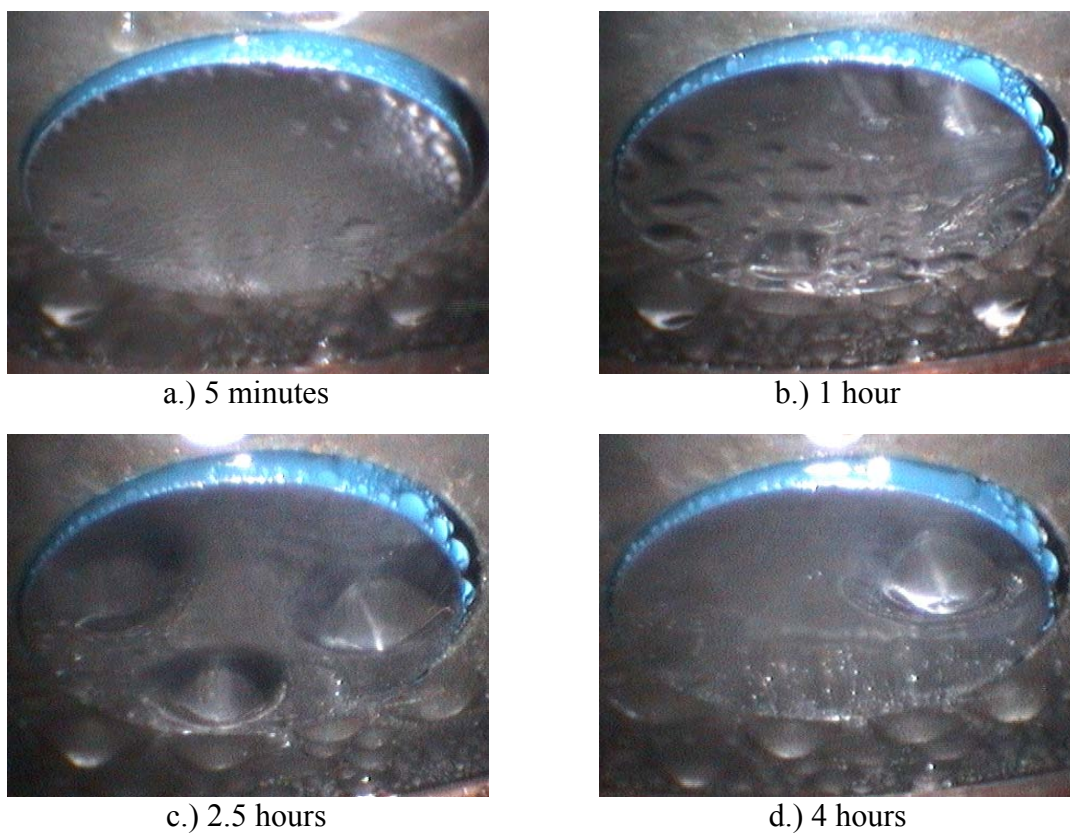


Figure 21: The observation of co-condensation process with time ( $T_v = 40 \pm 1^\circ\text{C}$ ,  $T_s = 27 \pm 2^\circ\text{C}$  and  $\text{WCR} = 0.08 \pm 0.02 \text{ mL/m}^2/\text{s}$ ,  $C_7\text{CR} = 0.5 \pm 0.15 \text{ mL/m}^2/\text{s}$ ).

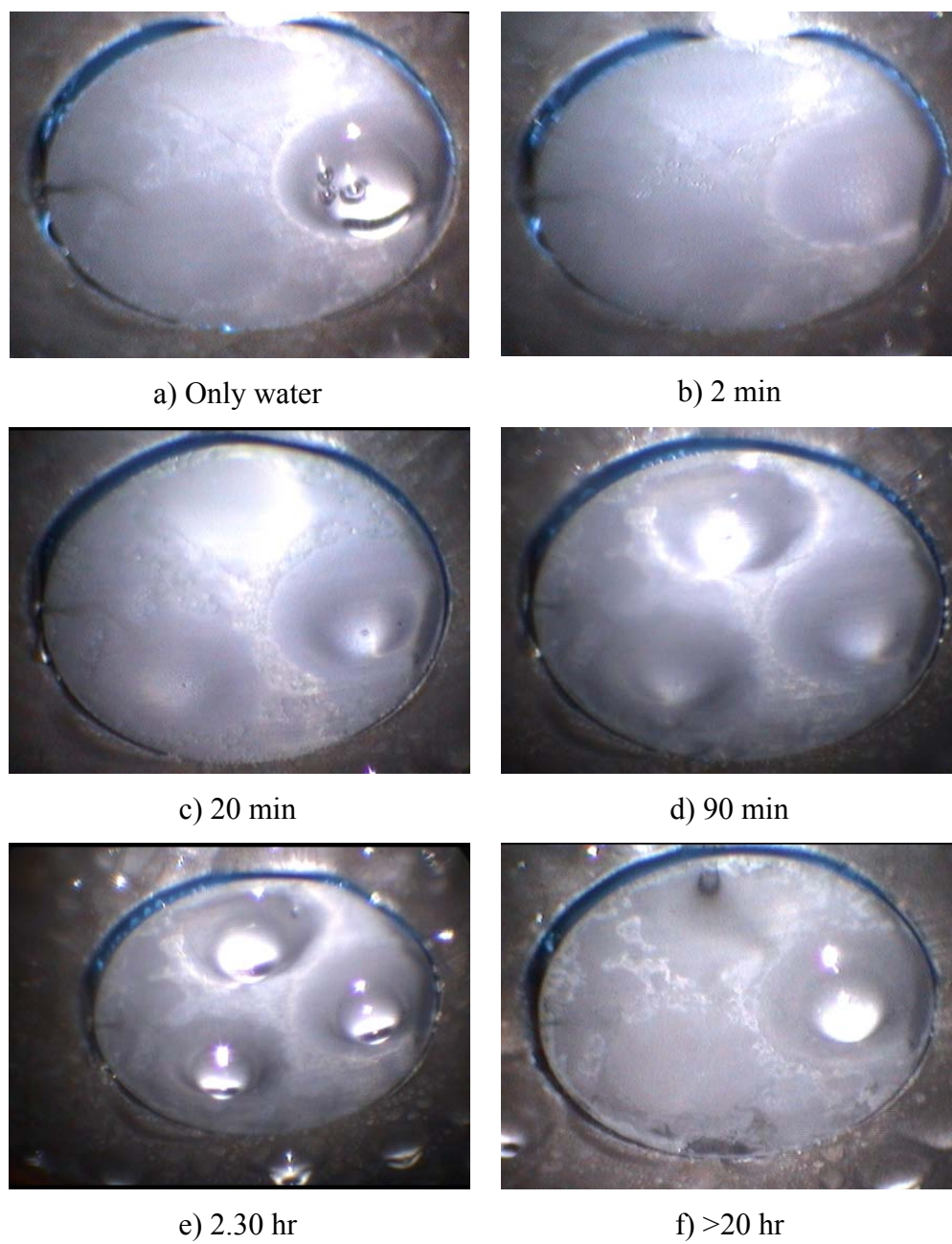


Figure 22: The observation of sequential condensation: Water condensed first followed by co-condensation ( $T_v = 40 \pm 1^\circ\text{C}$ ,  $T_s = 27 \pm 1^\circ\text{C}$  and  $\text{WCR} = 0.09 \pm 0.02 \text{ mL/m}^2/\text{s}$ ,  $C_7\text{CR} = 0.5 \pm 0.1 \text{ mL/m}^2/\text{s}$ ).

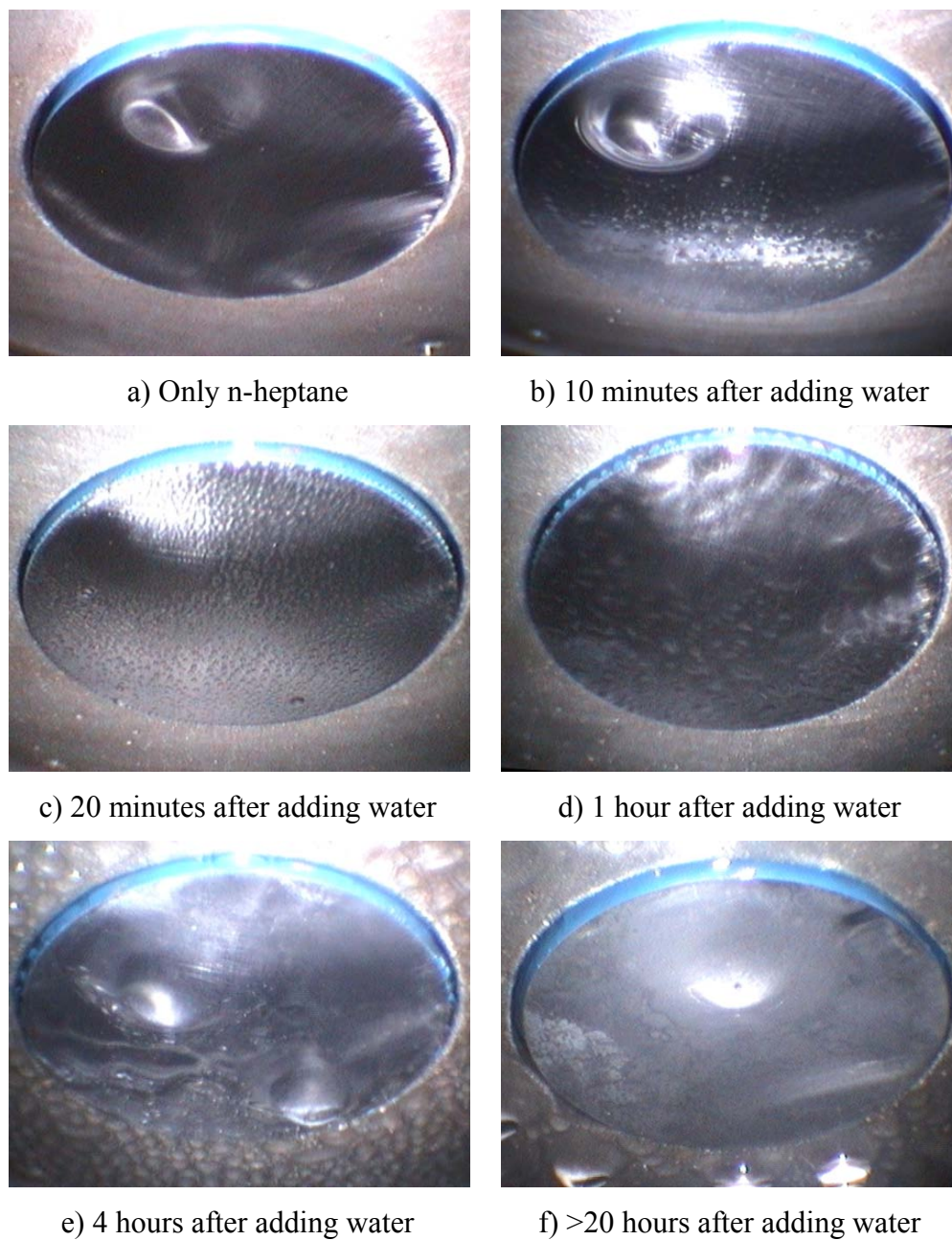


Figure 23: The observation of sequential condensation: n-heptane condensed first followed by co-condensation ( $T_v = 40 \pm 1^\circ\text{C}$ ,  $T_s = 27 \pm 1^\circ\text{C}$  and  $\text{WCR} = 0.09 \pm 0.02 \text{ mL/m}^2/\text{s}$ ,  $\text{C7CR} = 0.5 \pm 0.1 \text{ mL/m}^2/\text{s}$ ).

Overall, the borescope observations of the co-condensation processes were clear only at the beginning. When the process reached a steady state, (after 20+ hours), no phase distinction could be made using the borescope observations.

Moreover, the corrosion process takes place on the solid/liquid interface. Hence, what happens at the vapor/liquid interface cannot be easily related to the corrosion behavior. Therefore, an additional method was deemed necessary to monitor the condensation process on the carbon steel surface.

### 3.3.3. *Electrical-based techniques for condensation process investigation*

- Condensation process investigation using EIS

#### *Proof of concept: single liquid solution resistance*

Solution resistances of single liquids were first measured. Figure 24 presents the solution resistance of water at various salt concentrations. Expectedly, solution resistance decreased with increasing salt concentration. The DI-water, which was closely equivalent to the freshly condensed water, had a resistance of approximately  $4 \times 10^3 \Omega$ .

In a minimally conductive liquid such as hydrocarbons or DI water, the response of the EIS probe was noisy and difficult to interpret. It was sometimes necessary to increase the excitation voltage from the normal range of 5-10 mV to higher values [81]. The optimum excitation voltage for the DI water and n-heptane was 250 to 500 mV. It should be noted that high voltage may cause damage on the sample surface due to the effect of polarization. However, this could be prevented by avoiding the low frequency range so that the surface was not exposed to the high polarization stage for a long time.

Since the only interest was the solution resistance, it was not necessary to scan to low frequency in any cases.

Resistance of DI water, even though it was very high, was significantly lower than that of n-heptane (Table 4). Therefore, high frequency EIS could be used as an effective tool to distinguish which phase is in contact with the steel surface.

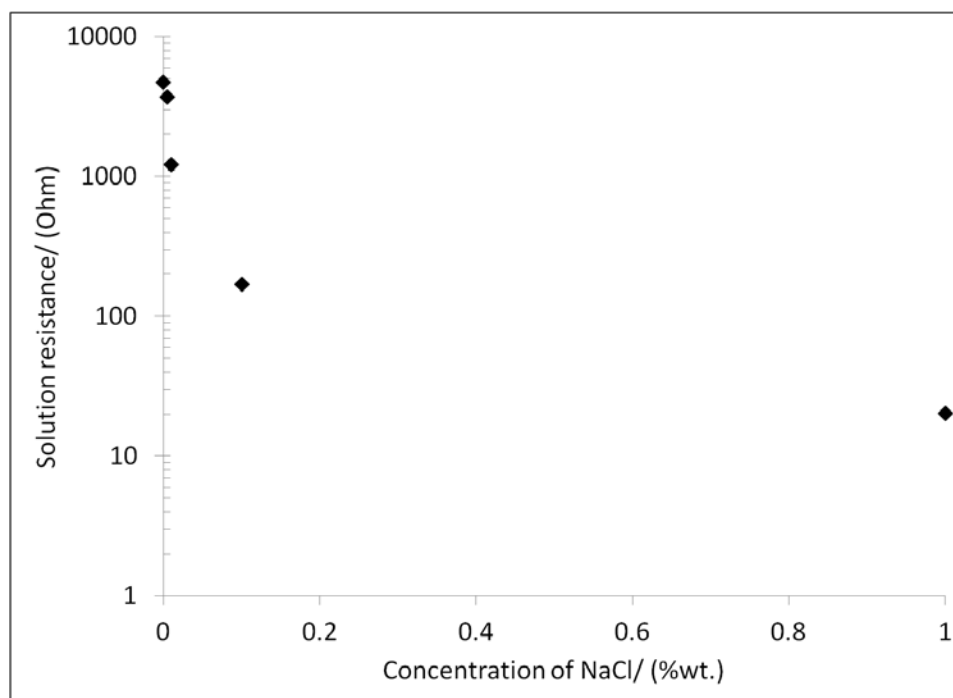


Figure 24: Solution resistance of water as a function of salt concentrations.

#### *Solution resistance as a function of surface area*

From the results shown above, the difference in the solution resistance of DI water and n-heptane was large. Therefore the EIS technique could be used to determine which liquid occupied the steel surface. If only water was present on the surface, solution

resistances of the magnitude of 5 k $\Omega$  would be anticipated and in the case of heptane it would be many orders of magnitude higher.

Table 4: Liquid solution resistance

Solution	Solution resistance (Ohm)
1wt.% NaCl	20 $\pm$ 1
0.1wt.% NaCl	170 $\pm$ 9
0.01wt.% NaCl	1,200 $\pm$ 103
0.005wt.% NaCl	3,700 $\pm$ 38.2
DI water	4,700 $\pm$ 96
n-heptane	10 <sup>9</sup> -10 <sup>11</sup>

*Solution resistance as a function of surface area*

From the results shown above, the difference in the solution resistance of DI water and n-heptane was large. Therefore the EIS technique could be used to determine which liquid occupied the steel surface. If only water was present on the surface, solution resistances of the magnitude of 5 k $\Omega$  would be anticipated and in the case of heptane it would be many orders of magnitude higher.

According to the visual observations, n-heptane disturbed the coalescence of water droplets by accumulating between them. Hence, in this scenario when both liquids were present on the steel surface at the same time, the measured resistance was expected to be in between the two values for DI water and heptane given in Table 4. The magnitude of the measured resistance could be used to determine how much area was

occupied by the water vs. the heptane. Therefore, this appeared to be a promising method for not only distinguishing which phase occupied the surface but also for quantifying how much surface was covered with water vs. hydrocarbon during the co-condensation process.

First, the relationship between the measured solution resistance and the surface area wetted with water was determined.

Figure 25 represents the experimental setup designed for relating the solution resistance to the surface area occupied with water. To vary the area, the EIS probe was immersed to different extents in the water phase. Experiments were performed in a deoxygenated, CO<sub>2</sub>-saturated solution at ambient temperature and pressure. CO<sub>2</sub> was purged through the water for 4 hours and the bubbler was lifted to the vapor phase during the experiments to avoid any disturbance it might cause.

The relationship of (solution) resistance and the percentages of surface coverage by water for three different water solutions is shown in Figure 26. Resistance values significantly increased with decreased surface coverage by water, and *vice versa*. Empirical correlations between solution resistance and surface area are given in Table 5. The solution resistance measured for a 30% water-wetted surface was not significantly different from a 100% water-wetted surface, which could lead to difficulties in defining surface coverage by this technique. Secondly, a slight amount of ionic substance decreased the solution resistance by an order of magnitude. The lifetime of water droplets in the condensation process could last for more than 30 minutes, especially when the condensation rate of water was low. During this period, corrosion processes also took

place and released ferrous ions which could significantly reduce the solution resistance. Therefore, lower resistance did not always correspond to a larger area occupied by the water phase. While this technique did not prove accurate enough to unambiguously determine the percentage of surface coverage by a given phase, it was still considered accurate enough to identify which phase wetted the steel surface.

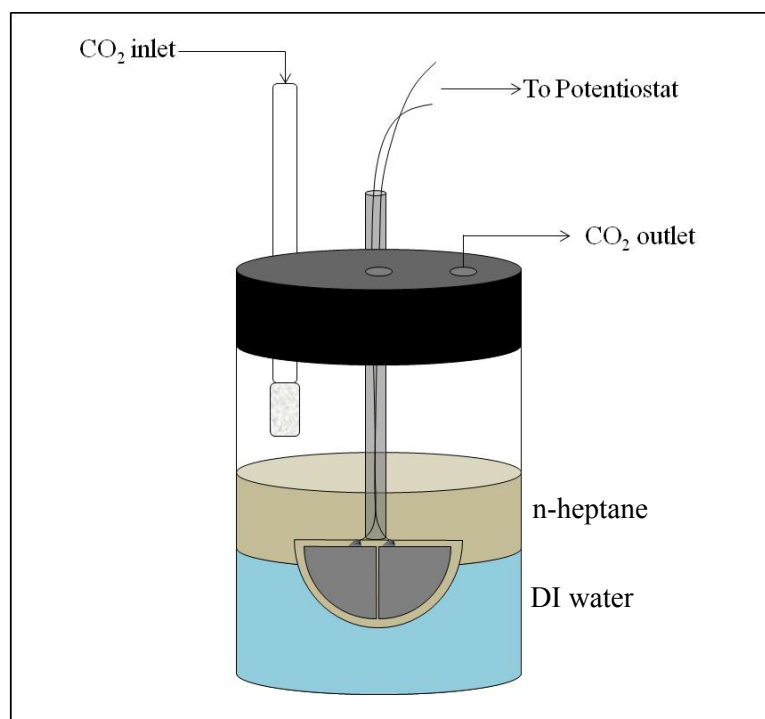


Figure 25: Experimental setup for the calibration of surface area and solution resistance using Electrochemical Impedance Spectroscopy (EIS).

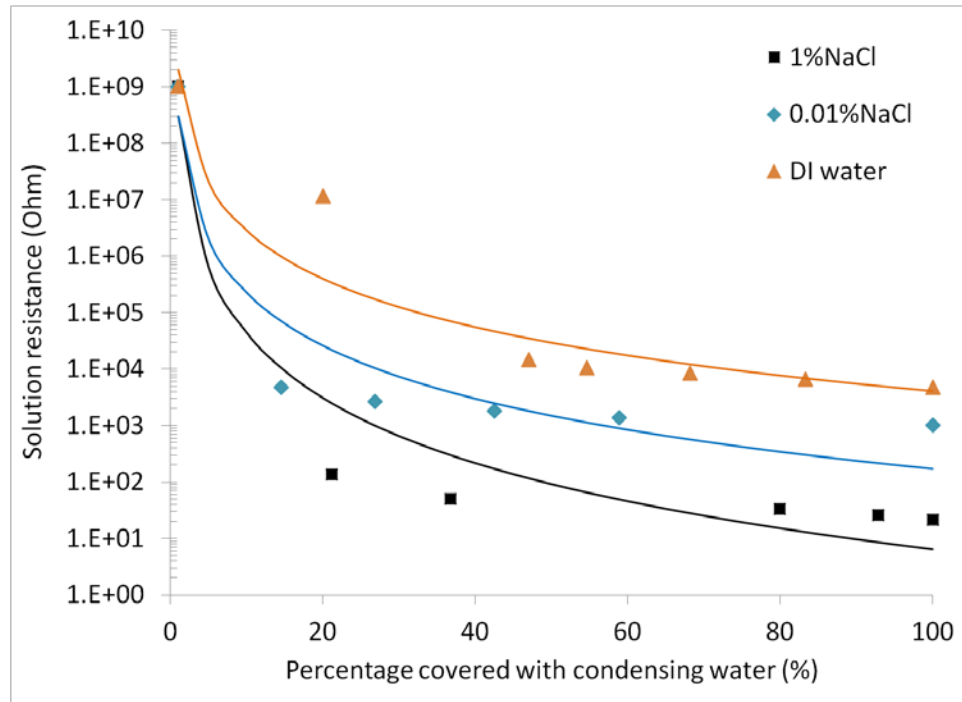


Figure 26: Resistances with percentage of area covered with conductive solution; Dots are experimental data, Lines are empirical correlations.

Table 5: Correlations between (solution) resistances and surface area with various salt concentrations.

Conductive solution	Correlation $R_s = a(Area)^b$	$R^2$
1 wt.% NaCl	$a = 3 \times 10^8$ , $b = -3.834$	0.9329
0.01 wt.% NaCl	$a = 3 \times 10^8$ , $b = -3.122$	0.9039
DI water	$a = 2 \times 10^9$ , $b = -2.848$	0.9046

- Condensation process investigation using the conductivity probe

Experiments reported in the previous section show that the electrical resistivity of the solution can be used to distinguish which phase wets the steel surface during the

various scenarios of co-condensation. Yet, the EIS probe developed for this study was not good enough to effectively quantify the water-wetted area.

Therefore an improved conductivity based probe (described in section 3.2.5) was used in a new set of experiments. A test matrix and procedures were similar to the those used in the previous test with the EIS probe. Since the new conductivity probe contained 20 flush mounted pins and the conductivity was measured almost simultaneously, quantifying the wetted surface area could be done directly by counting the number of pins that showed the presence of conductive solution.

The whole progression of the water only condensation process is shown in Figure 27 where Figure 28 focuses on what happened during the first 4 hours. The y-axis corresponds to the percentage of pins that showed high conductivity i.e. they were water wet. Within the first hour, approximately 80% of the surface was covered with water. This agreed with the previous observations using the borescope (Figure 19). This technique also showed good reproducibility. A lower water condensation rate, which corresponded to the lower vapor temperature, showed that less area was wetted with water in the first hour as coalescence proceeded more slowly. At the end of the test, the entire surface was covered with water; as happened in every test.

Figure 29 presents the water-wetted area when water co-condensed with hydrocarbons. The surface was primarily wetted with water in the co-condensation of water/n-heptane and n-octane environments. Compared to the visual observation (Figure 21) where only one liquid was observed on the surface, this technique indeed offered more precise information of what happened at the steel surface. Water was still the

predominant phase. Co-condensation of water and decane showed a slight difference in the wetting as less than 50% of the surface was wetted with water.

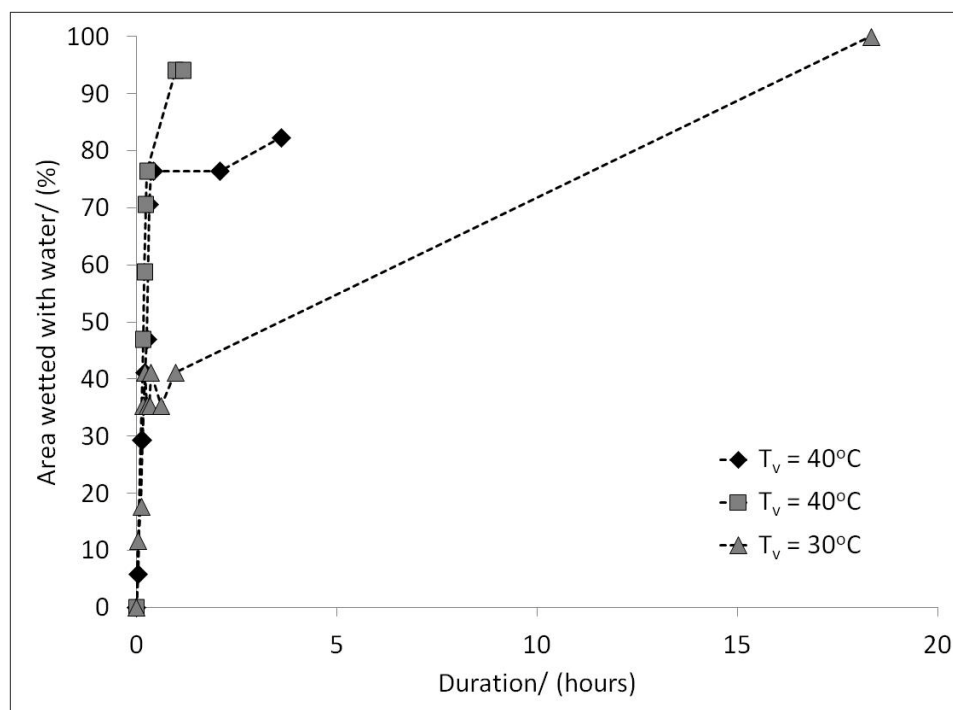


Figure 27: Percentage area wetted with water with time in water condensation process (From 0<sup>th</sup> hour to 20<sup>th</sup> hour)

Figure 30, Figure 31, and Figure 32 show the area wetted with water at various water condensation rates, when co-condensing with n-heptane, n-octane, and n-decane, respectively. The n-heptane and n-octane behaved similarly as the majority of the surface was occupied with water (60% to 100%). The large volume of n-heptane condensate did not overcome the hydrophilic nature of the steel surface. Hence, water gradually wetted more and more of the steel surface as time progressed.

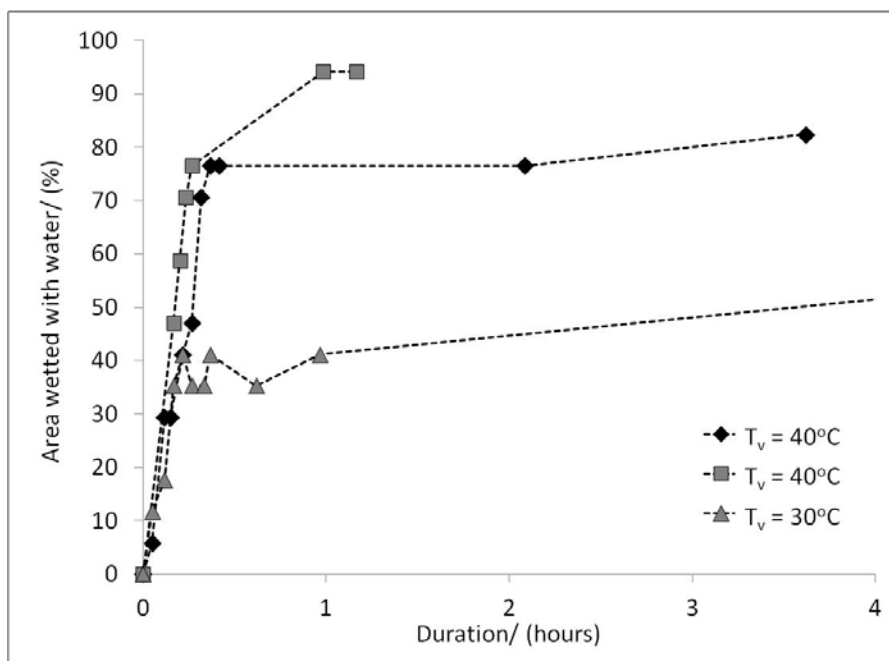


Figure 28: Percentage area wetted with water with time in water condensation process (From 0<sup>th</sup> hour to 4<sup>th</sup> hour)

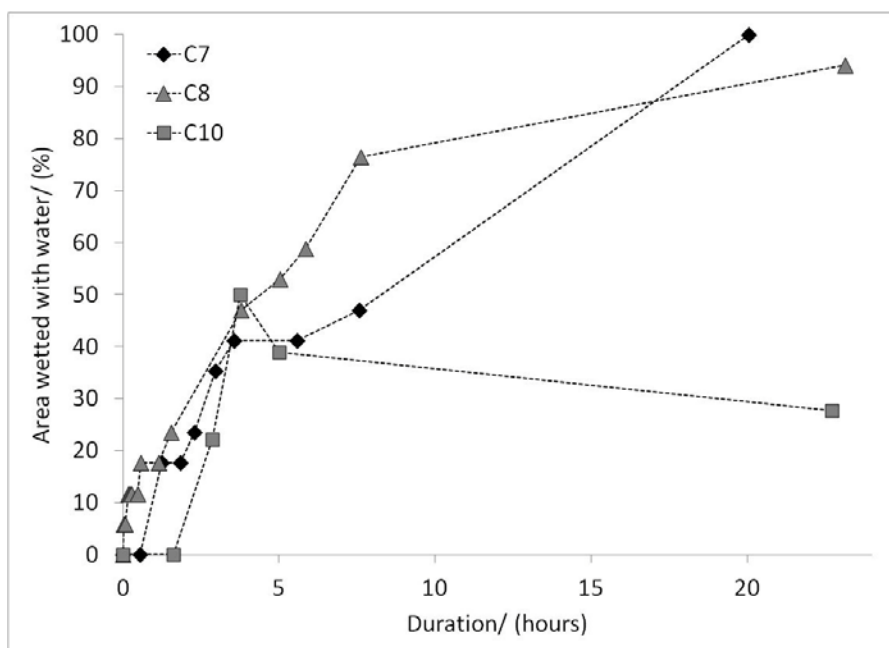


Figure 29: Responses from conductivity pins: Co-condensation of water and hydrocarbons ( $T_v = 40 \pm 2^\circ\text{C}$ ,  $\Delta T = 3^\circ\text{C}$ ).

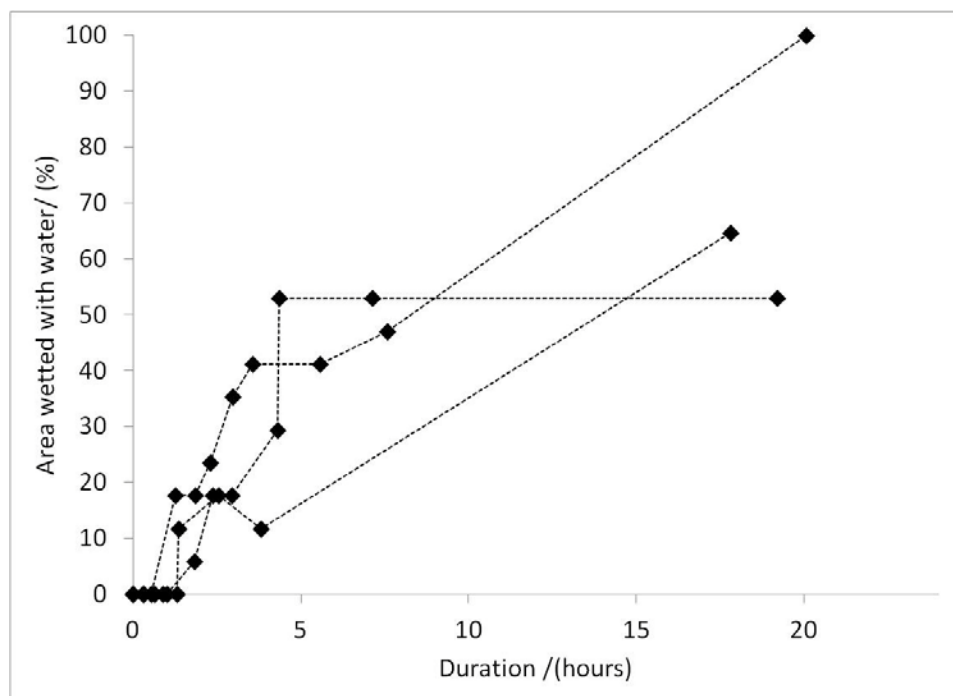


Figure 30: Responses from conductivity pins: Co-condensation of water and heptane ( $T_v = 30$  to  $50^\circ\text{C}$   $\text{WCR} = 0.019$  to  $0.03 \text{ mL/m}^2/\text{s}$  and  $C_7\text{CR} = 0.12$  to  $0.19$ ).

It appears that water had more difficulty occupying the steel surface when it co-condensed with n-decane even though the condensation rate of n-decane was lower than the water condensation rate (Figure 32). This is supported by contact angle measurements reported previously which showed that water was not effective in displacing n-decane in the same way as it was for n-heptane and n-octane.

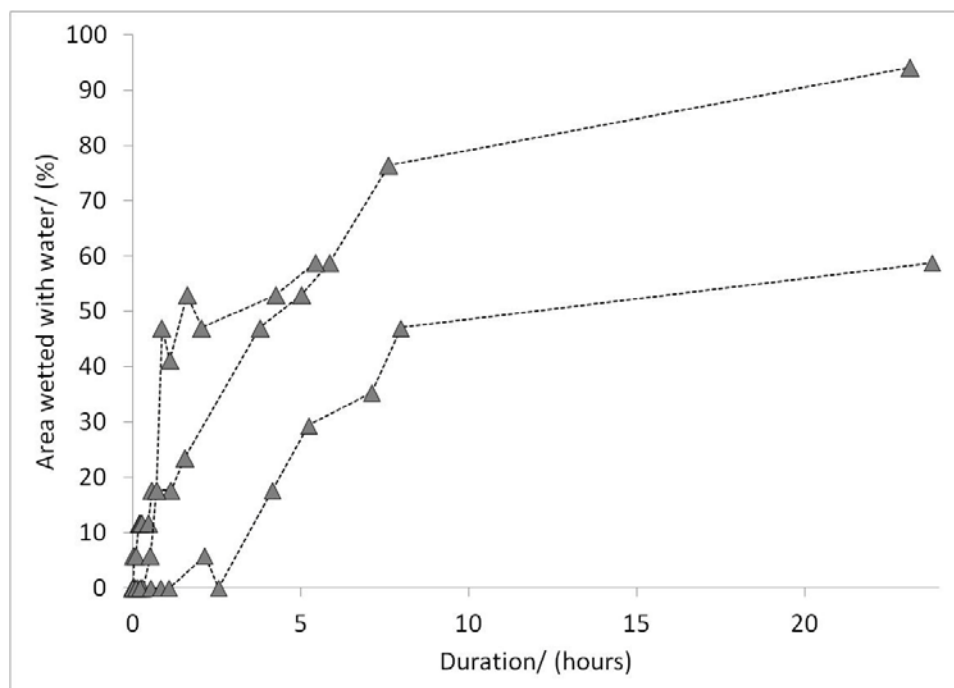


Figure 31: Responses from conductivity pins: Co-condensation of water and octane ( $T_v = 30$  to  $50^\circ\text{C}$   $\text{WCR} = 0.02$  to  $0.03$   $\text{mL}/\text{m}^2/\text{s}$  and  $\text{C}_8\text{CR} = 0.04$  to  $0.7$   $\text{mL}/\text{m}^2/\text{s}$ ).

Figure 33 presents the response from the conductivity probe when water was pre-condensed followed by co-condensation with n-heptane. The n-heptane appears to break up the water film as the area covered with water slightly decreased. Yet, water still dominated. This was in good agreement with the visual observation (Figure 22). For this wetting scenario, the results obtained with n-heptane, n-octane and n-decane are compared in Figure 34. After introducing the hydrocarbons, only n-heptane interrupted the full wetting of water. Octane and decane did not cause any disruption of the pre-condensed water film. In the n-heptane case, it was able to break the water film due to the significant amount of n-heptane condensing (7 times higher than water on a volume basis). However, this assumption could not be applied to octane and decane as the

condensation rates of both hydrocarbons were less than n-heptane or even less than that of water.

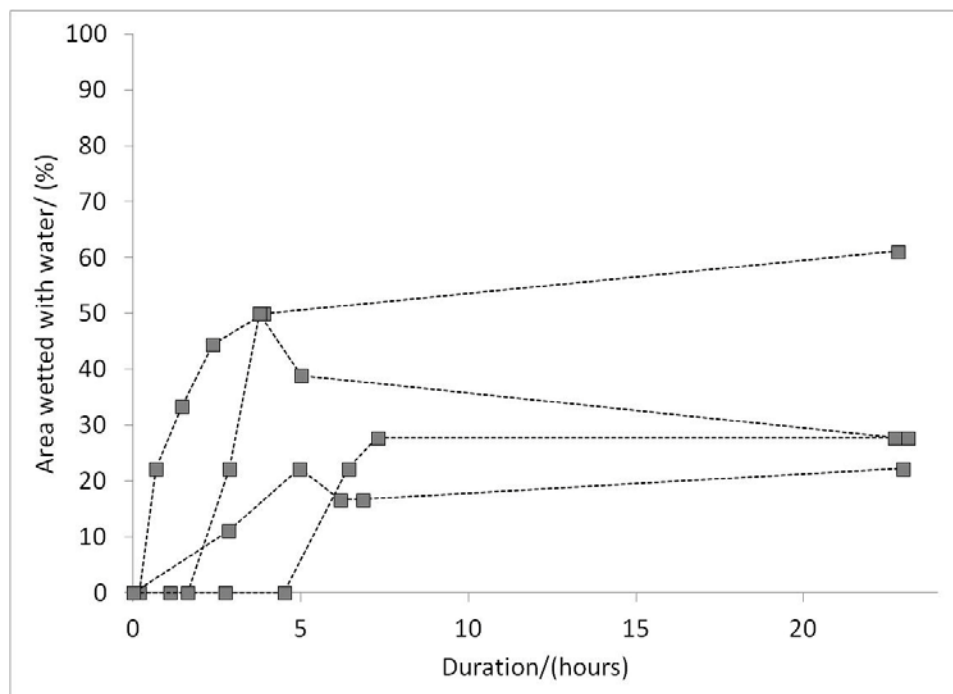


Figure 32: Responses from conductivity pins: Co-condensation of water and decane ( $T_v = 30$  to  $40^\circ\text{C}$  and  $\text{WCR} = 0.017$  to  $0.02 \text{ mL/m}^2/\text{s}$  and  $C_{10}\text{CR} = 0.005$  to  $0.007 \text{ mL/m}^2/\text{s}$ ).

The reverse sequence of condensation was then conducted. Initially, only the hydrocarbon was condensing on the surface. Subsequently, water was added creating a co-condensation scenario. The n-heptane condensed alone for 3 hours until a uniform hydrocarbon film formed on the electrode surface. Hence, no electrical response was obtained from the conductivity probe (Figure 35). Subsequently, water was added and the water-wetted area gradually increased. There was a one hour gap after water was added, what somewhat contradicted what was visually observed (Figure 23). It can be

hypothesized that this was caused by the hydrophobicity of the epoxy between electrodes. After one hour, the water began to disrupt the hydrocarbon layer and occupy more and more of the steel surface.

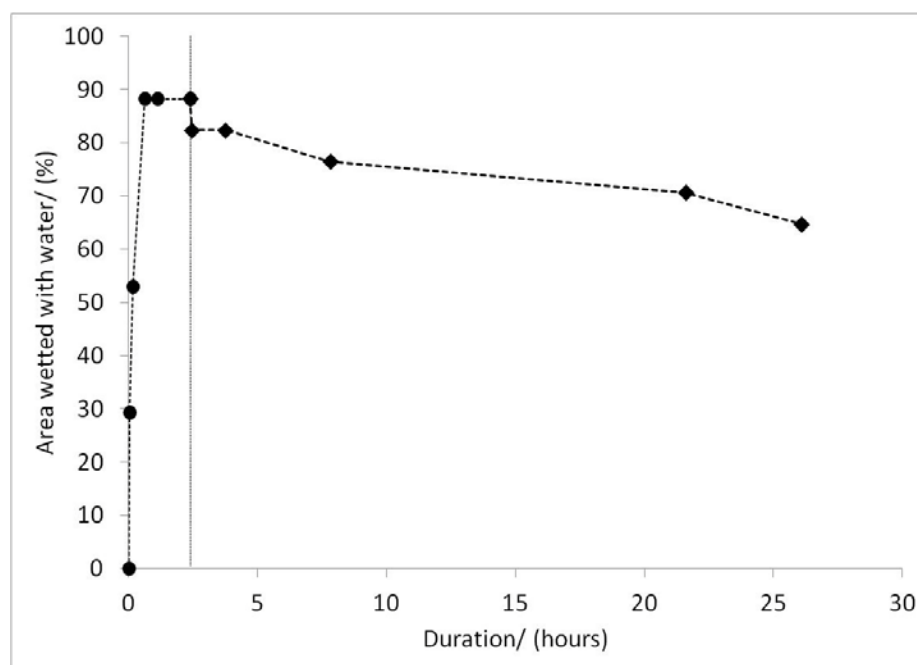


Figure 33: Responses from conductivity pins: Pre-condensation with water only followed by the co-condensation of water and n-heptane. ( $WCR = 0.02 \text{ mL/m}^2/\text{s}$  and  $C_7CR = 0.19 \text{ mL/m}^2/\text{s}$ ).

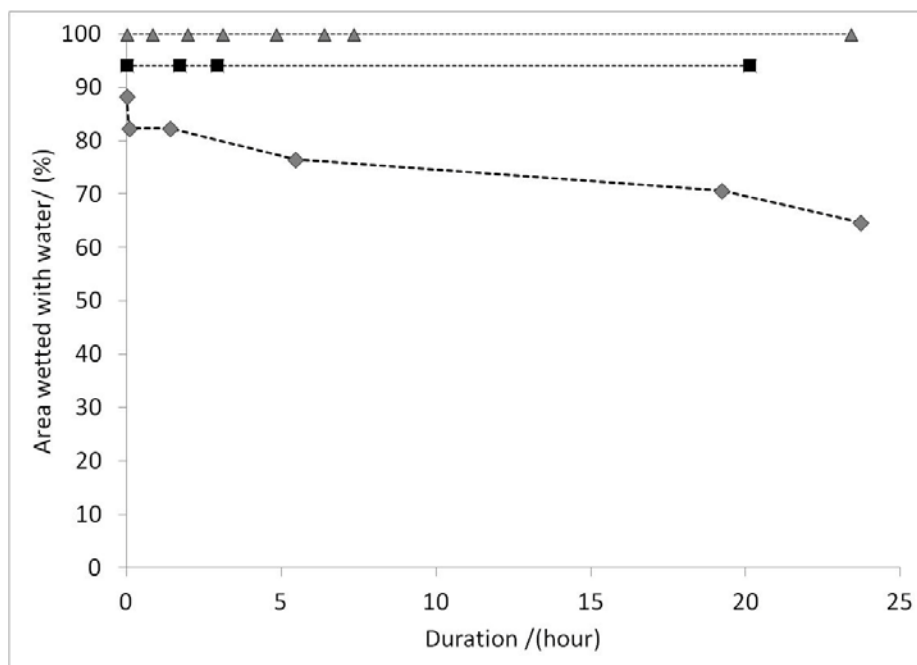


Figure 34: Responses from conductivity pins: Pre-condensation with water followed by the co-condensation of water and various hydrocarbons.

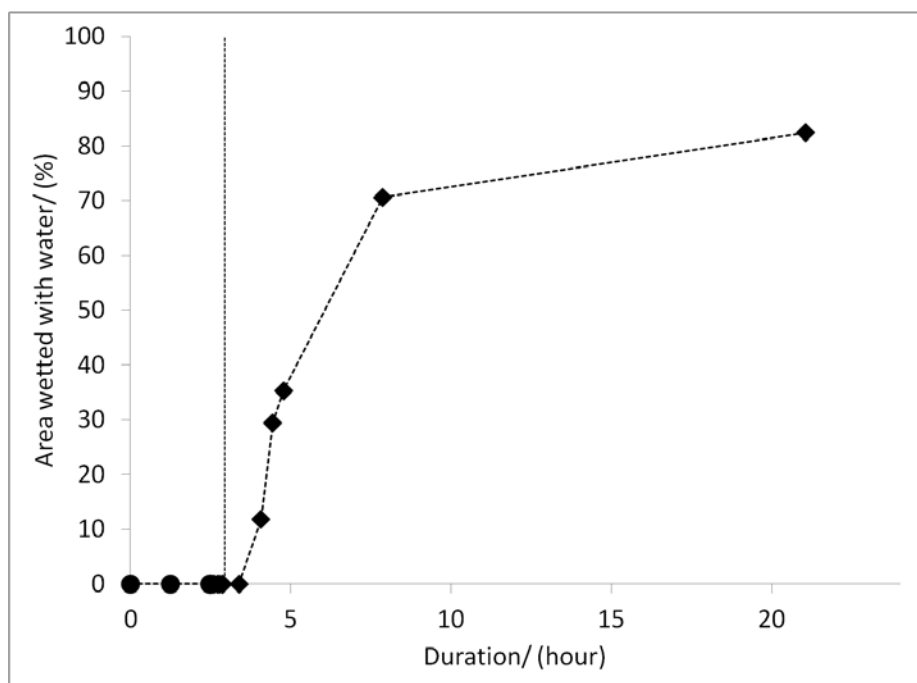


Figure 35: Percentage area wetted with water creating the co-condensation scenario of water and n-heptane ( $WCR = 0.017 \text{ mL/m}^2/\text{s}$  and  $C_7CR = 0.10 \text{ mL/m}^2/\text{s}$ ).

Similar tests were performed using different hydrocarbons and the results are compared in Figure 36. Heavier hydrocarbons such as n-octane and n-decane seemed to have a stronger influence on the wetting behavior of water, in this scenario.

To summarize, condensation processes of water and straight-chain hydrocarbons were investigated by exploiting the difference in their electrical conductivity. The results showed that octane had similar wettability to n-heptane since both have similar structures. Decane was slightly different and formed a stronger barrier against water wetting the steel surface. Yet, if the surface was pre-wetted with water, decane would not be able to break the water film as the decane condensation rate was less than that of water.

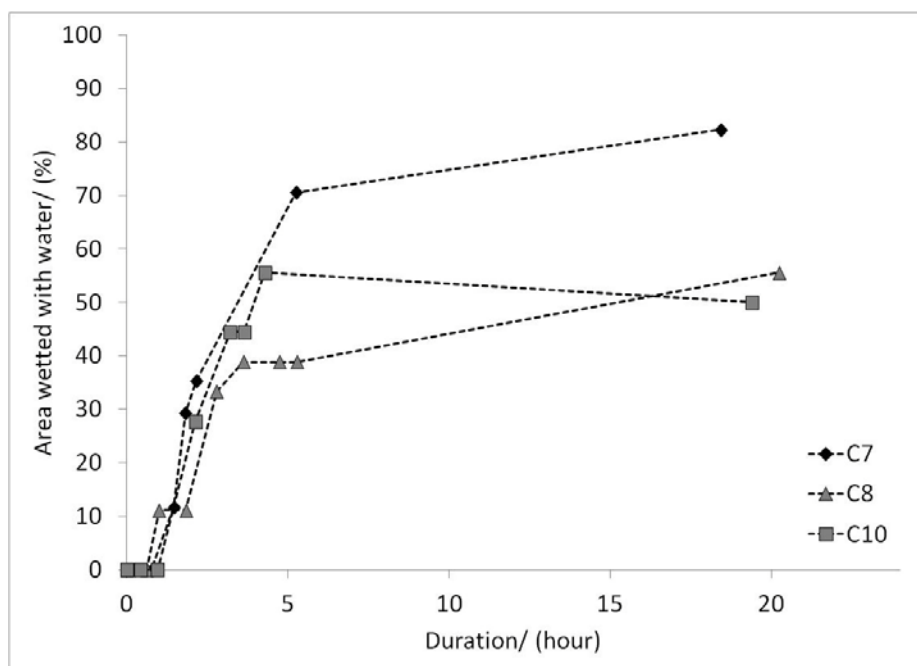


Figure 36: Percentage area wetted with water creating the co-condensation scenario of water and various hydrocarbons.

### 3.3.4. Discussion

The water condensation process has been extensively studied by others [9]. Therefore, this section only discusses the co-condensation process involving the presence of immiscible liquids. The co-condensation mechanisms proposed below accounted for following influential factors:

- the difference in the molecular structure of the two liquids having polar and non-polar characteristics respectively,
- the mutual solubility of water and hydrocarbons,
- the hydrophilicity of the steel substrate,
- the condensation rates of immiscible liquids.

Based on these mechanisms, three scenarios are discussed below:

- 1) Simultaneous co-condensation of two liquids
- 2) Sequential condensation: Pre-condensation with hydrocarbon
- 3) Sequential condensation: Pre-condensation with water

#### Scenario 1: Co-condensation of two liquids

From the vapor phase, two species can readily condense on a cold surface. The condensation process starts with the nucleation of droplets, followed by growth, coalescence and detachment from the surface. Each liquid phase starts condensing differently. Hydrocarbon droplets grow by spreading over the steel surface, forming a uniform film. This spreading of hydrocarbons takes place easily due to their low surface tension. Water, on the other hand, has a much higher surface tension. Water molecules

cluster together due to hydrogen bonding, thus condensed water forms discrete droplets which grow and eventually coalesce and fall.

However, the process of water droplet coalescence is retarded by the presence of hydrocarbons. Therefore a larger number of smaller water droplets form which take a longer time to grow and fall. The surface of the steel is wetted by both liquid phases with water eventually dominating. These stages are schematically illustrated in Figure 37.

In the co-condensation scenarios, dissimilarities between water and a given hydrocarbon phase influence the process more than the rate of condensation for that given phase. For instance, n-heptane condenses at a rate around 7 times higher than water on a volume basis. Still, water gradually displaced n-heptane and occupied the steel surface. On the other hand, n-decane condensed less than water but influenced the coalescence process of water the most.

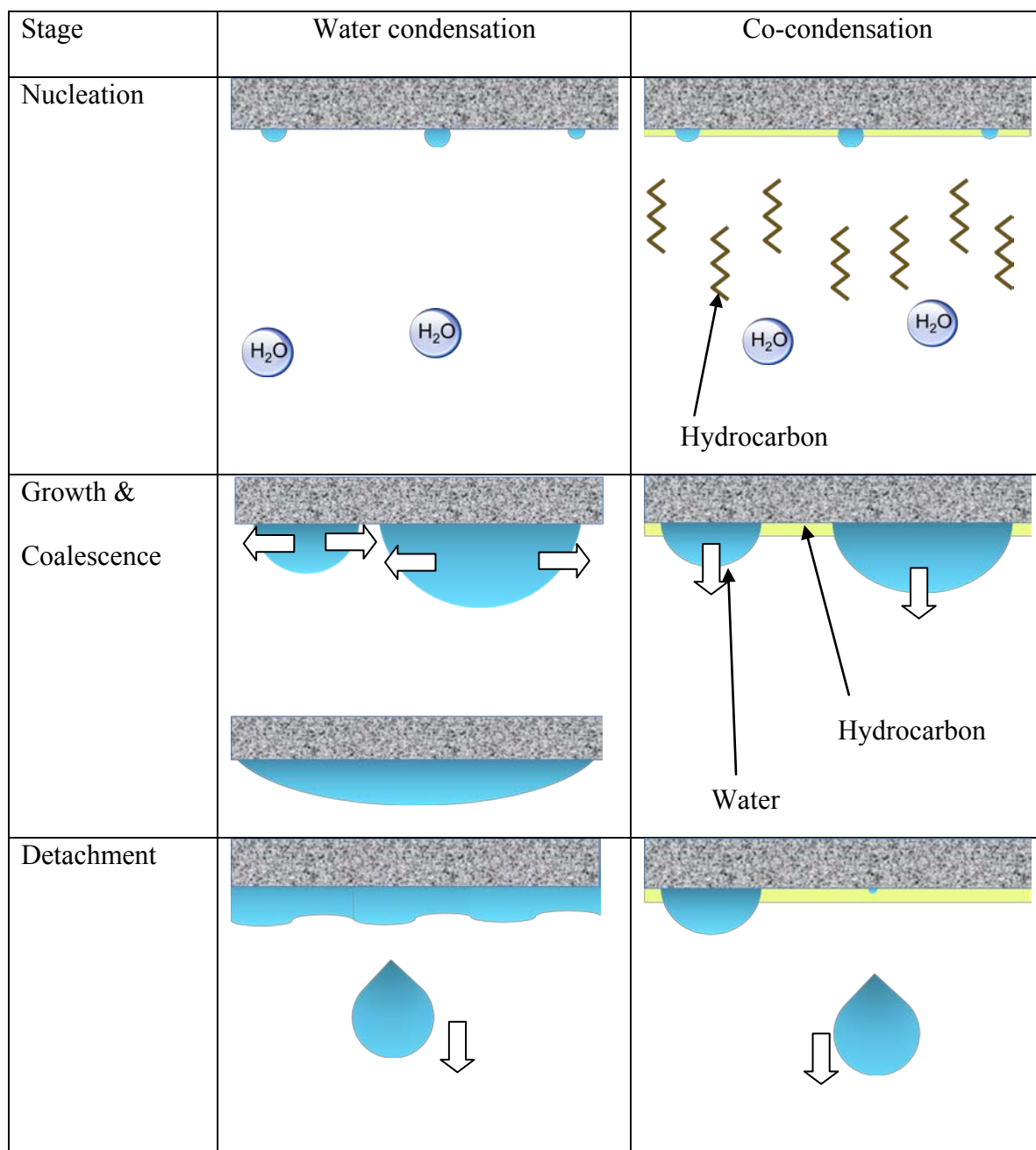


Figure 37: Illustration of condensation process in the absence and presence of hydrocarbon (blue: water; yellow: hydrocarbon).

*Scenario 2: Sequential condensation: Pre-condensation with hydrocarbons*

Pre-condensation of hydrocarbons on steel closely corresponds to an early production scenario during pipeline transportation of wet gaseous hydrocarbons.

The primary reason why water readily displaces the pre-wetted layer of hydrocarbons is the hydrophilicity of the steel surface. However, the question remains: why and how do water molecules travel through the hydrocarbon layer (against gravity) and attach to the steel surface?

Though water and hydrocarbon liquids are immiscible, water actually can dissolve in the hydrocarbon to a small extent. Tsonopoulos suggested that water can dissolve in hydrocarbon in a range of  $10^{-3}$  mole fraction [82]. Water molecules diffuse to the steel surface and once they get there, they can readily displace the hydrocarbon molecules, which are weakly adsorbed on the steel surface. Between water molecules, hydrogen bonds form and attract even more water molecules towards the metal surface. Consequently, water aggregates at a macroscopic level. Gradually, it occupies the majority of surface. This is illustrated in Figure 38. There is no direct evidence for this scenario and other explanations are possible. For example, as water condenses on the surface of n-heptane, it forms small discrete droplets, which grow in size and coalesce, just as they would on a steel surface. However, the shape of the droplets resembles a lens with the upper surface of the water droplet “bulging” out toward the steel surface. Given that the n-heptane film is thin, the water may therefore touch the steel surface and replace the n-heptane.

Scenario 3: Sequential condensation: Pre-condensation with water

When a hydrocarbon condenses on a water surface, it does not spread along the interface. Instead, hydrocarbon forms droplets on the water surface. When condensing in large quantities, the hydrocarbon droplets tend to segregate the water film. They may eventually disrupt and partially displace the water film at the surface, but this effect seems small and pronounced only with light highly condensable hydrocarbons such as n-heptane. The illustration is shown in Figure 39.

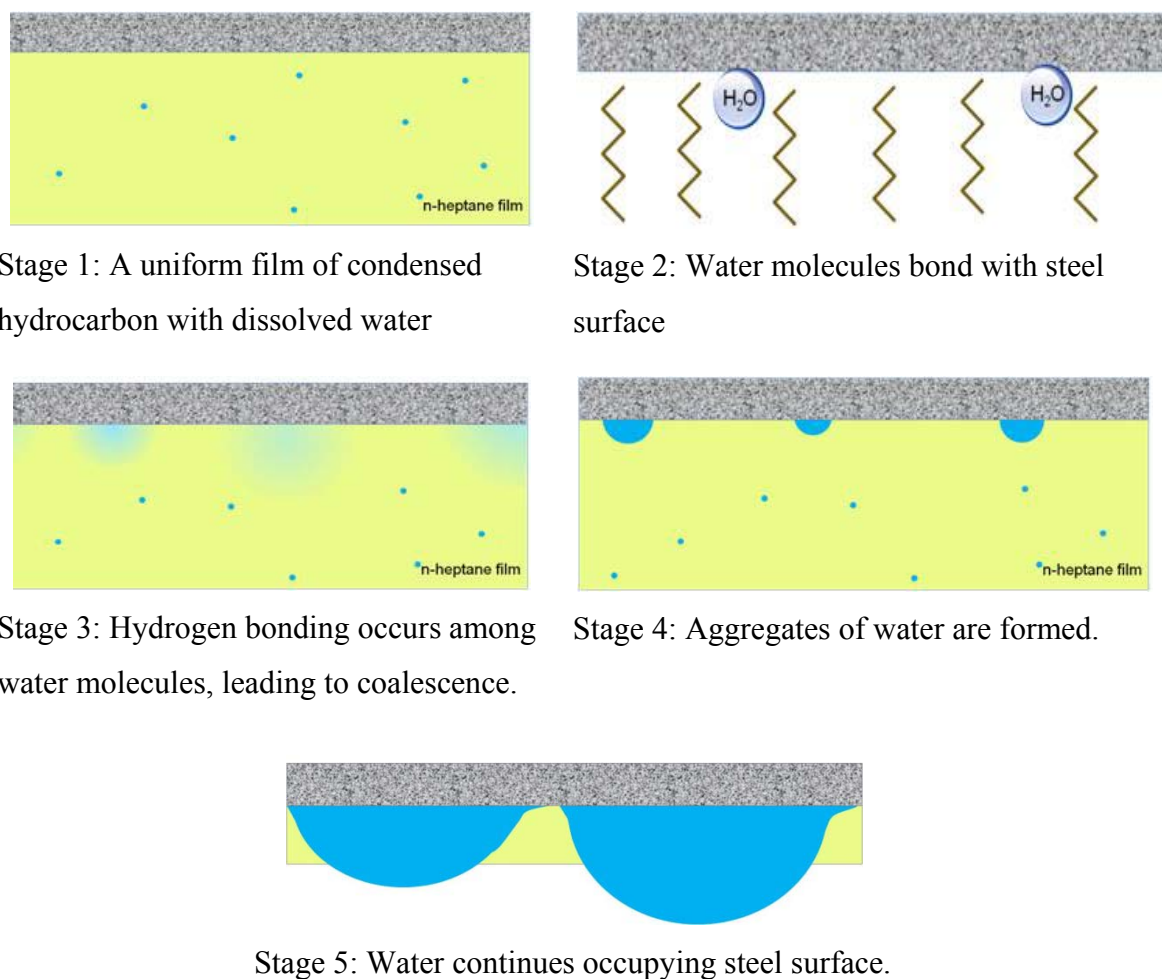


Figure 38: Replacement of pre-condensed n-heptane with water.

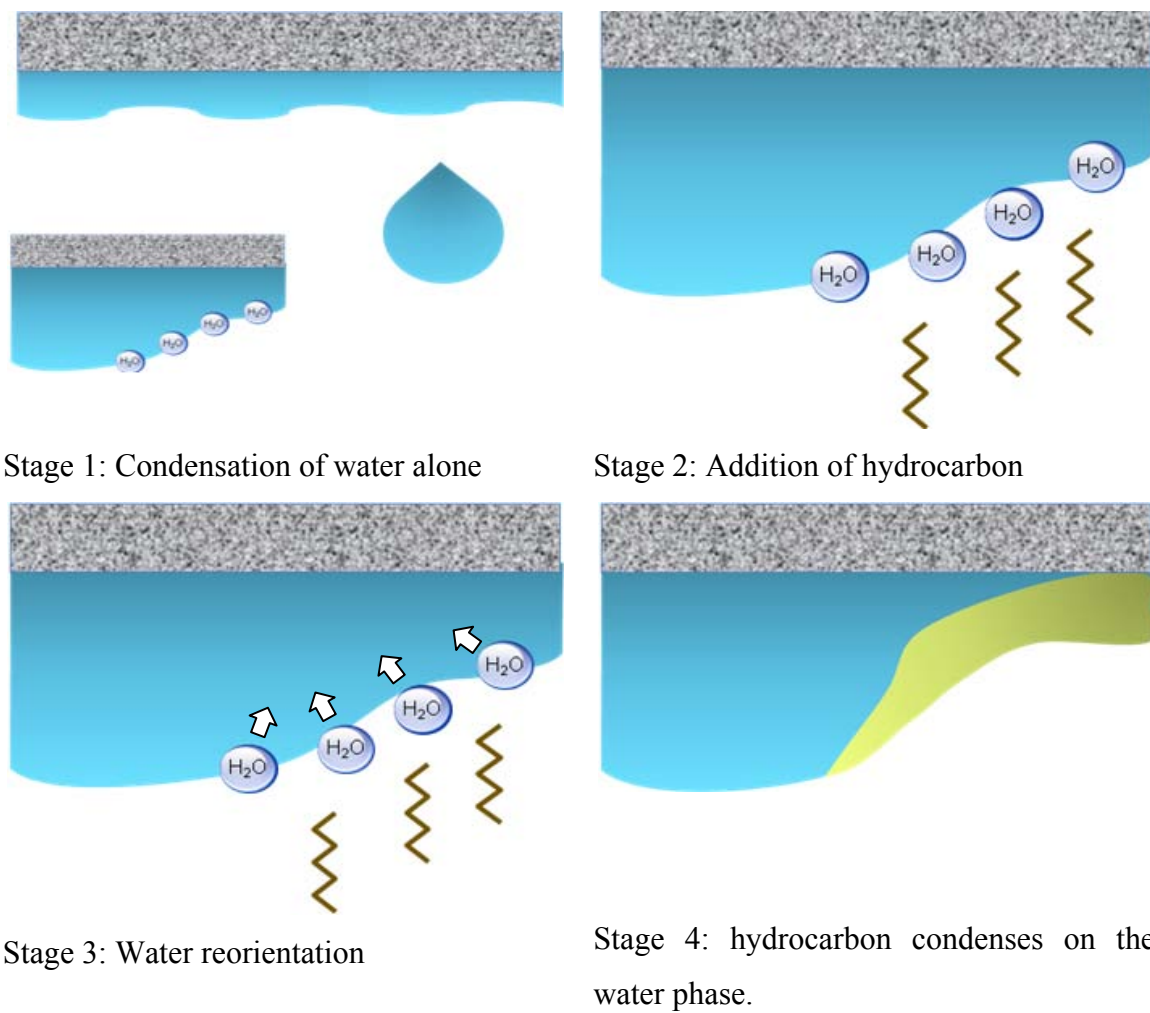


Figure 39: Illustration of the replacement of pre-condensed water with hydrocarbon.

## CHAPTER 4: STUDY OF TOP OF THE LINE CORROSION: THE CO-CONDENSATION SCENARIO

### 4.1. Introduction

Results reported in the previous chapter (condensation processes monitoring) showed that water predominantly occupied the carbon steel surface even though a part of the surface area became wetted with a hydrocarbon. Thus, relying on hydrocarbons co-condensation to protect TLC would incur a significant level of risk.

Nonetheless, it remains interesting to explore any possible influences that hydrocarbons might have on TLC aside from the displacement of water.

### 4.2. Experimental procedure

Two small scale experimental setups were used to investigate the corrosion behavior under the co-condensation environment. Please note that parts of this chapter have been presented and published [75], [83]

#### 4.2.1. Corrosion test in a stagnant condition

The same glass cell as the one described in section 3.2.4 (Figure 10) was utilized in these experiments, except that the borescope was not used. The sample assembly and its preparation were the same. Table 6 presents the test matrix for the short-term corrosion test in the absence of hydrocarbons (Test #1 and Test #2) and in the presence of co-condensation of water with three different straight chain hydrocarbons (Test #3 to Test #8).

Hydrocarbons were usually depleted from the test cell faster than water. To avoid this depletion, a deoxygenated hydrocarbon was periodically added into the system. The

vapor temperature was controlled at 35 and 50°C whereas the sample temperature was kept at 25 and 30°C, respectively. The corresponding condensation rates of water and hydrocarbons were calculated and listed in Table 6. The details of the calculation can be found in Appendix I.

In order to confirm the result of the short term tests, long term corrosion tests under the condensation of water alone and the co-condensation of water and n-heptane were also conducted lasting two weeks. The test matrix for the long term tests is shown in Table 7.

Table 6: Test matrix for corrosion test in a glass cell for 3 days

<b>Parameters</b>	<b>#1</b>	<b>#2</b>	<b>#3</b>	<b>#4</b>	<b>#5</b>	<b>#6</b>	<b>#7</b>	<b>#8</b>
Material	X65							
Hydrocarbons	–		n-heptane		n-octane		n-decane	
Total pressure (bar)	1							
pCO <sub>2</sub> (bar)	0.94	0.88	0.85	0.69	0.91	0.81	0.94	0.87
T <sub>v</sub> (°C)	35	50	35	50	35	50	35	50
T <sub>s</sub> (°C)	25	30	25	30	25	30	25	30
WCR (mL/m <sup>2</sup> /s)	0.06	0.22	0.05	0.19	0.05	0.2	0.06	0.22
HCCR (mL/m <sup>2</sup> /s)	–	–	0.33	1.21	0.13	0.5	0.02	0.08
Test duration (days)	3							

Table 7: Test matrix for corrosion tests in glass cell for 2 weeks

Parameters	#1	#2
Material	X65	
Hydrocarbons	–	n-heptane
Total pressure (bar)	1	
pCO <sub>2</sub> (bar)	0.85	0.69
T <sub>v</sub> (°C)	50	
T <sub>s</sub> (°C)	30	
WCR (mL/m <sup>2</sup> /s)	0.22	0.19
HCCR (mL/m <sup>2</sup> /s)	–	1.2
Test duration (weeks)	2	

#### 4.2.2. Corrosion tests in a flowing condition

A Teflon tube served as a sample holder and was sectioned to allow for two carbon steel samples to be attached at both ends, as shown in Figure 40. This tube was inserted into a 1” ID customized glass condenser as illustrated in Figure 41.

Warm vapors of water and n-heptane were prepared in separate flasks. CO<sub>2</sub>, acting as a corrosive gas and a carrier gas, was bubbled throughout the experiments at a constant rate of 10 mL/s. The flow condition in the Teflon tube was always in a laminar flow regime.

Thermistors were located at the inlet and outlet of the condenser to record the vapor temperature at the location of both samples. The cooling water flowed through the jacket of the condenser to cool the samples. The temperature of the entering and exiting

cooling water were also recorded. As a result, the rate of water and hydrocarbon condensing on the sample surface could be calculated based on the difference in the vapor and cooling water temperature.

A receiver was placed at the outlet of the condenser to collect the liquids condensed over the length of the condenser. This integral value is used in Chapter 5 when the condensation rate prediction model is discussed.

Table 8 and Table 9 show the test matrices for corrosion tests under water condensation alone and co-condensation with n-heptane, respectively. Due to safety concerns, the liquid reservoir temperature was kept below 75°C. Because n-heptane vapor has a lower specific heat capacity and a lower thermal conductivity than water, a temperature drop experienced in co-condensation scenario was larger than that in a pure water system. Hence, a vapor temperature of 50°C was the maximum that this setup could provide for the tests in co-condensation environment.

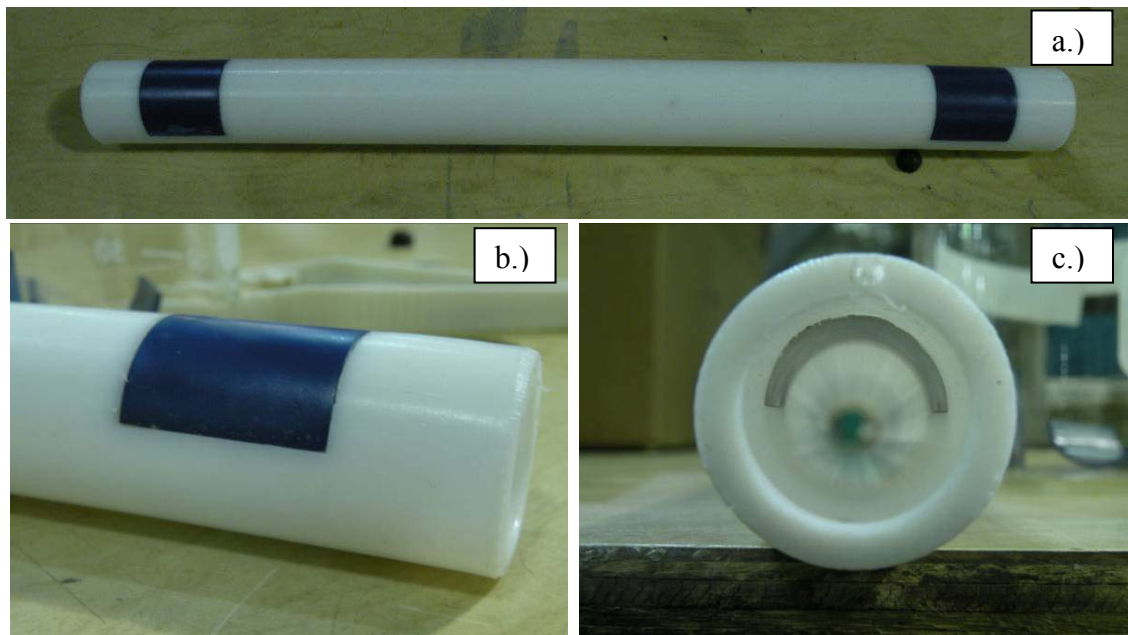


Figure 40: Sample assembly for corrosion tests under flow condition: a.) Top view, b.) Side view, and c.) Cross section view.

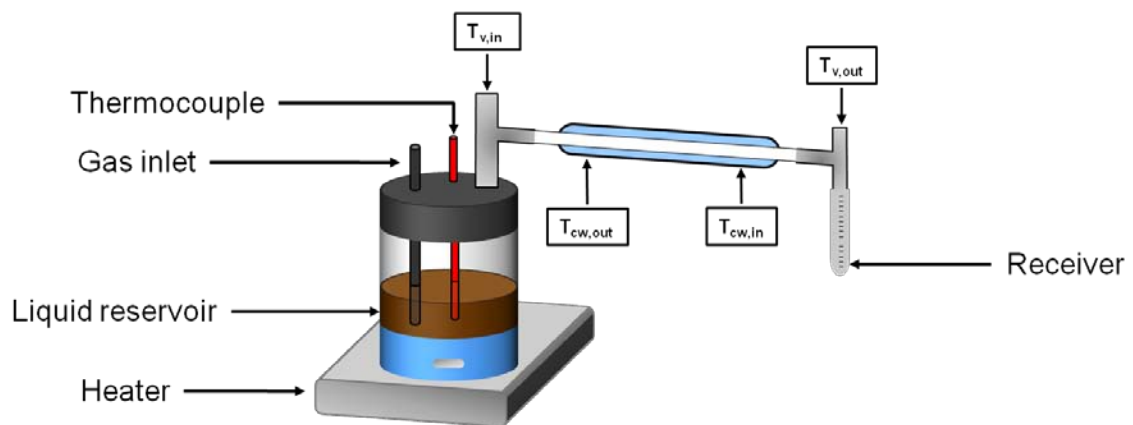


Figure 41: Schematic diagram of experimental setup for corrosion test in flowing conditions.

Table 8: Test matrix for corrosion in pure water condensation in a flowing condition

<b>Parameters</b>	<b>Conditions</b>
Steel type	X65
Vapor temperature ( $T_g$ ), °C	18-65
Water condensation rate (WCR), mL/m <sup>2</sup> /s	0.002-0.6
Total pressure, bar	1
Partial pressure of CO <sub>2</sub> , bar	0.75-0.98
Test duration (days)	1, 3

Table 9: Test matrix for corrosion in co-condensation in a flowing condition

<b>Parameters</b>	<b>Conditions</b>
Steel type	X65
Vapor temperature ( $T_g$ ), °C	18-50
Hydrocarbon	n-heptane
Water condensation rate (WCR), mL/m <sup>2</sup> /s	0.002-0.15
n-heptane condensation rate (HCCR), mL/m <sup>2</sup> /s	0.01-1
Total pressure, bar	1
Partial pressure of CO <sub>2</sub> , bar	0.69-0.94
Test duration (days)	1, 3

#### 4.2.3. Sample preparation

All tests were performed using X65 carbon steel. Its compositional analysis is given in Table 10. The steel was polished with 600 grit sand paper. After that, it was cleaned in an ultrasonic bath filled with isopropanol and air dried. Sample weight was recorded before exposure to the corrosive environment.

Figure 42a and Figure 42b illustrate the sample configurations for the two experimental setups. For stagnant condition tests, a circular sample was used. In flowing conditions, a 1" OD  $\times$  1" Length sample, with a thickness of 1/8", was cut in half (lengthwise).

Table 10: Compositional analysis of X65 carbon steel (balance is Fe)

Element	Al	As	B	C	Ca	Co	Cr	Cu	Mn	Mo	Nb
% Wt.	0.032	0.008	0.001	0.13	0.002	0.007	0.14	0.131	1.16	0.16	0.017
Element	Ni	P	Pb	S	Sb	Si	Sn	Ta	Ti	V	Zr
% Wt.	0.36	0.009	<0.001	0.009	0.009	0.26	0.007	<0.001	<0.001	0.047	<0.001

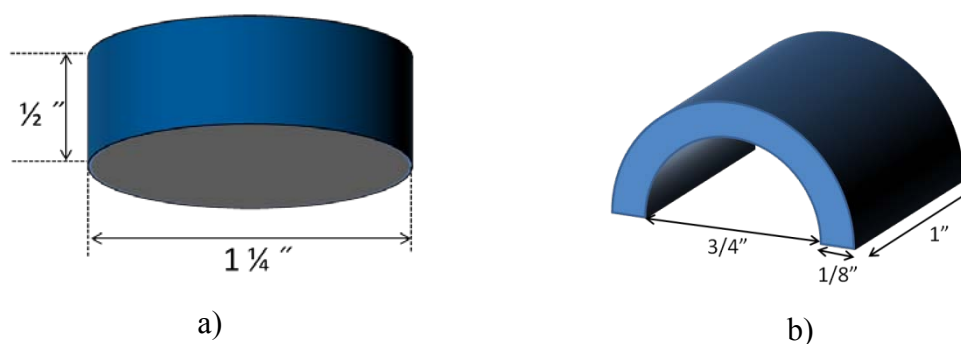


Figure 42: Drawings of sample configuration for corrosion tests in a) a stagnant condition and b) a flowing condition. Blue color represented the xylan paint for isolating area exposed to corrosive environment.

#### 4.2.4. Post processing and analysis

After each experiment was finished, the sample was taken out, rinsed with deionized water, isopropanol and air-dried. Subsequently, the sample was weighed and photographed. Scanning electron microscope (SEM) and Energy dispersive x-ray spectroscopy (EDX) were used to analyze the corrosion product formed on a corroded sample.

Clarke solution (93% HCl + 2% Sb<sub>2</sub>O<sub>3</sub> + 5%SnCl<sub>2</sub>) [84] was prepared to remove any corrosion products formed during the test. Samples were rinsed in Clarke's solution for 20 seconds, followed by deionized water and isopropanol. After that, the sample was air-dried and weighed. This process was repeated until sample weight was stable, which indicated that the corrosion product was completely removed. Corrosion rate was obtained by weight loss technique as calculated from Eq.4-1.

Once each sample was cleaned, its surface was observed again under SEM and IFM checking for the possibility of localized corrosion. The penetration depth was obtained from IFM and the penetration rate was calculated as shown in Eq.4-2.

$$CR_{WL} = \frac{\Delta WL}{\rho_{Fe}TA} \times 10 \times 365 \times 24 \quad \text{Eq.4-1}$$

Where:

- $CR_{WL}$  = Corrosion rate from weight loss, in mm/yr
- $\Delta WL$  = The difference in mass of carbon steel sample before the test and after cleaning with Clarke solution, in g
- $\rho_{Fe}$  = Density of carbon steel sample, in g/cm<sup>3</sup>

- $T$  = Test duration, in hr  
 $A$  = Surface area of carbon steel sample, in  $\text{cm}^2$

$$CR_{IFM} = \frac{d}{T} \times 365 \times 24 \quad \text{Eq.4-2}$$

Where:

- $CR_{IFM}$  = Penetration rate obtained from IFM, in mm/yr  
 $d$  = Penetration depth obtained from IFM, in mm  
 $T$  = Test duration, in hr

### 4.3. Results of corrosion experiments

During the corrosion tests, the following phenomena were observed:

- 1)  $\text{FeCO}_3$  precipitated in all tests performed in co-condensation environments. However,  $\text{FeCO}_3$  did not precipitate when water condensed alone.
- 2) Different levels of corrosion attack (non-uniform) were observed in co-condensation environments suggesting that the two liquids with very different corrosivity simultaneously occupied the steel surface.
- 3) Surface appearance showed that water was segregated into smaller droplets surrounded by hydrocarbon.
- 4) When only water condensed, TLC rate increased with water condensation rate. However, in co-condensation scenarios, the TLC rate remained independent of water condensation rate.

Results of each experiment are discussed in detail below.

#### 4.3.1. Corrosion experiments in a glass cell setup

- Corrosion of carbon steel under water condensation alone

Figure 43 shows the surface analysis of a sample exposed to water condensation alone (WCR = 0.09 mL/m<sup>2</sup>/s). No localized attack was visually observed (Figure 43a). The surface was uniformly corroded as shown in Figure 43b. EDX detected only Fe and C which suggested the likely presence of an iron carbide layer [85] (Figure 43c). Figure 43d is the SEM image of this sample after cleaning with Clarke solution showing uniform corrosion.

IFM analysis confirmed that under water condensation, corrosion proceeded uniformly (Figure 44). The profile and the distribution indicated that for the majority of the surface the depth varied between -1µm to +1µm, which can be thought of as the roughness of the sample.

Similar results were obtained when the sample was exposed to a higher water condensation rate.

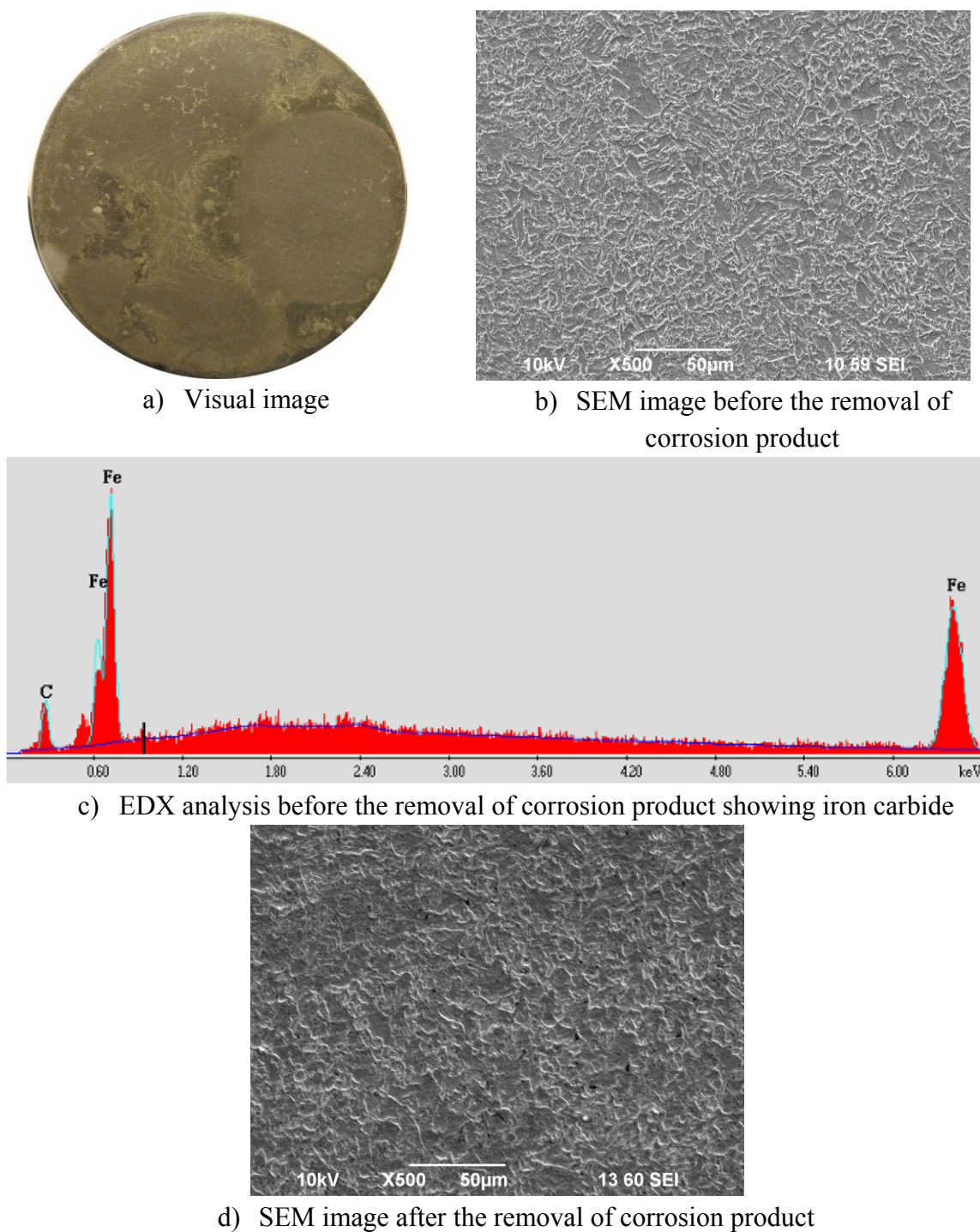


Figure 43: Surface characterization of sample exposed to corrosion in the pure water system ( $WCR = 0.09 \text{ mL/m}^2/\text{s}$ ).

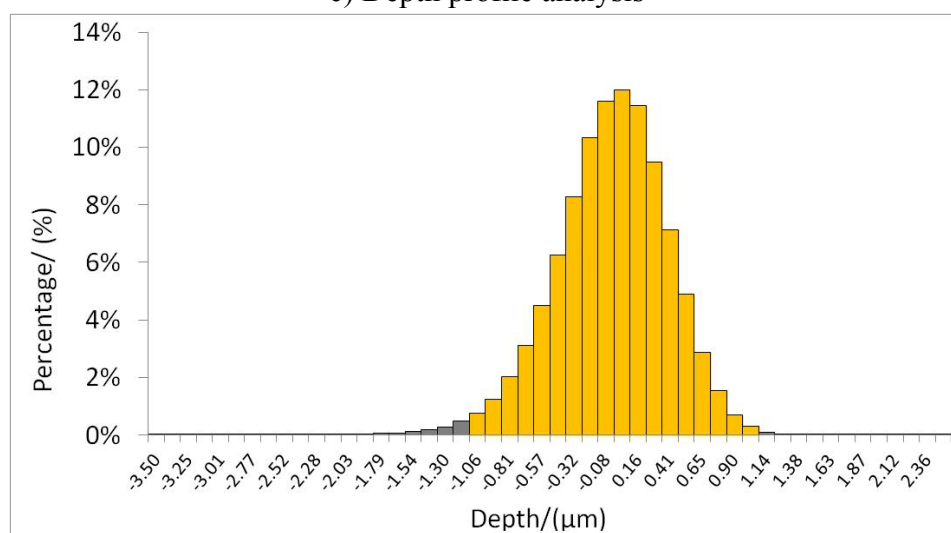
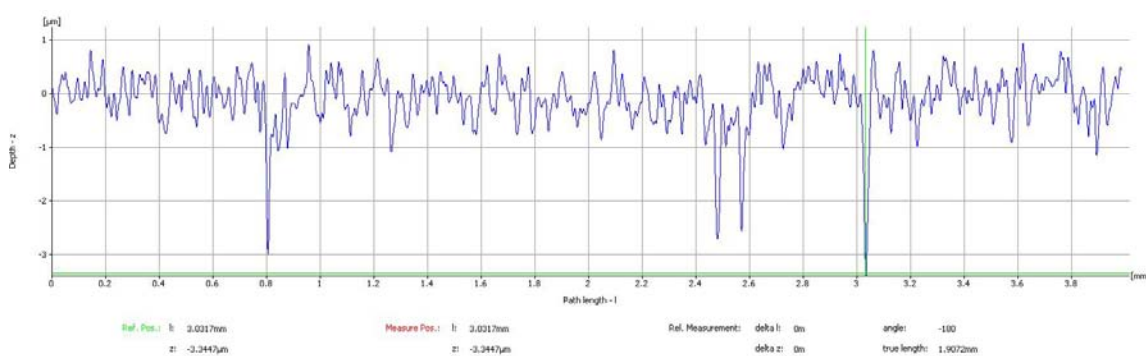
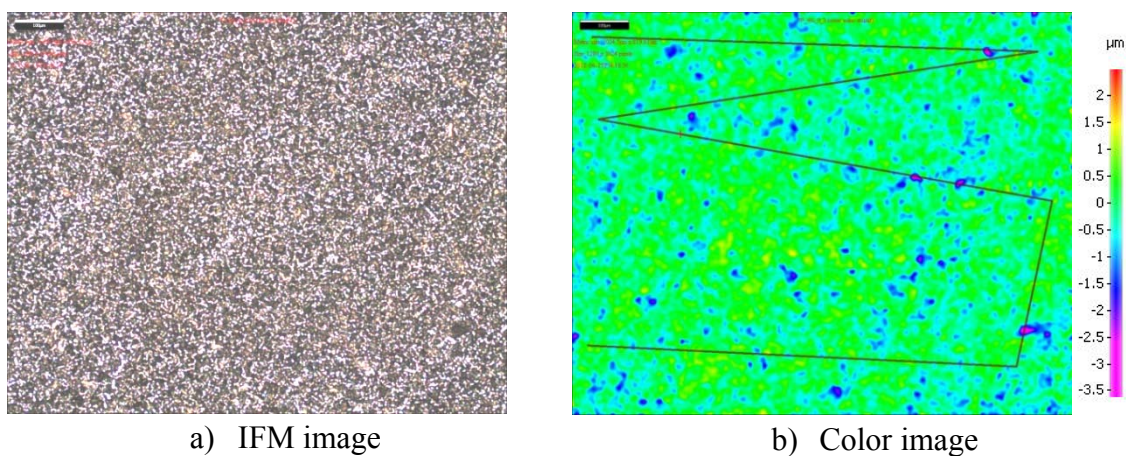


Figure 44: a) and b) are surface topography of sample exposed to water condensation ( $WCR = 0.22 \text{ mL/m}^2/\text{s}$ ) after the removal of corrosion product, c) is the depth profile and d) is the depth/area distribution of this sample.

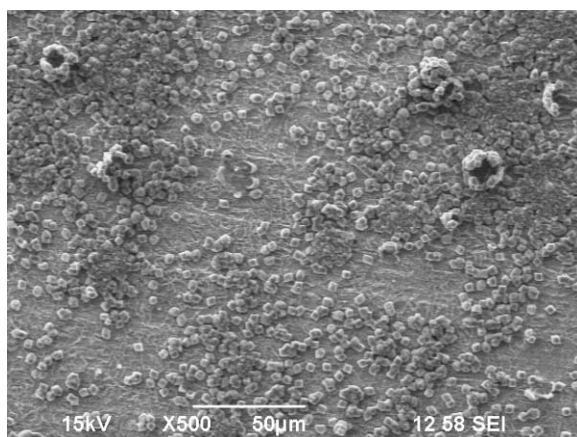
- Corrosion of carbon steel under co-condensation of water and n-heptane

Figure 45 shows the photograph of the sample exposed to co-condensation of water and n-heptane before the removal of corrosion products. Figure 46 is the SEM images and EDX analysis of this sample prior to cleaning with Clarke solution. Crystalline particles of iron carbonate were observed.

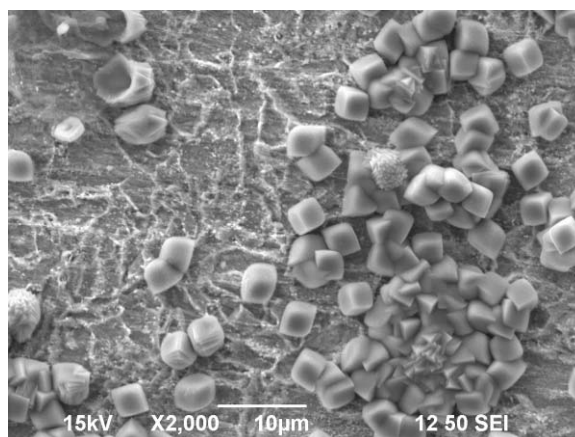
After cleaning the surface, SEM images (Figure 47) reveal that the polishing marks were still present on some areas while others were corroded.



Figure 45: Visual image of sample exposed to corrosion in the co-condensation of water and n-heptane ( $WCR = 0.19 \text{ mL/m}^2/\text{s}$ ,  $C_7CR = 1.2 \text{ mL/m}^2/\text{s}$ ).



a) SEM X500



b) SEM X2000

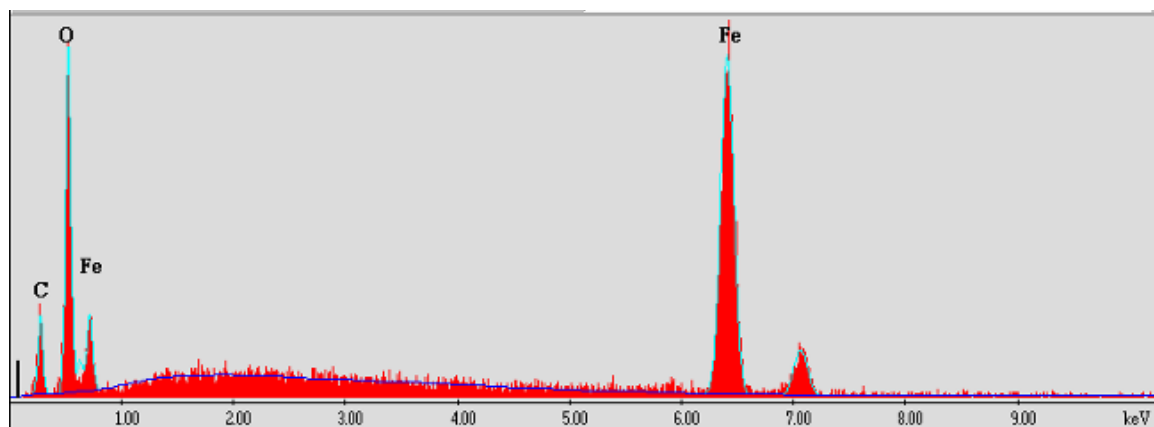
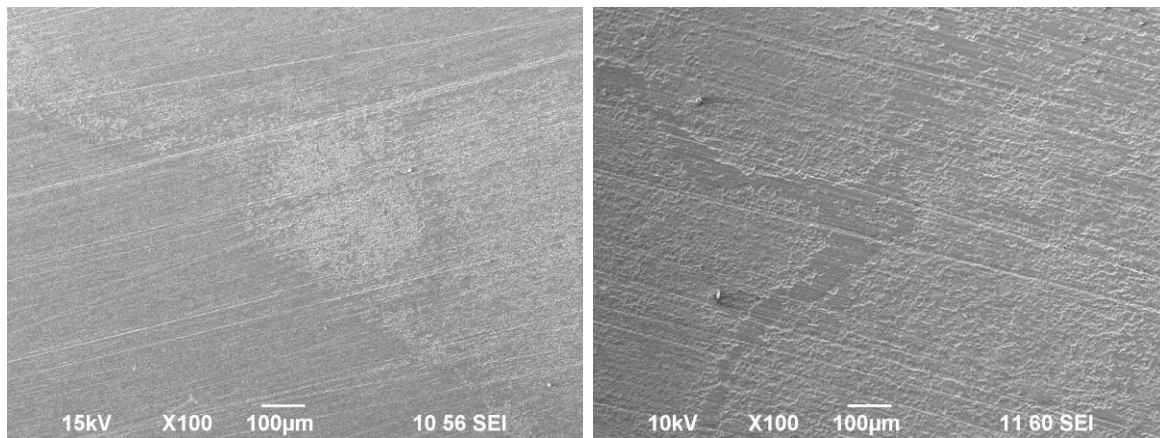
c) EDX analysis on crystal-like particle showing  $\text{FeCO}_3$  composition

Figure 46: SEM Images and EDX analysis of sample exposed to co-condensation of water and n-heptane ( $\text{WCR}$  and  $\text{C}_7\text{CR} = 0.19$  and  $1.2 \text{ mL/m}^2/\text{s}$ , respectively).



WCR = 0.05 and  $C_7$ CR 0.33 mL/m<sup>2</sup>/s

WCR = 0.19 and  $C_7$ CR = 1.2 mL/m<sup>2</sup>/s

Figure 47: SEM images of sample exposed to co-condensation of water and n-heptane after cleaning with Clarke solution.

IFM shows that some areas were shiny and the polishing marks were present, with the shape which resembles observed water droplets surrounded by a less-corroded area of the n-heptane wetted surface (Figure 48a and Figure 48b). The depth profile analysis was conducted as shown in Figure 48c. The difference between this higher and deeper area is approximately 1.5 microns corresponding to a corrosion rate of 0.18 mm/yr. However, the depth/area distribution (Figure 48d) did not show a significant difference as compared to what was observed in corrosion under water condensation alone (Figure 44d). However, on another location of the same sample (Figure 49), the distance between the high and deep areas was approximately the same, but the depth/area distribution shows a difference. This is possibly due to the short duration of tests. The corrosion attack was not deep enough to use the depth/area analysis to determine what percentage of area was wetted with water. Additionally, the dimension of IFM images is 1mm × 1mm and the

ratio to the actual sample is very low (1:1500). Hence, the depth/area distribution analysis on such a small area cannot be used to quantify the corroded area.

Therefore, only the depth profile was used to analyze the non-uniformity of the corrosion behavior. Average penetration depth ( $d$ ) refers to the general corrosion attack in the water-wetted area. Any deep pits are referred to with the maximum penetration depth ( $d_{\max}$ ) as shown in Figure 50.

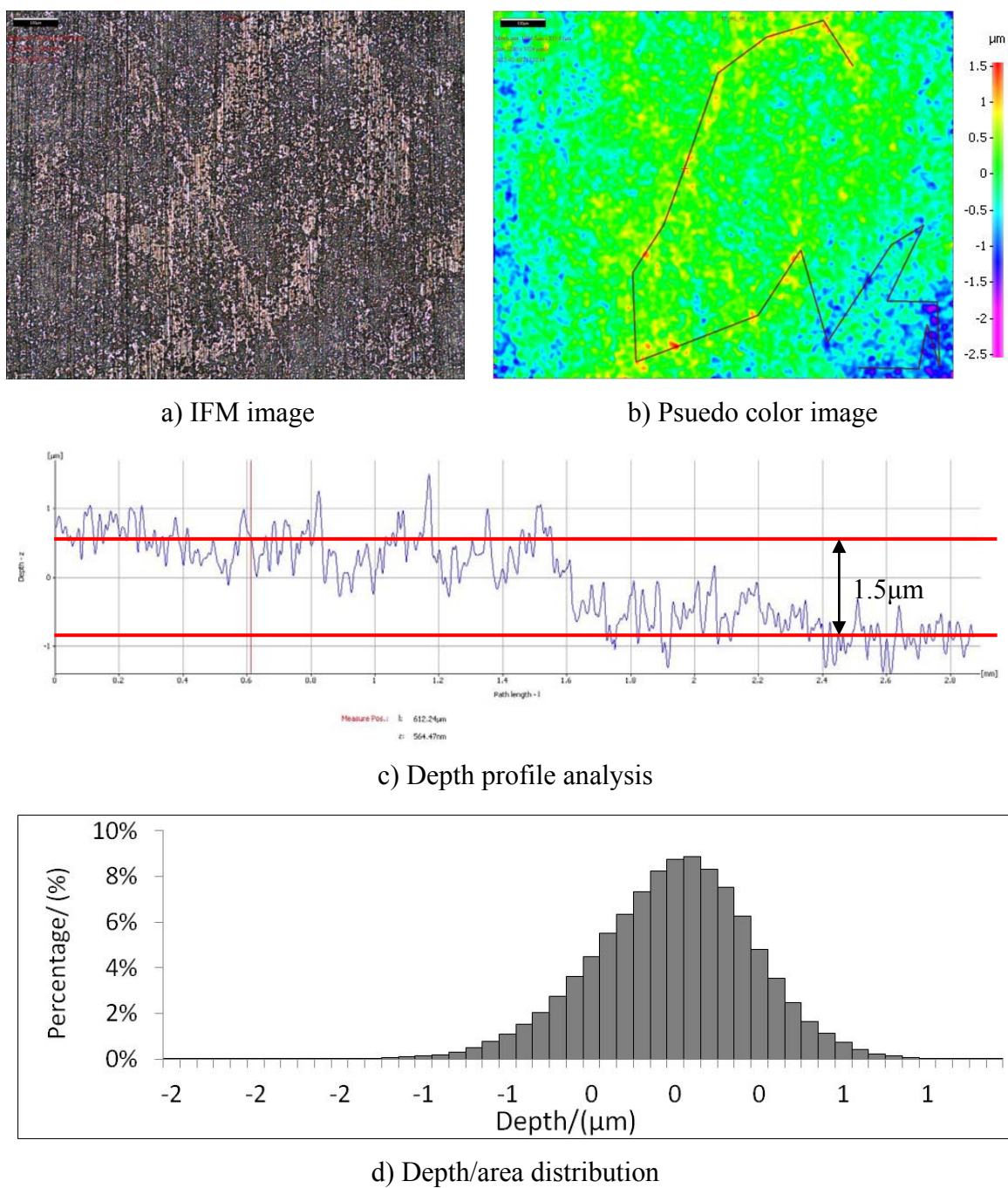
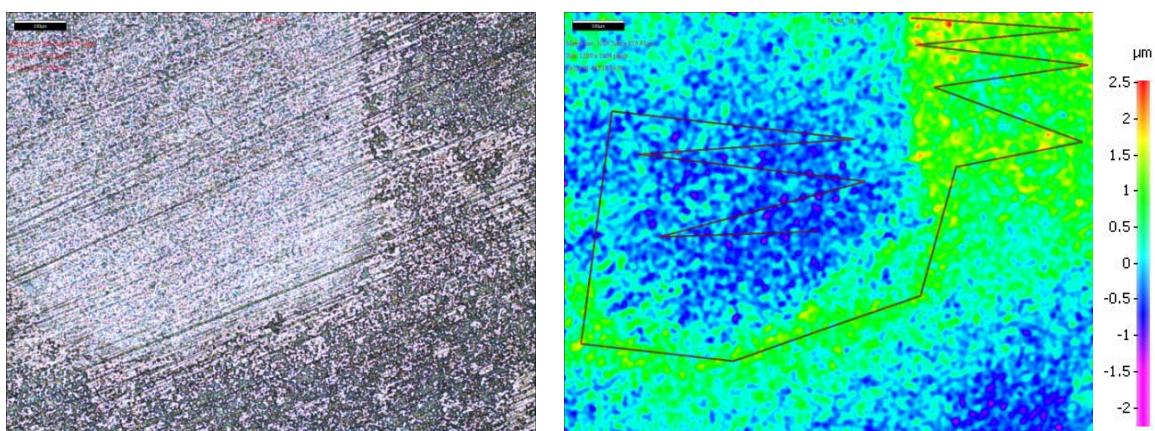
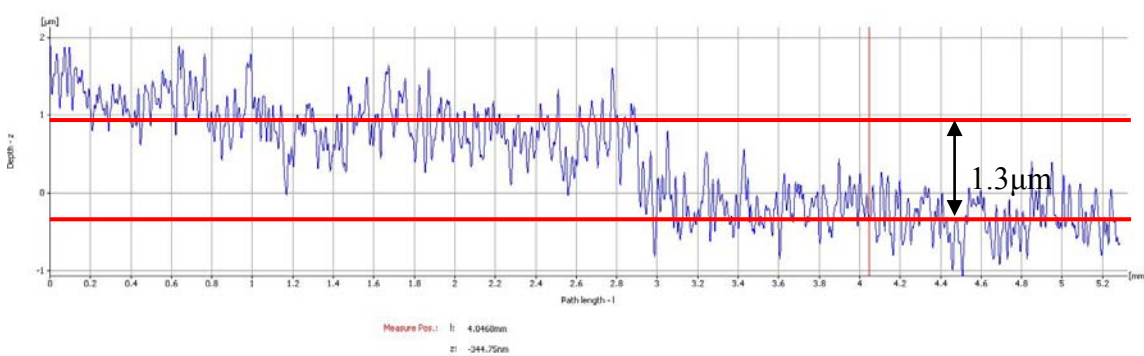


Figure 48: a) and b) are surface topography of sample exposed to co-condensation of water and n-heptane ( $WCR = 0.19 \text{ mL/m}^2/\text{s}$  and  $C_7CR = 1.2 \text{ mL/m}^2/\text{s}$ ) after the removal of corrosion product, c) is the depth profile and d) is the depth/area distribution of this sample (location 1)

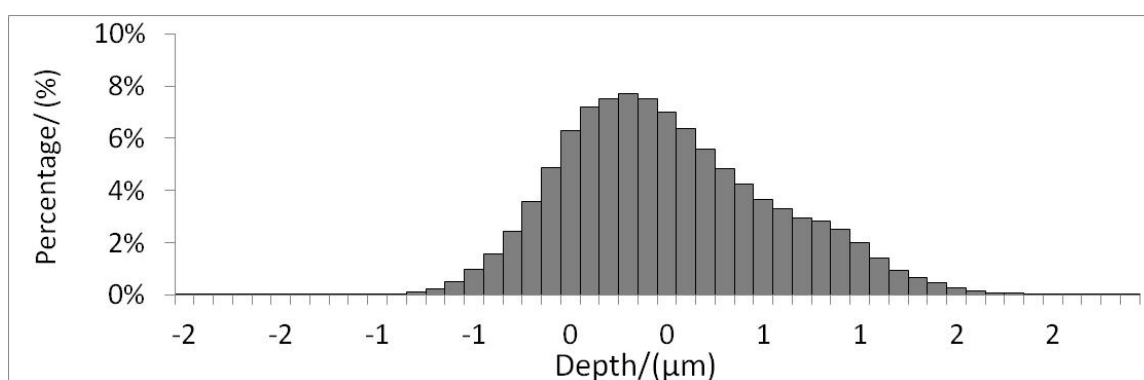


a) IFM image

b) Pseudo color image



c) Depth profile analysis



d) Depth/area distribution

Figure 49: a) and b) are surface topography of sample exposed to co-condensation of water and n-heptane ( $WCR = 0.19 \text{ mL/m}^2/\text{s}$  and  $C_7CR = 1.2 \text{ mL/m}^2/\text{s}$ ) after the removal of corrosion product, c) is the depth profile and d) is the depth/area distribution of this sample (location 2)

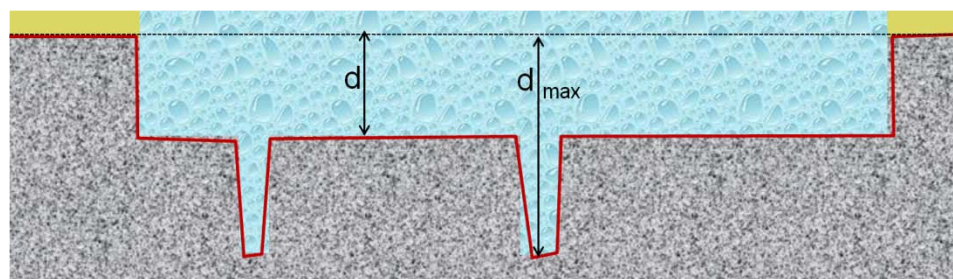


Figure 50: Schematic diagram of surface topography analysis

- Corrosion of carbon steel under co-condensation of water and n-octane

A picture of sample exposed to the co-condensation of water and n-octane is shown in Figure 51. The different appearance of the corroded surface can be seen; i.e. (A) a distinct droplet, (B) at the border of the droplet, and (C) a general area of the sample. SEM images corresponding to these locations are shown in Figure 52, Figure 53 and Figure 54. Location A (Figure 52) corresponds to the area under a large water droplet. Under this droplet, uniform corrosion was observed with a sparse distribution of iron carbonate particles. At the border of the droplet, location B (Figure 53), polishing marks were observed suggesting no corrosion. A denser  $\text{FeCO}_3$  layer was found in the general area, location C (Figure 54). Small segregated water droplets were suspected of covering the steel surface outside the big water droplet.

Additional SEM, EDX and the depth/profile analysis were reported in an internal report [29] and are shown in Appendix II.

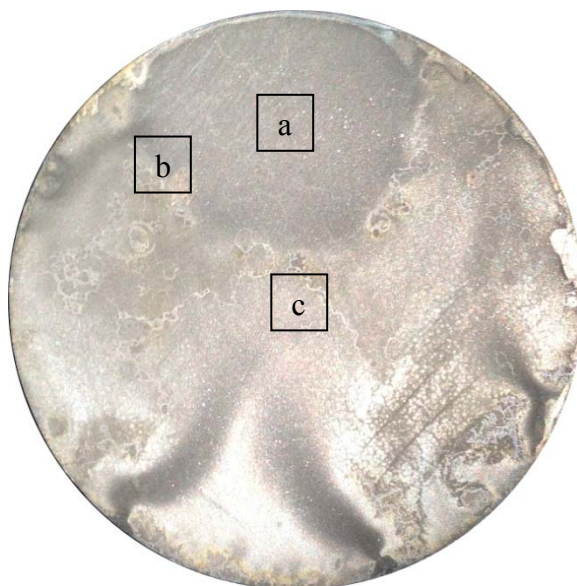
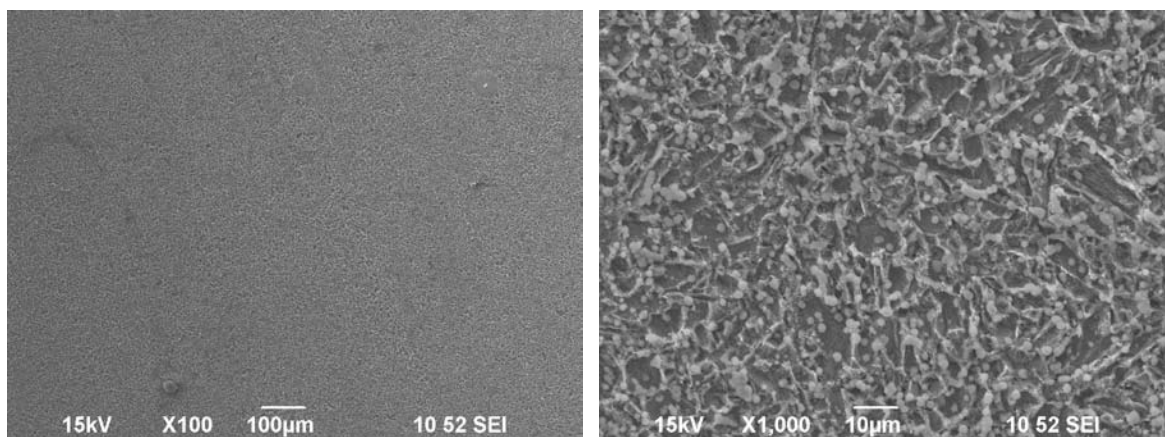
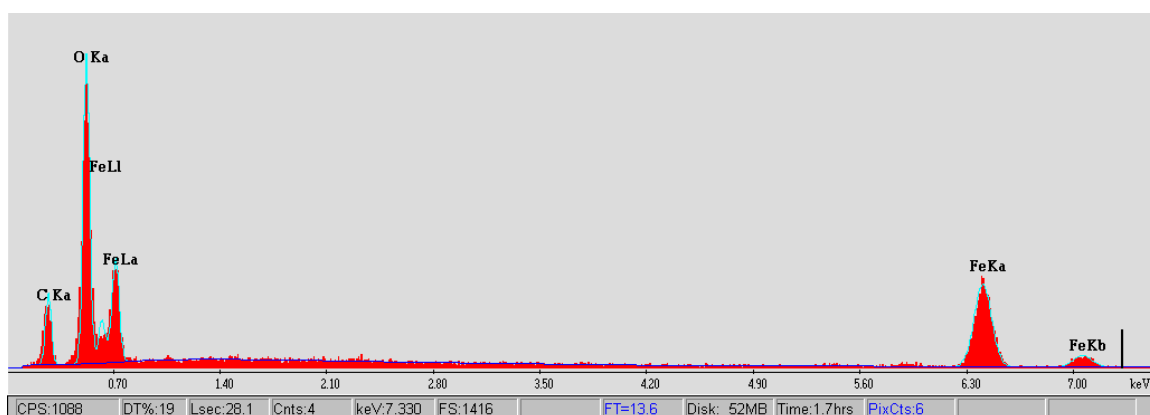
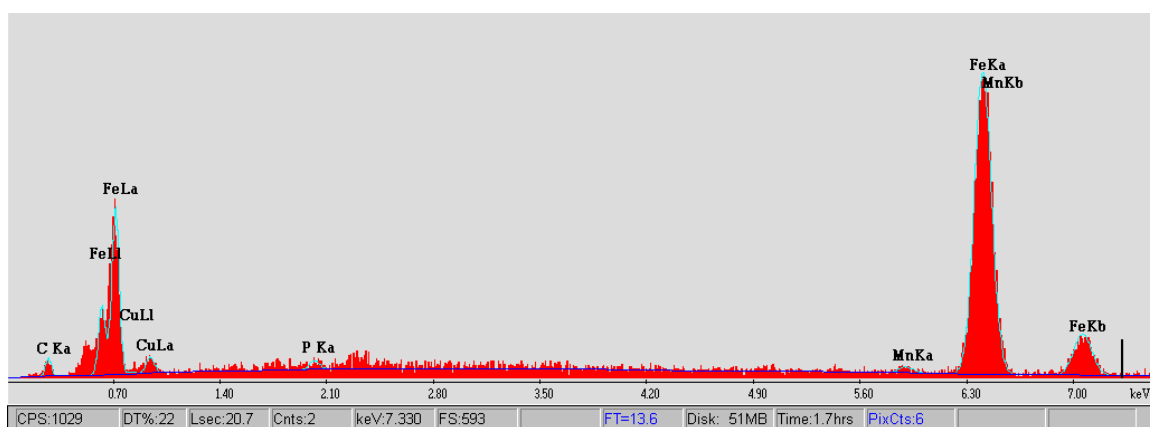


Figure 51: Visual image of sample exposed to co-condensation of water and n-octane ( $WCR = 0.2 \text{ mL/m}^2/\text{s}$ ,  $C_8CR = 0.5 \text{ mL/m}^2/\text{s}$ )



a) SEM X100

b) SEM X1000

c) EDX analysis on crystal-like particle showing the composition of  $\text{FeCO}_3$ 

d) EDX analysis on bare steel showing the composition of iron carbide

Figure 52: SEM and EDX analysis of sample exposed to co-condensation of water and octane ( $\text{WCR} = 0.2 \text{ mL/m}^2/\text{s}$  and  $\text{C}_8\text{CR} = 0.5 \text{ mL/m}^2/\text{s}$ ) – Location A

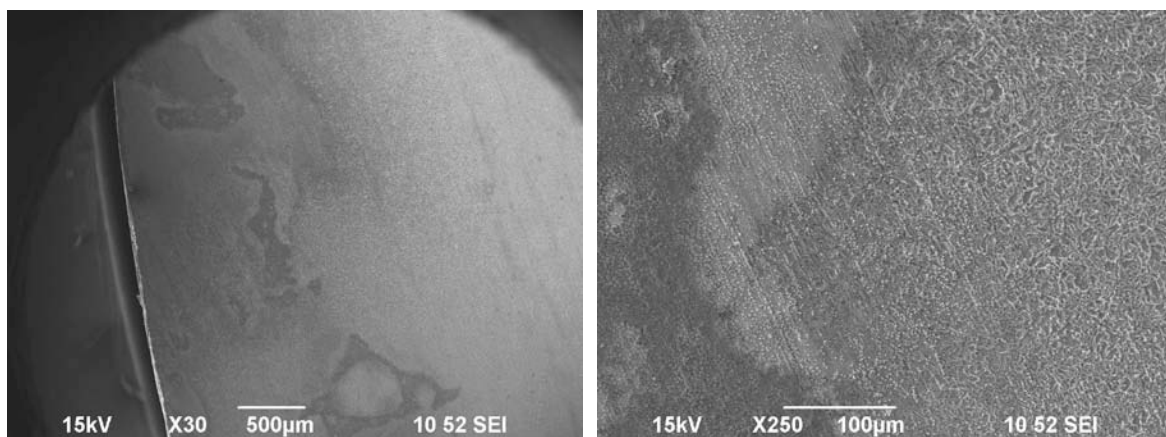


Figure 53: SEM Analysis of sample exposed to co-condensation of water and octane ( $WCR = 0.2 \text{ mL/m}^2/\text{s}$  and  $C_8CR = 0.5 \text{ mL/m}^2/\text{s}$ ) – Border of a big droplet (Location B).

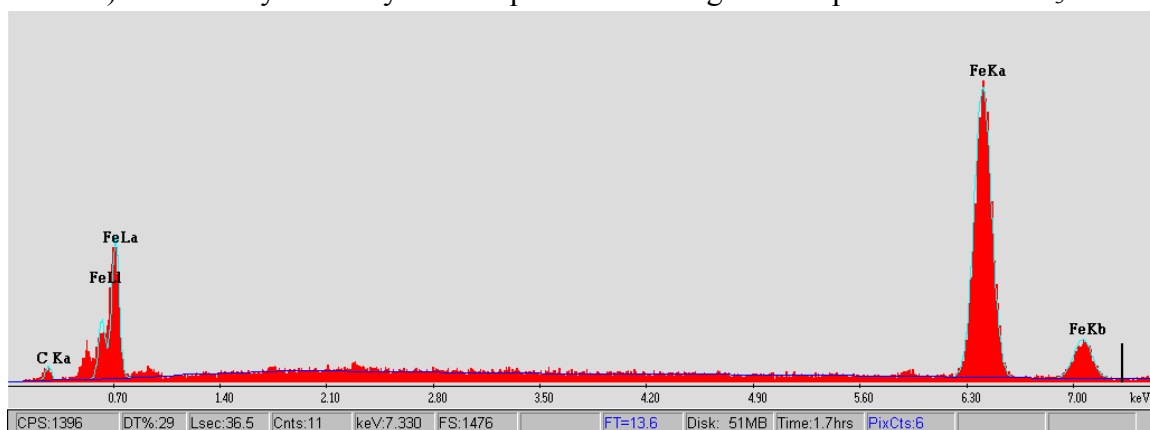
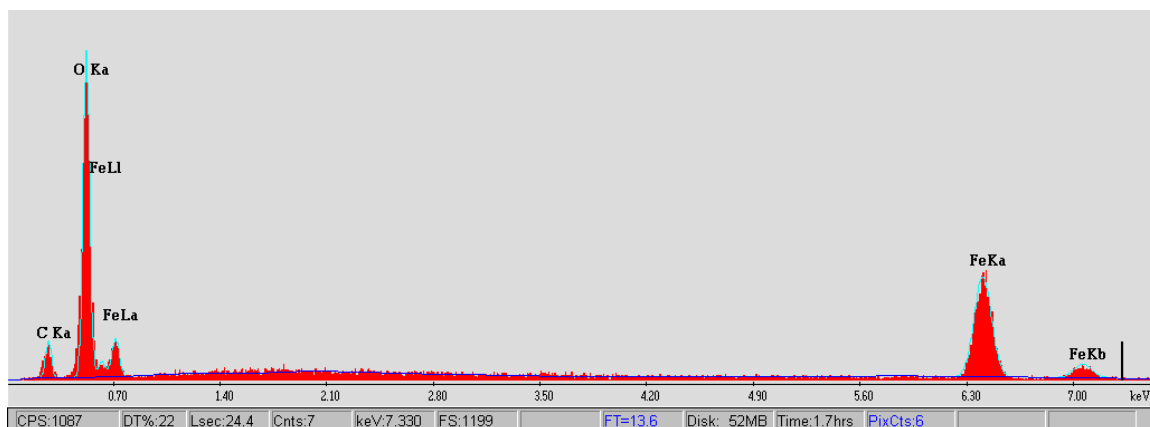
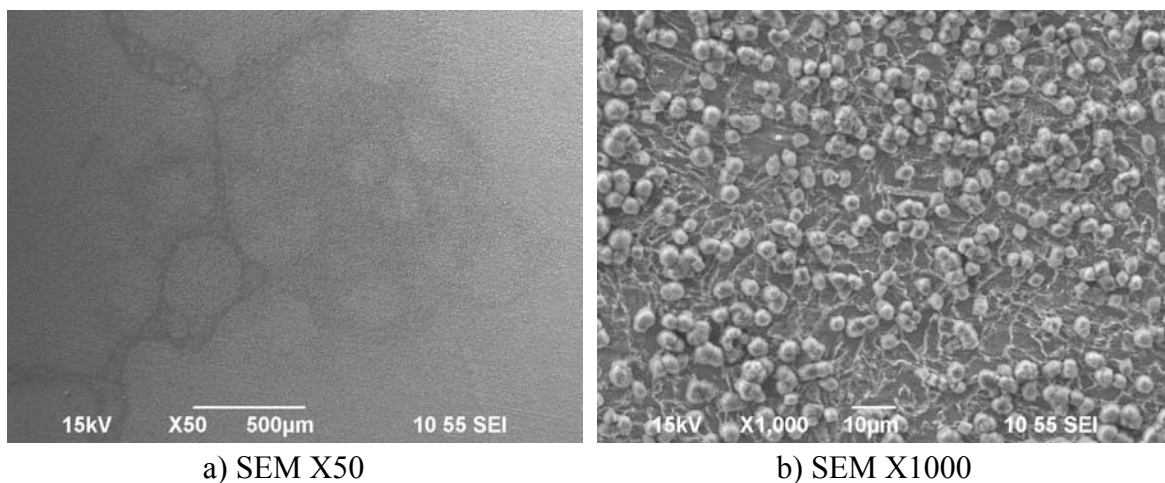
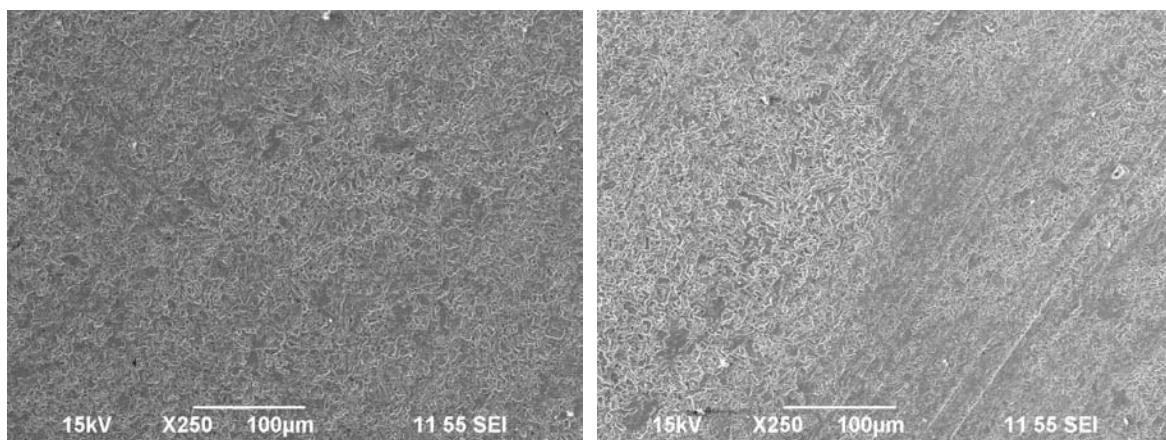


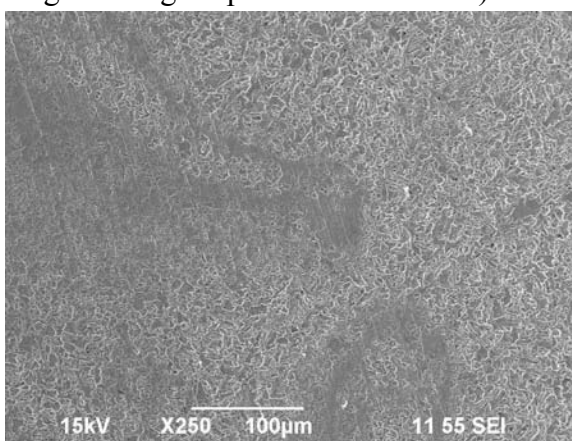
Figure 54: SEM Analysis of sample exposed to co-condensation of water and octane ( $\text{WCR} = 0.2 \text{ mL/m}^2/\text{s}$  and  $\text{C}_8\text{CR} = 0.5 \text{ mL/m}^2/\text{s}$ ) – On general area (Location C).

Figure 55a to c are SEM images of different areas of the sample after cleaning with Clarke solution. Figure 56 and Figure 57 are the surface topography under the large droplet (location A) and a general area (location C) of this sample. These images confirm that the big droplet was water. Additionally, the corrosion pattern confirms that small water droplets were present all over the sample as a result of segregation by n-octane.



Location A) within the big standing droplet

Location B) at the border of the droplet



Location C) at the center of the sample

Figure 55: presents SEM images of the sample exposed to the co-condensation of water and n-octane ( $WCR = 0.2 \text{ mL/m}^2/\text{s}$  and  $C_8CR = 0.5 \text{ mL/m}^2/\text{s}$ ) after the removal of corrosion products.

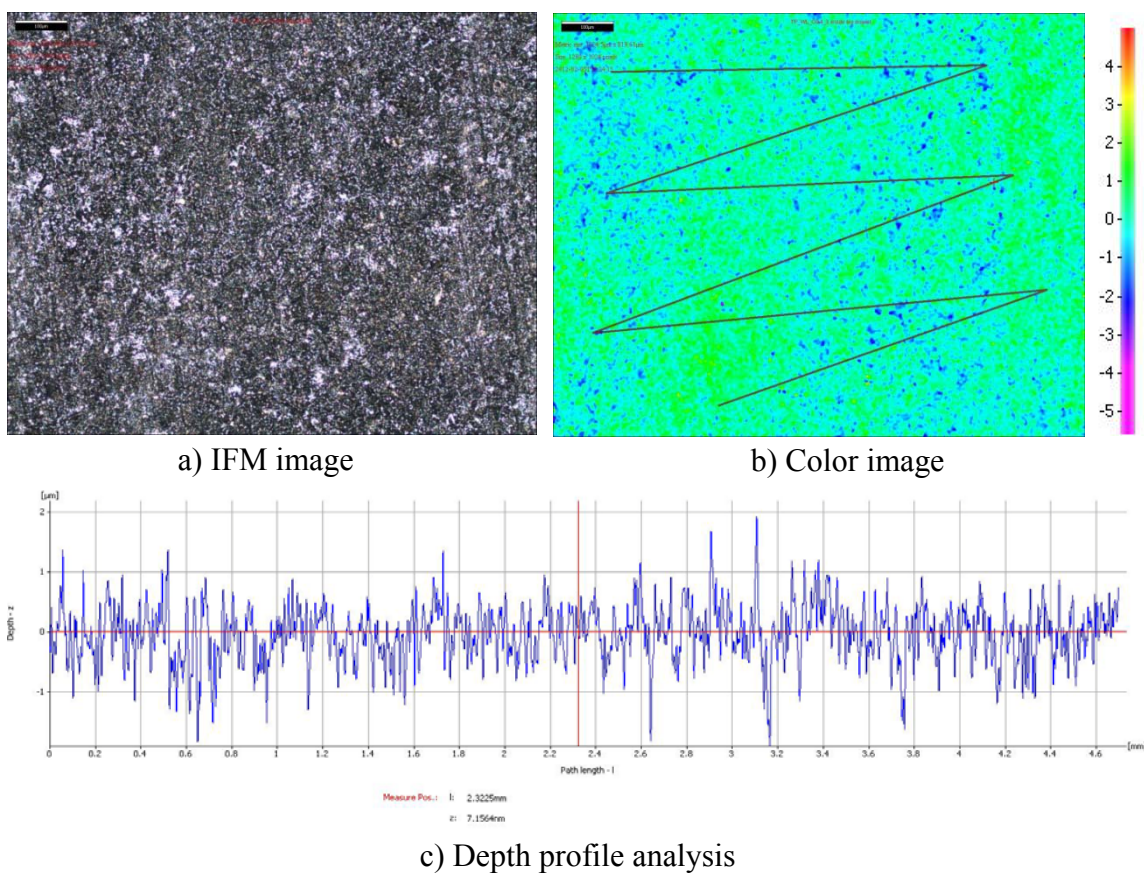


Figure 56: Surface topography of sample exposed to co-condensation of water and octane after the removal of corrosion product- Under a big water droplet (Location A).

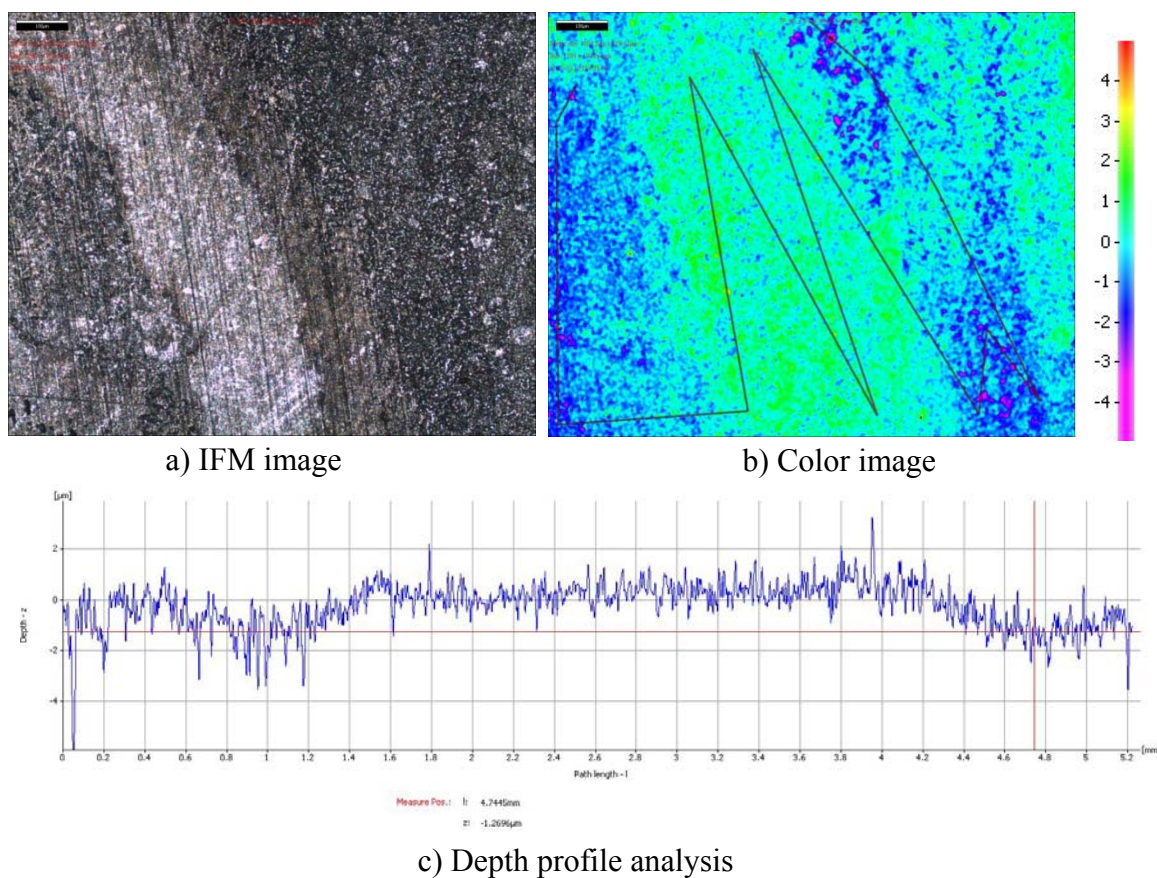


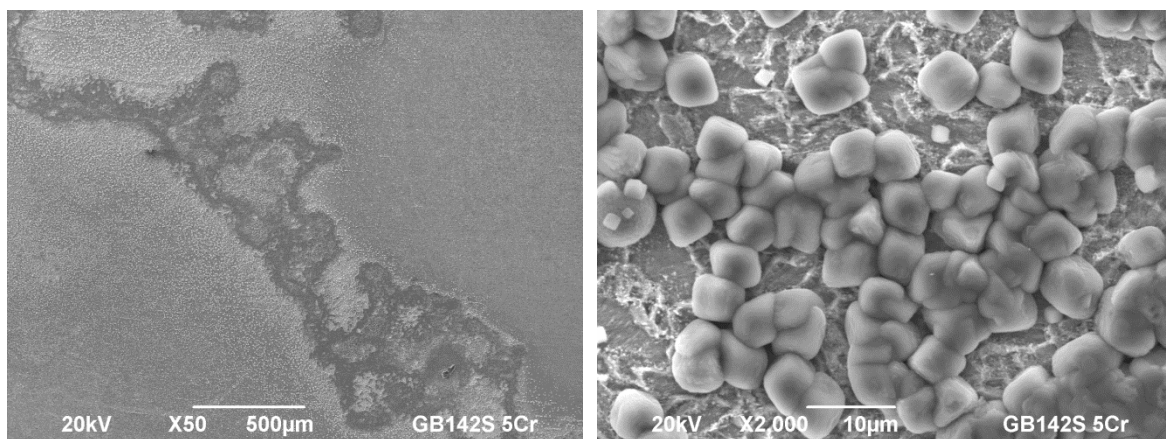
Figure 57: Surface topography of sample exposed to co-condensation of water and octane after the removal of corrosion product- At the border of the big droplet (Location B).

- Corrosion of carbon steel under co-condensation of water and n-decane

The last co-condensation scenario was water with n-decane. The n-decane is the heaviest hydrocarbon used in this study. Hence, its condensation rate is the lowest among the three hydrocarbons tested. Furthermore, n-decane condenses significantly less than water does. It was hypothesized that if the corrosion rate was solely the function of water and hydrocarbon condensation rates, the corrosion rate in this test would be similar to what was observed in the pure water system. However, the results reported in the

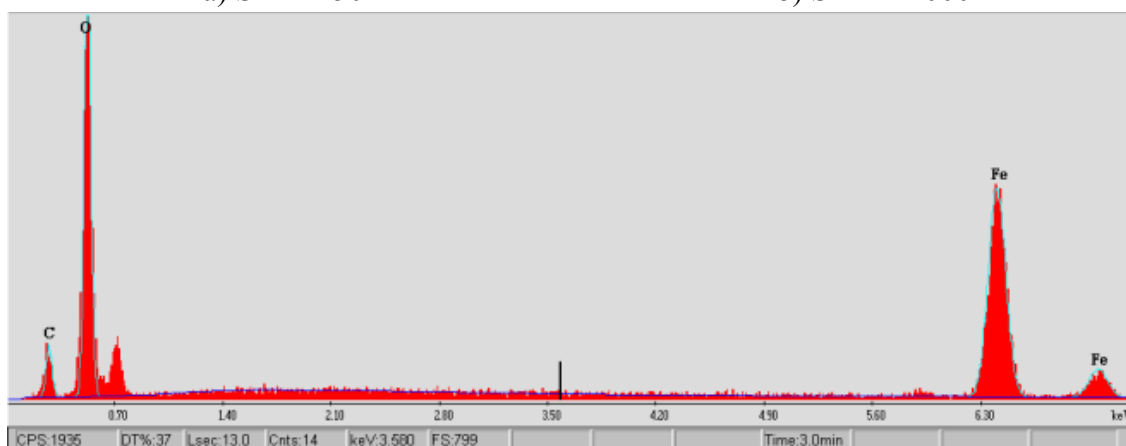
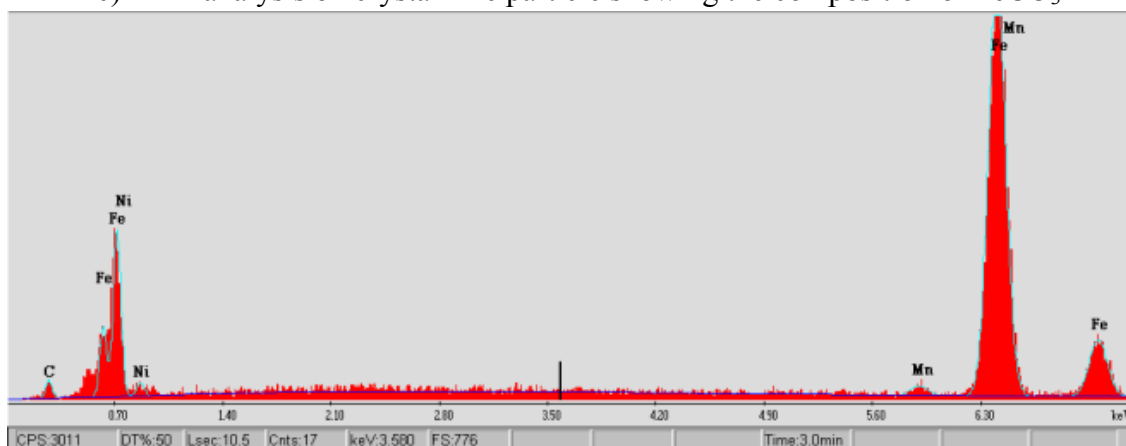
previous chapter show that n-decane had the highest ability to prevent water from coalescing.

SEM images before and after the removal of the corrosion product are shown in Figure 58 and Figure 59, respectively. Similar to the previous co-condensation tests,  $\text{FeCO}_3$  was observed and some areas were still protected by n-decane even though water condensation rate was greater. IFM analysis supports this finding as shown in Figure 60.



a) SEM X50

b) SEM X2000

c) EDX analysis on crystal-like particle showing the composition of  $\text{FeCO}_3$ 

d) EDX analysis on bare steel surface showing iron carbide

Figure 58: SEM Analysis of sample exposed to co-condensation of water and n-decane ( $\text{WCR} = 0.22 \text{ mL/m}^2/\text{s}$  and  $\text{C}_{10}\text{CR} = 0.08 \text{ mL/m}^2/\text{s}$ ).

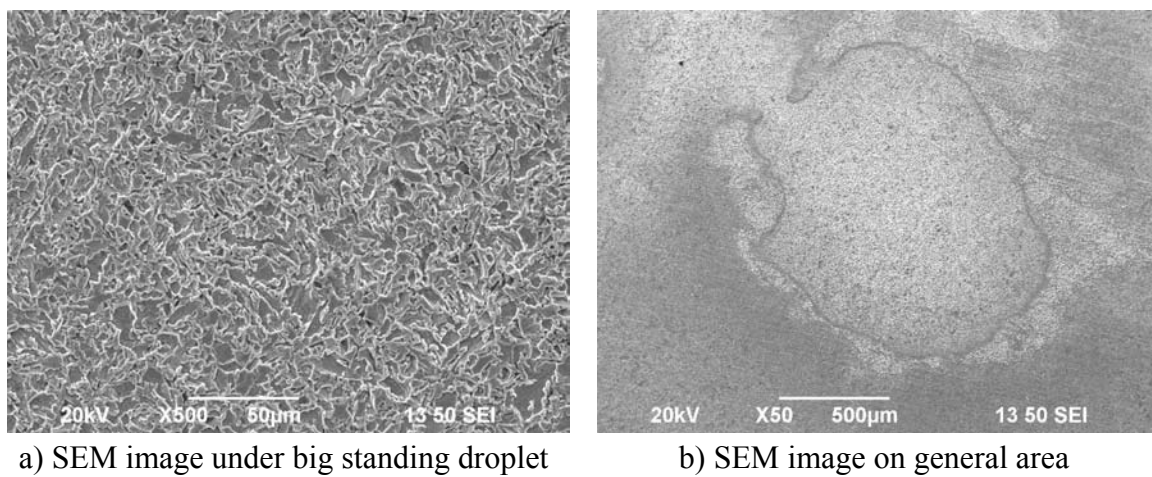


Figure 59: SEM Analysis of sample exposed to co-condensation of water and n-decane after the removal of corrosion product ( $WCR = 0.22 \text{ mL/m}^2/\text{s}$  and  $C_{10}CR = 0.08 \text{ mL/m}^2/\text{s}$ ).

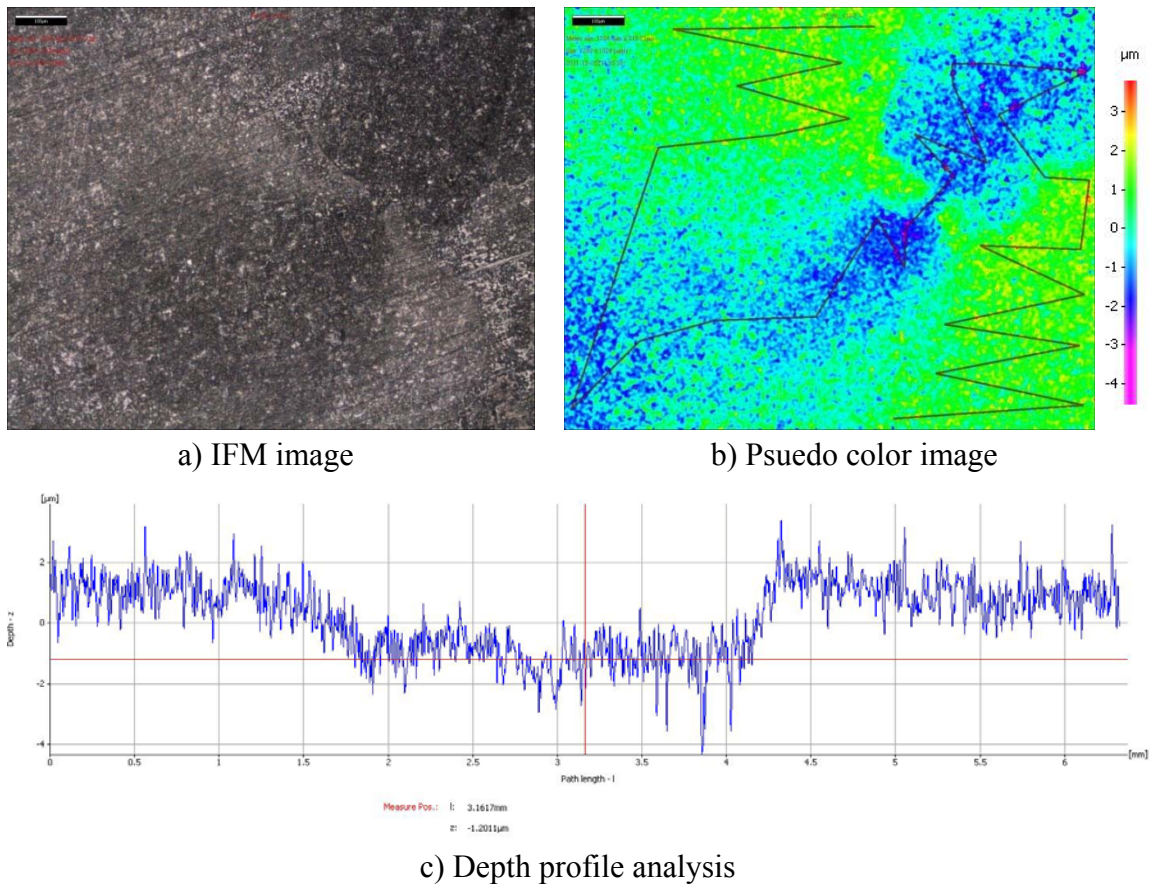


Figure 60: Surface topography of sample exposed to co-condensation of water and n-decane after the removal of corrosion product ( $WCR = 0.22 \text{ mL/m}^2/\text{s}$  and  $C_{10}CR = 0.08 \text{ mL/m}^2/\text{s}$ )

- Corrosion rates of carbon steel under various condensation scenarios

Figure 61 compares corrosion rates of samples exposed to the condensation of water at two different water condensation rates. Corrosion rates were obtained by two different methods; *i.e.* weight loss and the maximum penetration rate. Both weight loss and the maximum penetration rate increased with water condensation rates, which agreed with other researchers. Yet, this penetration rate was not severe enough for the attack to be referred to as pitting corrosion.

Figure 62 compares weight loss corrosion rates of samples exposed to various condensation scenarios. When water co-condensed with n-heptane or n-octane, at low co-condensation rates, it was unexpected to see that corrosion rates were higher than when water condensed alone. In higher co-condensation rates, the co-condensation with all three hydrocarbons exhibited lower corrosion rates as compared to when water condensed alone.

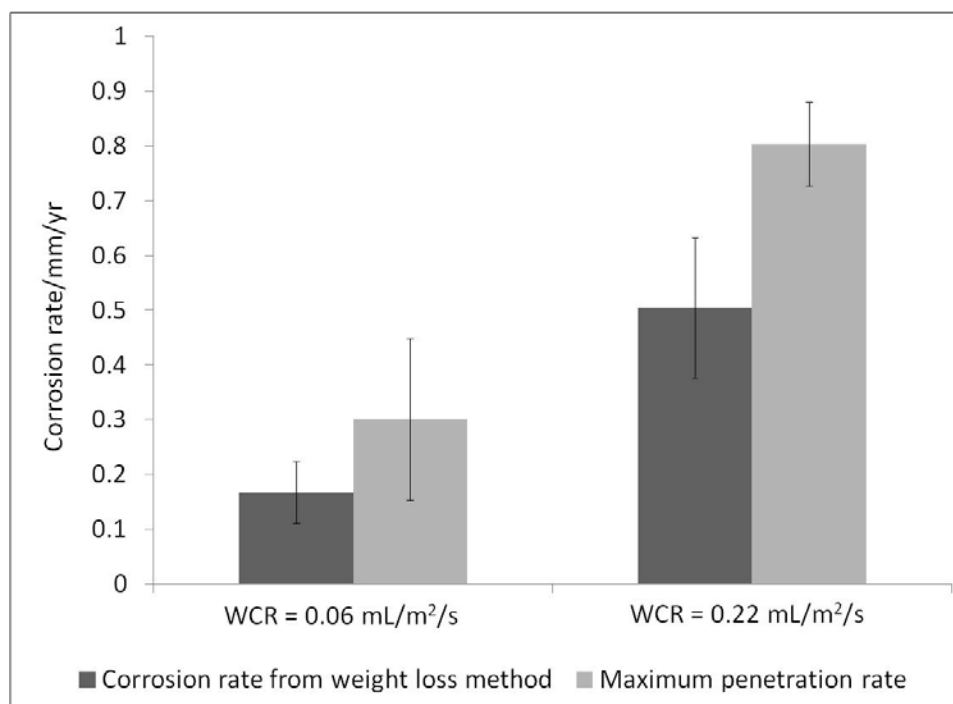


Figure 61: Comparison of corrosion rates obtained from weight loss and the maximum penetration rate of sample exposed to water condensation at two different water condensation rates. ( $T_g = 35^\circ\text{C}$  and  $50^\circ\text{C}$ ,  $T_s = 25^\circ\text{C}$  and  $30^\circ\text{C}$ , Total  $P = 1$  bar).

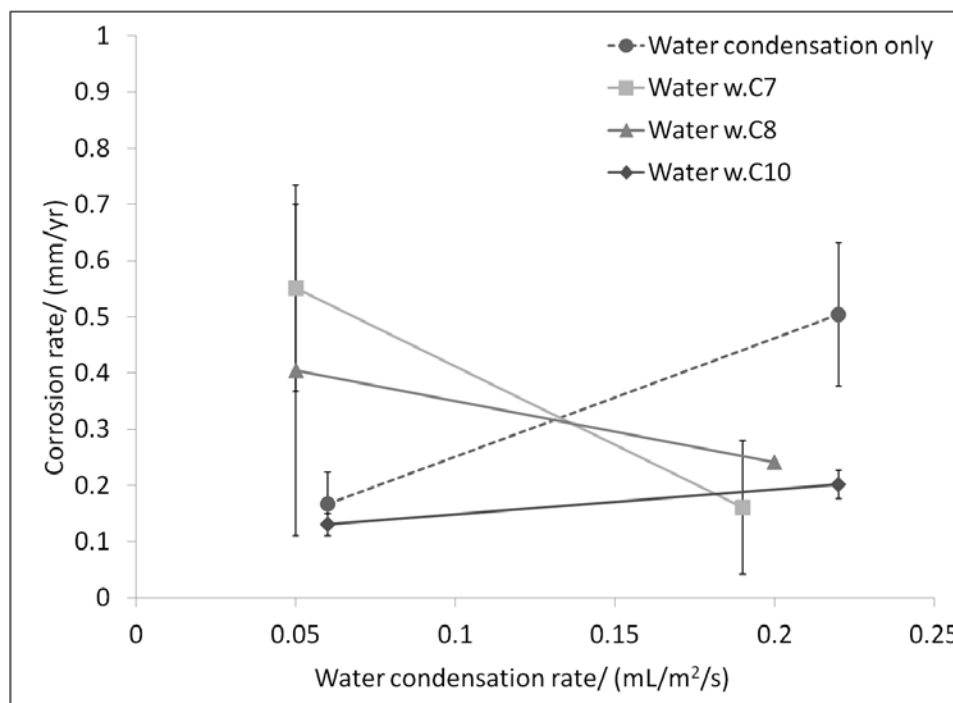


Figure 62: Comparison of corrosion rates obtained from weight loss in the various condensation scenarios ( $T_g = 35^\circ\text{C}$  and  $50^\circ\text{C}$ ,  $T_s = 25^\circ\text{C}$  and  $30^\circ\text{C}$ , Total  $P = 1$  bar).

As shown in SEM and IFM images, samples under co-condensation scenarios all exhibited areas with different degrees of corrosion attack. Figure 63 compares the average penetration rates of samples exposed to the co-condensation of water and various hydrocarbons. Only the area where water resides is corroded. Hypothetically, if the weight loss corrosion rate is divided by the average penetration rate, the result should be equivalent to the fraction of the area wetted with water. However, similar or higher weight loss corrosion rates compared to the average penetration rate were observed in all test scenarios except when water co-condensed with n-decane at low condensation rate.

This implied that water occupied the steel almost entirely in most cases, which agreed with the results obtained from the conductivity probe.

At low condensation rates, the corrosion rate obtained in the co-condensation scenario was higher than for the pure water condensation scenario (but only for heptane and octane). At high condensation rates, all condensations scenarios led to similar corrosion rates, obtained by weight loss and the average penetration rate.

Ratios of weight loss to average penetration were approximately 1 for all cases, indicating that water eventually occupied almost the entire steel surface. It is interesting to observe  $\text{FeCO}_3$  only in co-condensation scenarios but not in water alone. The difference in water chemistry could be one of the reasons why the corrosion rate decreased in co-condensation scenarios compared to the pure water condensation. Section 4.4.3 discusses this subject in greater detail.

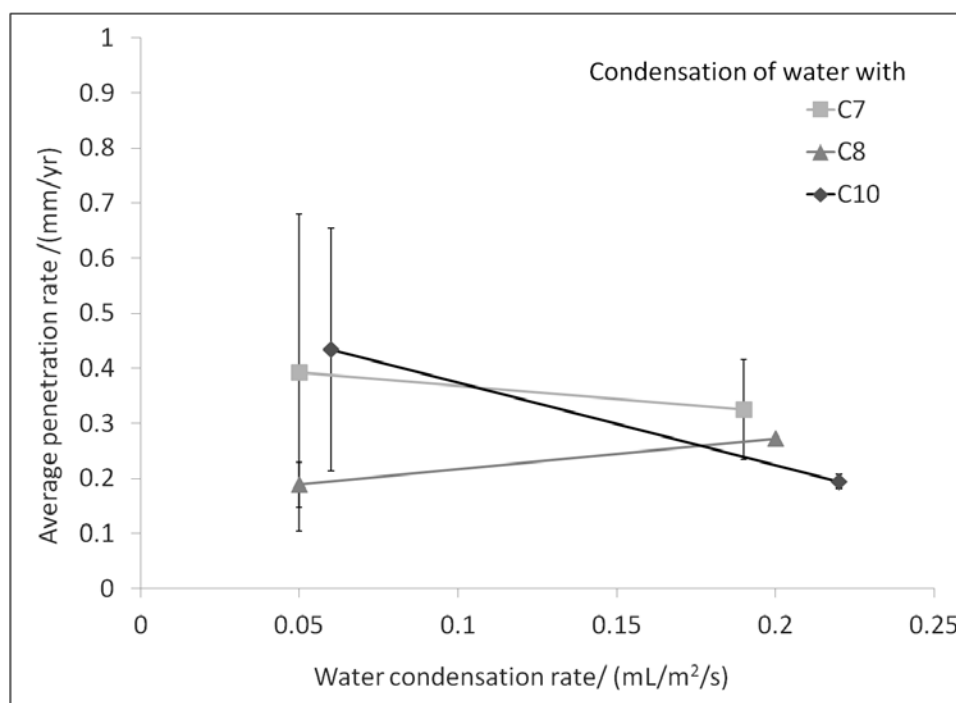


Figure 63: Comparison of the average penetration rate from various condensation scenarios ( $T_g = 35^\circ\text{C}$  and  $50^\circ\text{C}$ ,  $T_s = 25^\circ\text{C}$  and  $30^\circ\text{C}$ , Total  $P = 1$  bar)

The maximum penetration rates for various condensation scenarios were compared and shown in Figure 64. As previously found by others, the maximum penetration rates in pure water condensation increases with the water condensation rate. However, the maximum penetration does not vary with condensation rate in all co-condensation systems used here. This is a very important finding which needs to be accounted when modeling and analyzing TLC field data.

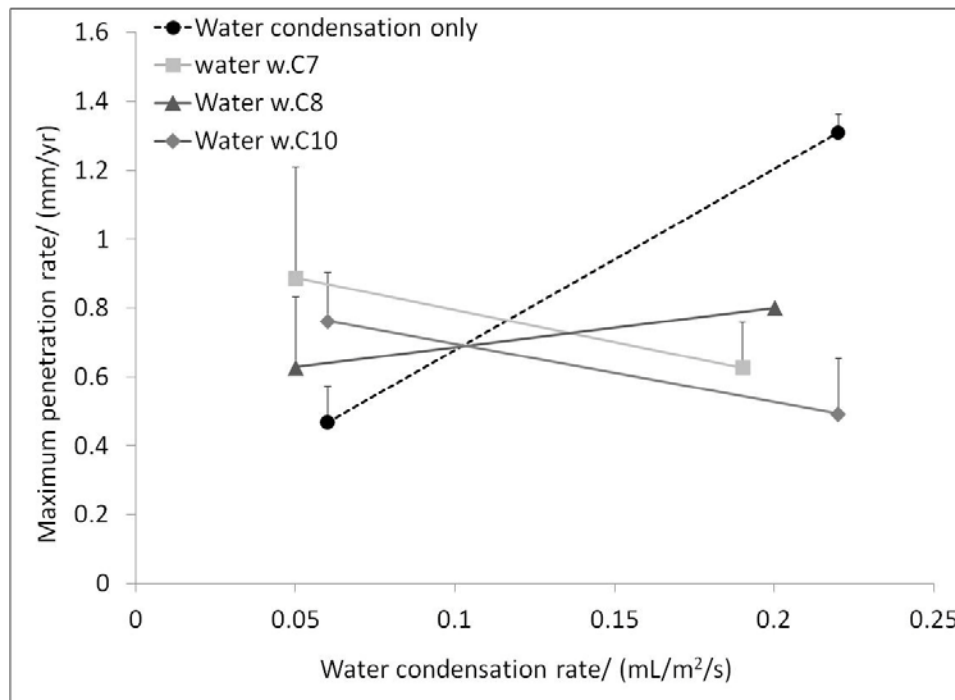


Figure 64: Comparison of the maximum penetration rate from the various condensation scenarios ( $T_g = 35^\circ\text{C}$  and  $50^\circ\text{C}$ ,  $T_s = 25^\circ\text{C}$  and  $30^\circ\text{C}$ , Total  $P = 1$  bar).

- Corrosion test under co-condensation of water and n-heptane for 2-weeks

Previous results show that hydrocarbons and water jointly occupied the steel surface. The area where water stayed was uniformly corroded and was surrounded by less-corroded areas of the hydrocarbon-wetted surface. However, the test duration was only 3 days. It is interesting to learn how this scenario would evolve in longer exposures, which obviously correspond better to field situations.

Two test conditions were selected for the long term experiments: corrosion when water only condensed and corrosion during co-condensation of water and n-heptane. The main reason why n-heptane was selected for the long term tests was that from a field perspective, it is the most common of the three hydrocarbons tested.

Figure 65 shows a photograph of the sample exposed to water condensation alone for 2 weeks. Apparently, the surface was uniformly corroded and was covered with  $\text{Fe}_3\text{C}$ , which was not protective (Figure 66). After cleaning with the Clarke solution, a uniform corroded surface was observed and a SEM image is shown in Figure 67. No distinct corrosion features were observed using the IFM showing that the entire surface was uniformly corroded (Figure 68).

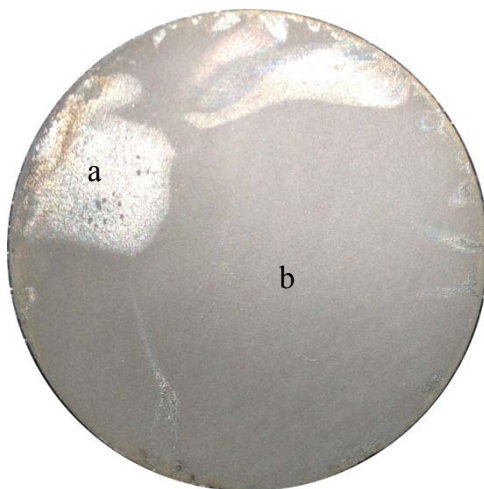


Figure 65: Visual image of sample exposed to water condensation of water for 2 weeks.

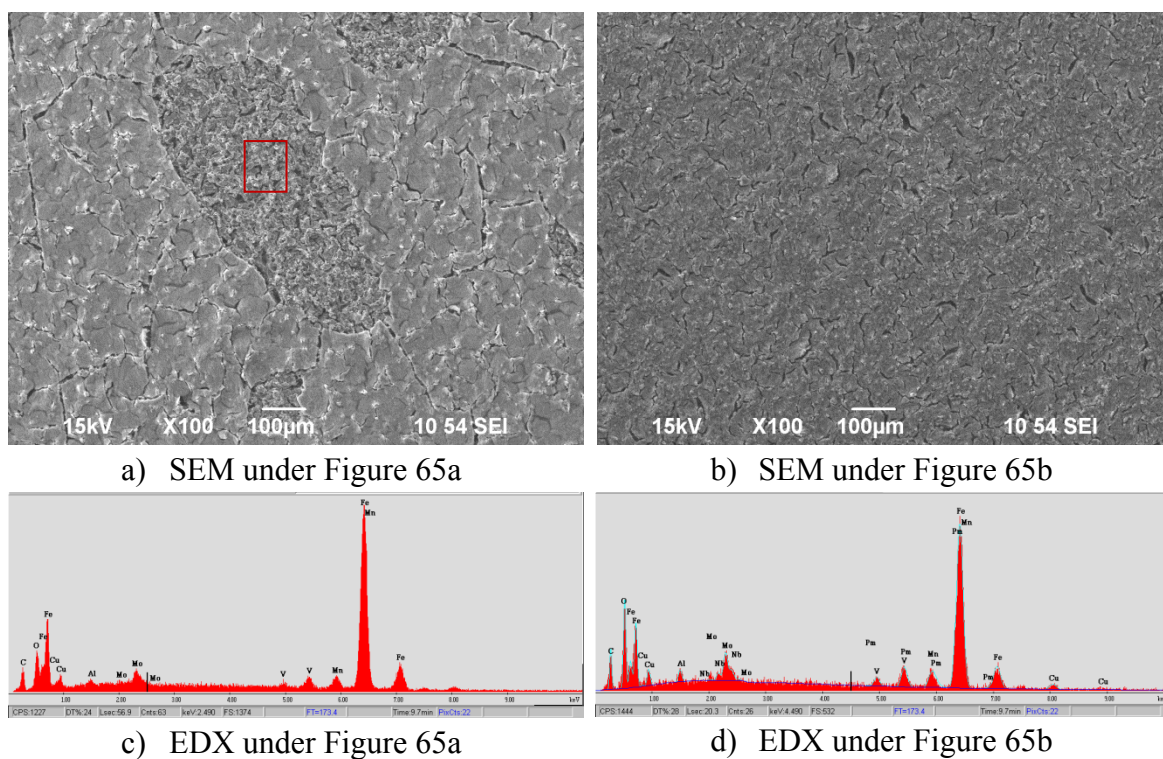


Figure 66: SEM and EDX images of sample exposed to the condensation of water for 2 weeks.

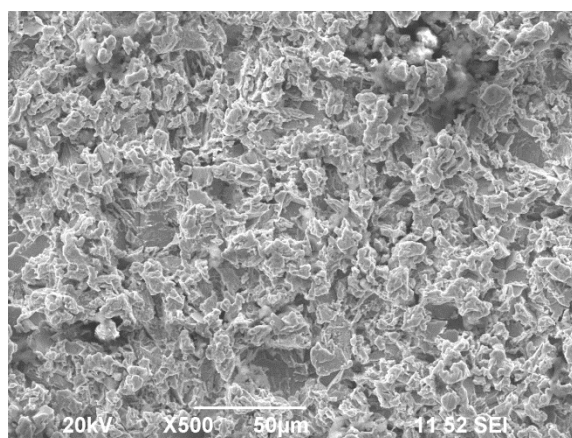


Figure 67: SEM image of sample after cleaning which was exposed to the condensation of water only for 2 weeks.

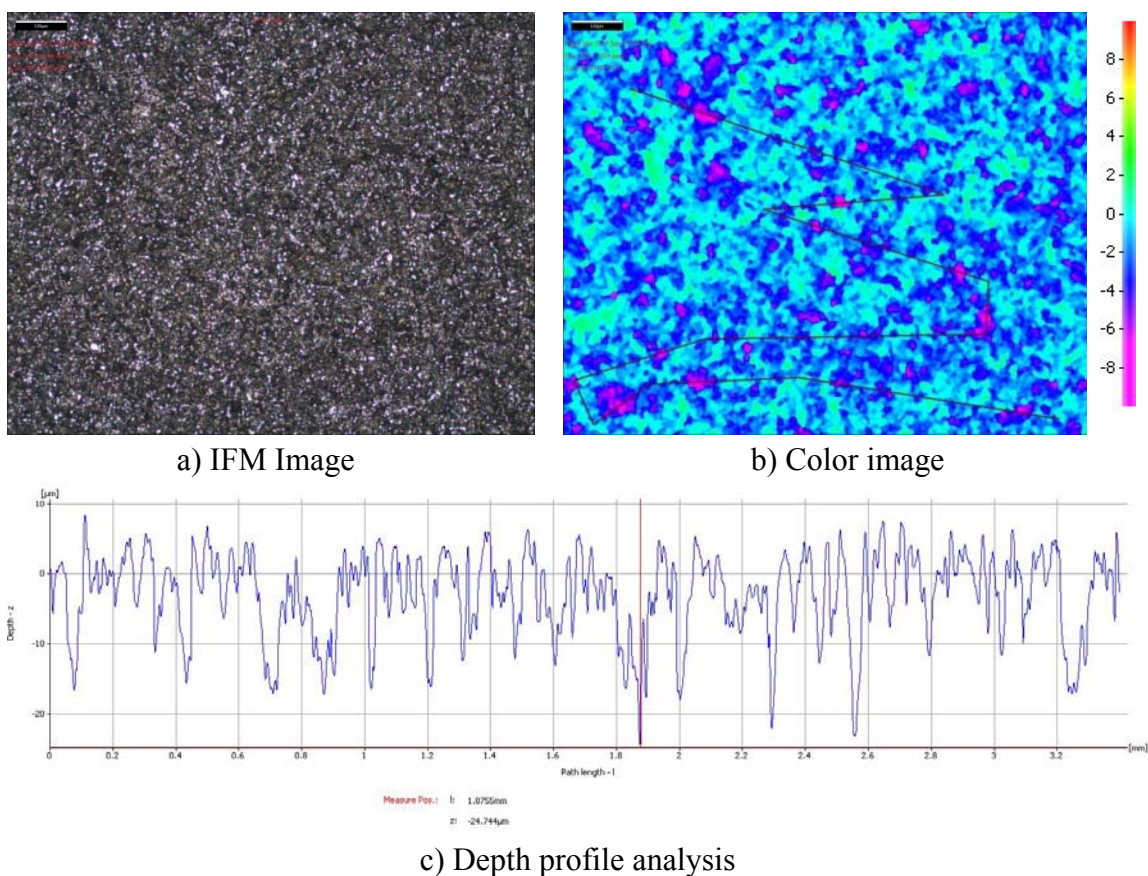


Figure 68: Surface topography of sample after the removal of corrosion product exposed to condensation of water only for 2 weeks ( $WCR = 0.22 \text{ mL/m}^2/\text{s}$ ).

Figure 69 presents the visual observation of sample exposed to co-condensation of water and n-heptane for 2 weeks. Different distinct features can be identified, such as: (A) area under a single large droplet, (B) area at the border of this droplet, (C) an area outside the droplets, and (D) the shiny area (Location D).

Figure 70a and Figure 70b show SEM images of the area under a large water droplet (location A). A sparse distribution of corrosion product particles was observed. Figure 70c shows the EDX analysis on one of the particles. The dominant peaks of Fe, C,

and O suggested that these were  $\text{FeCO}_3$  particles. Figure 70d is the EDX analysis on the bare steel area between those  $\text{FeCO}_3$  particles.

At the border of the droplet – location B (Figure 71), it is clearly seen that the corrosion product is densely populated with the density increasing as we move away from the droplet. This is obvious by looking at the area far away from the droplet – location C (Figure 72), where a lot of  $\text{FeCO}_3$  formation is observed. At location D (Figure 73) which appeared shinier than the other areas, an even denser  $\text{FeCO}_3$  layer is was observed.

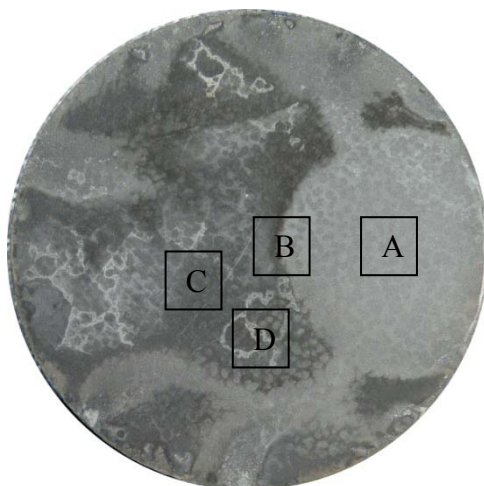
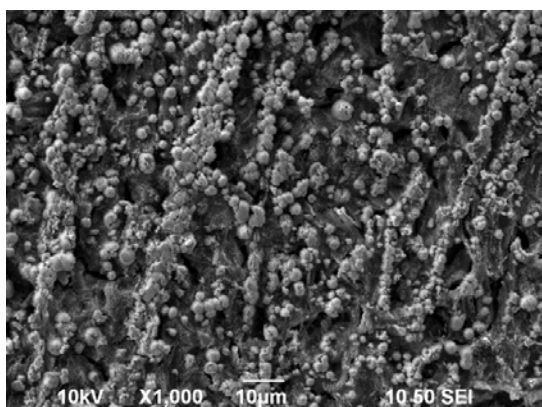
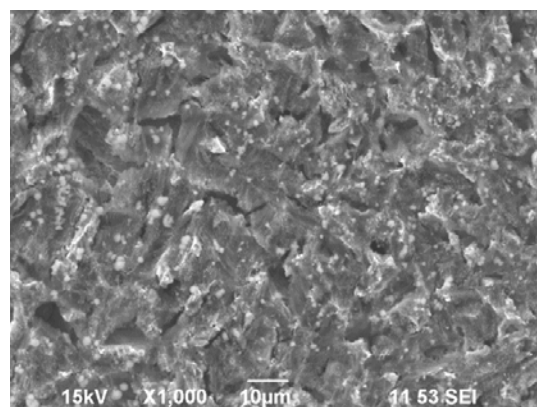


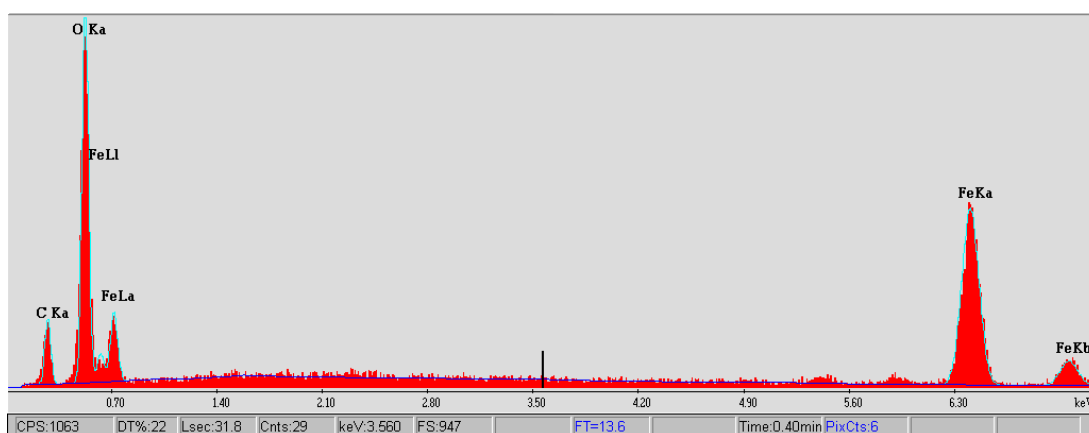
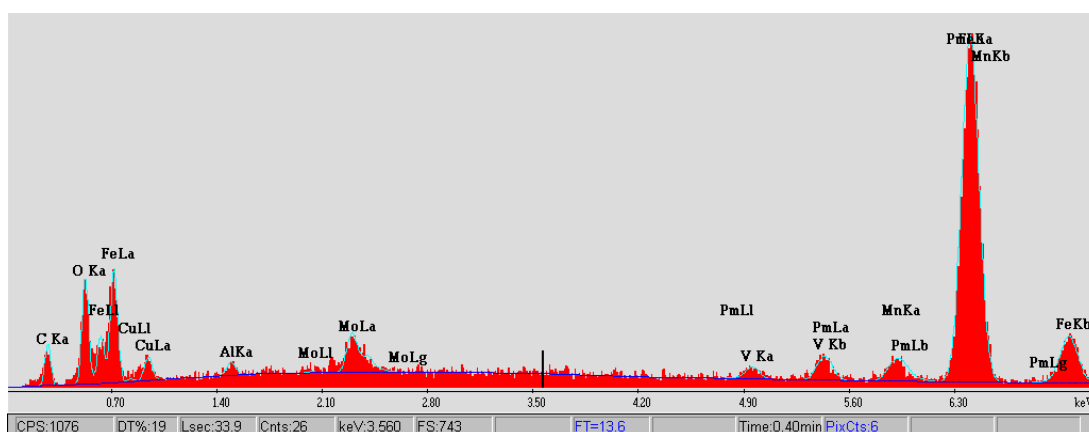
Figure 69: Visual image of sample exposed to co-condensation of water and n-heptane for 2 weeks.



a) SEM X1000



b) SEM X1000

c) EDX analysis on crystal-like particles showing the composition of  $\text{FeCO}_3$ 

d) EDX analysis on bare steel surface

Figure 70: SEM images of sample exposed to the co-condensation of water and n-heptane for 2 weeks ( $\text{WCR} = 0.19 \text{ mL/m}^2/\text{s}$ ,  $\text{C}_7\text{CR} = 1.21 \text{ mL/m}^2/\text{s}$ ) – Location A (under a water big droplet).

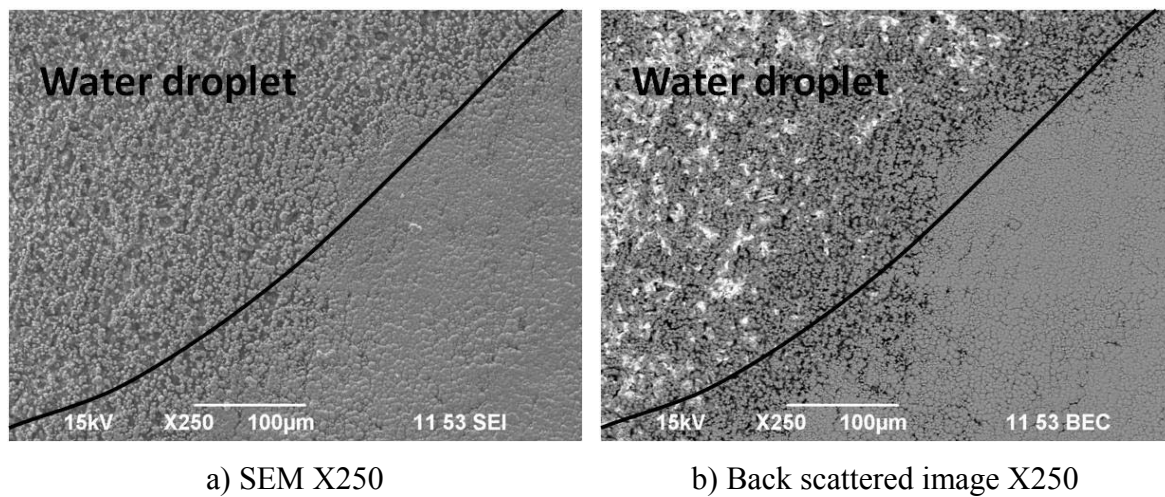
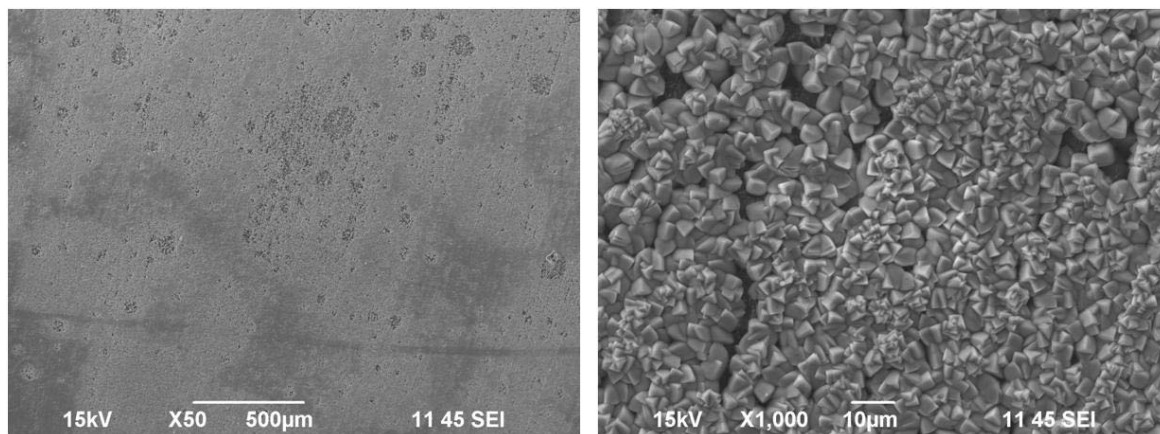


Figure 71: SEM images of sample exposed to the co-condensation of water and n-heptane for 2 weeks ( $WCR = 0.19 \text{ mL/m}^2/\text{s}$ ,  $C_7CR = 1.21 \text{ mL/m}^2/\text{s}$ ) – Location B (at the border of a big water droplet).



a) SEM X50

b) SEM X1000

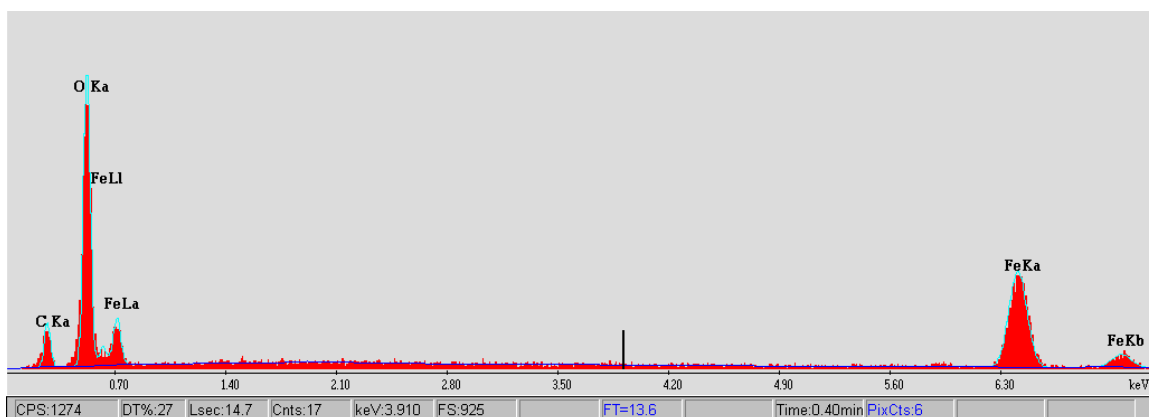
c) EDX analysis on crystal-like particles showing the composition of  $\text{FeCO}_3$ 

Figure 72: SEM images of sample exposed to the co-condensation of water and n-heptane for 2 weeks ( $\text{WCR} = 0.19 \text{ mL/m}^2/\text{s}$ ,  $\text{C}_7\text{CR} = 1.21 \text{ mL/m}^2/\text{s}$ ) – on a general area (Location C).

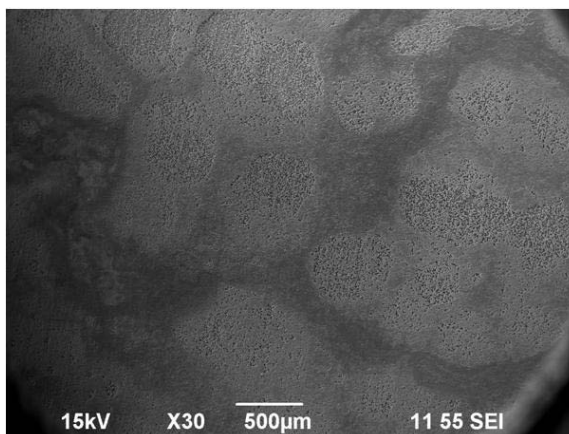


Figure 73: SEM images of sample exposed to the co-condensation of water and n-heptane for 2 weeks ( $WCR = 0.19 \text{ mL/m}^2/\text{s}$ ,  $C_7CR = 1.21 \text{ mL/m}^2/\text{s}$ ) – On the shining area (Location D).

After cleaning the surface, SEM images were taken. Uniform corrosion was observed under the droplet – location A (Figure 74a). Elsewhere SEM images show non-uniform attack, (Figure 74b-d).

The IFM analysis confirmed that under the big droplet – location A (Figure 75) the surface was uniformly corroded, which was consistent with this droplet being water.

Figure 76 shows an image at location B, which was taken at the border of the big water droplet, and here the most severe corrosion attack was found - at the interface of water and n-heptane. Further into the water droplet, IFM showed less attack. It is known that the most aggressive water is the “freshly” condensed water, which has the lowest pH, and which can always be found at the edges of the droplet, causing the highest rate of attack there.

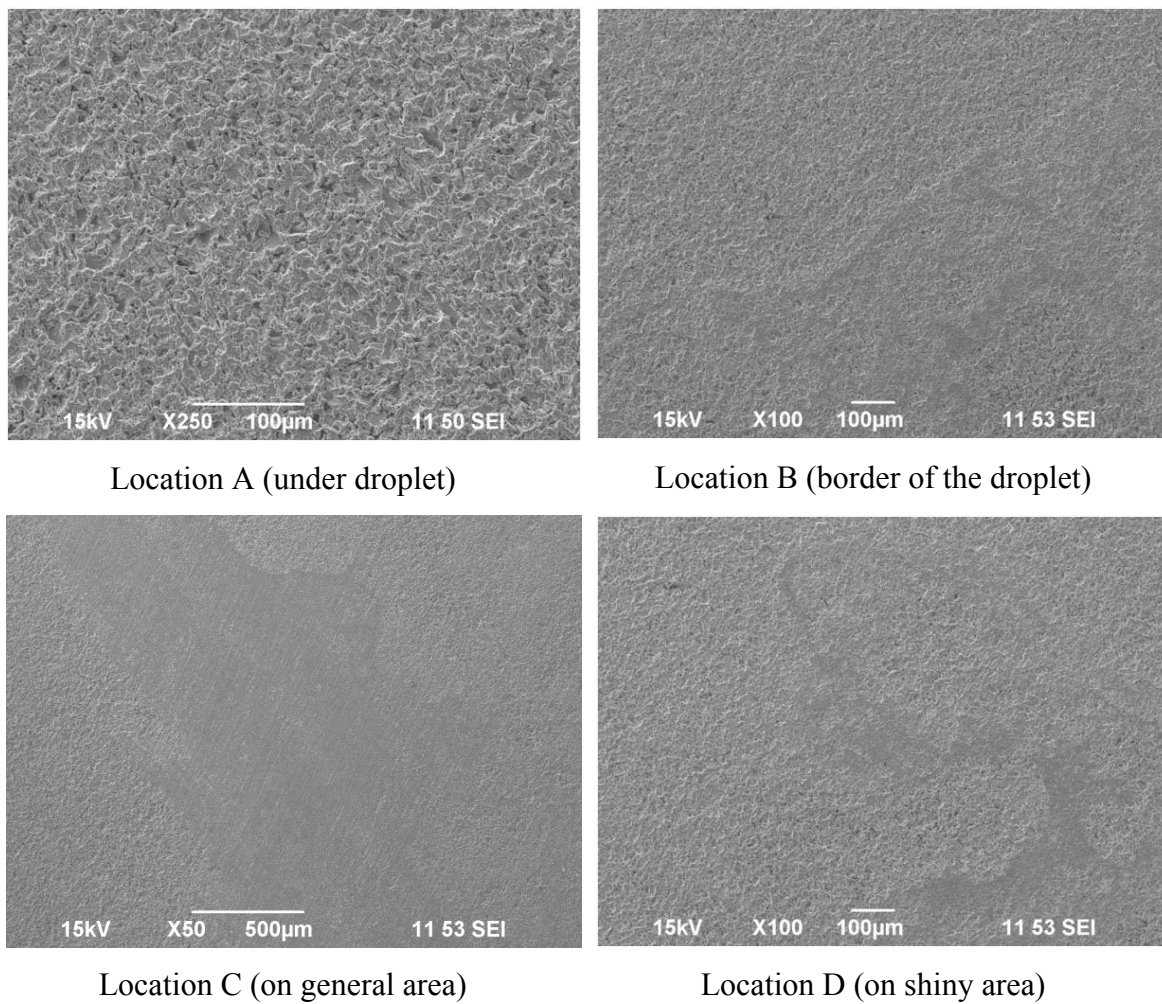


Figure 74: SEM images of sample exposed to the co-condensation of water and n-heptane for two weeks after the removal of corrosion product.

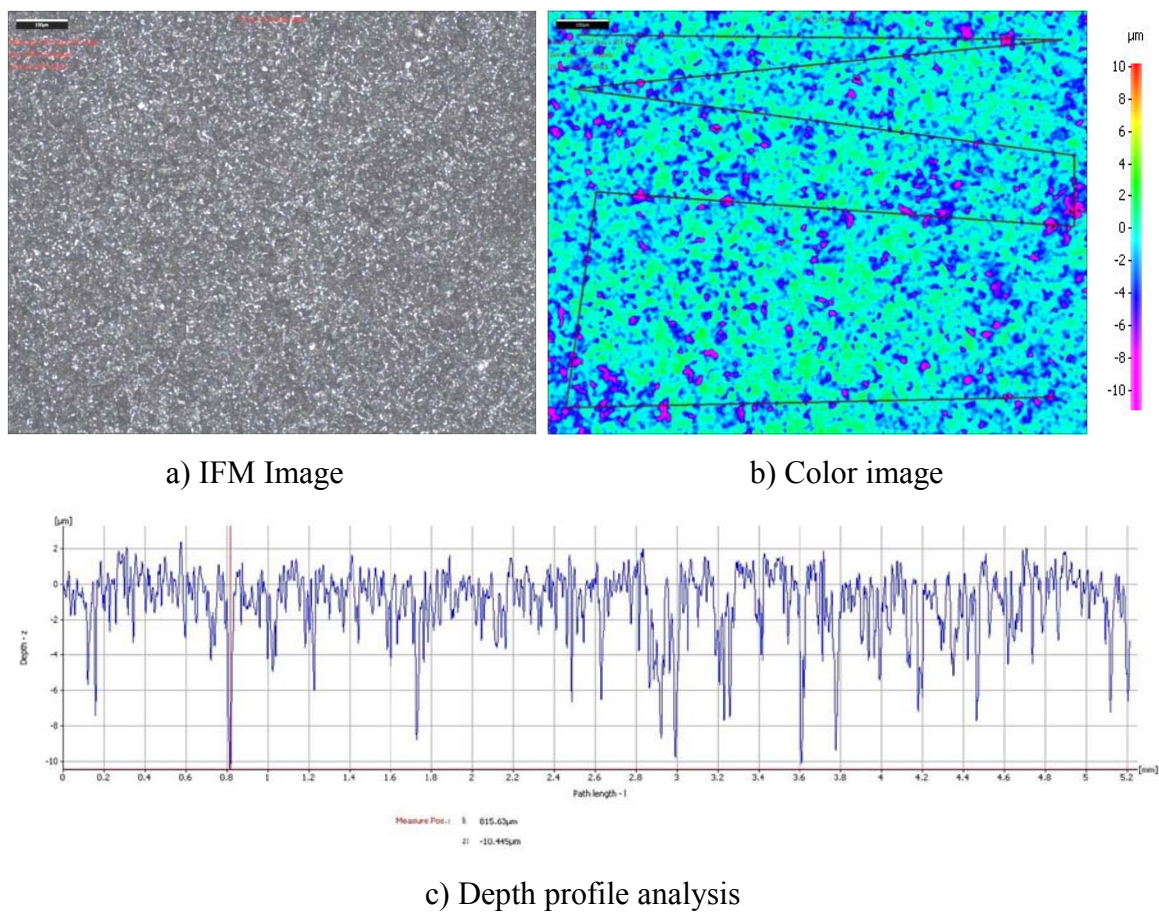


Figure 75: IFM image of sample exposed to the co-condensation of water and n-heptane for 2 weeks - Location A (under big droplet).

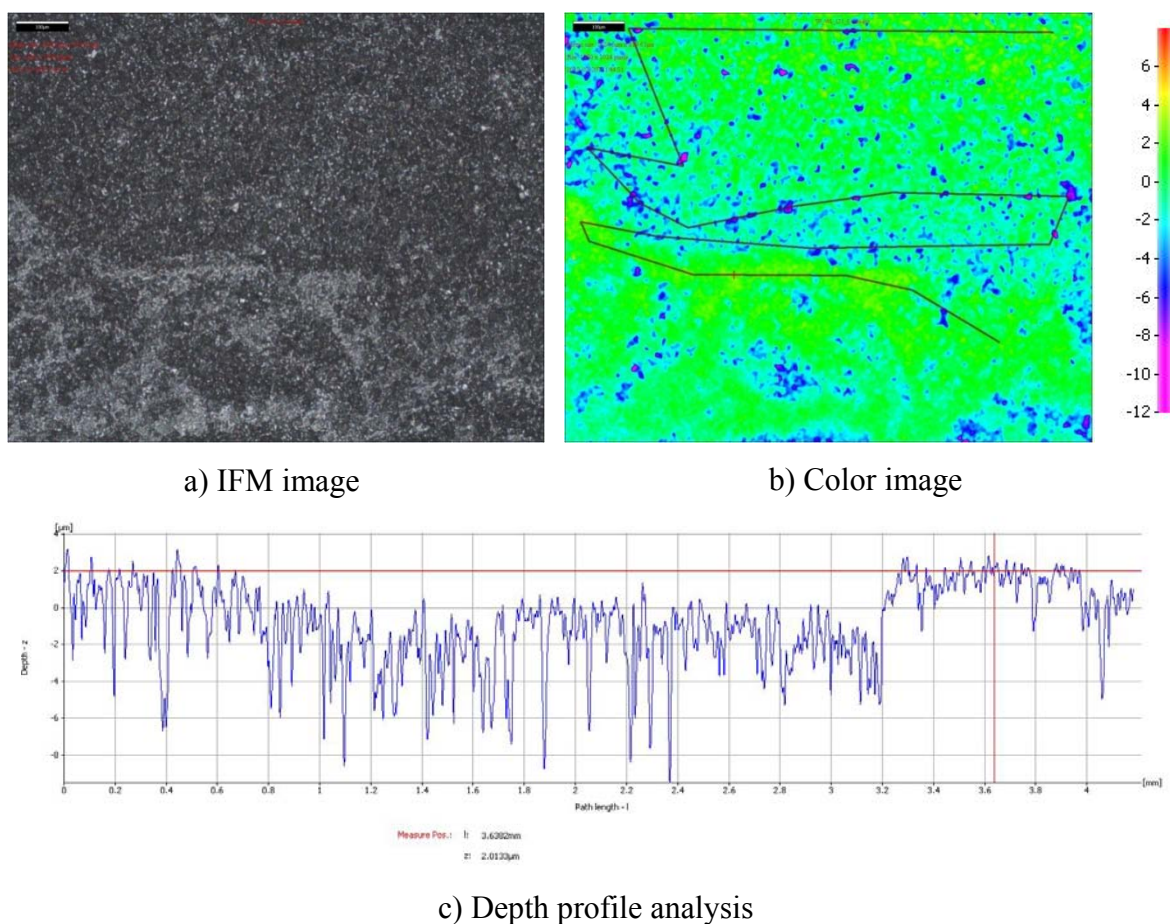


Figure 76: IFM image of sample exposed to the co-condensation of water and n-heptane for 2 weeks - Location B (border of big droplet).

The weight loss corrosion rate is shown in Figure 77 with the comparison to the shorter term test. For the co-condensation scenario, the general corrosion rates do not change within 2 weeks. However in the absence of hydrocarbons, the weight loss corrosion rate increased from 0.5 to 0.8 mm/yr. There are two possible explanations for the increase of corrosion rate. First of all, the presence of iron carbide may lead to a galvanic effect between iron carbide and bare steel, thus increasing corrosion rate.

Another possible explanation is an artifact of how corrosion rate is calculated. The test condition did not lead to the formation of any protective layer of  $\text{FeCO}_3$ . Over time, the surface was roughened by the corrosion creating an effective area for the corrosion process to increase. Hence, corrosion rate seemed to increase as an artifact of how corrosion rate was calculated.

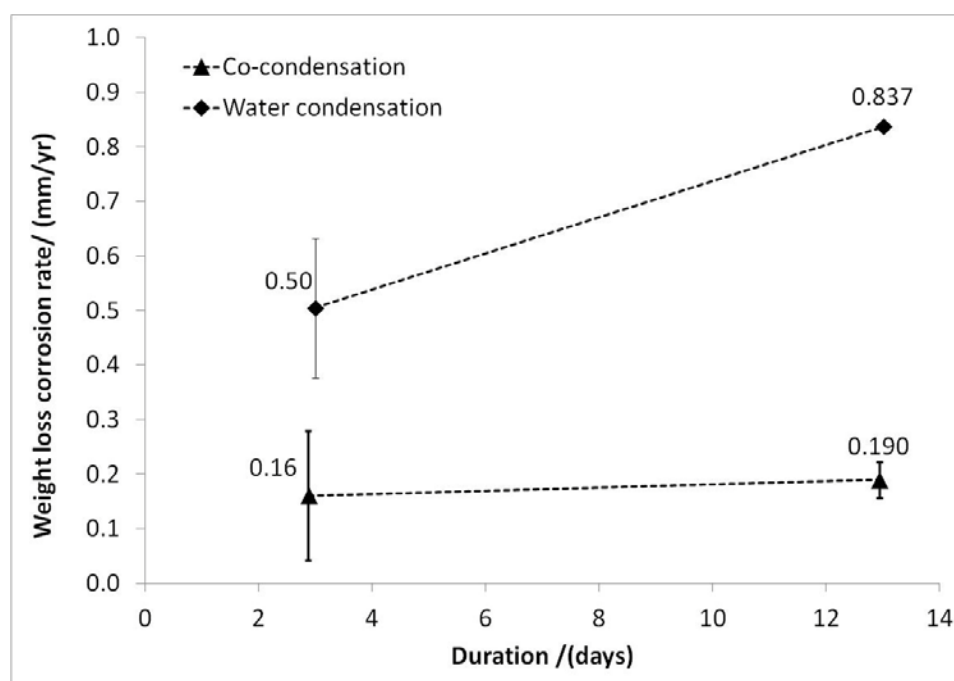


Figure 77: Weight loss corrosion rate against test duration.

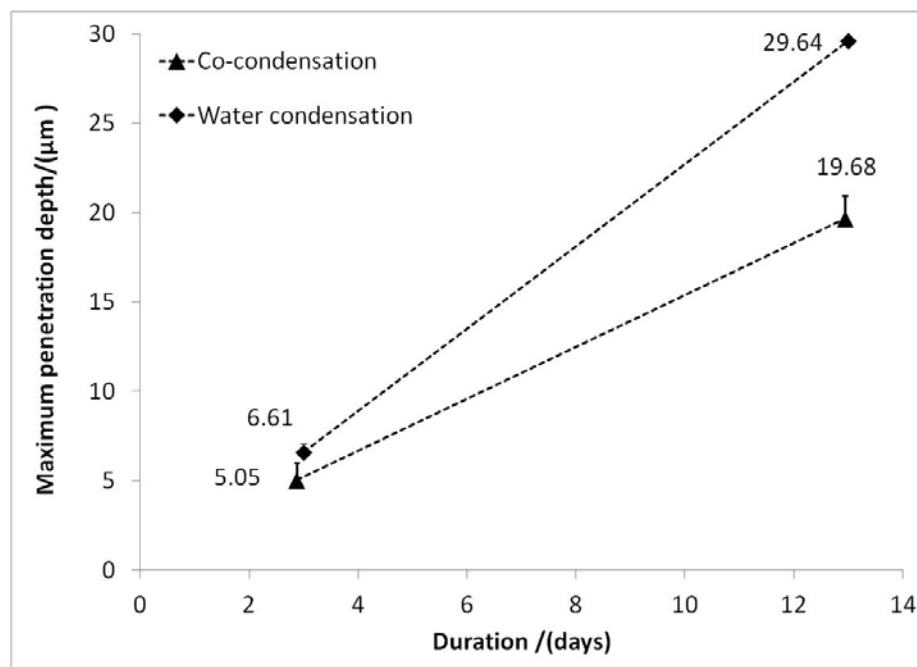


Figure 78: Maximum penetration depth against test duration.

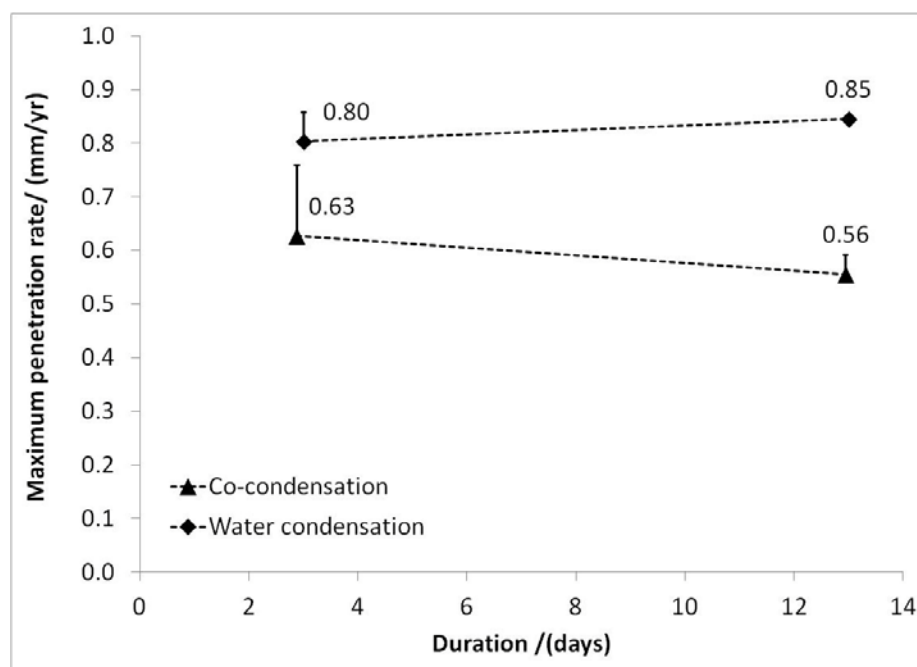


Figure 79: Maximum penetration rate against test duration.

Figure 78 plots the maximum penetration depth with test duration. As tests were duplicated, the maximum depth reported in the graph is the average value of the maximum penetration depth obtained in the duplicated test. Hence, the error bars are the maximum values from the duplicated tests. Both conditions, water alone and co-condensation, led to a similar increase in the maximum penetration depth at a constant rate as shown in Figure 79. It can be concluded that the 3-day and 2-week tests show similar results.

#### 4.3.2. *Corrosion in flowing conditions*

A very different test setup was used in order to introduce vapor phase velocity effects into the system. However, due to safety concerns, the dimensions of the system were limited. The flow velocity was small (3.5 cm/s). Corrosion under water condensation and co-condensation with n-heptane were studied in these experiments.

Figure 80 shows the SEM images of corroded samples at a water condensation rate of  $0.48 \text{ mL/m}^2/\text{s}$  after 1 day and 3 days. The steel surface was partially covered with iron carbonate ( $\text{FeCO}_3$ ) in the 1-day experiment and fully covered for longer test duration. Higher surface temperature ( $36^\circ\text{C}$ ) was more favorable for  $\text{FeCO}_3$  to form. At same vapor temperature but a lower surface temperature ( $16^\circ\text{C}$ ), no  $\text{FeCO}_3$  heterogeneously precipitates (Figure 81). On the downstream sample which had a very low surface temperature some  $\text{FeCO}_3$  formed probably because it was subjected to a very low water condensation rate. Thus, water droplets stayed in contact with the steel surface

longer before they reached the maximum size and fell. Therefore, the ferrous ion concentration within the droplets was sufficient to nucleate and crystallize some  $\text{FeCO}_3$ .

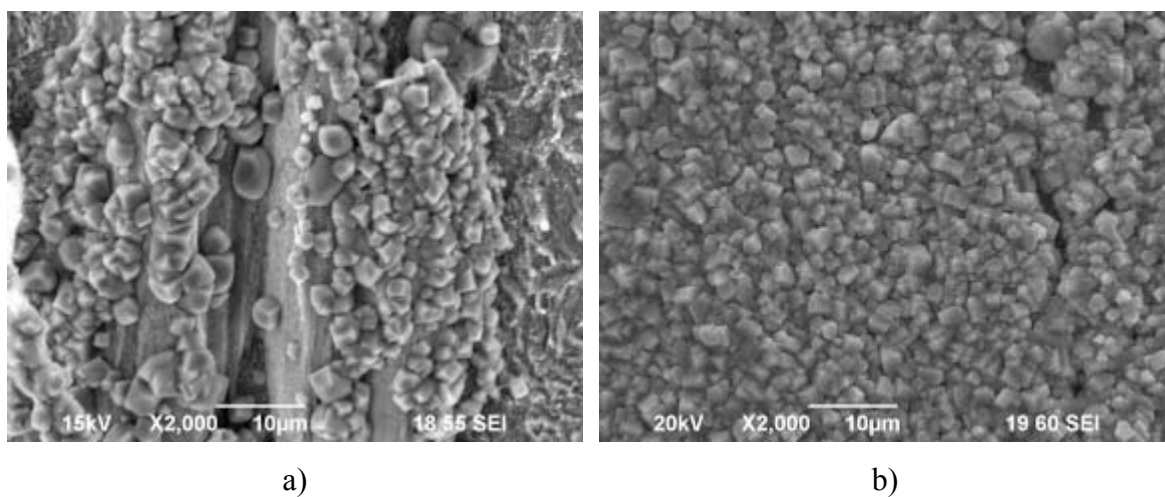


Figure 80: SEM Images of samples exposed to condensation rate of  $0.48 \text{ mL/m}^2/\text{s}$ ,  $T_g = 65^\circ\text{C}$ ,  $T_s = 36^\circ\text{C}$ , at a) 1 day and b) 3 days.

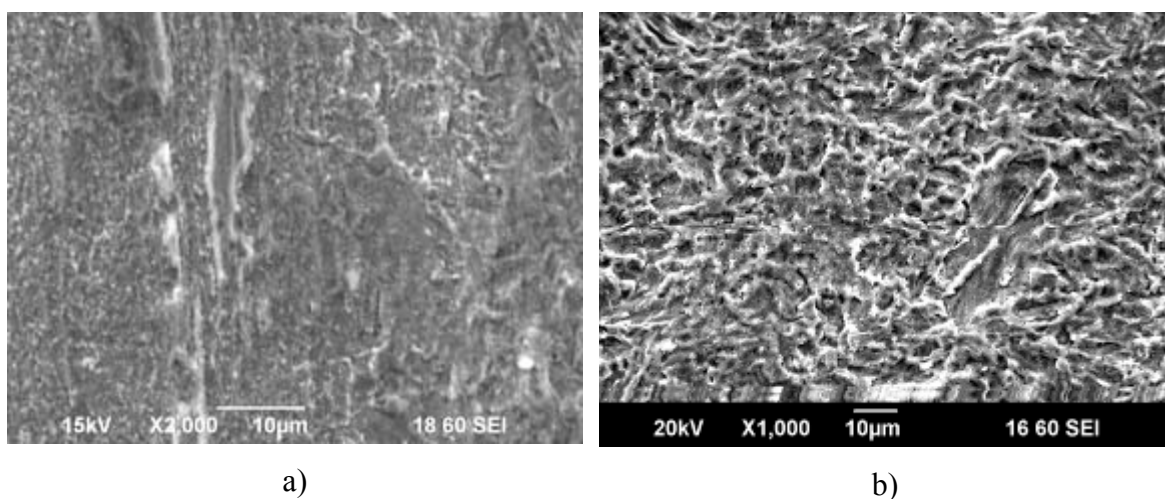


Figure 81: SEM Images of samples exposed to condensation rate of  $0.6 \text{ mL/m}^2/\text{s}$ ,  $T_g = 65^\circ\text{C}$ ,  $T_s = 16^\circ\text{C}$ , at a) 1 day and b) 3 days.

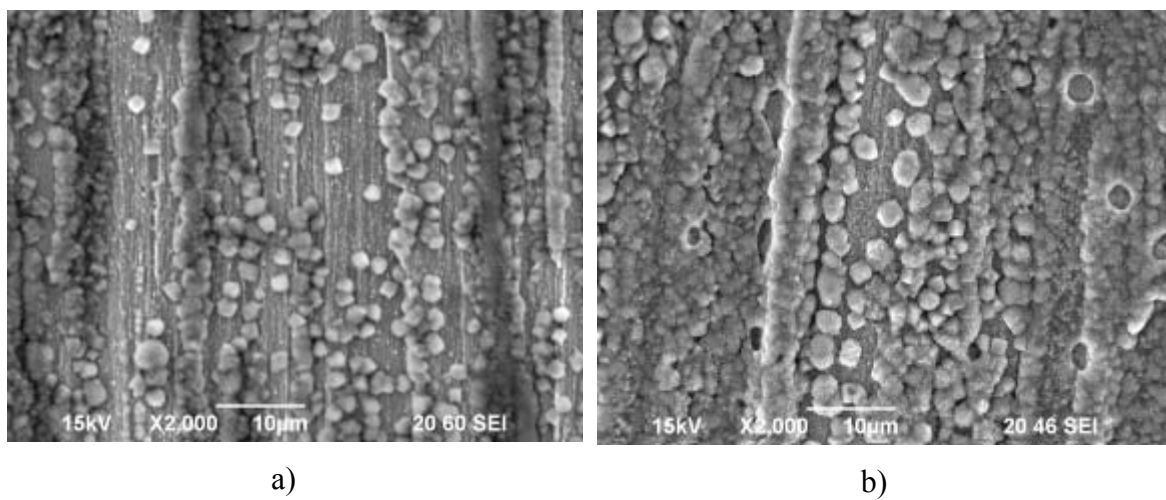
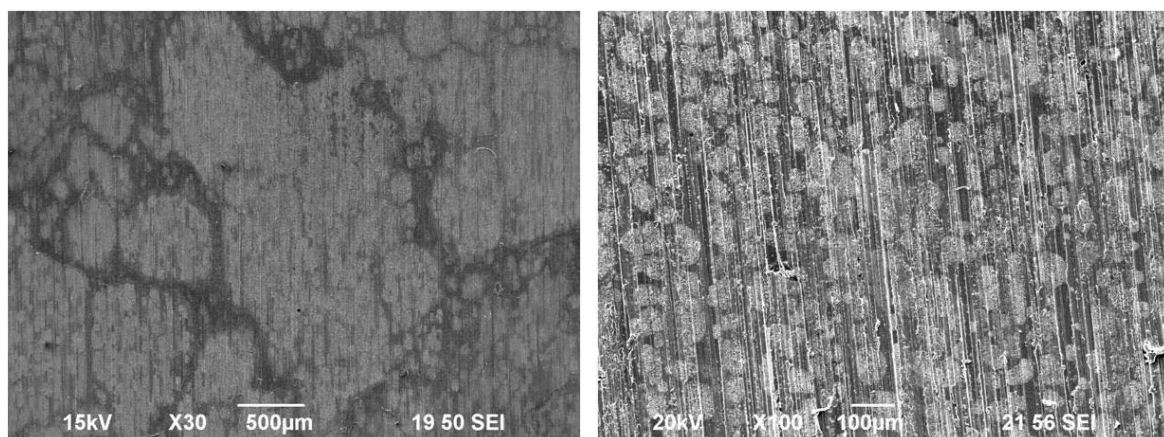


Figure 82: SEM Images of samples exposed to extremely low water condensation rate of  $0.004 \text{ mL/m}^2/\text{s}$ ,  $T_g = 18^\circ\text{C}$ , at a) 1 day and b) 3 days.

The presence of n-heptane caused a disruption of the continuous water film which led to distinct droplets separated by n-heptane. After 1 day exposure, the size of the water droplets seems to be related to the water condensation rate (Figure 83). When condensation rates of both liquids are relatively high, water droplets could be as large as 2 cm. *Vice versa*, with very low condensation rates, water condensed onto the surface forming very small droplets, with a diameter of approximately 0.1 mm. Longer test duration (3 days) indicated similar behavior (Figure 84).

SEM images show that these were water droplets since corrosion predominantly occurred at their interface with heptane. Similarly to previous corrosion tests in stagnant conditions, the water droplets were surrounded with a non-corrosive liquid - heptane. Noticeably, iron carbonate crystals were smaller than the ones observed in the water-

alone system. It was doubtful that this layer offered sufficient protection to the steel as only partial coverage was observed.



a.)  $T_b/T_o = 40/16.3^{\circ}\text{C}$

WCR =  $0.09 \text{ mL/m}^2/\text{s}$

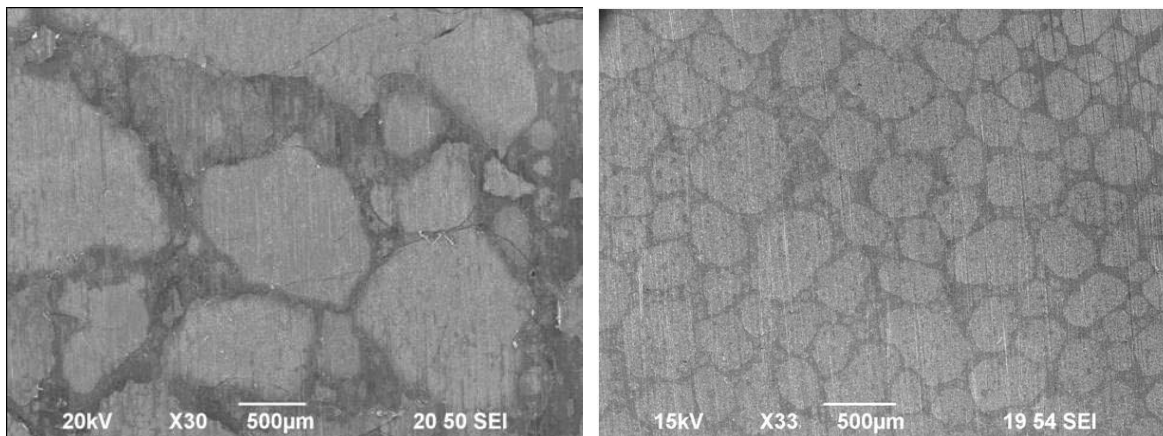
$C_7\text{CR} = 0.61 \text{ mL/m}^2/\text{s}$

b.)  $T_b/T_o = 18/15.3^{\circ}\text{C}$

WCR =  $0.005 \text{ mL/m}^2/\text{s}$

$C_7\text{CR} = 0.038 \text{ mL/m}^2/\text{s}$

Figure 83: Surface morphology of samples exposed to different co-condensation rates (test duration = 1 day).



a.)  $T_b/T_o = 40.5/15.7^\circ\text{C}$

WCR =  $0.1 \text{ mL/m}^2/\text{s}$

$C_7\text{CR} = 0.65 \text{ mL/m}^2/\text{s}$

b.)  $T_b/T_o = 19.3/17.6^\circ\text{C}$

WCR =  $0.003 \text{ mL/m}^2/\text{s}$

$C_7\text{CR} = 0.022 \text{ mL/m}^2/\text{s}$

Figure 84: Surface morphology of samples exposed to different co-condensation rates (test duration = 3 days).

Figure 85 presents corrosion rates as a function of water condensation rate. Note that the condensation rate of n-heptane is not fixed but varies with water condensation rate as shown by the secondary *x*-axis.

In the 1-day experiment, corrosion rate was a weak function of water condensation rate. Admittedly, weight loss corrosion rates obtained from the 1-day experiments are problematic. Increasing test duration from 1 to 3 days showed that corrosion rates were lower than those from 1-day tests. More importantly, corrosion rates during co-condensation showed no dependence on water condensation rate, which was in broad agreement with the results obtained under stagnant conditions.

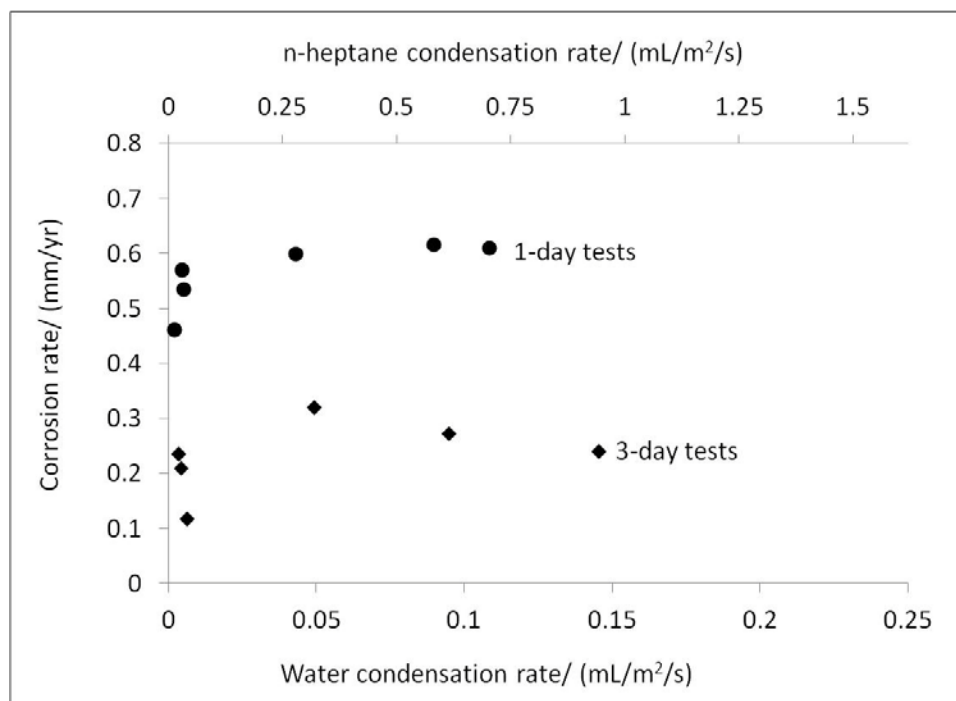


Figure 85: Corrosion rate in co-condensation scenario as a function of water condensation rate.

Comparison between the experiments with and without n-heptane shown in Figure 86 emphasizes the difference in the corrosion behavior in pure water and co-condensation environments. Corrosion rate in a co-condensation environment is less dependent on water condensation rate.

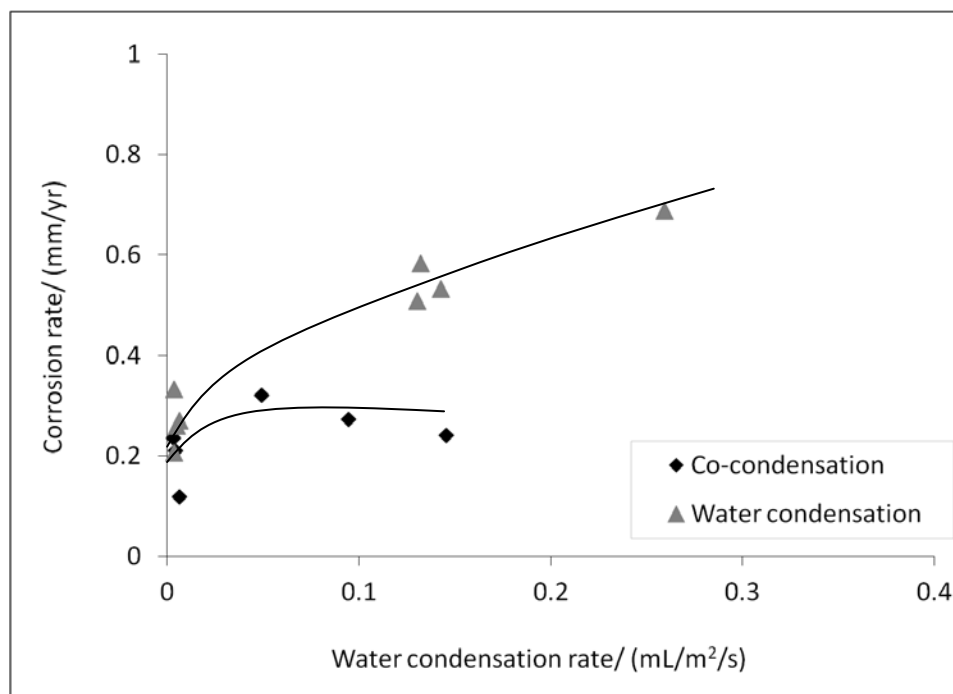


Figure 86: Corrosion rates in the absence and presence of n-heptane as a function of water condensation rate.

#### 4.4. Discussion of results from corrosion experiments

Even though water was the primary component that occupied the carbon steel surface, the corrosion rate obtained from weight loss decreased in all co-condensation scenarios and this was true for each of the three straight chain hydrocarbons used here. This section discusses some plausible explanations for this observation.

##### 4.4.1. The decrease in $pCO_2$

The test setup only accommodated atmospheric pressure and was an open system. Therefore, the total pressure was always 1 bar with  $CO_2$  purged continuously.

When a hydrocarbon is present, its vapor pressure reduces the partial pressure of CO<sub>2</sub>. Figure 87 shows the partial pressure of CO<sub>2</sub> as a function of temperature in the system with only water along with the case when water coexists with the three different hydrocarbons. For the water line, as temperature increases, the water generates more vapor, hence the partial pressure of CO<sub>2</sub> decreases. Because n-heptane is the lightest amongst the three hydrocarbons tested, it generates the most vapor pressure and the partial pressure of CO<sub>2</sub> decreases the most. For instance, at a vapor temperature of 50°C, the partial pressure of CO<sub>2</sub> decreases from 0.88 bar to 0.69 bar (21%) due to the presence of n-heptane. For heavier hydrocarbons, less vapor pressure is generated and the partial pressure of CO<sub>2</sub> does not decrease as much. The partial pressure of CO<sub>2</sub> is directly related to the corrosivity of the system.

However, the corrosion rate still decreased in the n-decane co-condensation system when the partial pressure of CO<sub>2</sub> was essentially the same, as shown in Figure 62. Therefore, there must be other factors which can be used to explain this reduction in corrosion rate.

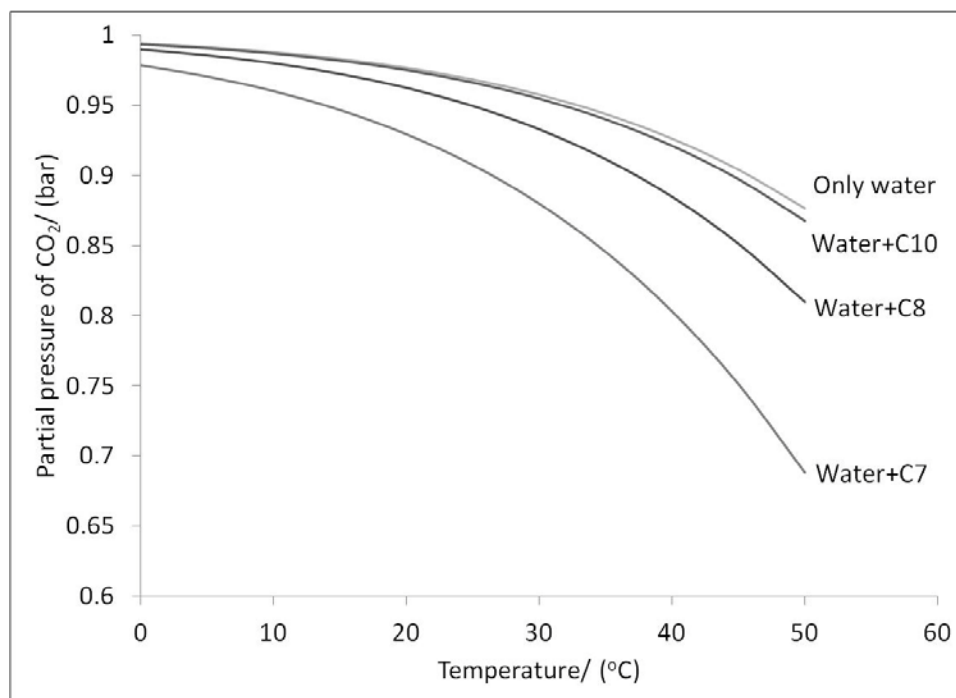


Figure 87: Calculated partial pressure of CO<sub>2</sub> in the presence of water and three hydrocarbons used in this study as a function of temperature.

#### 4.4.2. The decrease in corroded area

Hydrocarbons share a portion of the steel surface with water, shielding it from corrosion. Therefore, the corroded area in co-condensation experiments is not the full area of the samples, which was used in the corrosion rate calculations using weight loss. In other words, the corrosion rate in the co-condensation scenario can be higher than the reported value if the ratio of corroded area: total area  $\ll 1$ .

However, the surface characterization and electrical conductivity measurement did not lead to the same conclusion. All observations indicated that surface was wetted with water almost entirely. Therefore, this could contribute only slightly to the reduction

of corrosion rates in co-condensation scenarios. The large discrepancy seen in Figure 86 cannot be explained by this factor alone.

#### 4.4.3. *Changes in water chemistry*

Another possible explanation is the water chemistry change in the presence of co-condensation, as suggested by the precipitation of  $\text{FeCO}_3$

In the co-condensation scenario, water was segregated into smaller droplets ranging from 1 mm to as large as 2 cm. Figure 88 presents the covered steel surface to droplet volume ratio (A/V ratio) as a function of water droplet diameter. The A/V ratio decreased with the increase in droplet diameter. For instance, the A/V ratio increased from 150 to 3000  $\text{m}^{-1}$  when the diameter decreased from 2 cm to 1 mm.

The water chemistry within different size droplets evolved differently over time due to the different A/V ratio. For instance, with the same initial corrosion rate of 0.5 mm/yr, the  $\text{Fe}^{2+}$  concentration accumulated within different water droplet size varies and is shown in Figure 89. Consequently, the concentration of hydrogen ions within the droplet changes (Figure 90) with the pH in smaller droplet being higher than that in larger droplets, which would lead to a less corrosive solution.

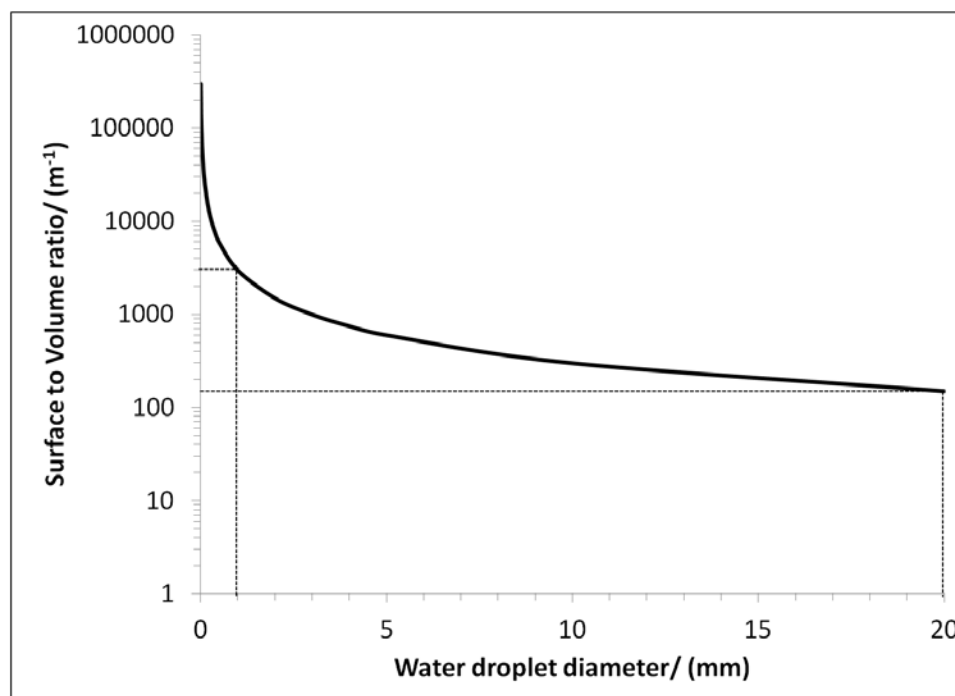


Figure 88: Surface to volume ratio as a function of water droplet size.

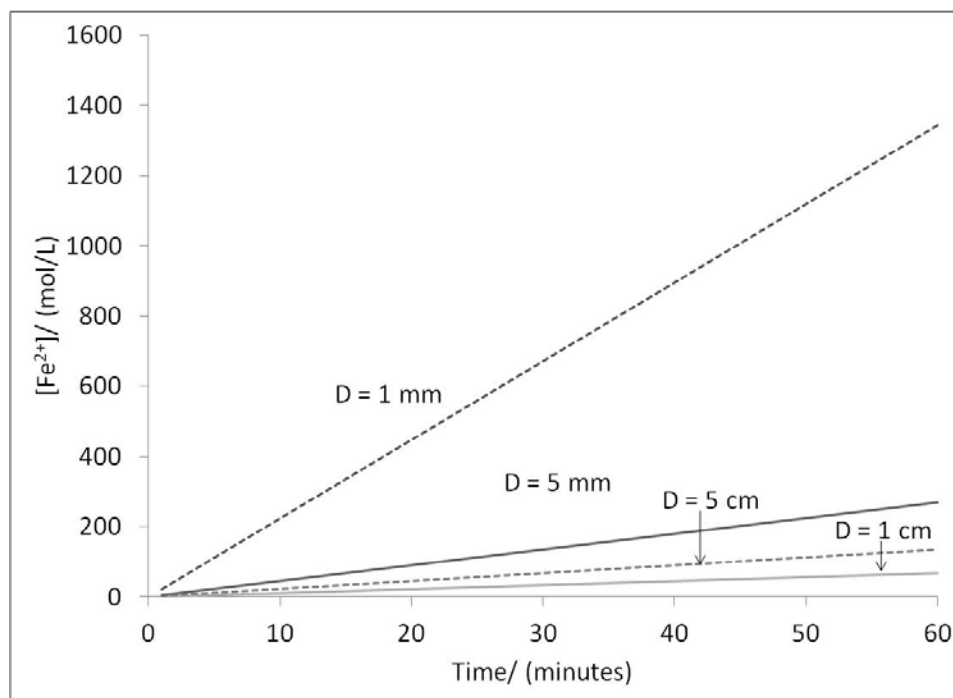


Figure 89: Calculated ferrous ion accumulation within water droplet of different diameters (D) against time (Common parameters:  $T_{\text{surface}} = 50^{\circ}\text{C}$ , Total P = 1 bar, Corrosion rate = 0.50 mm/yr).

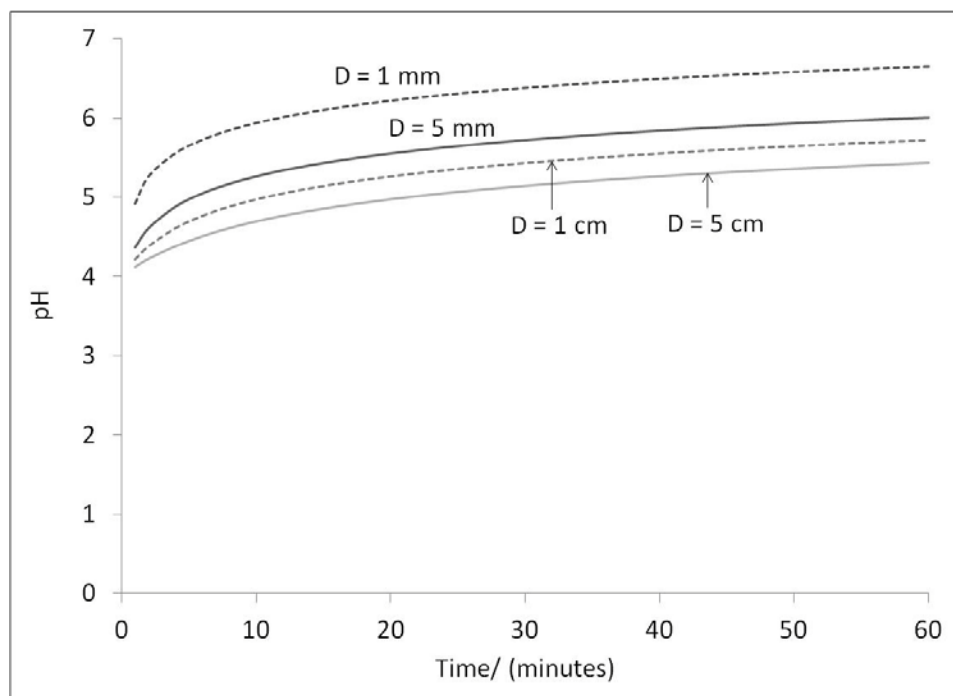


Figure 90: The change in pH within water droplet with different diameter ( $D$ ) against time (Common parameters:  $T_{\text{surface}} = 50^{\circ}\text{C}$ , Total  $P = 1$  bar, Corrosion rate =  $0.50$  mm/yr)

To explain why  $\text{FeCO}_3$  precipitated only in co-condensation scenarios, thermodynamics and kinetics of the precipitation of  $\text{FeCO}_3$  are discussed below.  $\text{FeCO}_3$  precipitates from  $\text{Fe}^{2+}$  and  $\text{CO}_3^{2-}$  according to Reaction 2-8. If the saturation ( $S$ ) is greater than 1, precipitation of  $\text{FeCO}_3$  is possible (Eq.4-3) [86–88]. However, the precipitated layer might not be well attached or protective if the precipitation rate is lower than the corrosion rate.

Sun and Netic [89] reviewed the existing  $\text{FeCO}_3$  precipitation kinetics models and proposed a new simpler one. The authors argued that when the  $A/V$  ratio was small, the calculated precipitation rate was over estimated by 1 to 2 orders of magnitude. The

authors proved that the  $\text{FeCO}_3$  did not precipitate on the steel sample but on the wall of the glass cell when A/V ratio was low. On the contrary, when the surface to volume ratio was high, the  $\text{FeCO}_3$  was deposited on the steel substrate.

In the current work, The A/V ratio was generally higher than that reported in Sun and Nesic [89]. The SEM results showed, the big water droplet was approximately 2 cm in diameter ( $A/V = 150 \text{ m}^{-1}$ ) in water condensation systems. Therefore, the precipitation rate proposed by Hunnik *et al.* [88] was used here, as shown in Eq.4-4.

$$S = \frac{c_{\text{Fe}^{2+}} c_{\text{CO}_3^{2-}}}{K_{sp}} \quad \text{Eq.4-3}$$

$$PR = k_r \frac{A}{V} K_{sp} (S - 1)(1 - S^{-1}) \quad \text{Eq.4-4}$$

Where;

- $PR$  = Precipitation rate, in  $\text{mol/m}^2/\text{hr}$
- $k_r$  = Kinetics constant,  $e^{A-B/RT}$  Where  $A = 52.4$  and  $B = 119.8$
- $S$  = Supersaturation level, dimensionless
- $A/V$  = Surface to volume ratio, in  $\text{m}^{-1}$
- $c_{\text{Fe}^{2+}}$  = Concentration of ferrous ion in aqueous phase, in  $\text{mol/L}$
- $c_{\text{CO}_3^{2-}}$  = Concentration of carbonate ion in aqueous phase, in  $\text{mol/L}$
- $K_{sp}$  = Iron carbonate solubility constant, in  $(\text{mol/L})^2$

Figure 91 illustrates that the precipitation rate of  $\text{FeCO}_3$  in a small water droplet is faster than that in a large water droplet. According to the observation, water droplet “lifespan” in a water system generally ranged from 10 to 30 minutes. Therefore, with this in mind, it is clear why the  $\text{FeCO}_3$  did not precipitate in a pure water system where the water droplets were much larger.

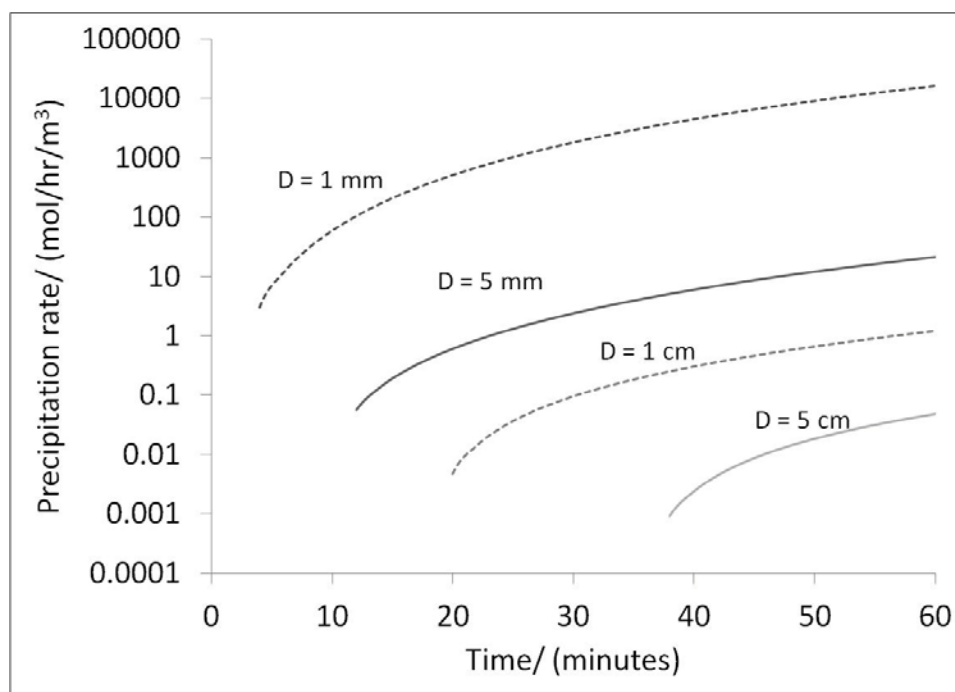


Figure 91: Iron carbonate precipitation rate within water droplet with different diameter (D) against time (Common parameters:  $T_{\text{steel}} = 50^\circ\text{C}$ , Total P = 1 bar, Corrosion rate = 0.50 mm/yr).

## CHAPTER 5: CONDENSATION RATE PREDICTION

### 5.1. Introduction

Top of the line corrosion prediction tools are discussed in detail in Chapter 2. All of the current models ignore the effect of the co-condensation of hydrocarbons.

A recent comparison between the prediction tools, which are conservative, and actual field tests showed discrepancies at the beginning of the lines which according to the models were suffering from the highest TLC rate while inspection data suggested otherwise [43]. Incorrect prediction of locations suffering from TLC could cause mistakes during the design phase or in maintenance. It is necessary to understand the gap between prediction and reality. Two hypotheses were proposed here and are described below.

#### *1.) Superheated water vapor*

It can be assumed that fluids entering the line contain superheated water vapor. In other words, the fluid is not saturated with water vapor upon entering the subsea line. Once fluid is transported along the line, pressure and temperature decrease and water was eventually saturates and condenses. Hence, in this case, the beginning of the line is not subject to TLC as water did not condense.

#### *2) The co-condensation of water and hydrocarbons*

From the two previous chapters, the results showed that the presence of hydrocarbons affects how water condenses and influences corrosion behavior. Water is segregated into smaller droplets and surrounded with co-condensing hydrocarbon. The water chemistry within these droplets is favorable for  $\text{FeCO}_3$  precipitation. Additionally,

the calculation described in section 4.4.3 shows that the pH is higher in small droplets than in large ones. This effect is more pronounced at moderate water condensation rates than at low water condensation rates. The corrosion rate is decreased by 50% at a moderate water condensation rate.

One of the most important parameters in TLC is the water condensation rate, which is affected by co-condensation. Therefore before any effect of co-condensation is implemented into the models, one has to be able to predict the onset and rate of co-condensation. Only then can the TLC models be improved to account for the presence of co-condensable hydrocarbons.

In order to expand upon the two hypotheses presented above, two calculation modules were developed and are presented below, which are: the *thermodynamics module* and the *co-condensation rate prediction module*.

The *thermodynamics module* predicts if the fluid entering the pipeline is saturated with water or hydrocarbons or both. For instance, if the fluid is not saturated with water, it would require a certain distance for the fluid to cool down and reach the saturation point. Another example: if the temperature and pressure within the pipeline reach the saturation point of both water and hydrocarbons, the co-condensation condition would take place. A similar model was already implemented in the corrosion prediction for well tubing. Farshad *et al.* used phase diagrams of water and condensate to predict the depth of the tubing where water dropout and corrosion was a concern [90].

The *co-condensation rate prediction module* calculates the condensation rate of both water and hydrocarbons. This module will be implemented only if the condition for the co-condensation is reached.

## **5.2. Thermodynamics calculation**

The objective of this calculation module is to determine if the fluid entering the pipeline is saturated with water and hydrocarbons or not. If not, at what point would water become saturated and readily condense?

The necessary inputs for this calculation include the total fluid composition and temperature and pressure at the pipeline inlet.

### *5.2.1. Phase envelope calculation*

A dew point/line and a bubble point/line are the same for a single component as they relate to the condensation and evaporation point/line for a pure substance. For instance, the vapor liquid equilibrium of a pure water system is shown in Figure 92. On the right side of the figure is where water exists only in a vapor form. *Vice versa*, on the left side of the figure is where water exists only in a liquid form. On the line is where vapor and liquid water are in equilibrium. If the system contains 0.3 bar of water and is at 80°C, this particular system will be in a vapor state. If temperature of this system drops to 70°C, water vapor is now in equilibrium with liquid water and the first drop of liquid water forms. The definition of bubble point is the opposite. It is defined as the condition where the first bubble of vapor is formed from a liquid phase. For instance, if the system contains 0.3 bar of water and is at 60°C, this particular system will be in a liquid state. When this system is heated to 70°C, the first bubble of water vapor is formed.

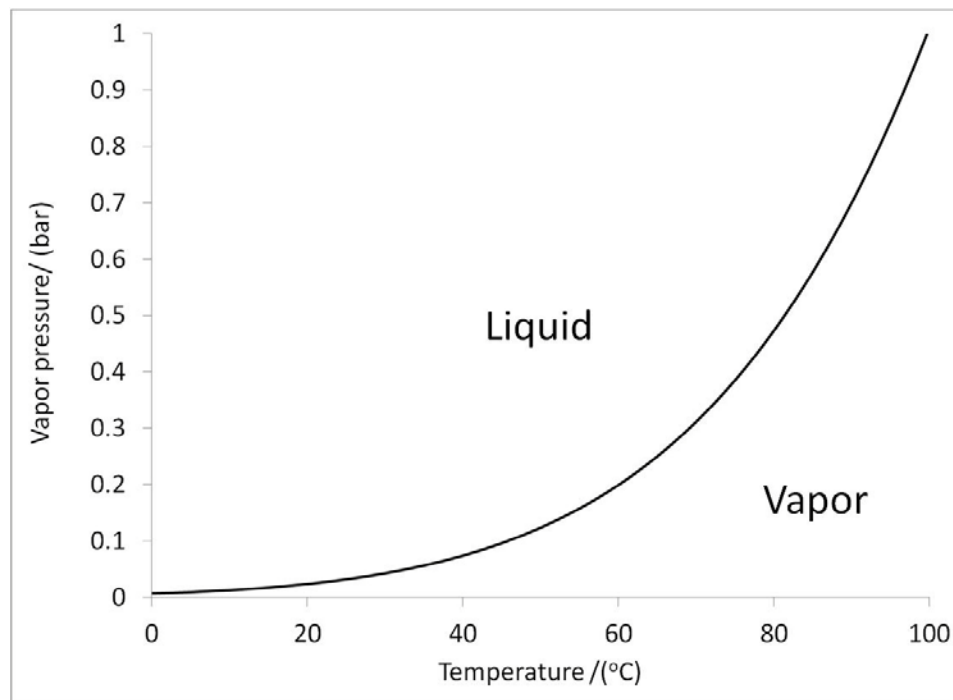


Figure 92: Dew line/Bubble line of a pure water system.

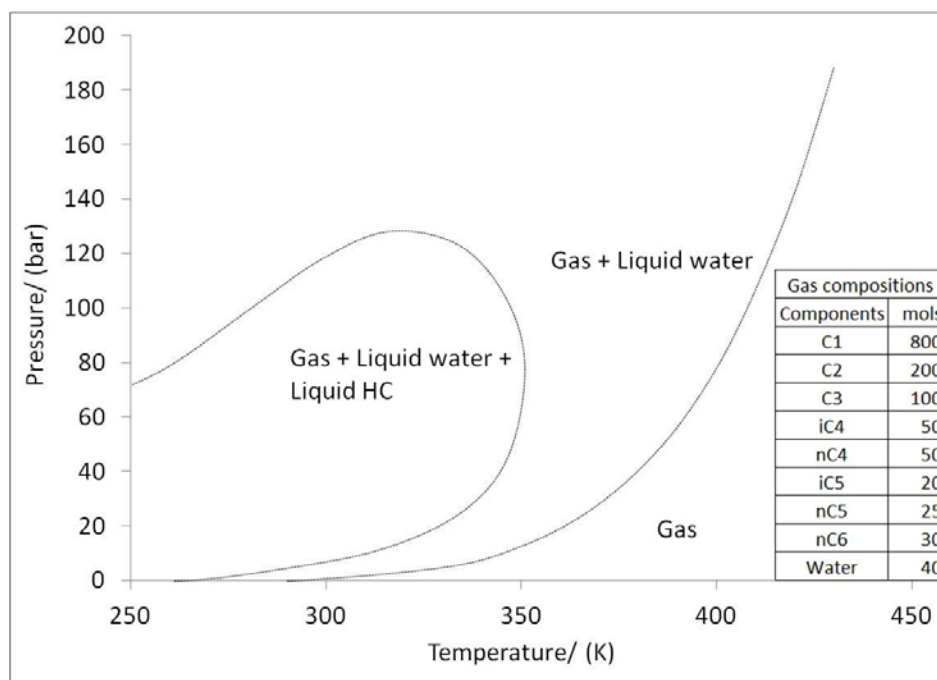
A wide range of hydrocarbons are present in transportation lines. The dewing and bubbling condition for a multi-component system cannot be represented by a single line any longer. A region called the phase envelope now represents the phase equilibrium diagram of multi components and graphically indicates when the system is in a single-phase or in two phases.

In the presence of water and hydrocarbons, the phase equilibrium diagram is normally represented by the phase envelope of hydrocarbons and the dew line of water. [91–93]. Figure 93a and b show phase equilibrium of two wet gases with different composition [93]. The difference is that the heaviest component in Figure 93a was n-hexane (n-C<sub>6</sub>) whereas Figure 93b was n-nonane (n-C<sub>9</sub>). Heavier components in the

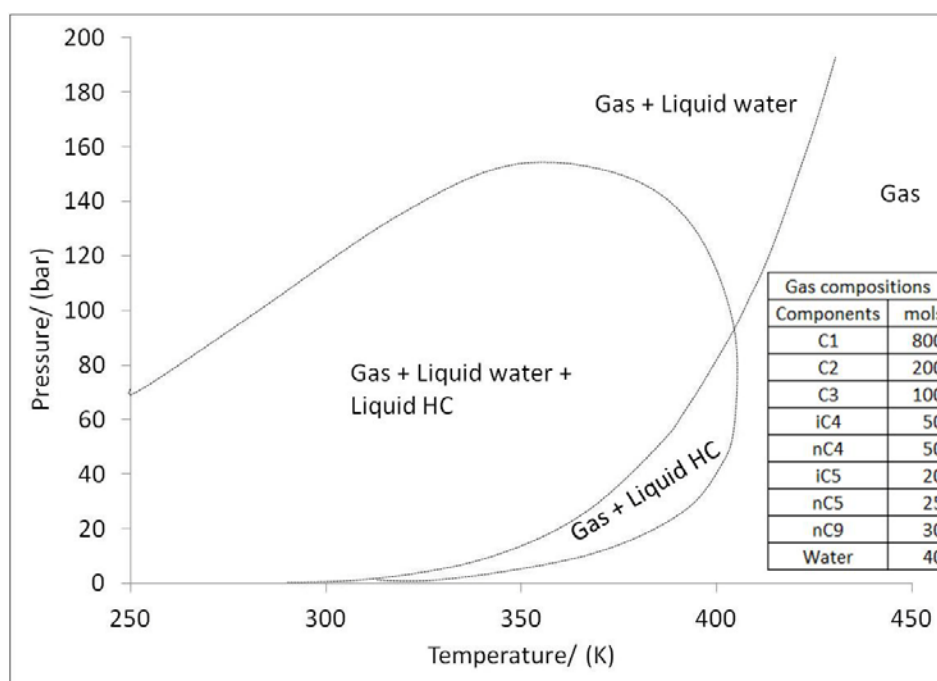
system have a higher dew point temperature, thus shifting the dew curve of the hydrocarbons to the right of the diagram. In the lighter system (Figure 93a), water condensed first while the vapor mixture consists of superheated hydrocarbons and saturated water vapor. Once temperature decreased further to the dew point of the hydrocarbons, the first liquid drop of hydrocarbons appeared and three-phase equilibrium was achieved.

On the other hand, when the heavier hydrocarbon is present in the system (Figure 93b) the phase envelope shifted to the right and the hydrocarbon condensed prior to liquid water. In this case, simultaneous hydrocarbon and water condensation possibly occurred once the dew point of water was reached.

Erbar & Maddox (1981) also suggested that the water line was independent of the presence of hydrocarbons since the water line remains almost constant. However, this representation can be applied only when acid gases are present at a low concentration.



a) Phase envelope of water and hydrocarbons for wet gas



b) Phase envelope of water and hydrocarbons for heavier wet gas

Figure 93: Phase behavior of water and hydrocarbons (Reproduced from Erbar and Maddox [93])

Therefore, the phase envelope can be useful in determining not only if water condensation is expected and if TLC is a concern at a given temperature and pressure, but also it can determine the likelihood of the co-condensation with hydrocarbons. To construct a phase envelope for a given system, three separate calculations are required including the dew line of water, the dew line of hydrocarbons and the bubble line of hydrocarbons. The mathematical calculations for all three lines are discussed below.

- Peng-Robinson Equation of State

In 1975, Peng and Robinson proposed a modification to the Van der Waals cubic equation of state [94]. Since then it has often been used in the oil and gas industry due to its simplicity and reasonably accurate performance [95], [96]. However, great uncertainty may be encountered when the system contains polar and certain non-hydrocarbon species. [96–99]. The inaccuracy was caused from the mutual solubility of the water and the hydrocarbon phase. Hydrogen bonding causes water to form clusters. Many researchers have proposed various techniques and mathematical solutions to improve the understanding of phase equilibria of systems containing water [92], [96], [98–100].

However, for the purpose of dew point and bubble point calculation, a starting point is to assume that water and hydrocarbons have no (significant) mutual solubility. Eq 5-1 is the Van der Waals cubic equation of state for a single component.

$$P = \frac{RT}{(V - b)} - \frac{a\alpha}{V(V + b) + b(V - b)} \quad \text{Eq 5-1}$$

Where;

- $a$  = A constant for Peng Robinson EoS  $\left(0.45724 \frac{R^2 T_c^2}{P_c}\right)$   
 $b$  = A constant for Peng Robinson EoS  $\left(0.07780 \frac{RT_c}{P_c}\right)$   
 $T_c, P_c$  = Critical temperature and critical pressure in Kelvin and Bar, respectively  
 $\alpha$  = A dimensionless parameter calculated from Eq 5-2 Eq 5-3

$$\alpha = [1 + m(1 - T_r^{0.5})]^2 \quad \text{Eq 5-2}$$

$$m = 0.3746 + 1.5423\omega + 0.2699\omega^2 \quad \text{Eq 5-3}$$

Where;

$T_r$  = Reduced temperature, dimensionless

$\omega$  = Acentric factor

Equivalent form of Van der Waals cubic equation expressed as a function of compressibility factor is shown in Eq 5-4. Solving Eq 5-4 may yield more than one real root. The smallest and the largest real roots correspond to the liquid phase and vapor phase compressibility factors, respectively. The middle real number has no physical meaning. If the equation leads to only one real root, the system will contain only one phase.

$$Z^3 - (1 - B)Z^2 + (A - 2B - 3B^2)Z - (AB - B^2 - B^3) = 0 \quad \text{Eq 5-4}$$

Where  $A$  and  $B$  are given as

$$A = \frac{a\alpha P}{(RT)^2} \quad \text{and} \quad B = \frac{bP}{RT}$$

$a$ ,  $b$  and  $\alpha$  are composition dependent constant. The following mixing rules are applied to constants  $a$ ,  $b$  and  $\alpha$  for a mixture (Eq 5-5 and Eq 5-6)

$$a\alpha_m = \sum_i \sum_j z_i z_j (a_i a_j \alpha_i \alpha_j)^{0.5} (1 - k_{ij}) \quad \text{Eq 5-5}$$

$$b_m = \sum_i \sum_j z_i z_j b_i \quad \text{Eq 5-6}$$

Where;

$z_i$  = Mole fraction of component  $i$  in the mixture, dimensionless

$k_{ij}$  = Binary interaction parameter between components  $i$  and  $j$  listed in Table

11 [92], dimensionless

Table 11: Binary interaction parameters used in Eq 5-8 and Eq 5-9

	C <sub>1</sub>	C <sub>2</sub>	C <sub>3</sub>	iC <sub>4</sub>	nC <sub>4</sub>	iC <sub>5</sub>	nC <sub>5</sub>	C <sub>6</sub>	C <sub>7</sub>	C <sub>8</sub>	CO <sub>2</sub>	H <sub>2</sub> S	N <sub>2</sub>	H <sub>2</sub> O
C <sub>1</sub>	0													
C <sub>2</sub>	0	0												
C <sub>3</sub>	0.14	0.001	0											
iC <sub>4</sub>	0.26	-0.01	-0.01	0										
nC <sub>4</sub>	0.013	0.01	0.003	0	0									
iC <sub>5</sub>	-0.01	0.016	0.011	0	0	0								
nC <sub>5</sub>	0.023	0.008	0.027	0	0.017	0.06	0							
C <sub>6</sub>	0.042	-0.01	0.008	0	-0.01	0	0	0						
C <sub>7</sub>	0	0	0	0	0	0	0	0	0					
C <sub>8</sub>	0	0	0	0	0	0	0	0	0	0				
CO <sub>2</sub>	0	0	0	0	0	0	0	0	0	0	0			
H <sub>2</sub> S	0	0	0	0	0	0	0	0	0	0	0	0		
N <sub>2</sub>	0.031	0.052	0.085	0.103	0.08	0.092	0.1	0.15	0	0	0	0	0	
H <sub>2</sub> O	0.651	0.635	0.53	0.69	0.69	0.5	0.5	0.5	0	0	0	0	0.48	0

Subsequently, fugacity coefficients of component  $i$  in both the vapor and liquids phase can then be calculated (Eq 5-7, Eq 5-8, and Eq 5-9).  $Z_v$  and  $y_i$  are used to calculate the fugacity coefficient of component  $i$  in vapor phase. On the other hand,  $Z_L$  and  $x_i$  are used when the fugacity coefficient of the liquid phase is calculated.

$$\ln \Phi_i^V = \frac{b_i}{b_m} (Z_v - 1) - \ln(Z_v - B) - \frac{A}{B(-2\sqrt{2})} \left[ \frac{2\psi_i}{\psi} - \frac{b_i}{b_m} \right] \ln \left[ \frac{Z_v + (1 - \sqrt{2})B}{Z_v + (1 + \sqrt{2})B} \right] \quad \text{Eq 5-7}$$

Where;

$$\psi_i = \sum_{j=1}^n y_j (a_i a_j \alpha_i \alpha_j)^{0.5} (1 - k_{ij}) \quad \text{Eq 5-8}$$

$$\psi = \sum_{i=1}^n \sum_{j=1}^n y_i y_j (a_i a_j \alpha_i \alpha_j)^{0.5} (1 - k_{ij}) \quad \text{Eq 5-9}$$

- The determination of water dew line

The saturation line of water can be calculated separately from that of hydrocarbons [101] as shown in Eq 5-10 .

$$P y_w = P_v \quad \text{Eq 5-10}$$

Where;

- $P$  = The dew point pressure of water, in bar
- $y_w$  = Mole fraction of water in the fluid, dimensionless
- $P_v$  = Vapor pressure of water as a function of temperature, in bar

- Dew line for hydrocarbons

The dew line is defined as the condition at which the first drop of liquid is formed. It is the line on the right side of the envelope. It can be stated that the vapor

phase composition is equal to the total composition as there is no liquid phase. Figure 94 illustrates the diagram for the dew line calculation. As the pressure in the system is normally high, the ideal gas law is not appropriate to be used. Instead, the equation of state is required to obtain the fugacity coefficient. The dew point is the equilibrium between vapor and the liquid phase, hence, the fugacity of component  $i$  in the liquid equals to that in the vapor phase (Eq 5-11). The fugacity coefficients of component  $i$  in vapor and liquid phase are then calculated as shown in Eq 5-12.

At equilibrium:

$$f_i^V = f_i^L \quad \text{Eq 5-11}$$

$$\Phi_i^V = \frac{f_i^V}{y_i P} \quad \text{and} \quad \Phi_i^L = \frac{f_i^L}{x_i P} \quad \text{Eq 5-12}$$

$$K_i = \frac{\Phi_i^L}{\Phi_i^V} = \frac{y_i}{x_i} \quad \text{Eq 5-13}$$

Where;

$f_i^V, f_i^L$  = Fugacities of component  $i$  in vapor and liquid phase, respectively, in bar

$\Phi_i^V, \Phi_i^L$  = Fugacity coefficient of component  $i$  in vapor and liquid phase, respectively, dimensionless

$x_i, y_i$  = Mole fraction of component  $i$  in vapor and liquid phase, respectively, dimensionless

$P$  = Total pressure, in bar

$K_i$  = Equilibrium coefficient calculated using Wilson Correlation (Eq 5-14)

$$K_i = \frac{P_{ci}}{P} \exp \left[ 5.37(1 + \omega_i) \left( 1 - \frac{T_{ci}}{T} \right) \right] \quad \text{Eq 5-14}$$

Figure 94 illustrates the diagram for the dew line calculation which is described below. The procedure was adopted from previous work [3],[102], [103].

*Step 1* Input parameters are the total fluid composition, which can be treated as the vapor composition for the dew point calculation, as mentioned earlier. The system pressure is then specified so that the temperature that makes the system at equilibrium is calculated.

*Step 2* Liquid composition is first estimated using Wilson correlation (Eq 5-14).

*Step 3* Fugacity coefficients of vapor and liquid phase of each component are calculated from Peng-Robinson equation of state (Eq 5-1 to Eq 5-9).

*Step 4* New equilibrium coefficients are obtained from the fugacity coefficients. New liquid composition is then calculated.

*Step 5* If the summation of liquid mol fractions is not unity, they are normalized. Fugacity coefficients are re-calculated using the normalized liquid compositions.

*Step 6* Again, at equilibrium,  $f_i^L = f_i^V$ , hence  $1 - f_i^V / f_i^L = 0$ . If the result satisfies the criteria, then T is the dew temperature. If not, new T is estimated.

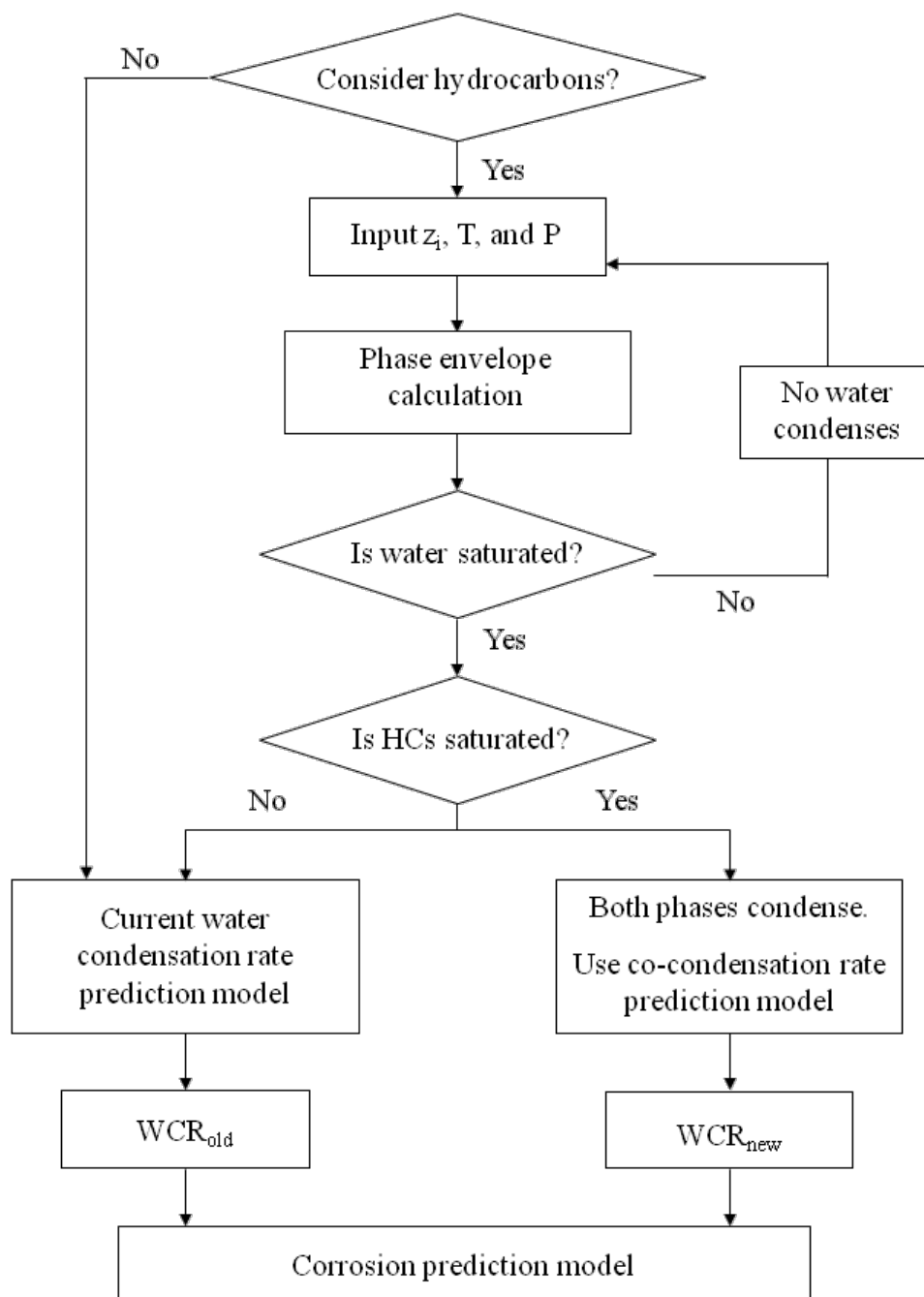


Figure 94: Diagram for the hydrocarbons dew line calculation.

- Bubble line for hydrocarbons

Similar calculation steps are applied for the bubble line as for the dew line. The total composition is now the liquid phase composition. The system temperature is now specified so that the system pressure that makes the system at equilibrium is calculated. Figure 95 shows the diagram of how the bubble line is calculated.

#### 5.2.2. *Comparison with literature data and commercial software results*

In order to validate the modeling approach, the phase envelope predictions are compared with the results obtained through the commercial software PVTsim V.20 and with published experimental data (see Figure 96). The simple calculations proposed in this work agreed reasonably well with the experimental data and other simulation results.

Table 12 gives wet gas compositions for 6 gases found in the literature. Their phase envelopes were calculated and then compared with published experimental data and the results obtained by using the commercial software.

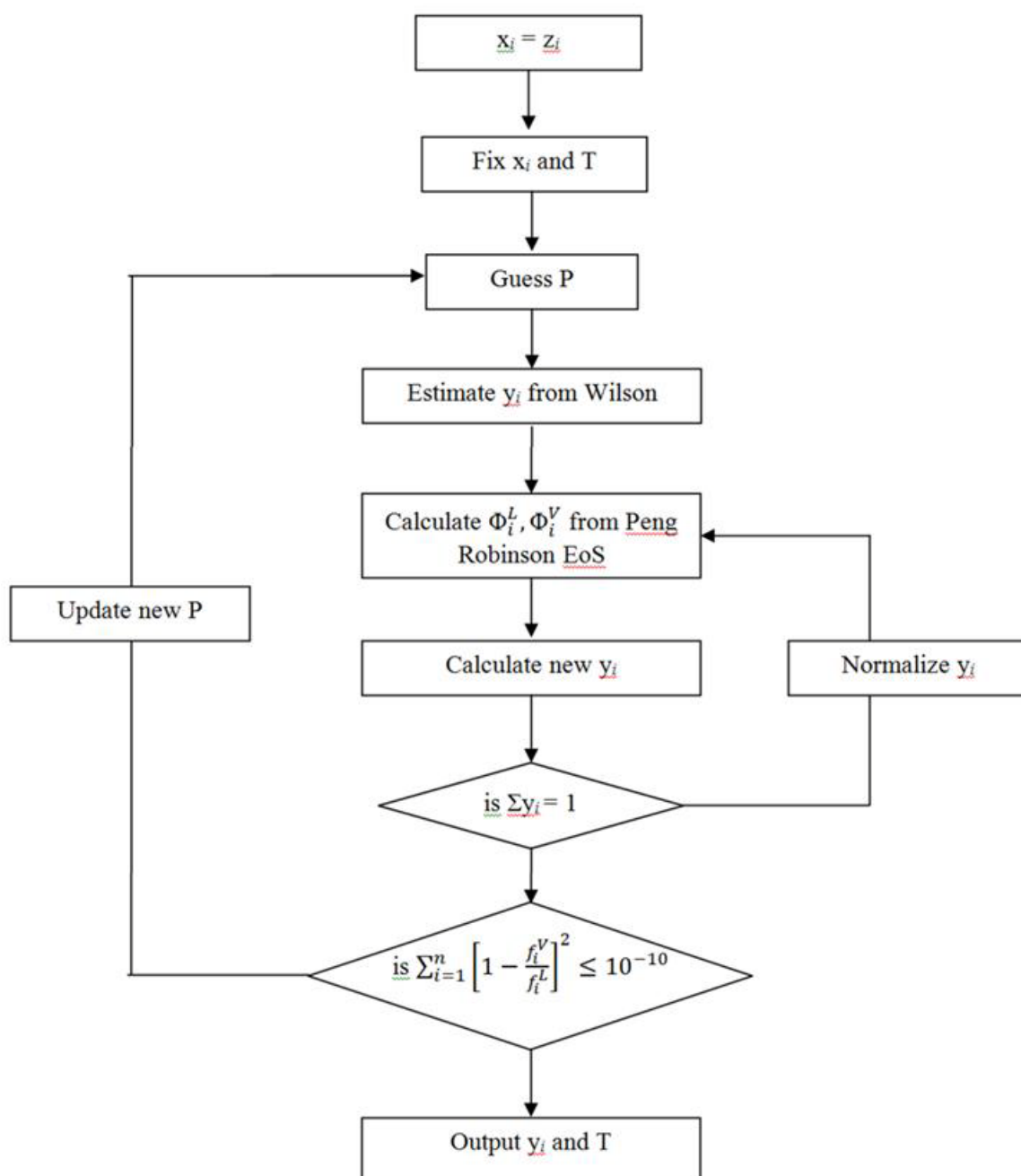
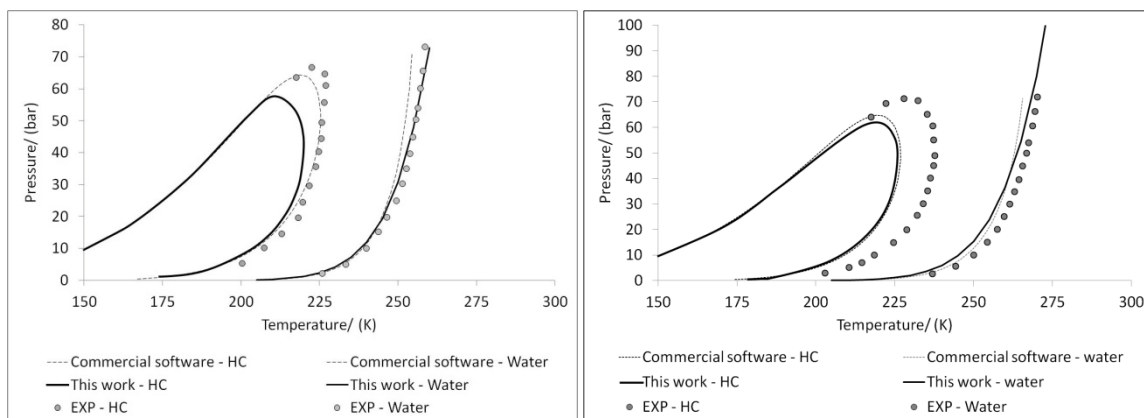


Figure 95: Diagram for the hydrocarbons bubble line calculation.

Table 12: Wet gas compositions (mole %) used for the comparison

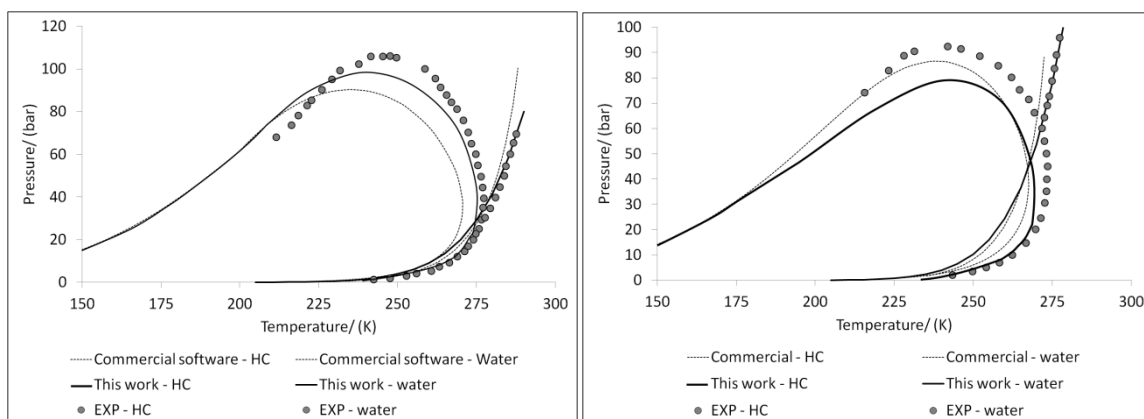
Component	Gas A[92]	Gas B[92]	Gas C [100]	Gas D [100]	Gas E [95]	Gas F [95]
C <sub>1</sub>	89.96	88.76	87.638	83.34	85.898	74.348
C <sub>2</sub>	8.22	8.54	2.72	7.526	8.499	12.005
C <sub>3</sub>	0.9	1.68	0.85	2.009	2.296	8.251
iC <sub>4</sub>	0.11	0.22	0.17	0.305	0.351	
nC <sub>4</sub>	0.13	0.29	0.32	0.520	0.347	3.026
iC <sub>5</sub>	0.0084	0.0182	0.085	0.120	0.051	
nC <sub>5</sub>	0.0032	0.0084	0.094	0.144	0.053	0.575
nC <sub>6</sub>			0.119	0.068		
nC <sub>7</sub>			0.0258	0.0138		
nC <sub>8</sub>			0.018	0.011		
CO <sub>2</sub>			0.51	0.284	1.498	1.028
H <sub>2</sub> S			0	0		
N <sub>2</sub>	0.67	0.48	6.9	5.651	1.007	0.537
H <sub>2</sub> O	0.003	0.006	0.0237	0.009		

The same results are shown in Figure 96. Simple calculation proposed in the present work fitted reasonably well with the experimental data and the other simulation results.



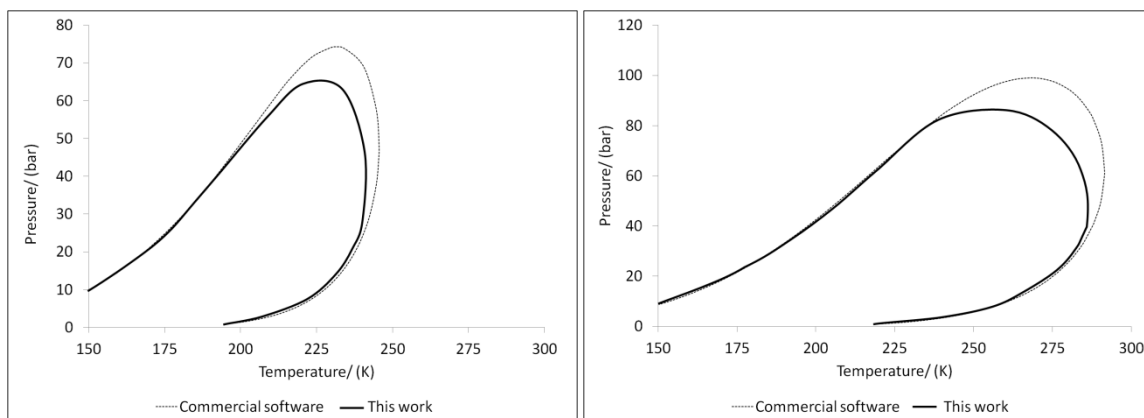
Gas A

Gas B



Gas C

Gas D



Gas E

Gas F

Figure 96: Comparison of hydrocarbons phase envelope and water dew line for Gas A to Gas F.

In some field gases, a heavier liquid fraction such as  $C_{7+}$  may be reported in the gas composition. The  $C_{7+}$  plus fraction lumps together n-heptane and all heavier components. The average molecular weight and specific gravity of all those components are usually reported along with the composition of  $C_{7+}$ . The amount of  $C_{7+}$ , molecular weight  $MW_{C_{7+}}$ , and specific gravity of  $C_{7+}$  all influence the shape of the phase envelope. Assuming use of properties of n-heptane instead of  $C_{7+}$  may lead to errors in prediction of heavier hydrocarbon dew points.

It should be noted that the water-hydrocarbons system is complicated due to the presence of hydrogen bonds of water. A simple cubic EoS such as Peng Robinson will not provide the accurate thermodynamic properties; such as the water solubility in hydrocarbons phase, and liquid densities [97], [99]. More complicated calculations have been developed to include this effect. However, for the sole purpose of dew point and bubble point prediction, Peng Robinson equation was proven to be sufficiently accurate.

### **5.3. Co-condensation rate prediction model**

The condensation of water and immiscible organic liquids has been of interest since the 1940s. Many efforts have been made to observe and understand the condensation patterns as well as to develop correlations to predict the heat transfer coefficient of the non-miscible multi-component condensate. Mechanistic models for the condensation of immiscible liquids could not be found in the publically available literature.

Major differences between the condensation rate calculation for single components and multi-component systems forming an immiscible condensate are described below.

- The heat transfer in the vapor phase can be calculated similar to previous work [8], [9]. On the other hand, the heat transfer coefficient of the two-phase condensate is somewhere in between those of pure condensed water and hydrocarbon. A correlation proposed by Bernhardt [50] is used to calculate the average heat transfer coefficient for the condensate.
- At the gas/liquid interface, all gaseous components need to be in thermodynamic equilibrium with the liquid phase. In other words, the composition within the liquid hydrocarbons is in equilibrium with the vapor at the interface. An additional calculation is needed to determine the composition of vapor phase hydrocarbons at the interface. A gradient of the vapor phase concentrations is the driving force for condensation.

### *5.3.1. Calculation method to obtain gaseous hydrocarbons composition at the interface*

The flash calculation is a thermodynamic method to determine composition of a mixture corresponding to a system at equilibrium, at a given temperature and pressure.

If the fluid contains a total amount of 1 mole, then the summation of the total amount of vapor phase (V) and the total amount of liquid phase (L) is equal to 1 (Eq 5-15). By performing a mole balance Eq 5-16 and Eq 5-17 are derived.

$$V + L = 1 \qquad \text{Eq 5-15}$$

$$\sum_{i=1}^n x_i = \sum_{i=1}^n \frac{z_i}{1 + V(K_i - 1)} = 1 \quad \text{Eq 5-16}$$

$$\sum_{i=1}^n y_i = \sum_{i=1}^n \frac{z_i K_i}{1 + V(K_i - 1)} = 1 \quad \text{Eq 5-17}$$

Where;

$V, L$  = Vapor fraction and liquid fraction, respectively, dimensionless

$z_i$  = Total fluid mole fraction of component  $i$ , dimensionless

$x_i, y_i$  = Mole fraction of component  $i$  in liquid and vapor phase, respectively, dimensionless

$K_i$  = Equilibrium coefficient of component  $i$  calculated from Wilson correlation  
Eq 5-14

Flash algorithm was here adopted from Dandekar [3] and Reid *et al.* [102]. The Peng Robinson Equation of State is used. The iterative procedure is illustrated in Figure 97 and is described below.

*Step 1* Input parameters include the total fluid composition, system pressure and temperature.

*Step 2* Calculate the equilibrium coefficient ( $K_i$ ) from Wilson Correlation (Eq 5-14).

*Step 3* Guess the liquid fraction ( $L$ ) and perform mole balance using Eq 5-16 and Eq 5-17. The results will be the composition of each component in vapor and liquid phase,  $y_i$  and  $x_i$ , respectively.

*Step 4* Check if the results meet the criteria, which is the summation of a mole fraction in liquid and vapor phase add up to unity for each phase. If the results do not satisfy the criteria, Liquid fraction (L) is adjusted according to Eq 5-18 [102]. If they do, use these  $x_i$  and  $y_i$  in Peng Robinson EoS to calculate the fugacity coefficient ( $\Phi_i$ ).

$$L_{new} = L_{old} - \frac{\sum_{i=1}^n \{z_i(K_i - 1)\} / [K_i + (1 - K_i)L]}{\sum_{i=1}^n \{z_i(K_i - 1)^2\} / [K_i + (1 - K_i)L]^2} \quad \text{Eq 5-18}$$

*Step 5* Peng Robinson EoS is described in the previous section from (Eq 5-1 to Eq 5-9).

The fugacity coefficient ( $\Phi$ ) of each component in the vapor and liquid phase are calculated. New equilibrium coefficients ( $K_i$ ) are obtained.

*Step 6* At equilibrium, the fugacity of each component in the vapor equals that in the liquid phase. Hence, if the results do not satisfy this criterion, Step 3 is repeated with the new  $K_i$  obtained from the Peng Robinson EoS. On the other hand, if the criterion is met, the final composition at the interface is obtained.

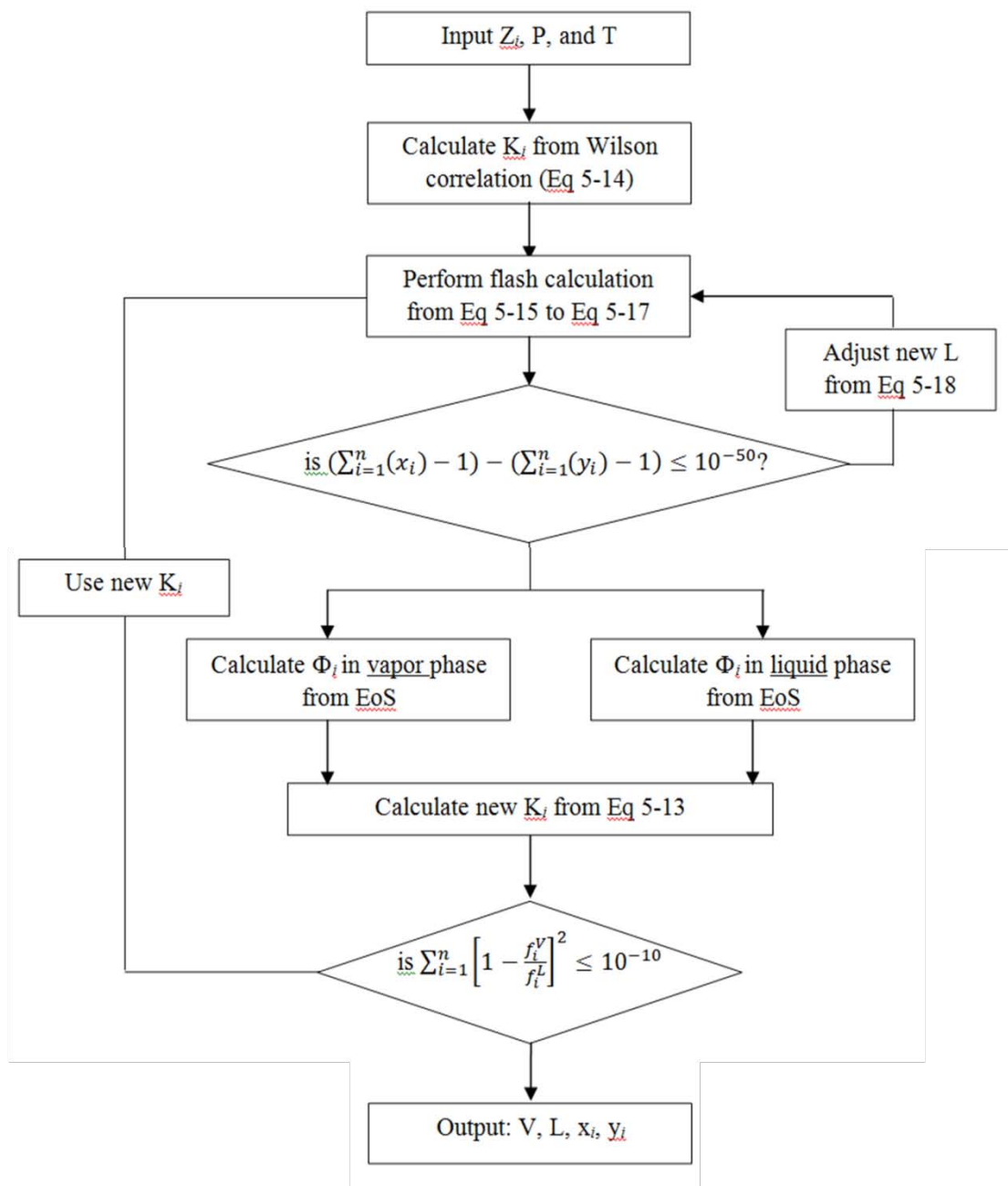


Figure 97: Diagram illustrating the flash calculation for the determination of vapor and liquid composition.

5.3.2. *The approach for co-condensation rates calculation for water and hydrocarbon mixtures*

The total heat flux from the bulk vapor phase to the liquid interface can be written as shown in Eq 5-19.

$$Q_T = Q_g + Q_w + Q_{HC} \quad \text{Eq 5-19}$$

Where:

$Q_T$  = Total heat flux, in  $\text{W}/\text{m}^2$   
 $Q_w, Q_{HC}$  = Heat flux released from the condensation of water vapor and hydrocarbons vapor (Eq 5-20 and Eq 5-21), respectively.

$$Q_w = \dot{m}_w H_{fg,w} \quad \text{Eq 5-20}$$

$$Q_{HC} = \dot{m}_{HC} H_{fg,HC} \quad \text{Eq 5-21}$$

Where:

$\dot{m}_w$  and  $\dot{m}_{HC}$  = Mass flux of water and hydrocarbons across the interface.  
 In other words, those are the condensation rates of water and hydrocarbons, respectively.

$H_{fg,w}$   $H_{fg,HC}$  = Latent heat of vaporization of water vapor and hydrocarbons.

$Q_g$  = Heat flux through the gas boundary layer to the liquid interface

$$Q_g = h_g(T_b^g - T_i^g) \quad \text{Eq 5-22}$$

Where:

$h_g$  = Heat transfer coefficient in the gas phase estimated from the following correlations Eq 5-23, in W/m<sup>2</sup>/K

$$Nu = 0.023Re^{0.8}Pr^{0.4} \quad \text{Eq 5-23}$$

Where:

$Nu$  = Nusselt number,  $(h_g D/k)$

$Re$  = Reynolds number,  $(Dv_g\rho/\mu)$

$Pr$  = Prandtl number,  $(c_p\mu/k)$

$C_p$  = Specific heat capacity, in J/kg

$D$  = Pipe diameter, in m

$k$  = Thermal conductivity of gas phase, in W/m/K

$v_g$  = Gas velocity, in m/s

$\rho$  = Gas density, kg/m<sup>3</sup>

$\mu$  = Gas viscosity, Pa.s

Eq 5-24 is used to calculate the condensation rates of water in which the difference of mass fraction in the bulk and at the interface is the driving force of the condensation. The same approach is also used for each hydrocarbon (Eq 5-25). The vapor

compositions of hydrocarbons at the interface are obtained from the flash calculation as described previously.

$$\dot{m}_w = \rho_w \beta_{g,w} (x_{w,b}^g - x_{w,i}^g) \quad \text{Eq 5-24}$$

$$\dot{m}_{HC} = \rho_{HC} \beta_g (y_{HC,b}^g - y_{HC,i}^g) \quad \text{Eq 5-25}$$

Where:

$\dot{m}_w$  = Condensation rate of water, mL/m<sup>2</sup>/s

$\rho_w$  = Liquid density of water, kg/m<sup>3</sup>

$\beta_{g,w}$  = Mass transfer coefficient of water calculated from Eq 5-26 and Eq 5-27, in m/s

$\beta_{g,HC}$  = Mass transfer coefficient of each hydrocarbon calculated from Eq 5-26 and Eq 5-27, in m/s

$y_{w,b}^g, y_{w,i}^g$  = Mass fraction of water vapor at bulk and vapor/condensate interface, respectively.

$y_{HC,b}^g, y_{HC,i}^g$  = Mass fraction of water vapor at bulk and vapor/condensate interface, respectively.

$$\rho_g \beta_g = \frac{h_g}{C_p} Le^{2/3} \quad \text{Eq 5-26}$$

$$Le = \frac{k_g}{\rho_g C_p D} \quad \text{Eq 5-27}$$

Where:

$Le$  = Lewis number, dimensionless

The total amount of heat ( $Q_T$ ) is carried from the gas-liquid interface through a series of thermal resistances, such as the pipe wall, layers of insulation, etc., to the outside environment.

In previous work, heat transfer from the vapor/liquid interface to the outside environment was considered only to be taking place through water droplets. Heat flux was calculated based on the dropwise condensation when only water is present [8], [9].

On the other hand, heat transfer through only a hydrocarbon layer is calculated according to laminar film type condensation, using Eq 5-28 [104].

$$h_{HC} = 0.954 \left( \frac{k_{HC}^3 \rho_{HC}^2 g H_{fg,HC}}{\mu_{HC} D (T_i - T_w^i)} \right)^{0.25} \quad \text{Eq 5-28}$$

Where:

$h_{HC}$  = Heat transfer coefficient of condensed hydrocarbons, in W/m<sup>2</sup>/K

$k_{HC}$  = Liquid thermal conductivity of condensed hydrocarbons, in W/m/K

$g$  = gravitational acceleration, in m/s<sup>2</sup>

$\mu_{HC}$	=	Liquid viscosity of condensed hydrocarbons, in Pa.s
$D$	=	Pipe diameter, in meter
$\rho_{HC}$	=	Liquid density of condensed hydrocarbons, in kg/m <sup>3</sup>
$T_i$	=	Vapor/Liquid interfacial temperature, in °C
$T_w^i$	=	Inner wall temperature, in °C

The heat conducted through the pipe wall:

$$Q_T = \frac{k_w}{\delta_w} (T_w^i - T_w^o) \quad \text{Eq 5-29}$$

The heat finally goes through the insulation layer (if there is any):

$$Q_T = \frac{k_l}{\delta_l} (T_w^o - T^o) \quad \text{Eq 5-30}$$

Thus, heat flux from the vapor/liquid interface to the outside surrounding is:

$$Q_T = \frac{T_i^g - T^o}{\frac{1}{h_f} - \frac{k_w}{\delta_w} - \frac{k_l}{\delta_l}} \quad \text{Eq 5-31}$$

Where:

$Q_T$	=	The total heat flux, in W/m <sup>2</sup>
$T_i^g$	=	The interfacial temperature, in Kelvin

$T^o$	=	The outside environment temperature, in Kelvin
$T_w^o$	=	The outer wall surface temperature, in Kelvin
$h_f$	=	Heat transfer coefficient of condensate mixture (water and hydrocarbons), in W/m <sup>2</sup> /K
$k_w$	=	Thermal conductivity of pipe wall, in W/m/K
$k_l$	=	Thermal conductivity of insulation layer, in W/m/K
$\delta_w$	=	Thickness of pipe wall, in m
$\delta_l$	=	Thickness of insulation layer, in m

The heat transfer coefficient of condensate mixture is calculated based on what Bernhardt proposed [50]:

$$h_f = \frac{\dot{m}_w h_w + \dot{m}_{HC} h_{HC}}{\dot{m}_w + \dot{m}_{HC}} \quad \text{Eq 5-32}$$

Where:

$\dot{m}_w$	=	Condensation rate of water, mL/m <sup>2</sup> /s
$\dot{m}_{HC}$	=	Condensation rate of hydrocarbons, mL/m <sup>2</sup> /s

The calculation steps are schematically shown in Figure 98.

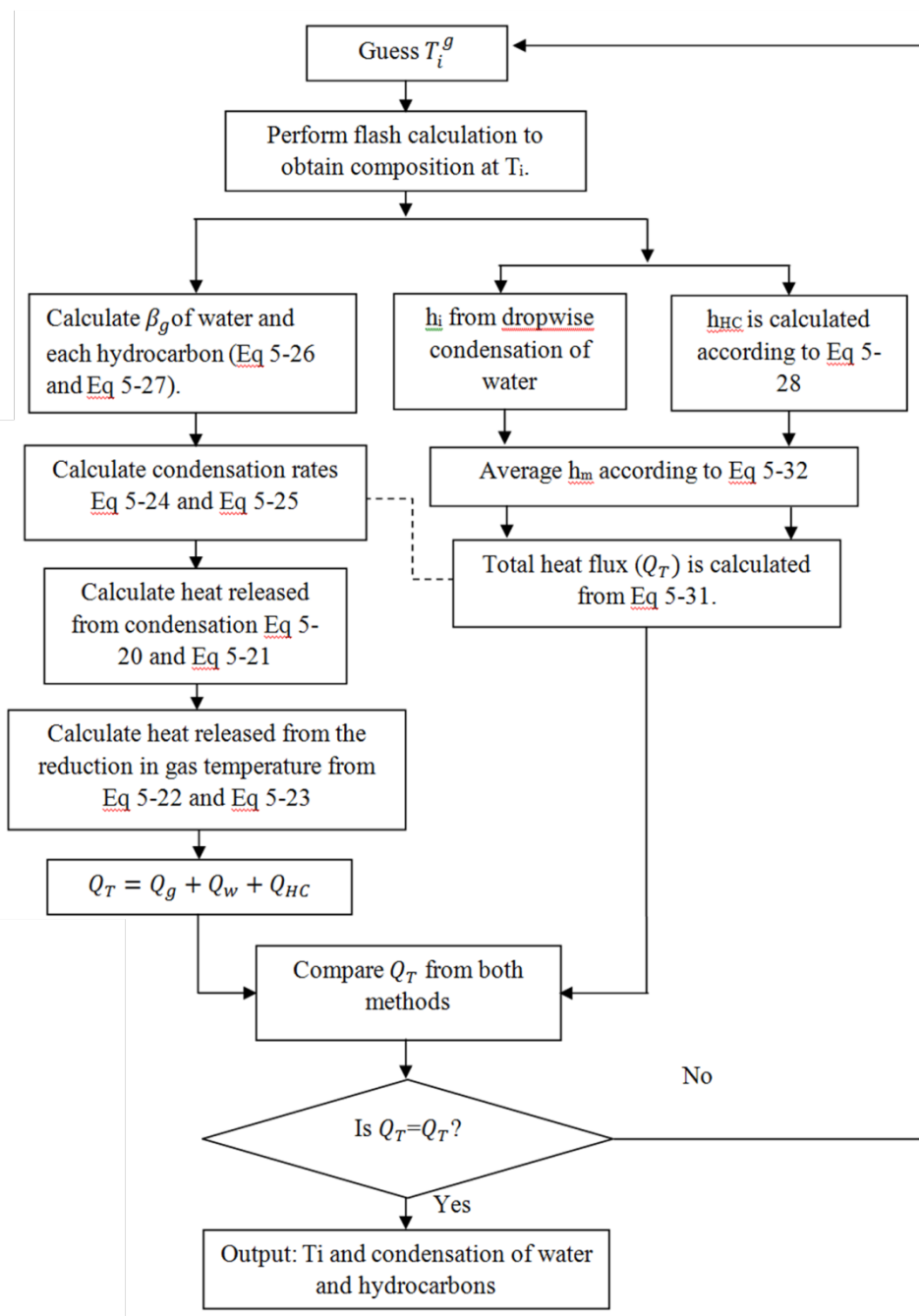


Figure 98: Schematic diagram for condensation rate calculation steps.

### 5.3.3. Comparison with the experiments

Experiments were conducted in the customized glass condenser as explained in section 4.2.2. The main purpose of those experiments was to investigate the corrosion behavior. Yet, condensed liquids were collected and recorded throughout the experiments. It was impossible to conduct the condensation test of water and multiple hydrocarbons. The vapor phase comprised of water vapor, hydrocarbon vapor, and CO<sub>2</sub> as the balance. In these experiments, water vapor partial pressure was independent of the liquid composition (water to hydrocarbon ratio) and was a function of only temperature.

- Calculation of vapor temperature profile along the condenser

Since the experimental design allowed only the integrated condensation rate to be measured, one cannot directly determine the condensation rate at a specific location where the carbon steel samples were. A straight pipe heat transfer correlation was employed to determine the temperature drop along the condenser. A detailed calculation was described in the literature [105]. A final equation is shown in Eq 5-33. The average heat transfer coefficient within a pipe for a laminar flow regime was suggested [106] as Eq 5-34.

$$T_g(x) = T_{liq} - (T_{liq} - T_{g,in}) \exp\left(\frac{-2\pi r x \bar{h}}{m c_p}\right) \quad \text{Eq 5-33}$$

$$\bar{h} = \frac{k}{d} \left[ 3.65 + \frac{0.0668 Re Pr (d/L)}{1 + 0.04 [Re Pr (d/L)]^{2/3}} \right] \left[ \frac{\mu}{\mu_w} \right]^{0.14} \quad \text{Eq 5-34}$$

Where:

$T_g(x)$	=	Vapor temperature at axial position $x$ , in °C
$T_{liq}$	=	Cooling water temperature, in °C
$T_{g,in}$	=	Vapor temperature at inlet of the condenser, in °C
$x$	=	Axial position, in m
$m$	=	Mass flow rate, in kg/s
$c_p$	=	Specific heat capacity of vapor, in kJ/kg/°C
$\bar{h}$	=	Average heat transfer coefficient of vapor in a tube, in W/m <sup>2</sup> /°C
$k$	=	Thermal conductivity of vapor, in W/m/°C
$d$	=	Tube diameter, in m
$Re$ and $Pr$	=	Reynolds number and Prandtl number, dimensionless
$L$	=	Total length of condenser, in m
$\mu$ and $\mu_w$	=	Vapor viscosity at $T_g$ and wall temperature, respectively, in Pa.s

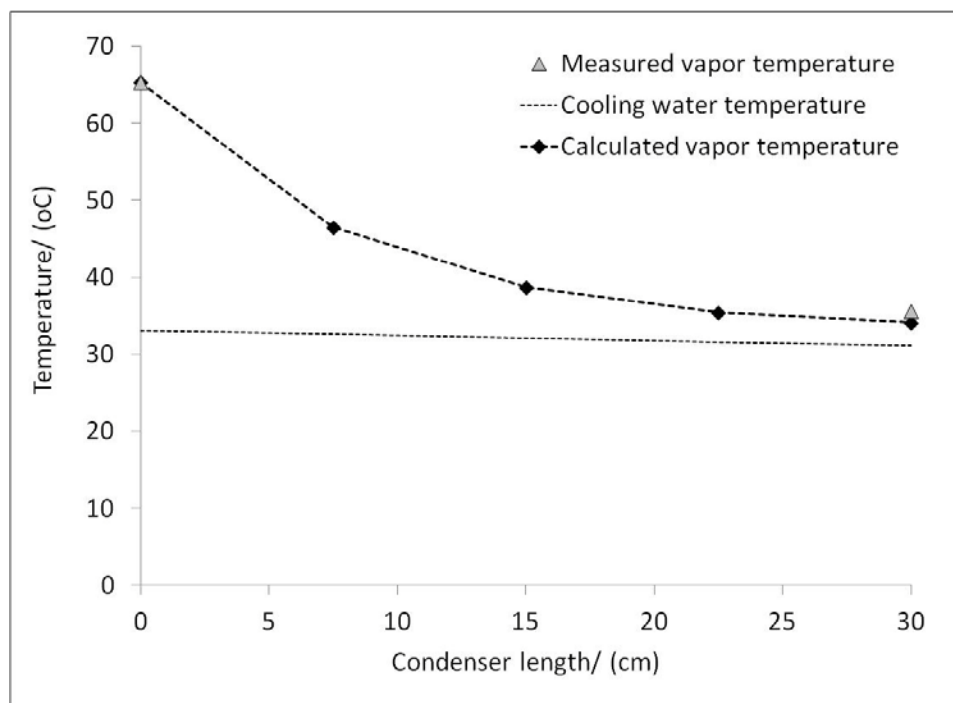


Figure 99: Vapor temperature profile along the length of condenser and the comparison with the measurement.

An example of the calculated temperatures along the condenser length are plotted in Figure 99 and fit well with the gas temperature measurements at the inlet ( $T_{\text{gas,inlet}}$ ) and outlet ( $T_{\text{gas,outlet}}$ ). For all of the experiments Figure 100 summarizes the difference between the measurements of the outlet temperature and the calculated values; 75% fall within a difference of 2°C and 90% fall within 3°C.

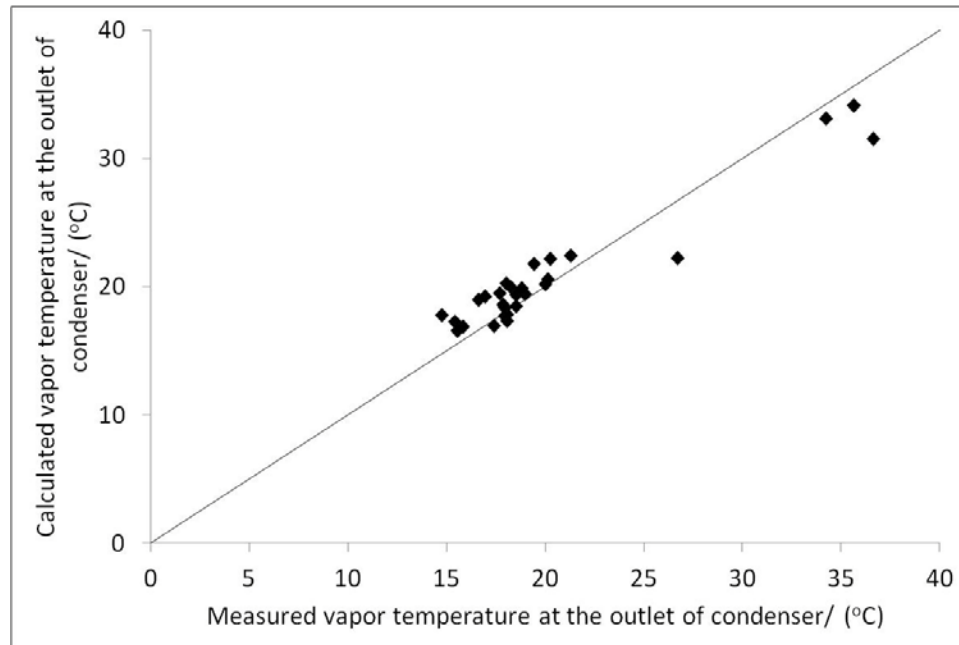


Figure 100: Difference in the calculated and the measured vapor temperature at the outlet of condenser.

- Comparison of the integrated condensation rate from the measurement and calculation

Subsequently, the condensation rate was calculated based on the temperature difference between the calculated vapor temperature and the cooling water temperature ( $T_{cw}$ ). Predicted condensation rates, integrated over the length of the condenser, are plotted against the actual measurements in the parity plots shown in Figure 101 and Figure 102. The good overall agreement indicates that the water condensation rates (WCR) on upstream and downstream samples were properly calculated. The correlation proposed by Bernhardt *et al.* [50] was accepted and used in the co-condensation rate prediction model. The calculation fitted reasonably well within 30%. For the water case,

one may argue that the calculation over-predicted the experimental results. However, it should be pointed out that the experiments contain an uncertainty, especially at the lower end of condensation rates due to the small volume of condensed water collected.

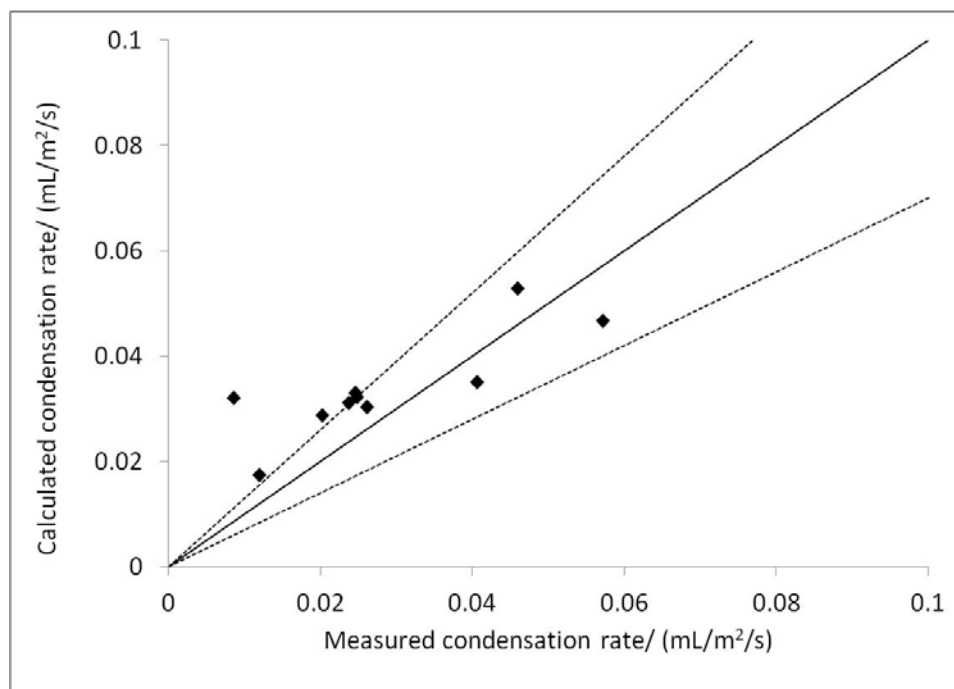


Figure 101: Comparison between the measurement and the predicted value of the integrated water condensation rate in a co-condensation scenario.

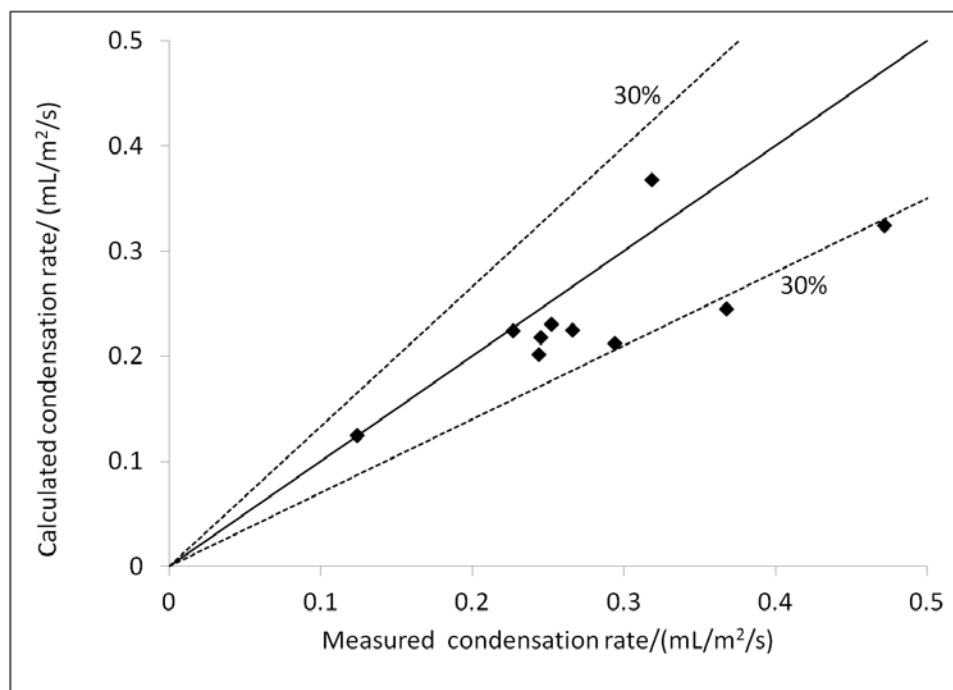


Figure 102: Comparison between the measurement and the predicted values of the integrated n-heptane condensation rate in a co-condensation scenario.

#### 5.3.4. Parametric study

The influence of various parameters (temperature gradient, total pressure, and gas velocity) on the prediction of water condensation rate was described previously [9]. In the present study, hydrocarbons are included in the calculations. Table 13 shows the examples of gas composition used for the present illustration of how the model performs. Water was assumed to be saturated in all cases and its vapor pressure is a function of bulk gas temperature. Hence, the amount of water is the same in all cases. Gas 1 considers no other hydrocarbons except methane. Gas 2 and Gas 3 represent two gases with different

composition. Gas 2 is slightly heavier than Gas 3 as it contains a greater amount of the heavier components.

Figure 103 shows the effect of temperature difference between bulk gas and outside temperature on the water condensation rate of Gas 1 and water/hydrocarbons co-condensation rate of Gas 2. Water condenses slightly less during the co-condensation in comparison to the pure water condensation system. Rates of each hydrocarbon that condense are shown in Figure 104.

When the vapor phase contains other condensable components, the properties of gas phase change so that the heat transfer coefficient of the gas phase increases. Thus, the difference between the bulk gas and the interfacial temperature becomes smaller.

Additionally, the diffusivity of water in the co-condensation system is lower than that in the pure water condensation system. Mass transfer coefficient of water in the mixture decreases. Consequently, water condensation rate decreases. However, only slight decrease in water condensation rate is experienced in the two cases described above because the latent heat of vaporization of water is significantly higher than that of hydrocarbons.

When a lighter gas, Gas 3, is considered, the hydrocarbon phase does not condense unless the temperature difference is high enough as shown in Figure 105. In this case, the presence of hydrocarbons is not significant enough to reduce the water condensation rate.

Table 13: Example of gas composition for co-condensation calculation in Figure 103 and Figure 104 ( $T_b = 70^\circ\text{C}$  and Total pressure = 30 bar)

Component	Gas 1		Gas 2		Gas 3	
	%Mol	Partial pressure (bar)	%Mol	Partial pressure (bar)	%Mol	Partial pressure (bar)
CO <sub>2</sub>	15	4.45	15	4.45	15	4.45
N <sub>2</sub>	0	0	0	0	0	0
H <sub>2</sub> S	0	0	0	0	0	0
C <sub>1</sub>	85	25.24	70	20.78	80	23.75
C <sub>2</sub>	0	0	5	1.48	1	0.30
C <sub>3</sub>	0	0	5	1.48	1	0.30
C <sub>4</sub>	0	0	2.5	0.74	1.2	0.36
C <sub>5</sub>	0	0	1	0.30	1.2	0.36
C <sub>6</sub>	0	0	0.5	0.15	0.5	0.15
C <sub>7</sub>	0	0	0.5	0.15	0.05	0.015
C <sub>8</sub>	0	0	0.5	0.15	0.05	0.015
Water	Sat.	0.31	Sat.	0.31	Sat.	0.31

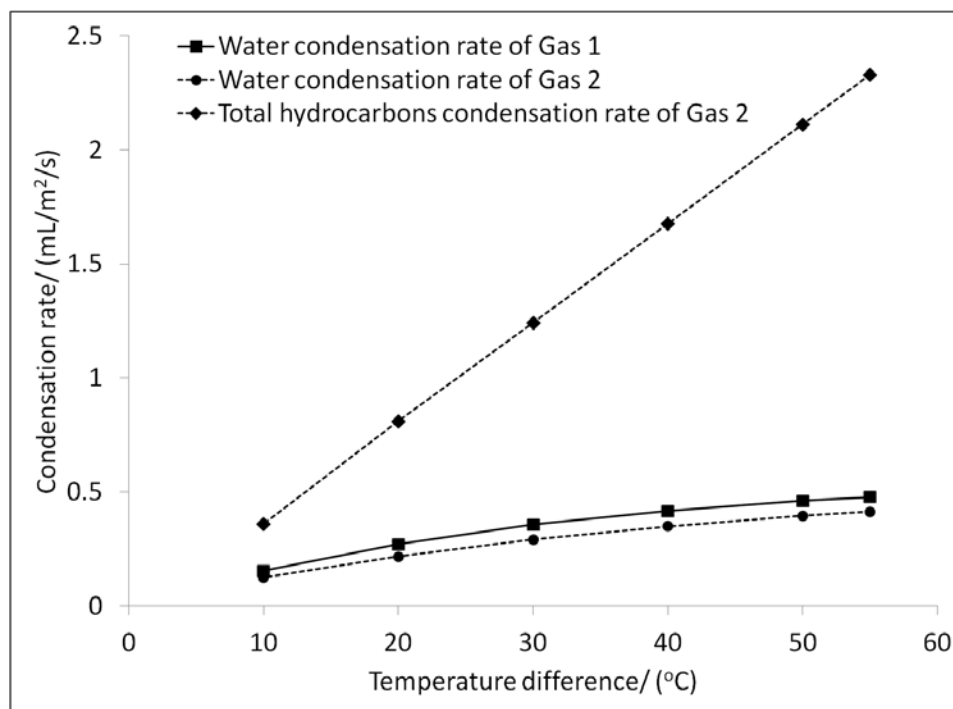


Figure 103: Effect of temperature gradient on condensation rate of water and hydrocarbons of Gas 1 and Gas 2; Total Pressure = 30 bar, Pipe Diameter = 0.2 m,  $v_g = 1$  m/s, and  $T_b = 70^\circ\text{C}$ .

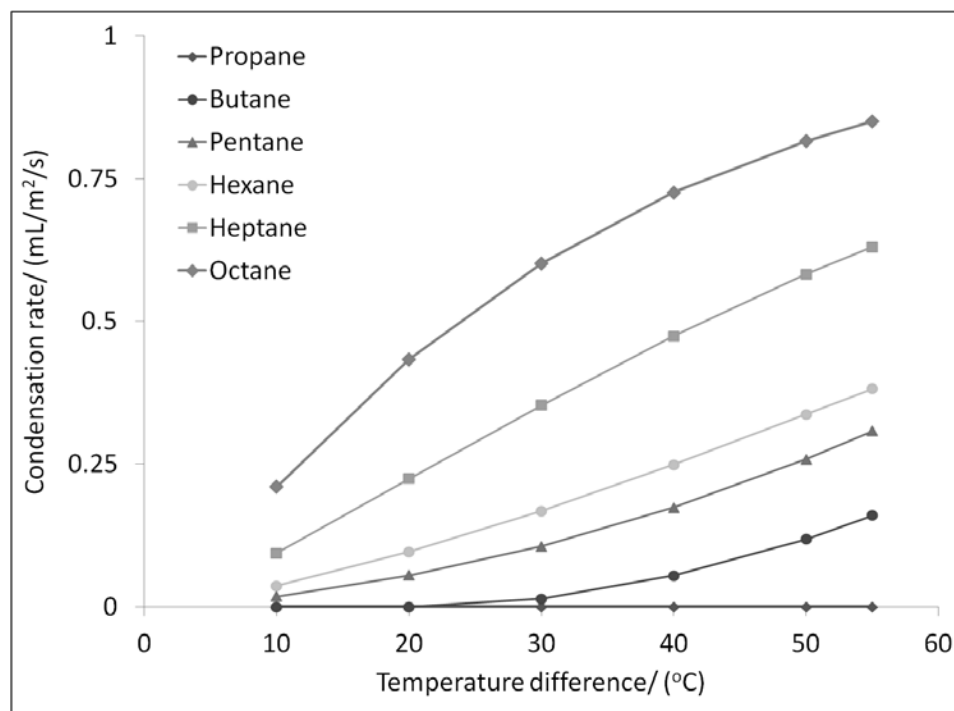


Figure 104: Effect of temperature gradient on condensation rate of each hydrocarbon of Gas 2; Total Pressure = 30 bar, Pipe Diameter = 0.2 m,  $v_g = 1$  m/s, and  $T_b = 70^\circ\text{C}$ .

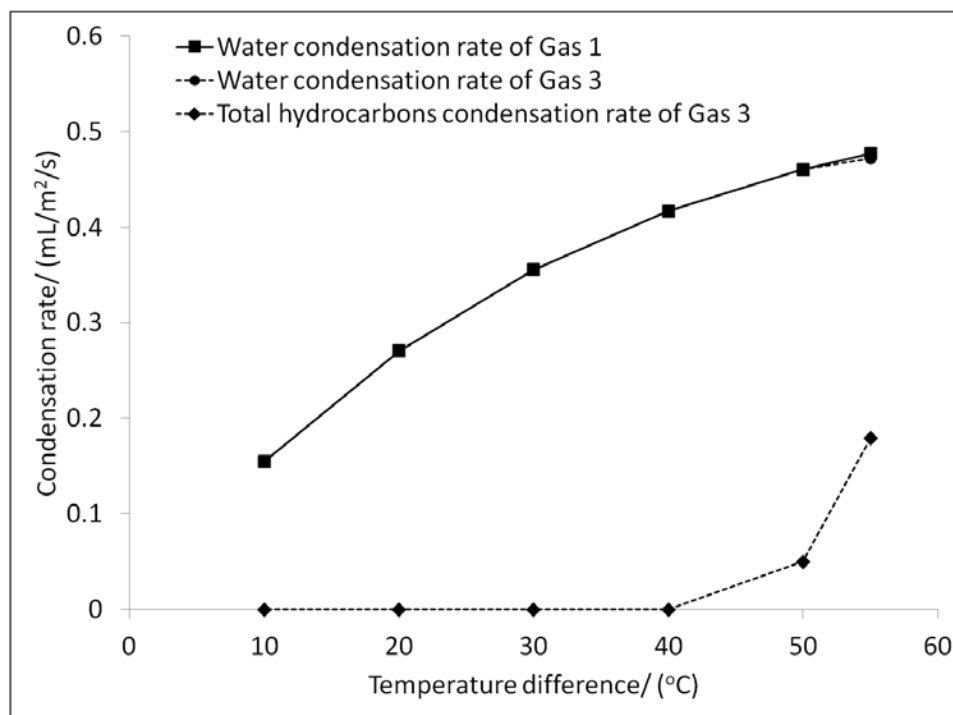


Figure 105: Effect of temperature gradient on condensation rate of water and hydrocarbons of Gas 1 and Gas 3; Total Pressure = 30 bar, Pipe Diameter = 0.2 m,  $v_g = 1$  m/s, and  $T_b = 70^\circ\text{C}$ .

#### 5.4. Implementation into TOPCORP

TOPCORP (Top of the line corrosion prediction software) is the fully mechanistic model developed within the TLC-Joint Industry Project at Ohio University, as one of the main deliverables to the industrial sponsors. It incorporates efforts based on research work dating back to 2003 from TLC-JIP phase I and phase II.

However, Kaewpradap *et al.* [43] showed that in some field conditions, a discrepancy between the calculation and the inspection result is seen (typically at the pipe entrance). It was suggested that the proposed reason was co-condensation of hydrocarbons and water and/or that the water vapor may not have been saturated when

entering the line. Two calculation modules developed in this study address this aspect and are now being incorporated into TOPCORP. Figure 106 schematically shows how these two new modules were implemented to the TOPCORP.

- Users decide whether to include the two additional calculation modules. To successfully utilize those two modules, additional parameters are required relating to the total fluid composition. Hence, if this information is unavailable, it is impossible to apply the two modules. If user chooses not to include the co-condensation and a thermodynamic calculation, water vapor is assumed to be saturated at the entrance. In this case, the condensation rate of only water is calculated. On the other hand, if the total fluid composition is available and user chooses to determine if the water is saturated or to verify the likelihood of co-condensation, the phase envelope will be calculated.
- Temperature and pressure profiles of the pipeline are generated and compared with the phase envelope. If the temperature and pressure do not reach the dew line of water, no water condensation rate is predicted and TLC is not a concern. As temperature/pressure further decrease, a dew line of either water or hydrocarbons may be reached. If the dew line of hydrocarbons is reached first, water is not condensing and TLC is not a concern. If the dew line of water is reached first, the condensation rate of only water is calculated. Co-condensation of water and hydrocarbons will be achieved when the condition in the pipeline crosses the dew points of both water and hydrocarbons.

- When a co-condensation rate is calculated, a water condensation rate will be less than that from the pure water system.
- New water condensation rate is used in the corrosion rate prediction model.

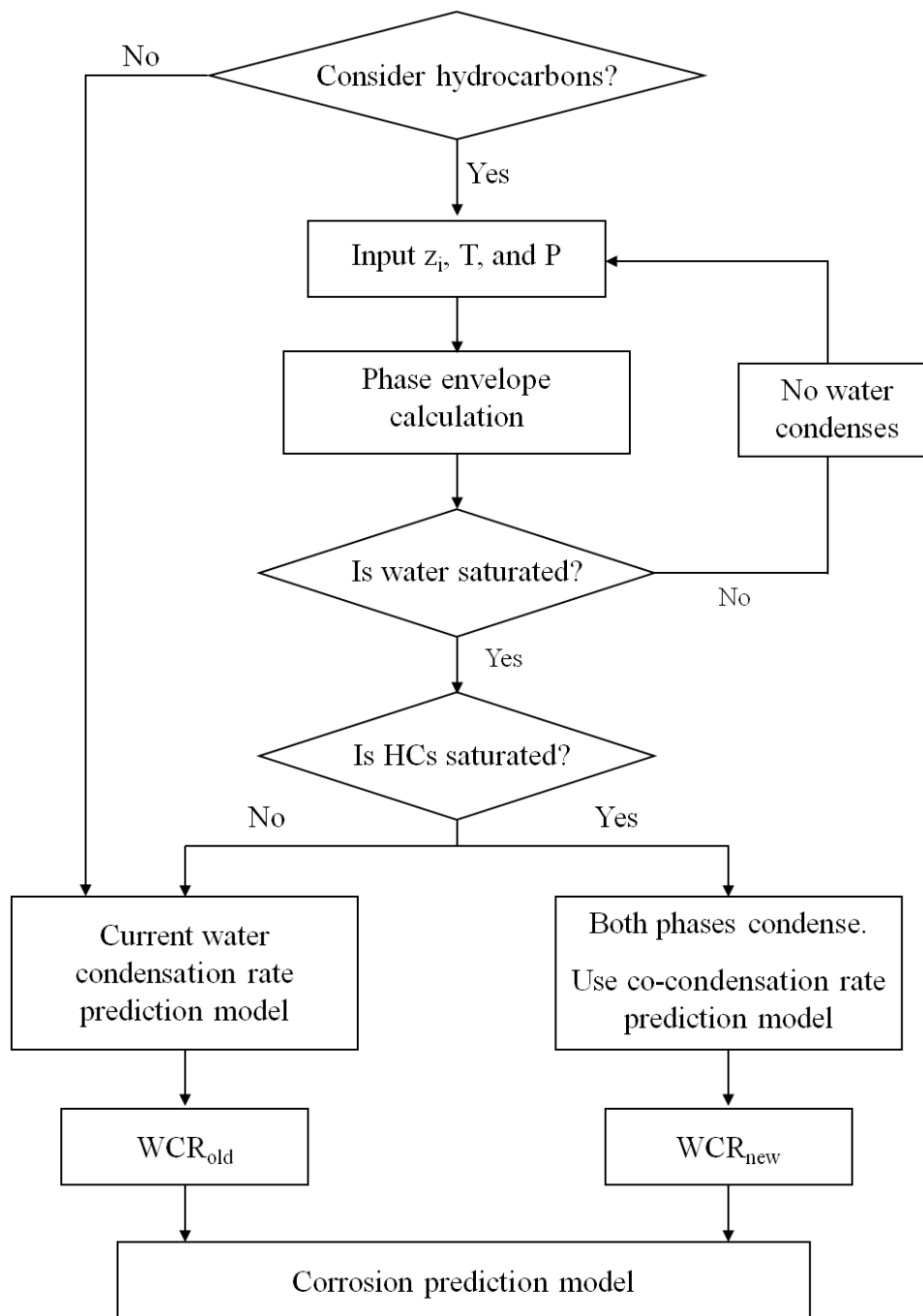


Figure 106: Schematic diagram of the implementation of co-condensation into TOPCORP

## CHAPTER 6: CONCLUSIONS

The influence of the co-condensation of water and straight chain hydrocarbons on Top-of-the-Line Corrosion (TLC) was investigated. The study focused on four aspects:

- **Wettability and co-condensation process monitoring:** the main conclusion is that, no matter the conditions, liquid water always seemed to be preferentially in contact with the hydrophilic steel surface.
- **Influence of co-condensation on Top-of-the-Line Corrosion (TLC).** The results showed that the corrosion rate in co-condensation environments was generally lower than that in pure water systems and less influenced by the water condensation rate.
- **Determination of hydrocarbon and water condensation rates:** The presence of condensing hydrocarbons affects the heat and mass transfer of a condensing system. Heat loss is shared between water and the hydrocarbon and less heat is consequently available for water condensation. A model was developed based on heat and mass transfer theory and was validated with experimental data. However, the predicted water condensation rate is only slightly decreased when the condensing hydrocarbons are considered.
- **The modification to the Top-of-the-Line Corrosion Prediction model (TOPCORP):** The multi-component condensation rate model was implemented in TOPCORP. Additionally, a thermodynamic phase diagram for water and hydrocarbons was developed and validated to predict the condition when water condenses and when TLC is encountered.

## CHAPTER 7: PROPOSALS FOR FUTURE WORK

Effects of condensing hydrocarbons on Top of the Line Corrosion were studied.

Yet, more work is needed.

- 1) The condensed liquid can be stagnant droplets or in the form of sliding rivulets, depending upon the hydrodynamics of the gas/liquid flow [9]. Consequently, corrosion behavior is probably different. The current experimental setups are limited to the laminar flow regime or stagnant. It would be valuable to examine corrosion behavior when water and hydrocarbons condense and “slide” along the pipeline surface.
- 2) Organic liquids with different molecular structures are not naturally present in the wet gas pipeline but may be encountered. For instance, aromatic components are added into the pipeline to remove sulfur deposited in an extremely sour system. These compounds are volatile and they can condense along with the water vapor. The wettability of aromatic compounds towards the steel could differ from aliphatic hydrocarbons due to the presence of the  $\pi$ -bonding.
- 3) Acetic acid is another corrosive species that has been reported to significantly increase TLC rate. Its solubility in condensed water differs from that in hydrocarbons phase. The interaction of acetic acid between aqueous phase and hydrocarbon phase could change the corrosion behavior.
- 4) Another direction that future research could focus on is how hydrocarbons influence the behavior of chemicals added into the pipeline such as inhibitors. Volatile corrosion inhibitors are being investigated as an effective method to

control TLC without disturbing the production process. The solubility of these compounds in water can either be lower or higher than in hydrocarbons. If the solubility of inhibitive compounds is lower in hydrocarbons, it is possible for them to be washed by or partition into hydrocarbons. Hence, less inhibitor is available to protect the pipeline and *vice versa*, if the solubility of inhibitive compounds is higher in hydrocarbons, it is possible that the efficiency of this inhibitor will be improved.

**LIST OF REFERENCES**

- [1] S. Mokhatab, W. A. Poe, and J. G. Speight, *Handbook of Natural gas transmission and processing*. Gulf Professional Publishing, 2006.
- [2] D. Webster, "Pipeline Construction Drivers, Corrosion Costs and Engineering Issues," in *Proc. NAPCA Convention*, 2010.
- [3] A. Y. Dandekar, *Petroleum reservoir rock and fluid properties*, 1<sup>st</sup> ed. CRC Press, 2006, pp. 257-302.
- [4] R. Paillassa, M. Dieumegard, and M. M. Estavoyer, "Corrosion control in the gathering system at LACQ sour gas field," in *Proc. 2nd International congress on metallic corrosion*, 1963, pp. 410-417.
- [5] C. D. Waard, U. Lotz, and D. E. Milliams, "Predictive model for CO<sub>2</sub> corrosion engineering in wet natural gas pipelines," *Corrosion Engineering*, vol. 47, no. 12, pp. 976-985, 1991.
- [6] F. Vitse, K. Alam, and Y. Gunaltun, D., "Semi-empirical model for prediction of the top of the line corrosion risk," in *Proc. Corrosion*, Denver, CO, 2002, paper no. 02245.
- [7] F. Vitse, S. Nestic, and Y. Gunaltun, "Mechanistic model for the prediction of Top-of-the-Line Corrosion risk," *Corrosion*, vol. 59, no. 12, pp. 1075-1084, 2003.
- [8] Z. Zhang, D. Hinkson, M. Singer, H. Wang, and S. Nestic, "A mechanistic model of Top-of-the-Line Corrosion," in *Proc. Corrosion*, Nashville, TN, 2007, paper no. 07556.
- [9] Z. Zhang, "A study of Top of the line corrosion under dropwise condensation," Ph.D. Dissertation, Russ College of Engineering, Department of Chemical Engineering, Ohio University, Athens, OH, 2008.
- [10] Y. Gunaltun, D. Supriyatman, and J. Achmad, "Top of line corrosion in multiphase gas lines. A case history," in *Proc. Corrosion*, San Antonio, TX, 1999, paper no. 99036.
- [11] Y. Gunaltun, S. Punpruk, M. Thammachart, and P. Tanaprasertsong, "Worst case top of the line corrosion: Cold spot corrosion," in *Proc. Corrosion*, San Antonio, TX, 2010, paper no. 10097.

- [12] M. A. Edwards and B. Cramer, "Top of Line Corrosion - Diagnosis, Root Cause Analysis and Treatment," in *Proc. Corrosion*, Orlando, FL, 2000, paper no. 00072.
- [13] A. Babakr and A. Bairamov, "Top of line corrosion in industrial wastewater pipelines: Here are the causes and the solution," *Hydrocarbon processing*, vol. 82, no. 9, pp. 93–97, 2003.
- [14] M. Singer, D. Hinkson, Z. Zhang, H. Wang, and S. Nestic, "CO<sub>2</sub> top of the line corrosion in presence of acetic acid: A parametric study," in *Proc. Corrosion*, Atlanta, GA, 2009, paper no. 09292.
- [15] J. Amri, E. Gulbrandsen, and R. P. Nogueira, "Effect of acetic acid on propagation and stifling of localized attacks in CO<sub>2</sub> corrosion of carbon steel," in *Corrosion*, Atlanta, GA, 2009, paper no. 09284.
- [16] Y. H. Sun, T. Hong, and W. P. Jepson, "Pipeline corrosion under wet gas conditions," *Materials Performance*, vol. 40, no. 10, pp. 48-52, 2001.
- [17] A. Dugstad, "Mechanism of protective film formation during CO<sub>2</sub> corrosion of carbon steel," in *Proc. Corrosion/98*, New Orleans, LA, 1998, paper no. 31
- [18] Y. Yang, B. Brown, N. Srdjan, M. E. Gennaro, and B. Molinas, "Mechanical strength and removal of a protective iron carbonate layer formed on mild steel in CO<sub>2</sub> corrosion," in *Proc. Corrosion*, San Antonio, TX, 2010, paper no. 10383.
- [19] M. Gao, X. Pang, and K. Gao, "The growth mechanism of CO<sub>2</sub> corrosion product films," *Corrosion Science*, vol. 53, no. 2, pp. 557-568, 2011.
- [20] B. Pots and E. Hendriksen, "CO<sub>2</sub> corrosion under scaling conditions - the special case of top of line corrosion in wet gas pipelines." in *Proc. Corrosion*, Orlando, FL, 2000, paper no.00031.
- [21] Y. Gunaltun and A. Belghazi, "Control of top of the line corrosion by chemical treatment," in *Proc. Corrosion*, Houston, TX, 2001, paper no. 01033.
- [22] M. Singer, S. Nestic, and Y. Gunaltun, "Top of the line corrosion in presence of acetic acid and carbon dioxide," in *Proc. Corrosion*, New Orleans, LA, 2004, paper no. 04377.
- [23] A. Camacho, "CO<sub>2</sub> Top of the line corrosion in the presence of H<sub>2</sub>S," M.S. Thesis, Russ College of Engineering, Department of Chemical Engineering, Ohio University, Athens, OH, 2006.

- [24] A. Camacho, M. Singer, B. Brown, and S. Nestic, "Top of the line corrosion in H<sub>2</sub>S/CO<sub>2</sub> environments," in *Proc. Corrosion*, New Orleans, LA, 2008, paper no. 08470.
- [25] D. Hinkson, M. Singer, Z. Zhang, and N. Srdjan, "A study of the chemical composition and corrosivity of the condensate for top of the line CO<sub>2</sub> corrosion," in *Proc. Corrosion*, New Orleans, LA, 2008, paper no. 08466.
- [26] D. V. Pugh, S.L. Asher, J. Cai, J. Sisak, J.L. Pacheco, F. Che Ibrahim, E.J. Wright, A. Dhokte, S. Venaik, D. Robson, "Top-of-line corrosion mechanism for sour wet gas pipelines," in *Proc. Corrosion*, Atlanta, GA, 2009, paper no. 09285.
- [27] R. Nyborg, A. Dugstad, and T. G. Martin, "Top of line corrosion with high CO<sub>2</sub> and traces of H<sub>2</sub>S," in *Proc. Corrosion*, Atlanta, GA, 2009, paper no. 09283.
- [28] J. Amri, E. Gulbrandsen, and R. P. Nogueira, "Role of acetic acid in CO<sub>2</sub> top of the line corrosion of carbon steel," in *Proc. Corrosion*, Houston, TX, 2011, paper no. 11329.
- [29] M. Singer, T. Pojtanabuntoeng, U. Kaewpradap, N. Yaakob, and S. Nestic, "Top of the Line Corrosion Joint Industry Project Experimental Results and Modeling Updates," Athens, Ohio, March 2012.
- [30] V. Fajardo, "Localized CO<sub>2</sub> corrosion in the presence of organic acid," M.S. Thesis, Russ College of Engineering, Department of Chemical Engineering, Ohio University, Athens, OH, 2011.
- [31] M. Singer, B. Brown, A. Camacho, and S. Nestic, "Combined effect of carbon dioxide, hydrogen sulfide, and acetic acid on bottom-of-the-line corrosion," *Corrosion*, vol. 67, no. 1, pp. 1-16, 2011.
- [32] D. Erickson, E. Buck, and J. Kolts, "Corrosion inhibitor transport in a wet-gas pipeline," *Material Performance*, vol. 32, no. 6, pp. 49-56, 1993.
- [33] E. N. Freeman, and G. C. Williamson, "New technology effective in reducing top-of-the-line corrosion rate," *Pipeline and Gas Journal*, vol. 212, no. 1, pp. 44-46, 2007.
- [34] I. Jevremovic, V.B. Miskovic-Stankovic, M. Achour, D. Blumer, T. Baugh, M. Singer, and S. Nestic., "A novel method to mitigate the top of the line corrosion in wet gas pipelines by corrosion inhibitor within a foam matrix," in *Proc. Corrosion*, Salt Lake City, UT, 2012, paper no. 01403.

- [35] M. H. Anchor, D. J. Blumer, and T. D. Baugh, "Controlling top of the line corrosion in hydrocarbon pipelines," U.S. Patent 0304018, December, 2010.
- [36] R. L. Martin, "Inhibition of vapor phase corrosion in gas pipelines," in *Proc. Corrosion*, New Orleans, 1997, paper no. 337.
- [37] G. Schmitt, M. Scheepers, and G. Siegmund, "Inhibition of the top-of-the-line corrosion under stratified flow," in *Proc. Corrosion*, Houston, TX 2001, paper no. 01032.
- [38] R. Nyborg, A. Dugstad, and L. Lunde, "Corrosion and glycol distribution in a large wet-gas pipeline," *Material Performance*, vol. 32, no. 9, pp. 57-61, 1993.
- [39] R. Nyborg and A. Dugstad, "Top of line corrosion and water condensation rates in wet gas pipelines," in *Proc. Corrosion*, Nashville, TN, 2007, paper no. 07555.
- [40] J. D. Garber, F. Farshad, H. Li, K. M. Yap, and R. Winters, "A corrosion predictive model for use in flowlines and pipelines integrity management," in *Proc. Corrosion*, New Orleans, LA, 2008, paper no. 08164.
- [41] J. D. Garber, F. F. Farshad, J. R. Reinhardt, and V. Tadepally, "A comprehensive model for predicting internal corrosion rates in flowlines and pipelines," in *Proc. SPE International Symposium on Oilfield Corrosion*, 2004, paper no. 87566.
- [42] Y. Gunaltun, U. Kaewpradap, M. Singer, N. Srdjan, S. Punpruk, and M. Thammachart, "Progress in the prediction of top of the line corrosion challenges to predict corrosion rates measured in gas pipelines," in *Proc. Corrosion*, San Antonio, TX, 2010, paper no. 10093.
- [43] U. Kaewpradap, M. Singer, S. Nestic, M. Technology, and S. Punpruk, "Top of the line corrosion Comparison of model predictions with field data," in *Proc. Corrosion*, Salt Lake City, UT, 2012, paper no. 01449.
- [44] C. G. Kirkbride, "Heat transmission by condensing pure and mixed substances on horizontal tubes," *Industrial & Engineering Chemistry*, vol. 25, no. 12, pp. 1324–1331, 1933.
- [45] W. Patterson, J. Weiland, S. Reeburgh, R. King, and R. Huntington, "The condensation of steam and heptane on vertical tubes," *Transactions of the American Institute of Chemical Engineers*, vol. 33, pp. 216–241, 1937.

- [46] E. M. Baker and U. Tsao, "Condensation of vapors on a horizontal tube: Heat transfer coefficient for condensation of vapors of water and nonmiscible organic liquids," *Industrial & Engineering Chemistry*, vol. 32, no. 8, pp. 1115-1121, 1940.
- [47] R. Hazelton and E. M. Baker, "Condensation of vapors of immiscible liquids," *AIChE Journal*, vol. 40, no. 1, pp. 1-28, 1944.
- [48] W. Akers and M. Turner, "Condensation of vapors of immiscible liquids," *AIChE Journal*, vol. 8, no. 5, pp. 587-589, 1962.
- [49] J. A. Sykes and J. M. Marchello, "Condensation of immiscible liquids," *Industrial & Engineering Chemistry Process Design and Development*, vol. 9, no. 1, pp. 63-71, 1970.
- [50] S. H. Bernhardt, J. J. Sheriden, and J. W. Westwater, "Condensation of immiscible mixtures," *AIChE Journal*, vol. 68, no. 118, pp. 21-37, 1972.
- [51] A. B. Ponter and I. G. Diah, "Condensation of vapors of immiscible binary liquids on horizontal copper and polytetrafluoroethylene-coated copper tubes," *Heat and Mass Transfer*, vol. 7, pp. 94-106, 1974.
- [52] R. Sardesai and D. Webb, "Condensation of binary vapours of immiscible liquids," *Chemical Engineering Science*, vol. 37, no. 4, pp. 529-537, 1982.
- [53] O. Fumimaru, K. Shuji, and M. Tokuro, "Condensation of binary vapors of immiscible liquids," *International Journal of Heat and Mass Transfer*, vol. 31, no. 2, pp. 245-250, 1988.
- [54] A. Boyes and A. Ponter, "Condensation of immiscible binary systems," *Chem. Proc. Eng. Heat Transfer Survey*, pp. 26-30, 1972.
- [55] D. Q. Kern, "Condensation of mixed vapors," in *Process Heat Transfer*, 1<sup>st</sup> ed., New York: McGraw-Hill, 1950, pp. 336-373.
- [56] O. Tutkun, "Local rates of heat and mass transfer during condensation of non-eutectic vapours of binary immiscible liquids," *Chemical Engineering and Processing*, vol. 33, pp. 429-436, 1994.
- [57] G. T. Polley and W. F. Calus, "The effect of condensate pattern on heat transfer during the condensation of binary mixtures of vapours of immiscible liquids," in *Proc. 6<sup>th</sup> International Heat Transfer Conference*, Toronto, Canada, 1978, pp. 471-476.

- [58] J. Kim and D. Webb, "Condensation of mixed vapours of hydrocarbons and water in a shell and tube condenser," *Chemical Engineering Research and Design*, vol. 67, no. a, pp. 87–95, 1989.
- [59] J. S. Smart, "Wettability - A major factor in oil and gas system corrosion," *Materials Performance*, vol. 40, no. 4, pp. 54-59, 2001.
- [60] P. Ajmera, W. Robbins, S. Richter, and S. Nestic, "Role of asphaltenes in inhibiting corrosion and altering the wettability of the steel surface," *Corrosion Science*, vol. 67, no. 10, pp. 1-11, 2011.
- [61] F. Ayello, W. Robbins, S. Richter, and S. Nestic, "Crude oil chemistry effects on inhibition of corrosion and phase wetting," in *Proc. 17<sup>th</sup> International Corrosion Congress*, Las Vegas, NV, 2008, paper no. 3149.
- [62] C. N. C. Lam, N. Kim, D. Hui, D. Y. Kwok, M. L. Hair, and A. W. Neumann, "The effect of liquid properties to contact angle hysteresis," *Colloids and Surfaces A: Physicochemical and Engineering Aspects*, vol. 189, no. 1–3, pp. 265-278, 2001.
- [63] D. Y. Kwok and A. W. Neumann, "Contact angle measurement and contact angle interpretation," *Advances in Colloid and Interface Science*, vol. 81, no. 3, pp. 167-249, 1999.
- [64] S. Papavinasam, A. Doiron, T. Panneerselvam, and R. W. Revie, "Effect of hydrocarbons on the internal corrosion of oil and gas pipelines," *Corrosion*, vol. 63, no. 7, pp. 704-712, 2007.
- [65] X. Tang, S. Richter, and S. Nestic, "Study of wettability of different mild steel surface," in *Proc. 17<sup>th</sup> International Corrosion Congress*, Las Vegas, NV, 2008, paper no. 3109.
- [66] U. Lotz, L. van Bodegom, and C. Ouwehand, "The effect of type of oil or gas condensate on carbonic acid corrosion," *Corrosion*, vol. 47, no. 8, pp. 635-644, 1991.
- [67] M. Simon-Thomas, K. G. Jordan, S. E. Lorimer, and P. B. Hebert, "Inhibition of Sweet Corrosion of Subsea Flowlines," in *Proc. Corrosion*, New Orleans, LA, 1998, paper no. 57.
- [68] F. Ayello, "Crude oil chemistry effects on corrosion inhibition and phase wetting in oil-water flow," Ph.D. Dissertation, Russ College of Engineering, Department of Chemical Engineering, Ohio University, Athens, OH, 2010.

- [69] H. J. Choi, "Effect of liquid hydrocarbons on flow-induced sweet corrosion of carbon steel," in *Proc. Corrosion*, New Orleans, LA, 2004, paper no. 04664.
- [70] A. Groysman and N. Erdman, "A study of corrosion of mild steel in mixtures of petroleum distillates and electrolytes," *Corrosion*, vol. 56, no. 12, p. 1266-1271, 2000.
- [71] M. B. Kermani and A. Morshed, "Carbon dioxide corrosion in oil and gas production—a compendium," *Corrosion*, vol. 59, no. 8, p. 659-683, 2003.
- [72] W. Hayduk, E. B. Walter, and P. Simpson, "Solubility of propane and carbon dioxide in Heptane, Dodecane, and Hexadecane," *Journal of Chemical and Engineering Data*, vol. 17, no. 1, pp. 59-61, 1972.
- [73] J. J. Carroll, J. D. Slupsky, and A. E. Mather, "The solubility of carbon dioxide in water at low pressure," *Journal of Physical and Chemical Reference Data*, vol. 20, no. 6, pp. 1201-1209, 1991.
- [74] M. Thammachart, Y. Gunaltun, and S. Punpruk, "The use of inspection results for the evaluation of batch treatment efficiency and the remaining life of the pipelines subjected to top of the line corrosion," in *Proc. Corrosion*, New Orleans, LA, 2008, paper no. 08471.
- [75] T. Pojtanabuntoeng, M. Singer, and S. Nestic, "Water/hydrocarbon co-condensation and the influence on top-of-the-line corrosion," in *Corrosion*, 2011, paper no. 11330.
- [76] R. H. Perry and D. W. Green, "Physical and Chemical Data," in *Perry's Chemical Engineers' Handbook*, 7<sup>th</sup> ed, New York: McGraw-Hill, 1999.
- [77] "DIPPR 801 student database of physical and thermodynamic properties of pure chemicals." [Online]. Available: <http://dippr.byu.edu/students/chemsearch.asp>. [Accessed: 17-May-2011].
- [78] A. Goebel and K. Lunkenheimer, "Interfacial tension of the water/n-alkane interface," *Langmuir*, vol. 13, no. 2, pp. 369-372, 1997.
- [79] X. Tang, "Effect of surface state on water wetting and carbon dioxide corrosion in oil-water two-phase flow," Ph.D. Dissertation, Russ College of Engineering, Department of Chemical Engineering, Ohio University, Athens, OH, 2012.

- [80] T. Segin, J. H. Masliyah, and S. Bhattacharjee, "Molecular dynamics simulation of the rupture of nanometer-sized oil/water interface," in *Proc. International Conference on MEMS, NANO and Smart Systems*, 2005.
- [81] E. Akbarinezhad, F. Rezaei, and J. Neshati, "Evaluation of a high resistance paint coating with EIS measurements: Effect of high AC perturbations," *Progress in Organic Coatings*, vol. 61, pp. 45-52, 2008.
- [82] C. Tsonopoulos, "Thermodynamic analysis of the mutual solubilities of normal alkanes and water," *Fluid Phase Equilibria*, vol. 156, pp. 21-33, 1999.
- [83] T. Pojtanabuntoeng, M. Singer, and S. Nestic, "Top-of-the-Line Corrosion in the presence of hydrocarbon Co-Condensation in Flowing Condition," in *Corrosion*, 2012, no. 1, paper no. 01534.
- [84] Standard practice for preparing, cleaning, and evaluating corrosion test, ASTM standard G1-90, 1999.
- [85] M. Singer, B. Brown, D. Hinkson, Z. Zhang, X. Jiang, and S. Nestic, "Top of the Line Corrosion Experimental Results and Modeling Updates," Athens, Ohio, October, 2006.
- [86] W. Sun, S. Nešić, and R. C. Woollam, "The effect of temperature and ionic strength on iron carbonate ( $\text{FeCO}_3$ ) solubility limit," *Corrosion Science*, vol. 51, no. 6, pp. 1273-1276, Jun. 2009.
- [87] W. Sun and S. Nestic, "Basic revisited: Kinetics of iron carbonate scale precipitation in  $\text{CO}_2$  corrosion," in *Proc. Corrosion*, San Diego, CA, 2006, paper no. 06365.
- [88] E. W. J. van Hunnik, B. F. M. Pots, and E. L. J. A. Hendriksen, "The formation of protective  $\text{FeCO}_3$  corrosion product layers in  $\text{CO}_2$  corrosion," in *Proc. Corrosion* 1996, paper no.6.
- [89] W. Sun and S. Nestic, "Kinetics of corrosion layer formation: part 1-iron carbonate layers in carbon dioxide corrosion," *Corrosion*, vol. 64, no. 4, pp. 334-346, 2008.
- [90] F. F. Farshad, J. D. Garber, and V. Polaki, "Comprehensive models for predicting corrosion rates in gas wells containing  $\text{CO}_2$ ," *SPE Prod. & Facilities*, vol. 15, no. 3, pp. 183-190, 2000.

- [91] R. N. Maddox and J. H. Erbar, "Natural gas-water system," in *Gas conditioning and processing. vol. 3 advanced techniques and applications*. Norman, OK: Campbell Petroleum Series, 1982, p. 438.
- [92] S. Avila, S. Blanco, I. Velasco, E. Rauzy, and S. Otin, "Thermodynamic properties of synthetic natural gases Part 4 . Dew point curves of synthetic natural gases and their mixtures with water: measurement and correlation," *Fluid Phase Equilibria*, vol. 202, pp. 399-412, 2002.
- [93] J. H. Erbar and R. N. Maddox, "Water hydrocarbon system behavior," *Oil & Gas Journal*, vol. 79, pp. 75-78, 1981.
- [94] D.Y. Peng and D. B. Robinson, "A new two-constant equation of state," *Industrial & Engineering Chemistry Fundamentals*, vol. 15, no. 1, pp. 59-64, 1976.
- [95] K. Nasrifar and O. Bolland, "Prediction of thermodynamic properties of natural gas mixtures using 10 equations of state including a new cubic two-constant equation of state," *Journal of Petroleum Science and Engineering*, vol. 51, pp. 253-266, 2006.
- [96] M. F. Alfradique and M. Castier, "Calculation of phase equilibrium of natural gases with the Peng-Robinson and PC-SAFT equations of state," *Oil and Gas Science and Technology*, vol. 62, no. 5, pp. 707-714, 2007.
- [97] P. Ghosh, "Prediction of vapor-liquid equilibria using Peng-Robinson and Soave-Redlich-Kwong equations of state," *Chemical Engineering & Technology*, vol. 22, no. 5, pp. 379-399, 1999.
- [98] J. Wu and J. M. Prausnitz, "Phase equilibria for systems containing hydrocarbons, water, and salt: An extended Peng-Robinson equation of state," *Industrial & Engineering Chemistry Research*, vol. 37, no. 5, pp. 1634-1643, 1998.
- [99] E. C. Voutsas, G. C. Boulougouris, I. G. Economou, and D. P. Tassios, "Water/hydrocarbon phase equilibria using the thermodynamic perturbation theory," *Industrial & Engineering Chemistry Research*, vol. 39, no. 3, pp. 797-804, 2000.
- [100] S. Avila, S. T. Blanco, I. Velasco, E. Rauzy, and S. Otin, "Thermodynamic properties of synthetic natural gases: Part 3 dew point curves of synthetic natural gases and their mixtures with water: Measurement and correlation," *Energy & Fuels*, vol. 17, no. 2, pp. 338-343, 2003.

- [101] J. Campbell, "Water-hydrocarbon phase behavior," in *Gas conditioning and processing. Vol. 1 The basic Principles*, 7<sup>th</sup> ed. Norman, OK: Penn Well Books, 1979, pp. 145-185.
- [102] R. C. Reid, J. M. Prausnitz, and B. E. Poling, "Fluid phase equilibrium in multicomponent systems," in *The properties of gases and liquids*, 4<sup>th</sup> ed. New York: McGraw-Hill, 1987, pp. 241-387.
- [103] M. J. Assael, J. P. M. Trusler, and T. F. Tsolakis, "Phase equilibrium calculation," in *Thermophysical properties of fluids: An introduction to their prediction*. London: Imperial College Press, 1996, pp. 207-252.
- [104] R. B. Bird, W. E. Stewart, and E. N. Lightfoot, *Transport Phenomena*, 2<sup>nd</sup> ed. New Jersey: John Wiley & Sons, 2001.
- [105] D. Hinkson, "A study of the chemical composition and corrosivity of the condensate for top of the line CO<sub>2</sub> corrosion," M.S. Thesis, Russ College of Engineering, Department of Chemical Engineering, Ohio University, Athens, OH, 2007.
- [106] K. J. Bell and A. C. Mueller, *Wolverine Tube Heat Exchanger Data Book II*. Wolverine Tube Inc., 2001.
- [107] W. L. McCabe, J. C. Smith, and P. Harriott, "Heat transfer to fluids without phase change," in *Unit Operations Of Chemical Engineering*, 6<sup>th</sup> ed. New York: McGraw-Hill, 2001, pp. 365-371.

**APPENDIX I: CONDENSATION RATE CALCULATION FOR  
EXPERIMENTAL CONDITIONS**

I.1. Condensation rate calculation in a stagnant condition

I.1.1. Mathematical

Although the CO<sub>2</sub> was continuously bubbled, the vapor phase was considered to be stagnant. In a stagnant condition, heat transfer in vapor phase is carried by mean of a natural convection. The correlation for heat transfer coefficient described above cannot be applied. Eq.I-1 [107] is to calculate heat transfer coefficient of vapor in a natural convection condition where the properties are evaluated at an average of bulk temperature and interface temperature.

$$Nu = a(GrPr)^b \quad \text{Eq.I-1}$$

$$\begin{aligned} \text{If } 10^5 < GrPr < 2 \times 10^7 & \quad ; a = 0.54, b = 0.25 \\ 2 \times 10^7 < GrPr < 3 \times 10^{10} & \quad ; a = 0.14, b = 0.33 \end{aligned}$$

Where;

$$Gr = \text{Grashof number} \left( \frac{D^3 \rho^2 g \beta \Delta T}{\mu^2} \right), \text{ dimensionless}$$

$$Pr = \text{Prandtl number} \left( \frac{c_p \mu}{k} \right), \text{ dimensionless}$$

$$h_g = \text{Heat transfer coefficient in the vapor phase, in W/m}^2\text{/K.}$$

$$D = \text{Diameter of glass cell, in m}$$

$$k = \text{Thermal conductivity of vapor phase, in W/m/K}$$

$$\rho = \text{Density of vapor phase, in kg/m}^3$$

$$\beta = \text{The coefficient of thermal expansion, in K}^{-1}$$

$\Delta T$  = The difference in temperature between outside of pipe and fluid distant from surface, in K

$\mu$  = Viscosity of vapor phase, in Pa.s

$c_p$  = Specific heat capacity of vapor phase, in J/kg/K

#### I.1.2. Experimental setup and procedure for the comparison

The comparison was conducted in a 2L glass cell as explained previously in Chapter 3.2.4. A receiver was placed underneath the sample and the condensed water was collected. Condensation rate of water was then calculated and compared to the measurements.

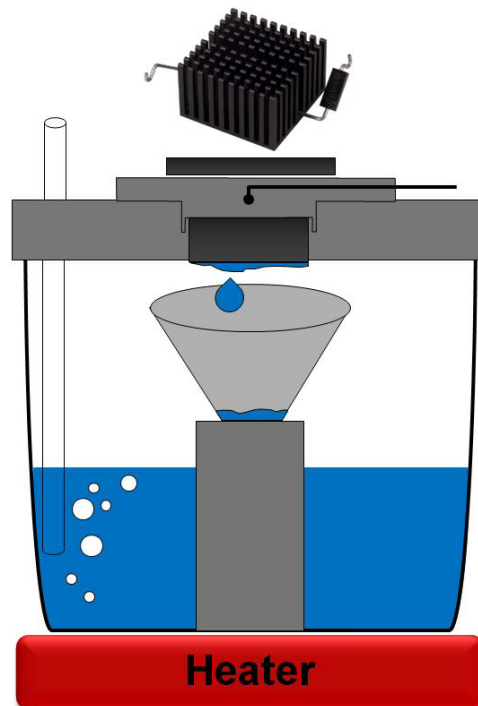


Figure I-1: Experimental setup for comparing condensation rates from measurement and calculation.

## I.1.3. Comparison between experiments and calculation

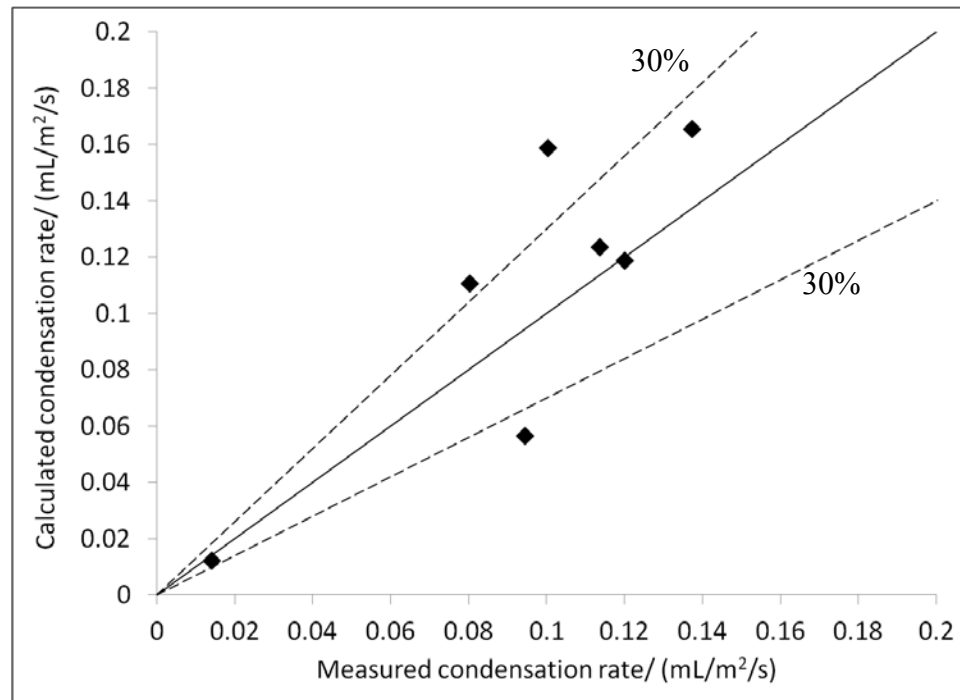


Figure I- 2: The comparison of calculated and measured condensation rate of water in a glass cell setup ( $T_v = 25$  to  $50^\circ\text{C}$ ,  $T_s = 25$  to  $30^\circ\text{C}$ )

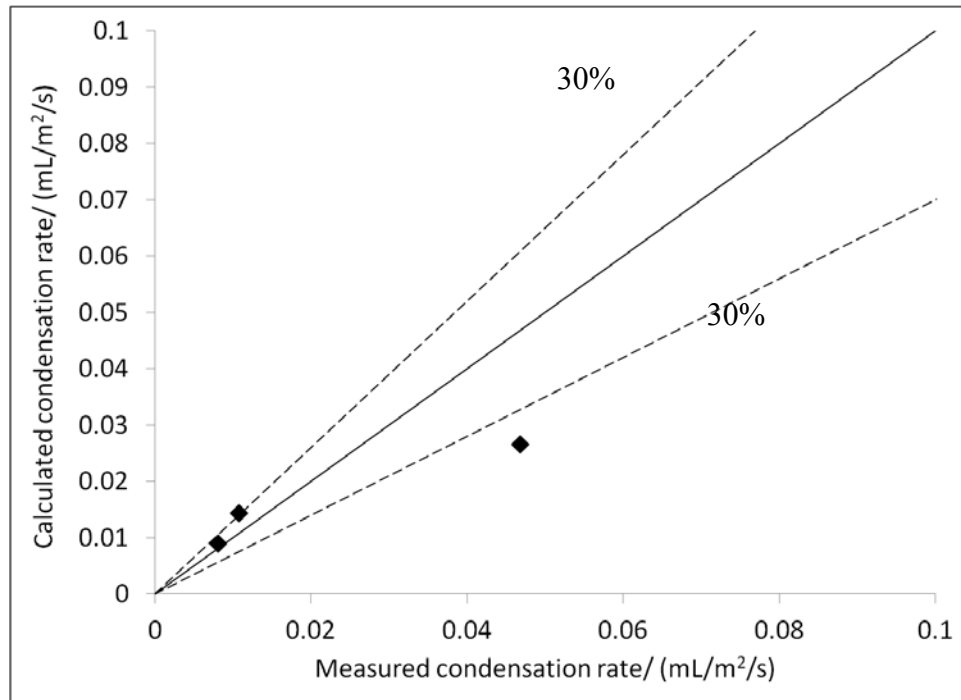


Figure I-3: The comparison of calculated and measured condensation rate of water in co-condensation scenario in a glass cell setup ( $T_v = 30$  to  $40^\circ\text{C}$ ,  $T_s = 30$  to  $35^\circ\text{C}$ ).

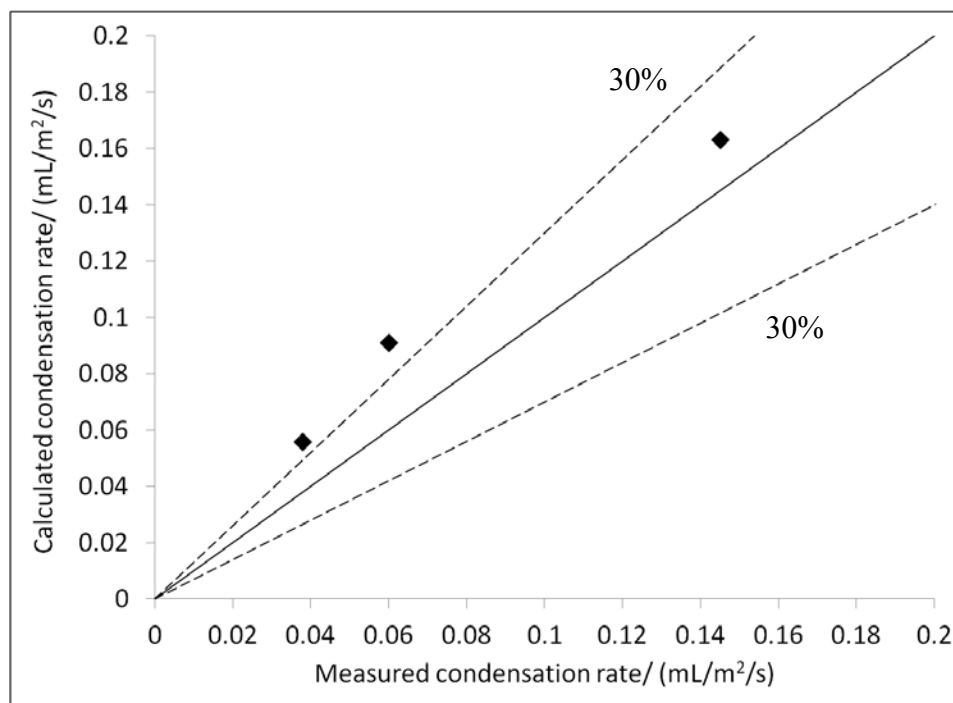
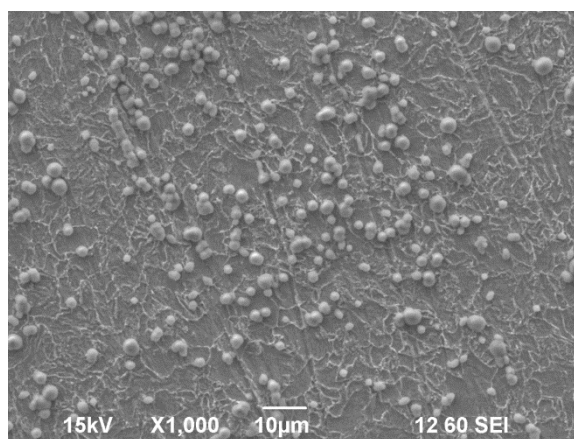


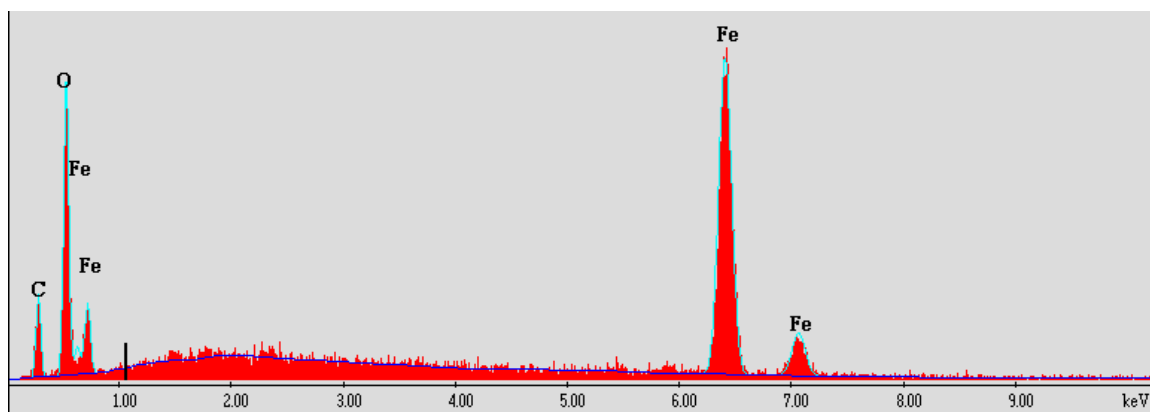
Figure I-4: The comparison of calculated and measured condensation rate of n-heptane in co-condensation scenario in a glass cell setup ( $T_v = 30$  to  $40^\circ\text{C}$ ,  $T_s = 30$  to  $35^\circ\text{C}$ ).

## APPENDIX II: SURFACE ANALYSIS OF CARBON STEEL EXPOSED TO CO-CONDENSATION

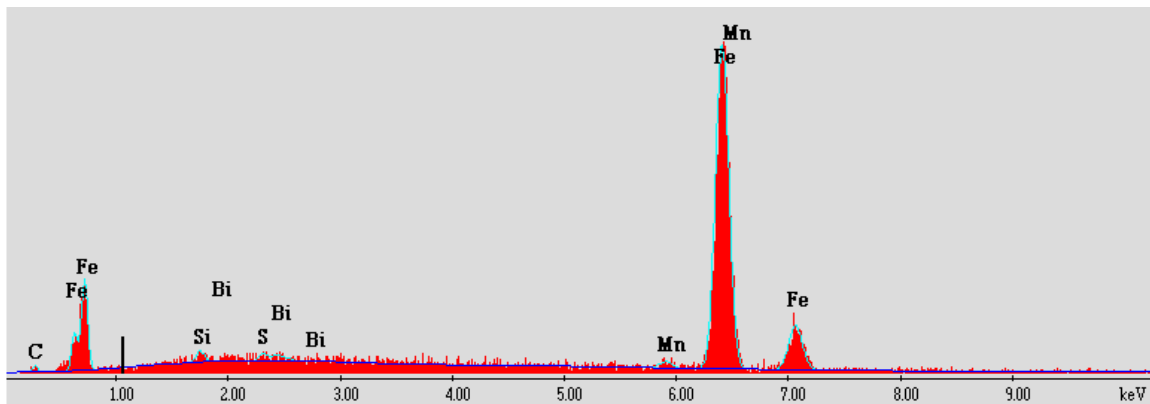
Additional surface analysis of samples exposed to co-condensation of water and three straight chain hydrocarbons are illustrated in this section.



a) SEM Image X1000

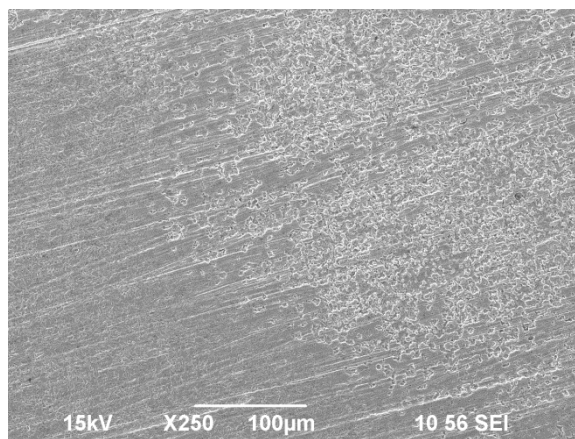


c) EDX analysis on corrosion product particles showing the composition of  $\text{FeCO}_3$



d) EDX analysis on area without corrosion product showing the composition of Iron carbide

Figure II-1: SEM Images and EDX analysis of sample exposed to co-condensation of water and n-heptane before cleaning ( $WCR = 0.05 \text{ mL/m}^2/\text{s}$  and  $C_7CR = 0.33 \text{ mL/m}^2/\text{s}$ ).



a) SEM Image on general area

Figure II-2: SEM Images of sample exposed to co-condensation of water and n-heptane after cleaning ( $WCR = 0.05 \text{ mL/m}^2/\text{s}$  and  $C_7CR = 0.33 \text{ mL/m}^2/\text{s}$ ).

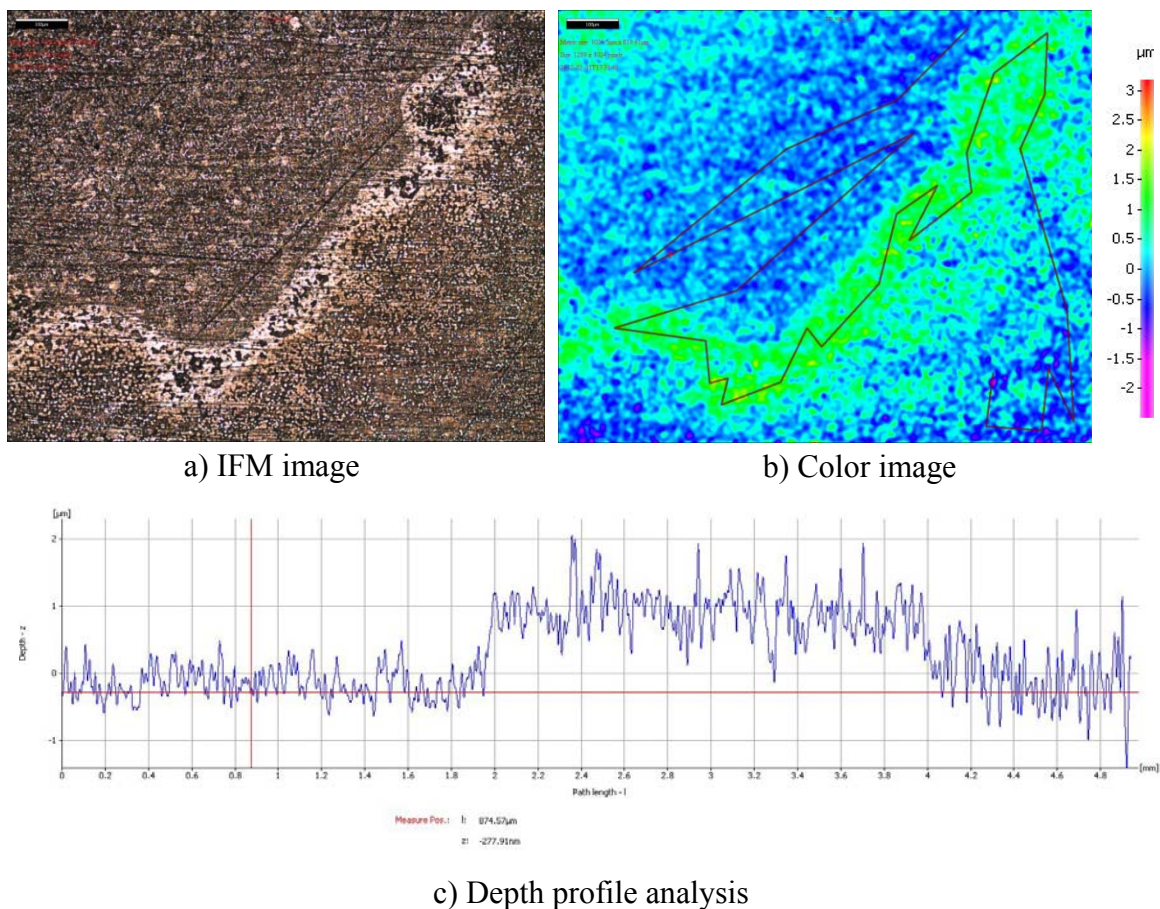
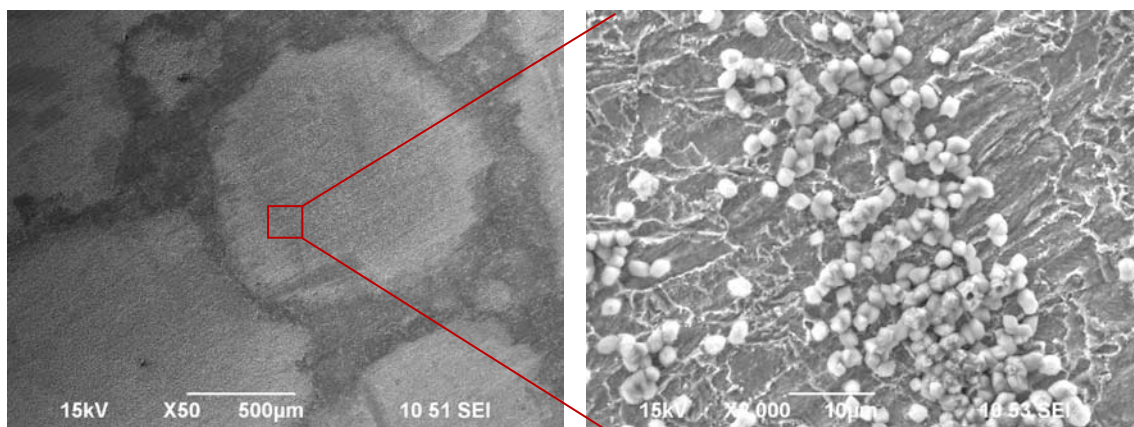


Figure II-3: Surface topography of sample exposed to co-condensation of water and n-heptane ( $WCR = 0.05 \text{ mL/m}^2/\text{s}$  and  $C_7CR = 0.33 \text{ mL/m}^2/\text{s}$ ) after the removal of corrosion product.



a) SEM Image X50

b) SEM Image X2000

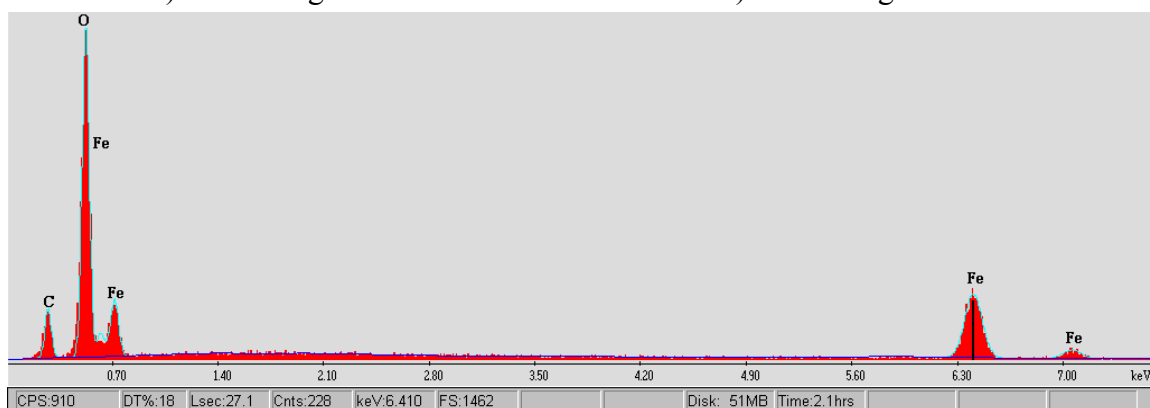
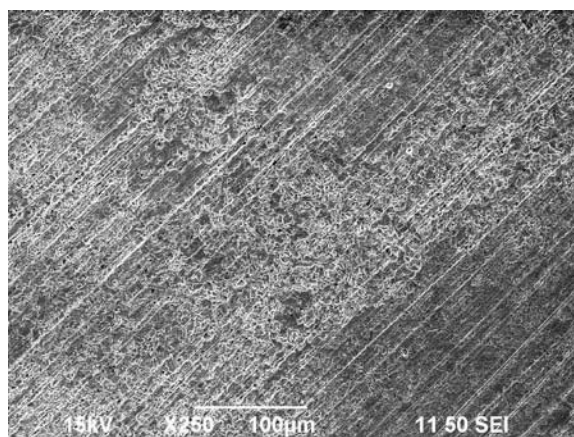
c) EDX analysis on corrosion product particles showing the composition of  $\text{FeCO}_3$ 

Figure II-4: SEM Images and EDX analysis of sample exposed to co-condensation of water and n-octane before cleaning ( $\text{WCR} = 0.05 \text{ mL/m}^2/\text{s}$  and  $\text{C}_8\text{CR} = 0.13 \text{ mL/m}^2/\text{s}$ ).



a) SEM Image X250

Figure II-5: SEM Images of sample exposed to co-condensation of water and n-octane after cleaning ( $WCR = 0.05 \text{ mL/m}^2/\text{s}$  and  $C_8CR = 0.13 \text{ mL/m}^2/\text{s}$ ).

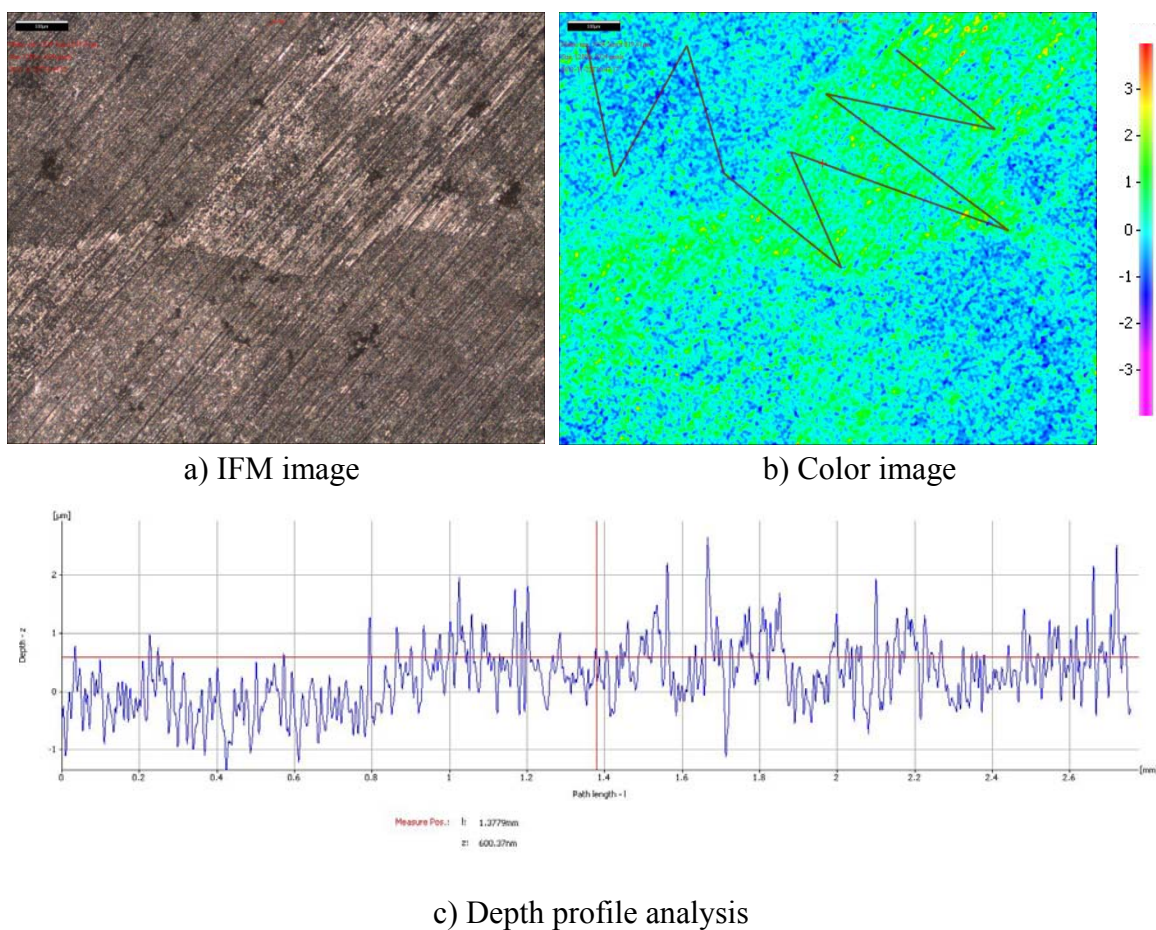
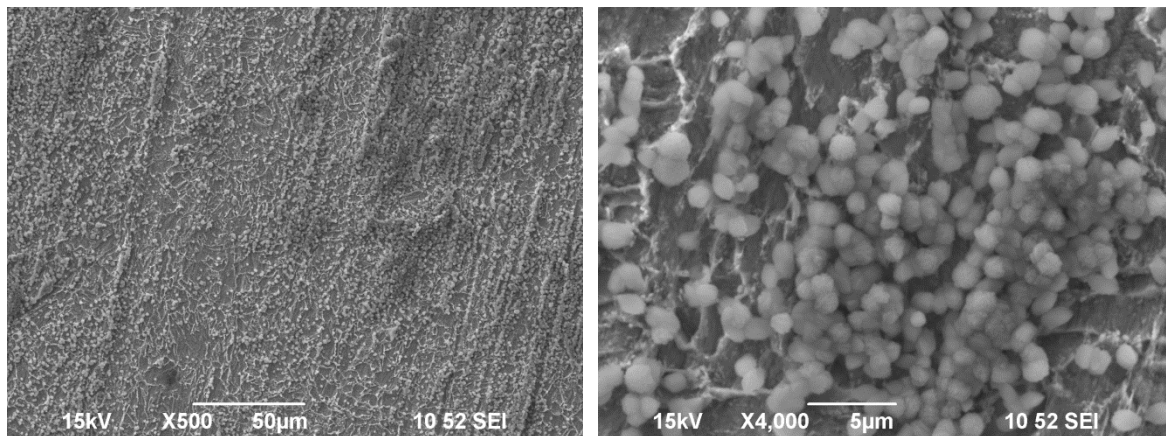
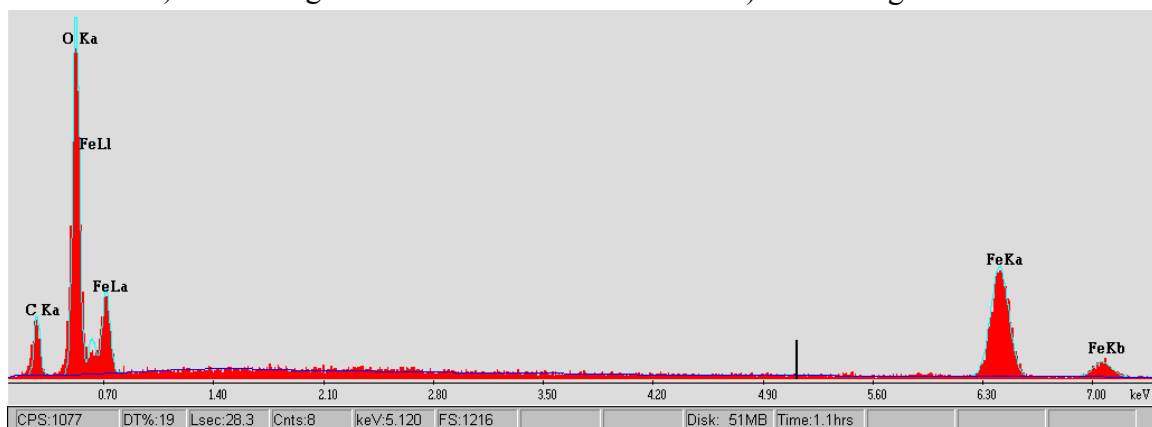
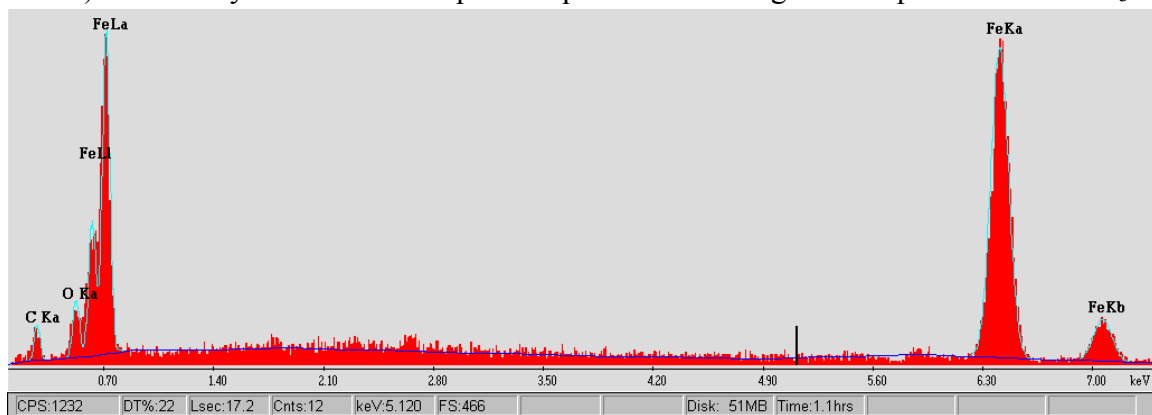


Figure II-6: Surface topography of sample exposed to co-condensation of water and n-octane ( $WCR = 0.05 \text{ mL/m}^2/\text{s}$  and  $C_8CR = 0.13 \text{ mL/m}^2/\text{s}$ ) after the removal of corrosion product.



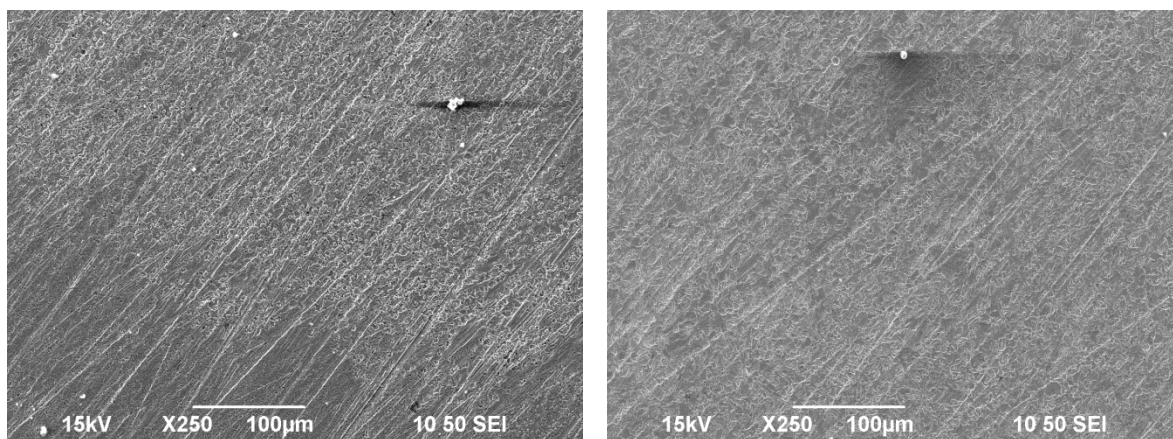
a) SEM Image X500

b) SEM Image X2000

c) EDX analysis on corrosion product particles showing the composition of  $\text{FeCO}_3$ 

d) EDX analysis on area without corrosion product showing the composition of Iron carbide

Figure II-7: SEM Images and EDX analysis of sample exposed to co-condensation of water and n-decane before cleaning ( $\text{WCR} = 0.06 \text{ mL/m}^2/\text{s}$  and  $\text{C}_{10}\text{CR} = 0.02 \text{ mL/m}^2/\text{s}$ ).



a) SEM Image on general area

b) SEM Image on area underneath the big  
water droplet

Figure II-8: SEM Images of sample exposed to co-condensation of water and n-decane after cleaning ( $WCR = 0.06 \text{ mL/m}^2/\text{s}$  and  $C_{10}CR = 0.02 \text{ mL/m}^2/\text{s}$ ).

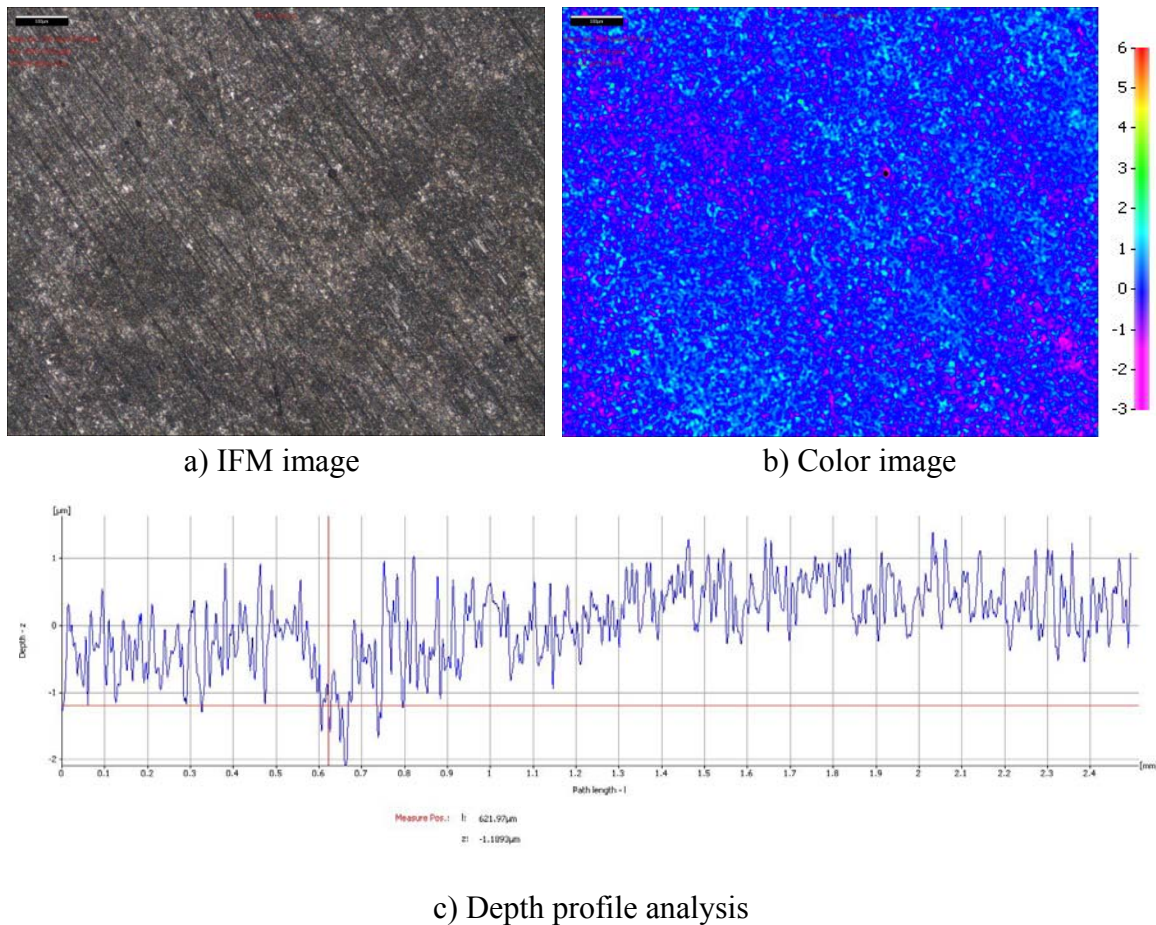


Figure II-9: Surface topography of sample exposed to co-condensation of water and n-decane ( $0.06 \text{ mL/m}^2/\text{s}$  and  $C_{10}CR = 0.02 \text{ mL/m}^2/\text{s}$ ) after the removal of corrosion product.



**OHIO**  
UNIVERSITY

Thesis and Dissertation Services